Imperial College London

The Effect of Debonding on the Vibration Behaviour of CFRP/Epoxy Sandwich Panels

A thesis submitted for the degree of Doctor of Philosophy of Imperial College London and Diploma of Imperial College

July 2019

Shang-Nan Tsai

Department of Mechanical Engineering

Imperial College London

Declaration of Originality

I confirm that the work presented in this thesis is my own work and I am the author of this thesis. I confirm that any other materials are appropriately referenced. This thesis has not been submitted for any other degree or diploma to any other university or institution.

Copyright Declaration

The copyright of this thesis rests with the author and is made available under a Creative Commons Attribution Non-Commercial No Derivatives licence. Researchers are free to copy, distribute or transmit the thesis on the condition that they attribute it, that they do not use it for commercial purposes and that they do not alter, transform or build upon it. For any reuse or redistribution, researchers must make clear to others the licence terms of this work.

Abstract

Fibre composite materials are widely used because they are light but strong. This work discusses two topics of composites: 1. Vibration behaviours of debonded sandwich structures. 2. The fracture and fatigue behaviours of carbon fibre reinforced polymers (CFRPs) with nanoparticle-modified sizing.

Debonds between the facesheets and the core of sandwich structures can weaken the structures, whilst affecting its vibration response. The vibration behaviours of sandwich structures were analysed by conducting hammer impact tests and finite element simulations on the structures with different debond configurations, facesheet stacking, matrix modifiers and curvatures. For the flat structure using the $[0°]_4$ facesheets, the natural frequency significantly decreased by 57 % when there was an 80 mm debonded region due to the reduction in the stiffness. The natural frequencies of the bending modes dropped most significantly when two debonds were present in the same location for both upper and lower facesheets. The curvature had more effect on the lateral modes than other modes since the mode shapes involved torsional movements. Reduction in the natural frequencies can cause a structure to vibrate at resonance and hence cause structural failure, which is critical for the applications of sandwich structures.

Fibre composites with thermoset polymer matrices are widely used, but the brittleness of thermoset polymers used as the matrix can limit their applications. In this work, silica nanoparticles (SNPs) were used to modify two carbon-fibre sizings. Mode I interlaminar fracture tests and fatigue crack growth tests were conducted on the sizing-modified CFRPs. Although there was no significant change in the fatigue crack growth rate, the fracture energy was significantly increased from 166 J/m^2 to 220 J/m^2 with the addition of only 0.89 wt% on fibre weight of SNPs. This is significantly more efficient than directly adding SNPs into the matrix to achieve the same improvement.

Acknowledgments

Foremost, I would like to express my gratitude to my supervisors, Dr. Ambrose C. Taylor and Dr. Soraia Pimenta. I would like to especially thank Dr. Taylor for the support, advice and guidance that he has provided through my PhD studies. I would like to thank Dr. Pimenta for her support of testing equipments and advice on simulation.

I would like to thank Dr. Felicity J. Guild for the help on finite element simulation and Dr. Christoph Schwingshackl for his support of experiments. A special thanks to Dr. Declan Carolan for his support of operating the FE-SEM and help on fracture and fatigue tests. I would also like to thank Dr. Stephan Sprenger of Evonik Nutrition and Care GmbH for the supply of materials and the related advice. I am thankful to Ruth, Suresh, Gani, Luke and Valentina for their help on experiments and equipment operation, especially to Ruth for her help and training on the equipments. I would like to thank Dr. Tsung-Han Hsieh and Dr. Meng-Kao Yeh in Taiwan for their help and career advice. My special thanks to the Ministry of Education, Republic of China (Taiwan), for a PhD studentship to support my studies.

I would like to thank my friends and colleagues in the Mechanics of Materials division: Tasnuva, Xinying, Fabian, Sammy, Sherry and Derek for many helpful suggestions and laughs, without these the years would have been much harder. Thanks goes to my friends in the UK and in Taiwan: especially for Chia-Han, Justin Chu and Hsi-Kai. There are too many of you to be named and I am grateful to all of you for being on my side. Also, a special thanks to Yan-Lun and Hsien-Yung having always been great listeners and encouraged me.

Last but not least, I must thank my family for their unconditional love and support, not just through my PhD studies but up until now. Without their support I would not have accomplished the present work.

Thanks!

Table of Contents

Abstract i

Acknowledgments ii

Table of Contents iii

List of Figures viii

List of Tables xii

Nomenclature xiv

1 Introduction 1

1.1 Background 1

1.2 Aims and Objectives 3

1.3 Thesis Structure 3

2 Literature Review 5

2.1 Introduction 5

2.2 Epoxy Polymers and Epoxy Toughening 5

2.2.1 Toughening of Epoxy Polymers Using Rubber Particles 7

2.2.2 Toughening of Epoxy Polymers Using Rigid Particles 9

2.3 Fibre Reinforced Polymer (FRP) Composites and FRP Toughening 11

2.3.1 Failure Mechanisms of FRPs 12

2.3.2 Toughening of FRPs 12

2.4 Toughening of Fibre Composites Using Modified Sizings 14

2.4.1 Fibre Sizings 14

2.4.2 Toughening Using SNP-Modified Sizings . . . 15
2.5 Sandwich Structures . . . 16
2.5.1 Vibration of Sandwich Structures . . . 16
2.5.2 Debonding of Sandwich Structures . . . 17
2.5.3 Effects of Debonded Regions on the Vibration Behaviours of Sandwich Structures . . . 17
2.5.4 Finite Element Simulation of the Vibration Behaviours of Sandwich Structures . . . 18
2.5.5 Discussion . . . 19
2.6 Conclusions . . . 19

3 Materials and Manufacturing 20
3.1 Introduction . . . 20
3.2 Sizing-modified Carbon Fibre Composites . . . 20
3.2.1 Carbon Fibre Composite . . . 20
3.2.2 Sizing Formulations . . . 21
3.3 Sandwich Structure Materials . . . 21
3.3.1 Carbon Fibres . . . 21
3.3.2 Epoxy Matrix . . . 22
3.3.3 Silica Nanoparticles . . . 22
3.3.4 Graphene . . . 23
3.3.5 Formulations . . . 23
3.4 Sandwich Structure Manufacturing . . . 24
3.4.1 Bulk Epoxy Plates . . . 24
3.4.2 Carbon Fibre Composite Facesheets . . . 25
3.4.3 Sandwich Structure Construction . . . 27
3.4.4 Location of Artificial Debonded Regions . . . 32
3.5 Conclusions . . . 34

4 Experimental Methods 35
4.1 Introduction . . . 35
4.2 Tensile Tests . . . 35
4.2.1 Bulk Epoxy Tensile Tests . . . 35
4.2.2 Carbon Fibre Composite Tensile Tests . . . 37
4.3 Density Tests . . . 38
4.4 Sizing-modified Carbon Fibre Composite . . . 39
4.4.1 Double Cantilever Beam (DCB) Specimen Preparation . . . 39
4.4.2 Mode I Interlaminar Fracture Tests . . . 40

4.4.3 Fatigue Crack Growth (FCG) . . . 41
4.4.4 Microscopy Analysis . . . 43
4.5 Fibre Volume Fraction . . . 43
4.6 Vibration Tests . . . 45
4.7 Replicates . . . 47
4.8 Conclusions . . . 48

5 Finite Element Simulation **49**
5.1 Introduction . . . 49
5.2 Flat Structure Model Development . . . 49
5.2.1 Flat Sandwich Structure Model . . . 49
5.2.2 Debonded Region Modelling . . . 50
5.3 Curved Structure Model Development . . . 51
5.4 Natural Frequency and Mode Shape Simulations . . . 52
5.5 Convergence Study . . . 52
5.6 Overlapping Inspection . . . 53
5.7 Conclusions . . . 56

6 Mechanical Properties Results **57**
6.1 Introduction . . . 57
6.2 Bulk Epoxy . . . 57
6.2.1 Tensile Tests . . . 57
6.2.2 Density . . . 59
6.3 Carbon Fibre Composites . . . 59
6.3.1 Fibre Volume Fraction of Sizing-modified Carbon Fibre Composite . . . 59
6.3.2 Carbon Fibre Composites of Sandwich Structures . . . 60
6.4 Conclusions . . . 63

7 Fracture and Fatigue Behaviours of Carbon Fibre Composites with Silica Nanoparticle Modified Sizings **65**
7.1 Introduction . . . 65
7.2 Interlaminar Fracture Energy . . . 65
7.3 Comparison with Carbon Fibre Composites Using SNP-modified Matrices . . . 69
7.4 Fatigue Crack Growth . . . 70
7.5 Fractographic Studies . . . 72
7.6 Conclusions . . . 75

8 Vibration Behaviours of Flat Sandwich Structures with Single or Double Face/-Core Debonding **76**

8.1 Introduction 76
8.2 Bending Stiffness Matrix of the Flat, Intact Sandwich Structures 77
8.3 Effects of Debonding Length on the Flat Sandwich Structures 78
8.4 Effects of CFRP Stacking Orientation on the Flat Sandwich Structures 80
8.5 Effects of Material Change on the Flat Sandwich Structures 83
8.6 Effects of Double Debonding on the Flat Sandwich Structures 83
8.6.1 Effects of Increasing the Separation (Δ) between Two Debonds (Flat) . 85
8.6.2 Effects of the Positions of Two Debonds (Flat) 86
8.6.3 Effects of Material Change on the Sandwich Structure with Two Debonds (Flat) 87
8.7 Conclusions 88

9 Vibration Behaviours of Curved Sandwich Structures with Debonding 89
9.1 Introduction 89
9.2 Curvature of Beam 90
9.3 Comparisons of Simulation and Experimental Results 90
9.4 Effects of Curvature on the Intact Sandwich Structure 91
9.5 Effects of Debonding Length on the Curved Sandwich Structures 94
9.6 Effects of CFRP Stacking Orientation on the Curved Sandwich Structures . . . 98
9.7 Effects of Double Debonding on the Curved Sandwich Structures 98
9.7.1 Effects of Increasing the Separation (Δ) between Two Debonds (Curved) 98
9.7.2 Effects of the Positions of Two Debonds (Curved) 100
9.8 Effects of Material Change on the Curved Sandwich Structures 101
9.8.1 Effects of Material Change on the Single-debonded Curved Sandwich Structures 103
9.8.2 Effects of Material Change on the Double-debonded Curved Sandwich Structures 104
9.9 Conclusions 105

10 Discussion 106
10.1 Introduction 106
10.2 Fracture and Fatigue Behaviours of Carbon Fibre Composites with Silica Nanoparticle Modified Sizings 106
10.3 Vibration Behaviours of Sandwich Structures with Debonded Regions 107
10.4 Conclusions 111

11 Conclusions and Future Work 112
11.1 Introduction 112

11.2 Fracture and Fatigue Behaviours of Carbon Fibre Composites with Silica Nanoparticle Modified Sizings . . . 113
11.3 Vibration Behaviours of Sandwich Structures with Debonded Regions . . . 113
11.4 Future Work . . . 114
11.4.1 Improving the Toughness of Fibre Composites Using Modified Sizings . 115
11.4.2 Vibration Behaviours of Debonded Sandwich Structures . . . 115

References **117**

Appendix A MATLAB Code **127**
Transferring Vibration Raw Data to Excel File . . . 127
Bending and Torsion Modes: Plotting Frequency Response Figure, Finding Resonance Frequencies and Identifying Mode Shapes . . . 129
Lateral Modes: Plotting Frequency Response Figure, Finding Resonance Frequencies and Identifying Mode Shapes . . . 137

Appendix B Simulation and Experimental Results of Sandwich Structures Using Unmodified Epoxy Resin **143**
Flat Structures . . . 143
15°-curved Structures . . . 149
30°-curved Structures . . . 153

Appendix C Publications **157**
Journal Publications . . . 157
Conference Papers . . . 157
Conference Abstracts . . . 157
Republication Permissions . . . 158

List of Figures

2.1 Epoxide group [1] . . . 6
2.2 Fracture energy of bulk epoxy modified with silica nanoparticles with different particle sizes [2] . . . 7
2.3 Sketch of a core-shell rubber particle [3] . . . 8
2.4 Sketch of toughening mechanisms of rubber-modified epoxy polymers [4]. $2r_y$ indicates the diameter of the process zone . . . 8
2.5 Crack pinning and tail-shape features [5, 6] . . . 9
2.6 Crack deflection in epoxies modified using microparticles (left) and nanoparticles (right) [7, 8] . . . 10
2.7 Rigid particle debonding followed by plastic void growth [7, 9] . . . 11
2.8 Failure modes in FRPs [10, 11] . . . 12
2.9 Mode I interlaminar fracture energy of composite versus fracture energy of matrix [12] (Enlarged) . . . 13
2.10 SEM images of fracture surfaces of quasi-isotropic GFRP [13] . . . 14
2.11 SEM images of fracture surfaces of GFRPs using unmodified and SNP-modified sizings [14] . . . 15
2.12 Bending rigidity of sandwich structures with delaminations of various lengths. Reproduced from [15] . . . 17
2.13 Fundamental natural frequency degradation of a 270 mm long sandwich structure with delaminations of various lengths. Reproduced from [15] . . . 18

3.1 UT-C300 fibre diameter measurement and principal axes of a lamina . . . 22
3.2 CFRP stacking orientations for the facesheets . . . 23
3.3 Lateral sketch of curved core plates with a curvature angle of 15° or 30° . . . 24
3.4 Oven curing cycle for making epoxy plates for sandwich structure cores . . . 26

3.5 Sketch of RIFT stacking . . . 26
3.6 RIFT set-up . . . 27
3.7 RIFT curing cycle for making CFRPs for sandwich structure facesheets . . . 27
3.8 Flat sandwich structure . . . 28
3.9 Sketch and local magnification of debonded region . . . 29
3.10 Sketches of the aluminium plates used for making 15° and 30°-curved sandwich structures by RIFT . . . 30
3.11 Sketch of RIFT set-up for making curved sandwich structures . . . 30
3.12 Curved aluminium mould and the RIFT stacking for making 30° sandwich structures 31
3.13 30°-curved sandwich structure manufactured using RIFT method, crack of core indicated . . . 31
3.14 Finite element models of flat sandwich structures with locations of debonded regions (shown in red) . . . 33
3.15 Finite element models of 30°-curved sandwich structures with locations of debonded regions (shown in red) . . . 33

4.1 Epoxy polymer tensile dogbone dimensions and video extensometer image . . . 36
4.2 Tensile stress-strain curve of unmodified epoxy polymer showing strain range used to calculate tensile modulus, E . . . 37
4.3 Pycnometer for measuring density . . . 39
4.4 Tested specimen of mode I interlaminar fracture test . . . 40
4.5 Max and 5 % increase in compliance for determining $G_{IC,init}$ for a mode I interlaminar fracture test; the reload curve has been offset by 5 mm for clarity [16] . . . 41
4.6 Sinusoidal waveform and displacements of FCG test . . . 42
4.7 Images for calculating fibre volume fraction of CFRPs . . . 44
4.8 Hammer test setup . . . 45
4.9 Points on the sample for hammer strike and accelerometer . . . 46
4.10 Example of amplitude, coherence and phase response of vibration tests . . . 47

5.1 Sketch of C3D8 element . . . 50
5.2 Tie constraint applied at the bonded regions of the sandwich structure model with an 80 mm debond . . . 51
5.3 Master (shown in red) and slave (shown in yellow) surfaces applied in the debonded region of the sandwich structure model with an 80 mm debond . . . 51
5.4 Convergence study: relative natural frequencies comparing to the coarsest mesh (1536 elements) for the modes . . . 53
5.5 Simulation mode shape of vibration mode 1 of the flat sandwich structure: unmodified resin, $[0°]_4$ facesheets, 80 mm debonded region . . . 54

5.6 Overlapping inspection of the deformation of vibration mode 1 of the flat sandwich structure: unmodified resin, $[0°]_4$ facesheets, 80 mm debonded region 54
5.7 Overlapping inspection of the deformation of vibration mode 5 of the sandwich structure: unmodified resin, $[0°]_4$ facesheets, 80 mm debonded region 55

6.1 Tensile modulus of the epoxy polymers used as the core and the facesheet matrix of the sandwich structures 58
6.2 Longitudinal tensile modulus and fibre volume fraction of the CFRP used as the facesheets of the sandwich structures 61
6.3 Lateral tensile modulus of the CFRP used as the facesheets of the sandwich structures 63

7.1 Fracture energies and fibre volume fraction comparison of the modified-sizing composites 66
7.2 Load-displacement and crack length-displacement comparison of unmodified (H0) and SNP-modified (H2) UD carbon fibre composites 68
7.3 R-curve (resistance curve) comparison of unmodified and SNP-modified UD carbon fibre composites 69
7.4 Fatigue crack growth (FCG) curve of UD carbon fibre composite using sizing N0 . 71
7.5 Silica nanoparticle dispersion and fibre/matrix adhesion (DCB fracture surfaces) . . 73
7.6 Fibre pull out and fragmentation (DCB fracture surfaces) 74
7.7 Fibre/matrix adhesion (fracture surfaces from FCG) 74

8.1 Simulation mode shapes of intact structure using unmodified resin and $[0°]_4$ stacking 80
8.2 Relative natural frequencies affected by central single debonding. The order of modes in the legends follows the increasing of natural frequency 82
8.3 Influence of material change on the natural frequencies of sandwich structures (simulation results) 84
8.4 Relative natural frequencies affected by double debonding (simulation results) . . . 85
8.5 Simulation mode shapes of S-debonded structure using unmodified resin and $[0°]_4$ stacking 87
8.6 Gradient m_f of double-debonded structures, $[0°]_4$ facesheets (simulation results) . . 88

9.1 Lateral sketch of curved sandwich structures 90
9.2 Simulation mode shapes of 30°-curved, intact structure using unmodified resin and $[0°]_4$ facesheets 93
9.3 Relative natural frequencies of intact, flat and curved sandwich structures (simulation results) 94
9.4 Relative natural frequencies of bending modes affected by a central debonding and curvature (simulation results) 96

9.5 Relative natural frequencies of torsion and lateral modes affected by a central debonding and curvature (simulation results) 97
9.6 Relative natural frequencies of bending modes affected by double debonding and curvature (simulation results) 99
9.7 Relative natural frequencies of torsion and lateral modes affected by double debonding and curvature (simulation results) 100
9.8 Simulation mode shapes of 30°-curved, S-debonded structure using unmodified resin and $[0°]_4$ stacking 102
9.9 Influence of material change on the natural frequencies of bending modes of intact, flat or curved structures, $[0°]_4$ facesheets (simulation results) 103
9.10 Influence of material change on the natural frequencies of bending modes of intact, flat or curved structures, all facesheets (simulation results) 103
9.11 Gradient m_f of single-debonded, flat or curved structures, $[0°]_4$ facesheets (simulation results) 104
9.12 Gradient m_f of double-debonded, flat or curved structures, $[0°]_4$ facesheets (simulation results) 105

List of Tables

3.1 Sizing formulations (wt% on fibre mass) 21
3.2 Sandwich formulations and compositions 23
3.3 Flat sandwich structure sizes 28
3.4 Curved sandwich structure sizes 31

4.1 Dimensions of CFRP and end tabs for tensile tests 38
4.2 FCG test recording intervals 42
4.3 Grinding and polishing process for measuring fibre volume fraction 44
4.4 Numbers of specimens used for mechanical property tests of sandwich structures . 48
4.5 Numbers of specimens of sizing-modified CFRPs 48
4.6 Numbers of specimens used for hammer impact tests 48

5.1 Overlapping inspection results of the 80-mm-debonded flat sandwich structure model using unmodified resin and $[0^\circ]_4$ facesheets 56

6.1 Measured mechanical properties of the bulk epoxy used as the core of the sandwich structures 58
6.2 Fibre volume fraction of the sizing-modified CFRP 60
6.3 Fibre volume fraction of the CFRP used as the facesheets of the sandwich structures 61
6.4 Measured mechanical properties of the CFRP used as the facesheets of the sandwich structures 62

7.1 Fracture energies of the modified-sizing composites 66
7.2 Improvement of $G_{IC,prop}$ compared with literature 70
7.3 Fatigue gradient of the sizing-modified composites and comparison with metals . . 71

8.1 Natural frequencies and mode shapes of intact structure using unmodified resin . . 79

8.2 Natural frequencies and mode shapes of 80-mm-debonded structure using unmodified resin 81

9.1 Natural frequencies and mode shapes of intact, 30°-curved structure using unmodified resin 91

9.2 Natural frequencies and mode shapes of 80-mm-debonded, 30°-curved structure using unmodified resin 92

Nomenclature

Abbreviations

3D	Three-dimensional
AEW	Anhydride equivalent weight
ASTM	American Society for Testing and Materials
BS	British Standard
CAD	Computer aided design
CFRP	Carbon fibre reinforced polymer
CNT	Carbon nanotube
CSR	Core-shell rubber
CTBN	Carboxyl-terminated butadiene-acrylonitrile
D	Debonded regions at diagonal positions
DCB	Double cantilever beam
DGEBA	Diglycidyl ether of bis-phenol A
EEW	Epoxy equivalent weight
FCG	Fatigue crack growth
FE	Finite element
FE-SEM	Field-emission scanning electron microscope
FEA	Finite element analysis
FFT	Fast Fourier transform
FRP	Fibre reinforced polymer

GFRP	Glass fibre reinforced polymer
ILSS	Interlaminar shear strength
ISO	International Organization for Standardization
MCC	Modified compliance calibration
MWCNT	Multiwalled carbon nanotube
NDT	Non-destructive testing
PE	Polyester
PTFE	Polytetrafluoroethylene
RIFT	Resin infusion under flexible tooling
rpm	Revolutions per minute
S	Debonded regions at symmetric positions
SD	Standard deviation
SEM	Scanning electron microscope
SNP	Silica nanoparticle
UD	Unidirectional
VARI	Vacuum assisted resin infusion
wt%	Weight percentage

English Alphabet

$2h$	Specimen thickness
$2r_y$	Diameter of the process zone
a	Crack length
b	Specimen width
C	Compliance
C_0	Initial compliance
d	Element of bending stiffness matrix, D
D	Bending stiffness matrix of the intact sandwich structure
D_0	Bending stiffness matrix of the intact sandwich structure using $[0°]_4$ facesheets
D_{90}	Bending stiffness matrix of the intact sandwich structure using $[90°]_4$ facesheets

$D_{\pm 45}$	Bending stiffness matrix of the intact sandwich structure using [+45°/-45°]$_s$ facesheets
E	Tensile modulus or Young's modulus
E_1	Longitudinal tensile modulus
$E_{1,\text{flex}}$	Flexural modulus
E_2	Transverse tensile modulus
E_3	Out-of-plane tensile modulus
f_n	Natural frequency of mode n
$\text{f}_{\text{n,intact}}$	Natural frequency of mode n of the intact structure
$\text{f}_{\text{n,flat,intact}}$	Natural frequency of mode n of the flat, intact structure
F	Large-displacement correction factor
G_I	Mode I fracture energy
G_IC	Composite fracture energy
$G_{\text{IC,init}}$	Composite fracture energy at crack initiation
$G_{\text{IC,prop}}$	Composite fracture energy during crack propagation
G_{Imax}	Maximum strain energy release rate
G_th	Threshold fracture energy
h	Half of specimen thickness
K_I	Mode I stress intensity factor
l_1	Distance from the centre of the pin hole to the mid-plane of the specimen
l_2	Distance from the centre of the pin hole to the edge of the load block
L	Specimen length
m	Slope of the straight line fitted to the $(bC/N)^{1/3}$ against $(a/2h)$ data
m_G	Gradient of steady crack growth (Paris law constant), G_I used as the horizontal axis
m_K	Gradient of steady crack growth (Paris law constant), K_I used as the horizontal axis
m_f	Gradient of natural frequency to $\sqrt{E_{1,\text{flex}}/\rho_\text{sand}}$
N	Load block correction factor
P	Load

r_y	Radius of the process zone
R	Displacement ratio for the cyclic loading
S_{12}	In-plane shear modulus
S_{13}	Out-of-plane shear modulus
S_{23}	Orthotropic shear modulus
t	Specimen thickness
T_g	Glass transition temperature
V_f	Fibre volume fraction
W_A	Mass of pycnometer filled with deionised water
W_B	Mass of pycnometer containing sample and filled with deionised water
W_S	Mass of dry sample
W	Specimen width

Greek Alphabet

Δ	Separation between debonded regions
$\Delta\varepsilon_{lat}$	Lateral strain
$\Delta\varepsilon_{long}$	Longitudinal strain
δ	Displacement
$\delta_{f,max}$	Maximum displacement for the cyclic loading
$\delta_{f,mean}$	Mean displacement for the cyclic loading
$\delta_{f,min}$	Minimum displacement for the cyclic loading
ε	Strain
ν	Poisson's ratio
ν_{12}	In-plane Poisson's ratio
ν_{13}	Out-of-plane Poisson's ratio
ν_{23}	Orthotropic Poisson's ratio
ρ	Density
ρ_{sand}	Effective density of sandwich structure
ρ_w	Density of water
σ	Stress

Chapter 1

Introduction

1.1 Background

Composite materials have been widely used in many areas such as the aerospace, ship-building, automotive and energy industries [17–19]. Within composites, sandwich structures and fibre reinforced polymers (FRPs) are widely used because of their light weight and high mechanical strength.

For practical applications of composite materials, adhesion is an important issue since it affects the performance of structures. Poor adhesion is not desired as it can result in the formation of cracks and reduce the strength and stiffness of the structures, which can lead to failure and cause safety problems. The adhesion of composites can be classified into two types: macroscopic and microscopic adhesion. For the macroscopic scale, it can be the adhesion between two different materials, e.g. in sandwich structures which are manufactured by adhering two facesheets to a core. While for the microscopic scale, it can be the adhesion in a material, e.g. fibre-matrix adhesion in FRPs. Micro-scale cracks can grow and lead to macro-scale cracks in structures, which can further result in large-scale debonding and even failure of the structures. Both macroscopic and microscopic adhesion can affect the mechanical properties, such as strength, stiffness and toughness, of composite structures and have a significant influence on their applications.

As its name implies, a sandwich structure is composed of a core between two facesheets, which are adhesively bonded together. These facesheets take most of the load and provide most of the resistance to bending, therefore they are usually made of high stiffness materials, e.g. FRPs or metal panels, whereas the core only takes shear stress, so it can be light and relatively

low strength [20].

The shapes of sandwich structures can affect their stiffness and hence also have an influence on their uses. In practical applications, in addition to flat structures, curved sandwich structures are also widely used, for example in wind turbine blades. On the other hand, structures which are designed to be flat can become curved during in service, which affects the stiffness, strength and safety of the structures.

Perfect adhesion between the facesheets and the core of sandwich structures is critical for their applications. However, due to manufacturing defects or in-service damage, debonding may easily occur between the facesheets and the core of sandwich structures. These debonded regions reduce the strength and the stiffness of the structure and also influence its response to vibration. For practical applications, avoiding resonance is extremely important for preventing large displacements and failure. Vibration may cause debonded regions to grow further, weakening the structure even more. The vibration response of sandwich structures can also be affected by the composition of the materials and the stacking sequence of the facesheet laminate (if FRPs are used), and of the shapes of the structures. Therefore, how debonded regions, materials and shapes affect the vibration response of sandwich structures is a critical issue in practical applications.

Since debonded regions affect the stiffness of the structures and hence affect the vibration response, by measuring the vibration response of damaged structures, the damaging conditions can be identified, which is one method of non-destructive testing (NDT). NDT uses techniques to evaluate the properties of objects without causing damage to them. However, there are difficulties when conducting different types of NDT, for example, ultrasonic inspection requires the tested targets to be good conductors of sound and to have accessible surfaces. While for measuring vibration response, contacting the surfaces is not necessary if non-contact devices (e.g. laser Doppler vibrometer) are used. Therefore, measuring the vibration response of structures provides an alternative choice of NDT and has the ability to detect debonding in sandwich structures.

FRPs can be found in our daily lives such as sportscar bodies, aircraft fuselages, ship hulls and wind turbine blades. Such fibre composites are typically composed of continuous fibres embedded in a thermoset polymer matrix. However, thermoset polymers are very brittle because they are highly crosslinked, which can reduce the toughness of the fibre composite parts and limit their applications. To overcome this disadvantage, second-phase modifiers which have been used to modify thermoset polymers are added into the thermoset matrices to improve the toughness of the FRPs. Within different modifiers, silica nanoparticles (SNPs) have been found to improve the toughness and fatigue behaviour of fibre composites [13, 21–26]. However, directly adding modifiers into the matrices of fibre composites requires significant addition of modifiers which leads to an increased cost for practical applications.

Sizings are the agents applied to raw fibres to protect the fibres, they affect the adhesion between the fibres and the matrix in the composites, and hence affect the strength and toughness. Modifying the sizings of fibres to improve the adhesion between the fibres and the matrix has been reported to improve the fracture and fatigue behaviours of glass fibre composites and can be more efficient than adding a significant amount of modifiers into the matrices [14].

1.2 Aims and Objectives

There are two main aims of this study. The first is to investigate how the vibration behaviours of debonded sandwich structures are affected by different factors. The second aim is to improve the toughness of carbon fibre reinforced polymers (CFRPs) using a more efficient method than directly adding modifiers into the matrix. This thesis involves the study of the following objectives on:

1. Vibration behaviours of debonded sandwich structures by investigating the effect of:
   - Single face/core debonded region of different lengths
   - Double face/core debonded regions of different configurations
   - Facesheet CFRP stacking orientations
   - Different materials (achieved by adding modifiers into the core epoxy polymer and facesheet CFRP matrix)
   - Curvature of the sandwich structures

   Since the effects of these factors when combined have been rarely discussed. The aim is to identify the effects of these factors on the vibration response of sandwich structures and compare their relative significance.

2. Fracture and fatigue behaviours of CFRPs with SNP-modified sizing. The aim is to reduce the addition levels of SNPs required to improve the fracture toughness and the fatigue life of the fibre composites by introducing the SNPs into the fibre sizings rather than into the matrix.

1.3 Thesis Structure

This thesis is divided into ten chapters. A brief introduction to the contents of each chapter is presented below:

Chapter 1 (this chapter) gives a brief introduction to this work, outlining the aims and objectives.

Chapter 2 reviews the literature related to this study, including the vibration behaviours of sandwich structures and the effects of debonded regions, and the toughening of epoxy polymers and FRPs using modifiers.

Chapter 3 introduces the materials and the manufacturing processes used in this study. The materials include epoxy polymer, modifiers (SNP and graphene), carbon fibres and SNP-modified sizings. The manufacturing processes used to produce the sizing-modified CFRPs and the core and facesheets for the sandwich structures are described. The procedure used to assemble the flat and curved sandwich structures is also presented.

Chapter 4 briefly describes the experimental methods used, including the tensile tests, density measurements, fibre volume fraction measurements, hammer impact tests, mode I interlaminar fracture tests and fatigue crack growth (FCG) tests.

Chapter 5 describes the finite element simulation method used for modelling the vibration behaviours of the sandwich structures. The development of the models, modelling of debonded regions, vibration simulations and a convergence study are presented.

Chapter 6 discusses the measured mechanical properties of the materials used in this study. Mechanical properties including the tensile moduli, shear moduli, Poisson's ratios and densities of the core epoxy polymers and facesheet CFRPs of the sandwich structures are presented. The fibre volume fractions of the facesheet CFRPs and the sizing-modified CFRPs are also discussed in this chapter.

Chapter 7 presents the results of mode I interlaminar fracture tests and FCG tests conducted on the sizing-modified CFRPs. A comparison of the fracture energies with carbon fibre composites using SNP-modified matrices is also discussed. The toughening mechanisms are identified by studying scanning electron microscope (SEM) images of the fracture surfaces.

Chapter 8 and Chapter 9 discuss the vibration behaviours of the sandwich structures affected by the studied factors (debonded regions, facesheet stacking orientations, materials and shapes). The results of the flat structures are discussed in Chapter 8, and the results of the curved structures are presented in Chapter 9.

Chapter 10 presents the discussions of this study: 1. The effects of SNP-modified sizings on the fracture and fatigue behaviours of carbon fibre composites (Chapter 7). 2. The effects of debonded regions on the vibration behaviours of flat and curved sandwich structures with different configurations (Chapters 8 and 9).

Chapter 11 presents the conclusions from this study, and some recommended research areas for future works which are related to this study.

Chapter 2

Literature Review

2.1 Introduction

The main topic of the present work is the adhesion of composite materials, which is discussed in two aspects: 1. How debonded regions affect the vibration behaviours of composite sandwich structures, and 2. The effects of silica-nanoparticle-modified fibre sizings on the fibre to matrix adhesion, toughness and fatigue resistance of carbon fibre reinforced polymers (CFRPs). In this chapter, the relevant materials are introduced, including epoxy, fibre reinforced polymers (FRPs) and sandwich structures. The additives (e.g. rubber, ceramic particles) typically used to toughen epoxies are discussed. The toughening mechanisms which are active in epoxy polymers and fibre composites are also reviewed. The vibration behaviour of sandwich structures is then presented, and the effect of debonded regions is reviewed.

2.2 Epoxy Polymers and Epoxy Toughening

Thermoset polymers such as epoxy are widely used in many areas such as the aerospace and automotive industries due to their high glass transition temperatures and low creep. Epoxy resins are molecules which contain multiple epoxide groups [1]. The epoxide group, which is also known as a glycidyl or oxirane group, has one oxygen atom on the outside of the carbon chain, see Figure 2.1. Epoxy resins can be cured (crosslinked) to form epoxy polymers by reacting with this epoxide group. Different curing agents (hardeners), such as anhydrides, amines, amides etc., can be used to cure the epoxy resins and can affect the properties of the cured epoxy. Other factors including the type of epoxy resin, curing temperature and time can

also affect the properties of the cured epoxy [1].

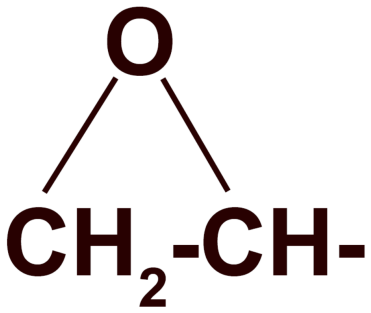


Figure 2.1: Epoxide group [1]

Adding modifiers such as carbon nanotubes (CNTs) [27–33], graphene [31, 33–37] or silica nanoparticles [2, 13, 30, 38] into the polymers can improve their thermal and mechanical properties. For example, adding 0.5 wt% of CNTs and graphene at a ratio of 9:1 can increase the flexural modulus of bulk epoxy by 17 %, while using only CNTs or graphene at same concentration can only increase the flexural modulus by 9 % and 5 % respectively [33].

The sizes and shapes of the modifiers can also have influence on the mechanical properties of the modified polymers [39, 40]. For example, for toughening polymers, it has been reported that when the modifier's aspect ratio (length to diameter) tends to infinity, e.g. CNTs, the toughening is more efficient than having the ratio of 1, i.e. spherical particles [39].

Although epoxy polymers have many beneficial properties such as a high glass transition temperature and low creep, they have a major disadvantage of being very brittle since they are highly crosslinked. This brittleness can limit the applications of epoxy polymers. To overcome this brittleness for engineering applications, epoxy polymers are toughened by adding second-phase modifiers into the resin. There are many potential modifiers that have been used to improve the toughness of thermoset polymers. These include pre-formed particles such as core-shell rubber (CSR) [41–44], thermoplastic polymer [45, 46], aluminium [47], ceramic [38, 47–50] and carbon (e.g. carbon nanotubes and graphene [28, 37, 51]) particles. Phase-separable modifiers such as thermoplastics [52–55], rubbers [56–58] and block copolymers [59] have also been used. For example, the fracture energy of the epoxy was increased by 260 % with an addition of 2.0 wt% graphene [37]. When silica nanoparticles (SNPs) are added to epoxy polymers, the toughness increases as the concentration is increased (see Figure 2.2); while the sizes of the SNPs were reported to have no significant effects on the toughness, as the fracture energies do not show a consistent trend with the particle sizes [2]. It is noted that in Figure 2.2, the gradient of the increase of the fracture energy shows a significant drop after the initial addition of 2.5 wt% SNPs. The reason for the drop of the gradient is that once a SNP debonds and forms void in the matrix, which absorbs energy (discussed later in Section 2.2.2), the nearest neighbour particles are sheltered from the applied stress field, therefore, no debond-

ing of the neighbouring particles occurs. It was predicted that only 14.3 % of the particles will debond, which results in a limitation of the toughening effect [2]. The fracture toughness and fracture energy of the epoxy were also increased by 49 % and 53 % with an hybrid addition of both 6.0 wt% SNPs and 0.18 wt% multiwalled carbon nanotubes (MWCNTs) [30].

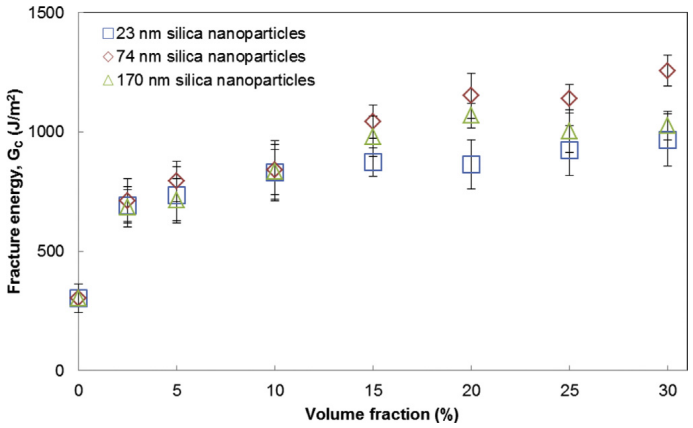


Figure 2.2: Fracture energy of bulk epoxy modified with silica nanoparticles with different particle sizes [2]

2.2.1 Toughening of Epoxy Polymers Using Rubber Particles

The rubber particles used to toughen epoxy polymers include reactive liquid rubbers such as carboxyl-terminated butadiene-acrylonitrile (CTBN) or core-shell rubber (CSR) particles, and have been reported to improve significantly the toughness of epoxy polymers [8, 13, 38, 41–44, 56–58, 60–65]. It is noted that the low modulus CTBN and CSR particles reduce the Young's modulus of epoxy polymers [8, 13, 38, 61, 62, 65]. CTBN is a liquid rubber, which is initially soluble in epoxy resins. It phase-separates into micron-sized particles during the curing of the epoxy. CSR particles have a soft rubber core and a harder polymer shell, as shown in Figure 2.3. CTBN can provide more toughening effect than CSR particles due to the higher rubber content for an equal volume fraction (i.e. there is no hard shell), however, it reduces the glass transition temperature of the epoxy polymer since some CTBN does not phase-separate during curing and remains dissolved in the epoxy [3]. It is also hard to control the particle size of the CTBN particles because this depends on the curing cycle, type of hardener used and the structural properties of the rubber itself [66]. CSR particles are preformed, so the sizes of the CSR particles are already determined before adding into the epoxy resin and are not affected by the curing cycle [61, 62]. Another side-effect of reactive liquid rubbers is that they can increase the viscosity of the epoxy resin significantly when used at higher concentrations [3], which is not suitable for manufacturing FRP composites by the resin infusion method.

The toughening mechanisms of epoxy polymers using rubbers include: 1. rubber particle bridging, 2. shear band yielding of the epoxy, and 3. cavitation of rubber particles followed by

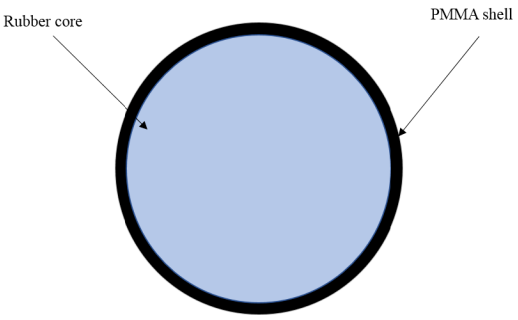


Figure 2.3: Sketch of a core-shell rubber particle [3]

plastic void growth of the matrix epoxy, as shown in Figure 2.4. In rubber particle bridging, the rubber particles are attached to the crack surfaces and stretched, which absorbs energy during crack growth [67]. Toughening by rubber particle bridging happens only if the rubber particles are large enough to bridge between the crack surfaces. However, it has been reported that rubber particle bridging only accounts for 10 % of the total fracture energy [4].

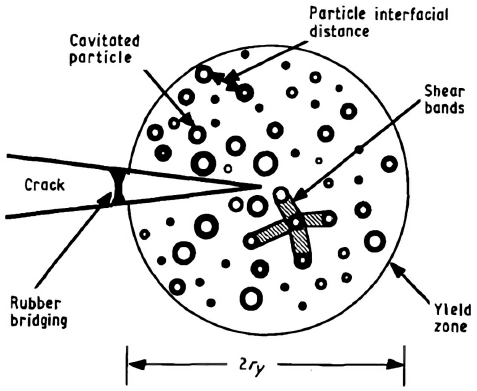


Figure 2.4: Sketch of toughening mechanisms of rubber-modified epoxy polymers [4]. $2r_y$ indicates the diameter of the process zone

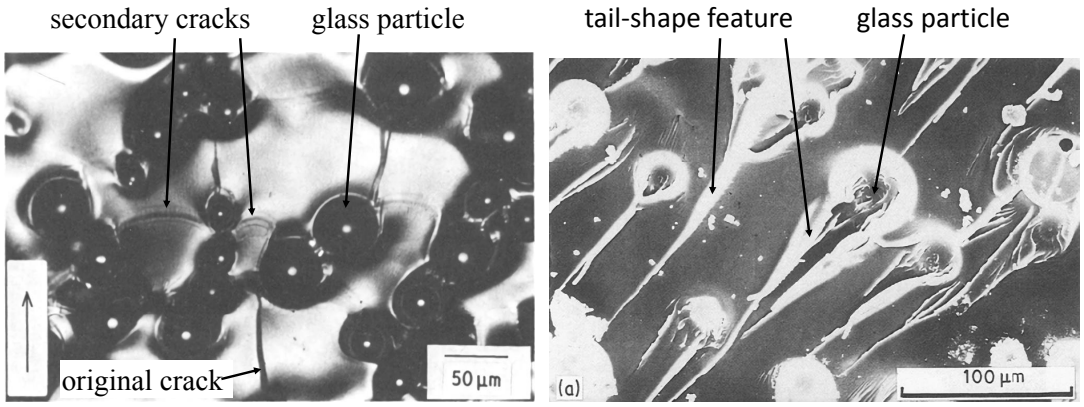
Localised shear band yielding is the major toughening mechanism in rubber-modified epoxy polymers. Shear band yielding is reported to form between two rubber particles at 45° to the direction of the applied stress [68, 69]. The particles cause stress concentrations in the epoxy matrix, which increase as the volume fraction of the particles increases, and cause local shear plastic deformation of the epoxy. This contributes to the absorption of energy and the improvement of the toughness [70, 71].

Another important toughening mechanism in rubber-modified epoxy polymers is rubber particle cavitation and the subsequent plastic void growth [38, 70, 72]. When cavitation starts, a void forms inside a rubber particle which relieves the constraint on the epoxy and enables the matrix epoxy to deform plastically. Although the cavitation of the rubber particles absorbs only a small amount of energy since the rubber particles are very soft, the plastic void growth of the epoxy matrix absorbs a significant amount of energy. Therefore, the toughness of the epoxy

polymer is improved significantly.

2.2.2 Toughening of Epoxy Polymers Using Rigid Particles

The toughening mechanisms of epoxy polymers toughened using rigid particles include crack pinning, crack deflection, shear band yielding, particle debonding and plastic void growth. For crack pinning by glass particles of micron size [5, 6], when a growing crack meets the rigid particles which are impenetrable in the polymers, the crack front becomes pinned. Secondary cracks are then generated between the rigid particles due to splitting of the original crack, see Figure 2.5a. The secondary cracks then propagate and form tail-shape features behind the particles, as shown in Figure 2.5b.



(a) Pinned crack front (optical microscope image) [5]

(b) Tail-shape features (electron microscope image) [6]

Figure 2.5: Crack pinning and tail-shape features [5, 6]

The toughening mechanism of crack deflection by glass beads of micron size has also been reported [73, 74]. When the crack tip reaches the rigid micro particles, crack deflection occurs: the crack deviates from its original direction of propagation. The crack deflection results in the interfacial fracture between the glass beads and the matrix, and the crack is deflected such that the crack tip experiences a mixed mode fracture rather than only mode I fracture [73]. Mixed mode fracture requires more energy than mode I fracture so extra energy is absorbed. If the adhesion between the particles and the matrix is good, the crack tends to be attracted to the poles of the particles; while if the adhesion between the particles and the matrix is poor, the crack grows along the equators of the particles [73]. Both crack pinning and crack deflection also generate an increased area of new surfaces, therefore the energy dissipation increases and hence the toughness is improved.

Both crack pinning and crack deflection are induced by micron-sized particles, while for particles of nano size, for example silica nanoparticles, these two mechanisms cannot occur since the nanoparticles are much smaller than the crack opening displacement [7], see Figure

2.6. Instead of crack pinning and crack deflection, debonding of rigid nanoparticles from the epoxy matrix followed by plastic void growth has been reported as the toughening mechanism induced by nano-sized particles [9, 75], see Figure 2.7. Although the debonding process does not absorb much energy since the interfacial fracture energy is relatively low, debonding generates voids. These voids reduce the constraint in the plastic zone at the crack tip. Therefore, these voids are able to grow by plastic deformation of the matrix and this process absorbs a significant amount of energy, which results in the improvement of the toughness. Debonding and plastic void growth can occur for both nanometre sized (see Figures 2.7a and 2.7b) and micron sized rigid particles (see Figure 2.7c).

Shear band yielding, which is found in the rubber-modified epoxy polymer, as discussed in Section 2.2.1, can also occur in the epoxy polymers modified using rigid particles. Shear band yielding causes stress concentrations in the epoxy and hence results in local shear plastic deformation, which absorbs energy and contributes to the increase of the toughness.

In conclusion, shear band yielding and plastic void growth, which occur in both the rubber- and rigid-particle-modified epoxy polymers, are the major toughening mechanisms which absorb the most energy and contribute significantly to the increase of the toughness. Bridging of rubber particles, crack pinning and crack deflection of rigid particles are minor contributors since only a small amount of energy is absorbed by these mechanisms.

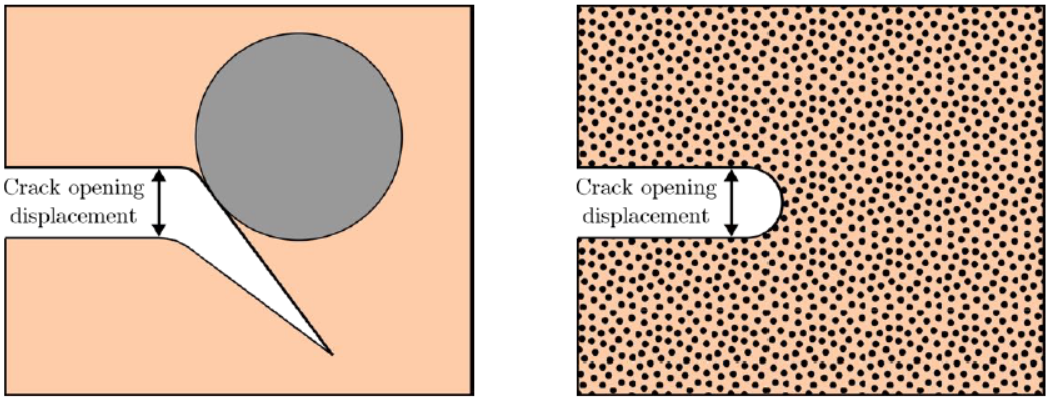
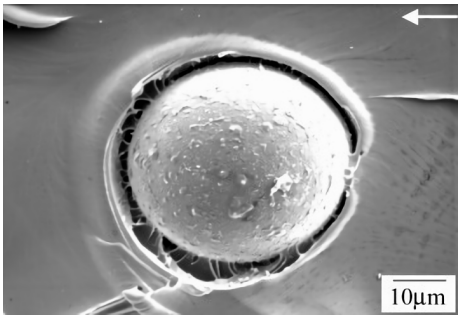
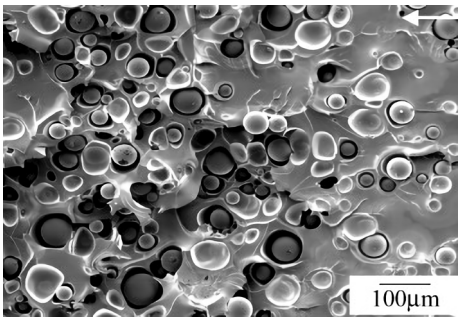


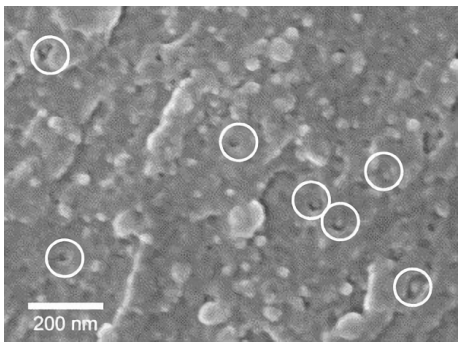
Figure 2.6: Crack deflection in epoxies modified using microparticles (left) and nanoparticles (right) [7, 8]



(a) Debonding between glass particle and matrix with void growth [9]



(b) Debonding between glass particles and matrix with void growth[9]



(c) SNPs debonding, void growth indicated [7]

Figure 2.7: Rigid particle debonding followed by plastic void growth [7, 9]

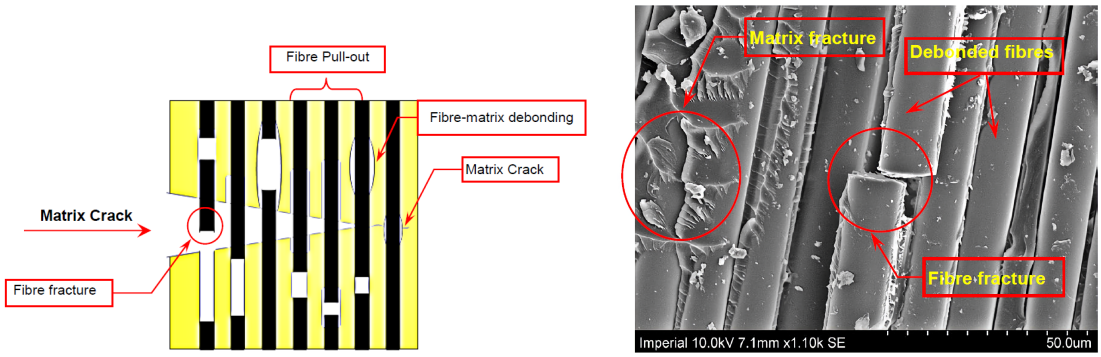
2.3 Fibre Reinforced Polymer (FRP) Composites and FRP Toughening

Fibre composites are widely used because of their light weight and high mechanical strength and stiffness. Fibre composites can be found in daily lives in structural applications, such as the frames of bicycles, car bodies, ship hulls and aircraft fuselages. Such fibre composites typically comprise continuous fibres embedded in a thermoset polymer matrix.

Thermoset polymers such as epoxy are widely used as the matrices of the FRPs which are common materials for the facesheets of sandwich structures because of their good thermal properties, chemical resistance and low creep [10]. The modifiers used to increase the mechanical properties and toughness of epoxy polymers can be used to modify FRPs manufactured by infusion methods only if the particles are small enough to flow between the fibres [21]. The modifiers mentioned in Section 2.2 have been used by various researchers to modify the matrices of FRPs [21, 23, 26, 76]. For example, adding 4 wt% graphene into the resin can improve the tensile modulus and thermal conductivity of the CFRP by 11 % and 45 % respectively [76].

2.3.1 Failure Mechanisms of FRPs

Since fibre reinforced polymers are anisotropic materials, the different fibre orientations result in complex failure mechanisms in FRPs [77]. Large numbers of the failure modes in fibre reinforced polymers have been summarised [78]. These failure modes include intralaminar matrix cracking, plastic flow, debonding between fibre and matrix, fibre pull-out from the matrix and fibre fracture [78], as shown in Figure 2.8. Generally, the failure modes related to the fracture of the matrix or interphase region result in lower fracture energies, while the failure modes related to fibre fracture result in higher fracture energies [79]. Since the failure modes containing fibre fracture contribute to higher fracture energies which make FRP composites tougher, a good adhesion between the fibres and the matrix is critical for transferring the stress to the fibres. However, if the fibre to matrix adhesion is increased too much then the fibres will not pull out, reducing the energy absorbed, and the overall toughness will decrease [46].



(a) Sketch [10, 11] **(b)** SEM image [11]

Figure 2.8: Failure modes in FRPs [10, 11]

2.3.2 Toughening of FRPs

Although thermoset polymers are widely used as the matrices of the FRP composites, the brittleness of thermoset polymers can limit the applications of fibre composite parts since they require not only high strength, but also good resistance against impact, fracture and fatigue to prevent premature and catastrophic failure. To overcome this brittleness, thermoset polymers toughened using second-phase modifiers can also be used as the matrices of the FRPs. A comparison of the fracture energies of fibre composites with those of the matrix polymers is shown in Figure 2.9. In Figure 2.9, the slope of the fit line for the thermoset polymers (the triangle marks) is greater than 2, which indicates that the fracture energies of the fibre composites using the thermoset polymer matrices are greater than those of the corresponding bulk polymers [12]. While for the toughened thermoset polymers (diamond marks), the fit line has a slope of about 0.31, which indicates that the fracture energies of the fibre composites using the toughened polymer matrices are smaller than those of the corresponding bulk polymers [12].

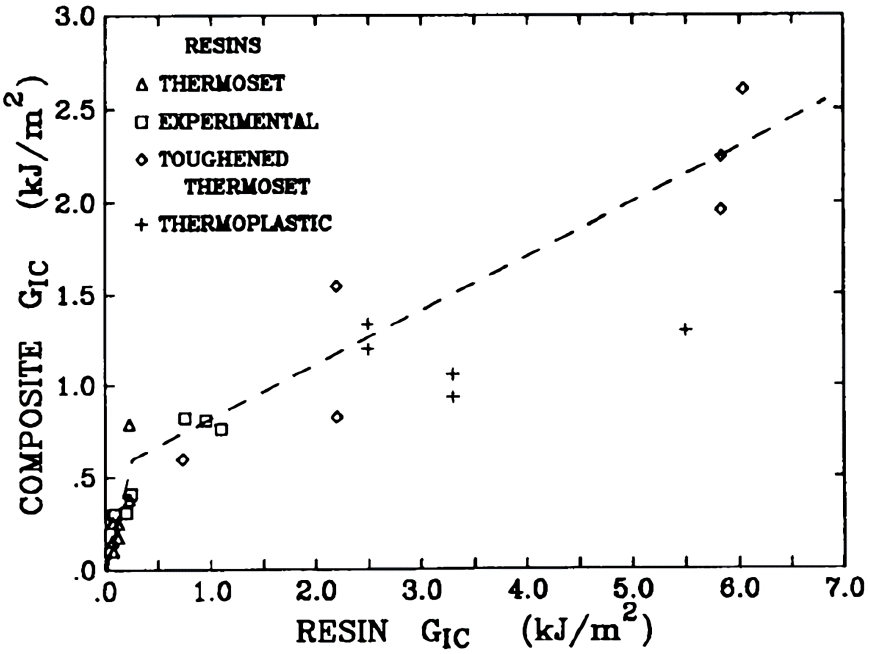


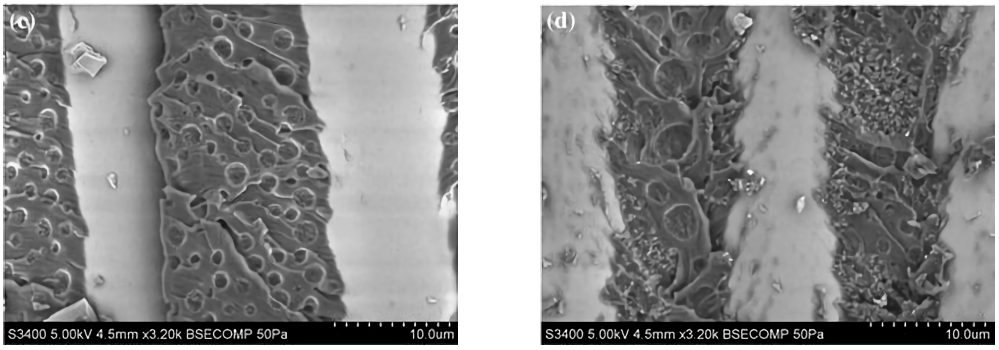
Figure 2.9: Mode I interlaminar fracture energy of composite versus fracture energy of matrix [12] (Enlarged)

Increasing the fracture energy of fibre composites is more difficult than for bulk thermoset polymers, as the size of the plastic zone at the crack tip is constrained by the stiff fibres, therefore less energy is absorbed during crack growth. This can result in a poor transfer of toughness from the bulk polymer to the composite, see Figure 2.9, and a limiting fracture energy can be reached where further increases in the matrix toughness do not increase the toughness of the composite [80]. It was reported that for the fibre composites using brittle matrices, the toughening effect was more significant since the fracture energies were fully transferred from the matrices to the fibres (the triangle marks in Figure 2.9); while for the fibre composites using tougher matrices, the toughening effect was not as significant since the fracture energies were only partially transferred from the matrices to the fibres (the diamond marks in Figure 2.9) [12]. The reason for the limited toughening effect is that the stiff fibres at the crack tip constrain the development of the plastic zone so that it is significantly smaller than in the corresponding bulk thermoset polymer [12]. Moreover, many of the modifiers discussed above increase significantly the viscosity of the resin, especially at the high volume fractions required to achieve the highest toughness values, and thus manufacturing fibre composites using infusion processes with these modified resins can become impossible as the resin is too viscous to flow between the fibres.

One modification that has been particularly successful is the addition of silica nanoparticles. These particles are typically 20 nm in diameter and are surface-treated to prevent agglomeration. Thus the increase in resin viscosity is very small, and they can readily flow between the fibres during infusion. Silica nanoparticle-modified epoxy resins have been found to give

improvements of fibre composite toughness and fatigue behaviour [13, 21–26]. For example, adding 10 wt% of SNPs into the matrix epoxy increased the fracture energy of a unidirectional (UD) glass fibre reinforced polymer (GFRP) by 200% [13], and also extended the tensile fatigue life by 3 to 4 times because of the reduction of crack growth rate which results from the toughening mechanisms of shear band yielding plus particle debonding and subsequent plastic void growth [23].

For the fibre-induced toughening mechanisms in fibre composites, it was reported that pull-out of fibres from the matrix, fibre bridging between the fracture surfaces and fibre breakage constitute the main contributions to the energy absorption [13, 79, 81, 82]. If the matrices of the fibre composites are toughened using particulate modifiers, the toughening mechanisms of bulk polymers (i.e. particle cavitation or debonding, plastic deformation and void growth) can also be identified in the resin-rich regions between the fibres [13], see Figure 2.10.



(a) CTBN-modified matrix **(b)** CTBN&SNP-modified matrix

Figure 2.10: SEM images of fracture surfaces of quasi-isotropic GFRP [13]

2.4 Toughening of Fibre Composites Using Modified Sizings

Although directly adding modifiers into the matrices of fibre composites can improve the toughness, see Section 2.3.2, it requires significant addition of modifiers, e.g. up to 20 wt% of the matrix resin [25], which leads to an increased cost in materials and manufacturing (due to the higher viscosity of the modified resin) for practical applications.

2.4.1 Fibre Sizings

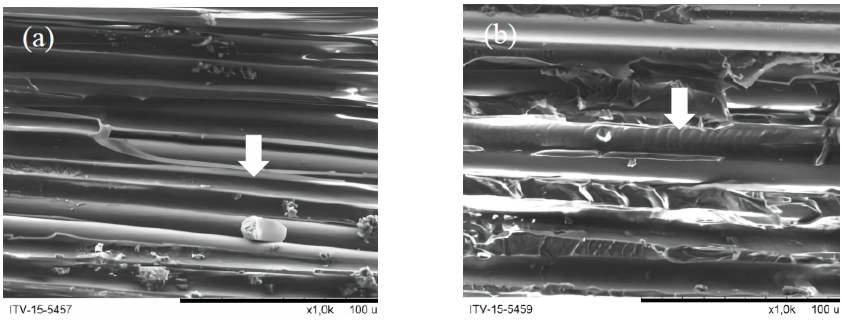
Sizings are the agents applied to raw fibres during fibre manufacturing, they protect the fibres during processing and control the adhesion between the fibres and the matrix in the composite. Since the fibres take most of the load when fibre composites are in service, good adhesion between the fibres and the matrix means that stress is transferred effectively to the fibres, which contributes to better mechanical properties of the composite. Therefore, as discussed in

Section 2.3.1, good adhesion contributes to more energy absorption and hence to the improvement of the toughness of fibre composites [46].

2.4.2 Toughening Using SNP-Modified Sizings

Instead of directly modifying the matrices of fibre composites using a significant addition of modifiers, modifying the sizings on the fibres is an alternative approach. Research has shown that adding silica nanoparticles (SNPs) into fibre sizings can increase the interlaminar shear strength (ILSS) of carbon fibre composites [83] and improve the fracture toughness and fatigue performance of GFRPs [14]. Although the fracture energies of GFRPs can be improved by 200 % by adding SNPs in to the matrix polymer, it requires an addition of 10 wt% (of the matrix) of SNPs [13]. An improvement of the fracture energies by 40 % can be achieved by modifying the sizings using 0.24 wt% (on the fibre mass) of SNPs [14]. Although the improvement level is lower, modifying the sizings on the fibres significantly reduces the addition of SNPs. Using SNP-modified sizings has another benefit that the viscosity of the matrix resin does not increase since the resin itself has not been modified.

It has been reported that modifying fibre sizings using SNPs can improve the adhesion between the fibres and the matrix, and enhance the fibre bridging effects of GFRPs [14]. In Figure 2.11a, the glass fibre surfaces are clean and smooth, which indicates poor adhesion between the fibres and the matrix; while in Figure 2.11b, ridges can be found on the fibre surfaces, which indicates that the fibre bridging effect is improved. As discussed in Sections 2.3.1 and 2.3.2, fibre bridging absorbs energy. Therefore, more fibre bridging indicates more energy absorption and hence results in the improvement of the toughness.



(a) Unmodified sizing **(b)** SNP-modified Sizing

Figure 2.11: SEM images of fracture surfaces of GFRPs using unmodified and SNP-modified sizings [14]

In conclusion, modifying the sizings of fibres using SNPs has the potential to improve the toughness and fatigue lives of fibre composites, while reducing the addition levels of SNPs required and having no effects on the viscosity of the matrix resin, which contributes to more efficient manufacturing of the fibre composites.

2.5 Sandwich Structures

Sandwich structures, which are lightweight but have good mechanical properties such as high stiffness and high durability to flexural loading, have been widely used in many areas, for example in the aerospace, automotive, marine and energy industries, and even in construction. A sandwich structure is manufactured by adhering a core between two thin but strong facesheets. High stiffness materials such as fibre reinforced polymer (FRP) or metal panels are commonly used as the facesheets; light materials such as honeycomb panels or polymers are usually chosen as the core.

Many works have been published concerning sandwich structures, e.g. [84–88]. To reduce the weight, if the sandwich structure is subjected to lower loads, typical materials such as polymer foam can be used as the core and glass fibre reinforced polymer (GFRP) can be used as the facesheets; while if the sandwich structure is subjected to higher loads, carbon fibre reinforced polymer (CFRP) facesheets and steel square honeycomb core are ideal for taking the load and reducing the weight of the structure [86]. If the core of a sandwich structure has a lower density, failure of the core resulting from the shear deformation causes damage to the structure; while if the structure has a denser and thicker core, the main reason for the damage is the fracture of the facesheets [87]. The adhesive layers between the facesheets and the core of sandwich structures, on the other hand, also have a significant influence on the stiffness and failure of sandwich structures [88], as the adhesive layers are where the early-stage damage often initiates because they are the interfaces between two different materials.

2.5.1 Vibration of Sandwich Structures

For practical applications, vibration is an important issue since resonance can cause severe vibration and damage of structures. The vibration behaviours of sandwich structures have been widely studied [89–93], and different approaches have been developed to predict the natural frequencies and deformation modes of sandwich structures [91–93]. For example, the spline finite strip method was developed by Yuan and Dawe [91], and the results showed a good agreement with other literature. The geometry and the materials of the core and facesheets can affect the vibration of sandwich structures significantly [27]. If the thickness of the core is increased, the damping properties can be increased since the loss factor is increased. Changing the facesheet stacking orientations can have a significant influence on the natural frequencies since the stiffness of the structure is changed. It was also found that the effects of the mass of vibrators (devices which generate vibration) used in testing can not be neglected if their mass is too large [94].

2.5.2 Debonding of Sandwich Structures

For sandwich structures, it is critical to bond the core and facesheets together firmly to prevent debonding, crack propagation and subsequent failure in-service. However, due to defects in the manufacturing process or in-service damage (e.g. impact from stones or vehicles), debonding may occur between the core and facesheets, which can decrease significantly the stiffness and strength of the structure, thus leading to failure. Delamination between the core and facesheets, or failure of the adhesive layer, has been indicated to be a critical problem in sandwich structures [95]. By four-point bending tests, it was reported that the stiffness and strength decrease more when there is a longer debonded region [96]. The bending rigidity of sandwich structures was also reported to decrease when the delamination length increased [15], see Figure 2.12.

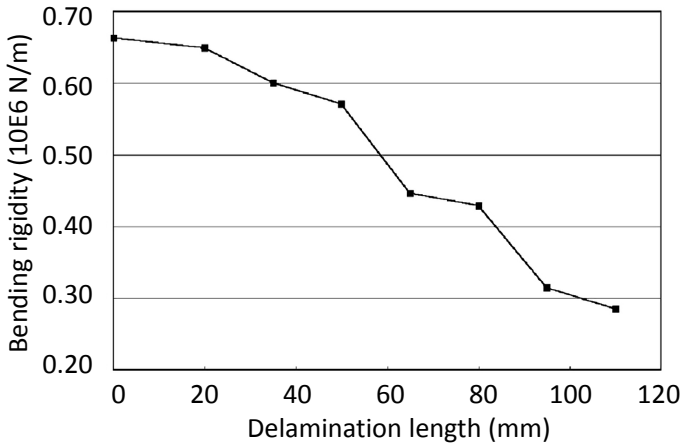


Figure 2.12: Bending rigidity of sandwich structures with delaminations of various lengths. Reproduced from [15]

2.5.3 Effects of Debonded Regions on the Vibration Behaviours of Sandwich Structures

Debonding can affect the vibration response of sandwich structures significantly. The influence of debonded regions on structures is not only affected by the size and location of the debonded regions but also by the shape of the structure, the boundary conditions and the modes of vibration [97, 98]. It was indicated that the natural frequencies of sandwich structures decrease more when the debonded region becomes longer [15, 99], and drop significantly when the debonded region is longer than a critical length (e.g. a critical debond length of 50 mm for a 270-mm-long cantilever beam) [15], see Figure 2.13. For a CFRP laminate beam, if there are multiple debonded regions which are located at the same place, the natural frequencies of the beam can decrease further [99]. The damping coefficient of sandwich structures can also be

affected by debonded regions [100], the damping increases as the damage area increases. The natural frequencies of sandwich structures are also reported to be sensitive to curvature since the stiffness of the structures are affected by curvature [98]. Lower natural frequencies are undesired since they can be excited more easily in service and result in resonance, which can lead to high displacement magnitudes and failure of structures.

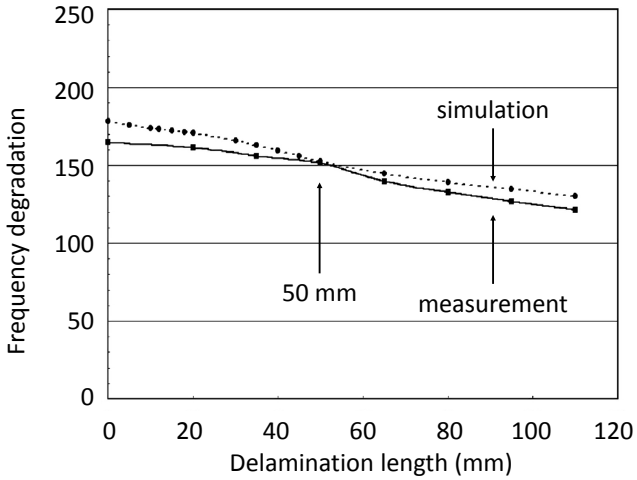


Figure 2.13: Fundamental natural frequency degradation of a 270 mm long sandwich structure with delaminations of various lengths. Reproduced from [15]

It is also noted that the reduction in stiffness caused by debonds can be identified by the reduction in natural frequencies since natural frequencies are positively correlated to the stiffness. Therefore, observing the vibration behaviour of imperfect structures can identify damaging conditions (i.e. damage areas and locations), which is one way of non-destructive testing (NDT) which has become widely used in many areas [101]. Some methods of identifying damage in structures by observing the vibration behaviours include measuring the dynamic properties of the structures [102], using eigensolution [103] and measuring the vibration frequencies and damping of the structures [104]. The theory of high-frequency vibrations was used, combined with vibration experiments, to verify the feasibility of detecting damage in the sandwich structures used in marine vessels [105]. The predictions and experimental results showed good agreement.

2.5.4 Finite Element Simulation of the Vibration Behaviours of Sandwich Structures

Finite element analysis (FEA) simulation has become widely used to solve engineering problems since it reduces the time and costs. There has been research using FEA to solve debonded and intact sandwich structures [90, 93, 106]. The vibration behaviours of debonded sandwich structures were investigated using FEA software Abaqus, which introduced different

elements or methods to model the debonded regions. It was reported that when the delamination gets longer, the natural frequencies of the structures decrease [107–109]. FEA software ANSYS was also used to simulate the problem, bilinear element LINK10 was used to prevent the debonded region from overlapping, which can be utilized as a tension-only or compression-only element, to model the delamination regions [110].

2.5.5 Discussion

According to the literature, the materials, facesheet stacking orientations and debonded regions have significant effects on the mechanical properties (strength, stiffness and failure) and vibration behaviours of sandwich structures. Debonding, which can occur easily at the adhesive layers in sandwich structures, can significantly reduce the stiffness of the structures and hence affect their natural frequencies. Changes in the natural frequencies caused by debonded regions can make a structure which was designed not to vibrate at its resonant frequencies experience resonance at the lowered frequencies, which can cause further damage and failure of the structure. Therefore, understanding how debonded regions and the other factors (i.e. facesheet stacking and materials) affect the vibration behaviour of sandwich structures is important. However, the effects of these factors when combined have been rarely considered in the literature. This work presents and discusses how the natural frequencies are affected by these factors. The aim is to identify the effects of these factors on the vibration response of sandwich structures.

2.6 Conclusions

A brief literature review has been presented in this chapter. Epoxy polymers have been introduced. The toughening of bulk epoxy polymers, and the toughening of fibre reinforced polymers using modified matrices and modified sizings have been reviewed. The compositions of sandwich structures and their vibration behaviours have been presented. The effects of debonded regions on sandwich structures and their vibration behaviours have also been discussed. The materials and the manufacturing processes used in this study are presented in the next chapter.

Chapter 3

Materials and Manufacturing

3.1 Introduction

In this chapter, the selected materials and the manufacturing processes are introduced. The sizing-modified fibre reinforced plastic (FRP) panels are composed of an epoxy polymer matrix and carbon fibres with two types of fibre sizing agents modified with silica nanoparticles. For the sandwich structures for the vibration tests, the core materials are bulk epoxy polymer modified with silica nanoparticles or graphene; the facesheets are carbon fibre reinforced polymer (CFRP) infused with the same resin formulations as the core.

3.2 Sizing-modified Carbon Fibre Composites

3.2.1 Carbon Fibre Composite

The carbon fibre used for the modified sizing work was HF10-12k from Hengshen, China [111]. The matrix used was a diglycidyl ether of bis-phenol A (DGEBA) epoxy resin E54 and a methyl tetrahydrobenzoic anhydride hardener HK021, both from Hengshen, China [111], who also manufactured the unidirectional (UD) laminates from the sizing-modified fibres by vacuum assisted resin infusion (VARI). The linear density of the HF10-12k fibre was 800 g/1000 m, the tensile strength was greater than 3530 MPa, and the tensile modulus was about 221 to 242 GPa [112].

Two types of commercial sizing agents were applied on the fibres: HS-1 from Hengshen and Neoxil 965 from Aliancys, Switzerland [113]. The purposes of using two sizing agents is

to make a comparison and to investigate whether the results are sizing-dependent. Neoxil 965 is a epoxy-based sizing agent and composed of: 1. Bisphenol-A(epichlorhydrin) epoxy resin (25-50 %), 2. phenol, 4,4'-(1-methylethylidene)bis-, polymer with 2-(chloromethyl)oxirane (10-25 %), and 3. oxirane, methyl-, polymer with oxirane (5-10 %) [114]. The ingredients of HS-1 are unavailable. FW404 [115], an aqueous emulsion of F400 [116] (introduced in Section 3.3.3), containing silica nanoparticles, was used to modify the two sizing agents. The solid content of F400 in FW404 was 56 % and the concentration of silica nanoparticles was 40 wt% on solid [115].

The carbon fibres were raw fibres without any sizing in the beginning, the modified sizings containing silica nanoparticles were applied to the fibres by Hengshen. These sizing-modified fibres were then used to manufacture the UD laminates.

3.2.2 Sizing Formulations

The formulations of the modified sizings used are shown in Table 3.1, where the concentrations are the weight percentage on solid on the mass of fibres.

Table 3.1: Sizing formulations (wt% on fibre mass)

N0	4 wt% Neoxil 965	H0	4 wt% HS-1
N1	2.67 wt% Neoxil 965 + 1.33 wt% Nanopox FW 404 (SNP content: 0.53 wt%)	H1	2.67 wt% HS-1 + 1.33 wt% Nanopox FW 404 (SNP content: 0.53 wt%)
N2	1.78 wt% Neoxil 965 + 2.22 wt% Nanopox FW 404 (SNP content: 0.89 wt%)	H2	1.78 wt% HS-1 + 2.22 wt% Nanopox FW 404 (SNP content: 0.89 wt%)

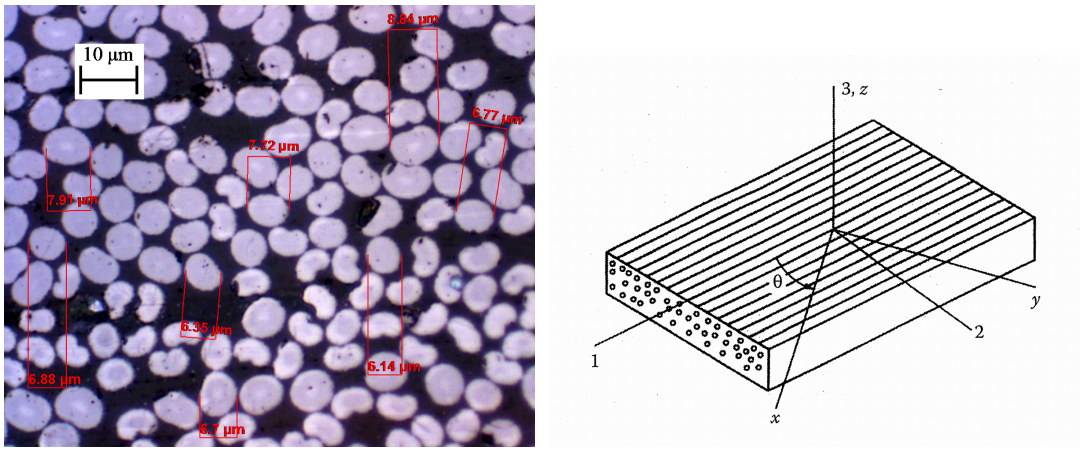
3.3 Sandwich Structure Materials

3.3.1 Carbon Fibres

The fibre used for the facesheets of the sandwich structures was the unidirectional (UD) carbon fibre fabric UT-C300 manufactured by Gurit and supplied by Marineware, UK. The primary fibre was 12k (i.e. 12000 filaments per tow) carbon fibre with a fibre tex (linear density) of 800 g/1000 m; the areal density was 300 g/m^2; the cross-stitching fibre was polyester (PE) fibre [117]. The average fibre diameter of UT-C300 was about 7 µm (see Figure 3.1a).

Fibre reinforced polymers (FRPs) are anisotropic materials, which means that they have different mechanical properties in different directions, such as tensile/shear modulus, strength

and Poisson's ratio. Furthermore, a UD carbon fibre lamina is transversely isotropic, so the mechanical properties in the directions perpendicular to the fibre direction are almost the same [118]. Conventionally, the direction of fibres in a lamina is defined as axis 1, the direction which is normal to the lamina is defined as axis 3, and the axis perpendicular to the other two axes is defined as 2, as shown in Figure 3.1b.



(a) UT-C300 fibre diameter measurement **(b)** Principal axes of a lamina [118]

Figure 3.1: UT-C300 fibre diameter measurement and principal axes of a lamina

3.3.2 Epoxy Matrix

The resin used for the sandwich structures was DGEBA, supplied as Araldite LY 556 epoxy resin from Huntsman, UK, with an epoxy equivalent weight (EEW) of 185 g/eq [119]. The resin was cross-linked using an accelerated methylhexahydrophthalic acid anhydride, Albidur HE 600 hardener supplied by Evonik, Germany. The hardener had an anhydride equivalent weight (AEW) of 170 g/eq [120]. The mixing ratio used for making unmodified epoxy plates was 1 : 0.91 (LY556 : HE600) by weight.

3.3.3 Silica Nanoparticles

The silica nanoparticles (SNPs) used to modify the epoxy were Nanopox F400 from Evonik, Germany. The SNPs were supplied as a masterbatch dispersed in DGEBA epoxy resin at a concentration of 40 wt%. The EEW was 295 g/eq or 301 g/eq depending on different batches. The average diameter of the silica nanoparticles was 20 nm [116]. The required amounts of LY556, HE600 and F400 were calculated according to the stoichiometric ratio of 1:1 and the intended weight concentration of silica nanoparticles.

3.3.4 Graphene

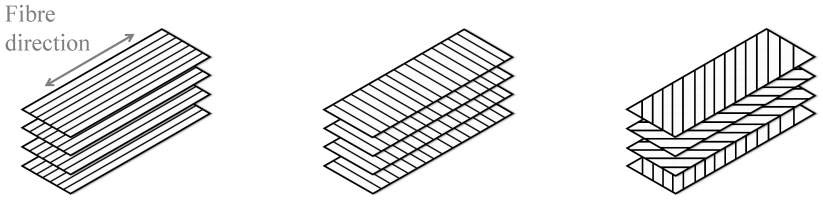
The graphene used to modify the epoxy was xGnP M-25, supplied by XG Sciences, USA, with carbon content higher than 99.5 % [121]. The xGnP M-25 particles had an average thickness of about 6 to 8 nm, an average diameter of 25 μm and a typical surface area of 120 to 150 m^2/g [121]. The required amount of LY556, HE600 and xGnP M-25 were calculated based on the intended weight concentration of graphene.

3.3.5 Formulations

The formulations and the facesheet stacking orientations of the sandwich structures are shown in Table 3.2. For the facesheets in this study, 0° means that the fibres of the lamina are aligned with the longitudinal direction of the structure, therefore 90° means that the fibres are in the lateral direction. For the angled fibres, +45° indicates a 45° clockwise rotation from the longitudinal direction, and -45° indicates 45° counter-clockwise rotation. For the subscript, in the $[0°]_4$ and $[90°]_4$ facesheets the "4" means a stack of 4 layers, and in the $[+45°/-45°]_s$ facesheets the "s" means a stack which is symmetrical about the middle plane. Figure 3.2 shows the three types of CFRP orientation used for the sandwich structures in this study.

Table 3.2: Sandwich formulations and compositions

Epoxy for core and matrix of facesheet	unmodified epoxy (LY556 & HE600)
	silica nanoparticles: 5, 10, 15 (wt%)
	graphene: 0.5, 1.0 (wt%)
Facesheet fibre stacking	UT-C300 carbon fibre: $[0°]_4$, $[90°]_4$, $[+45°/-45°]_s$



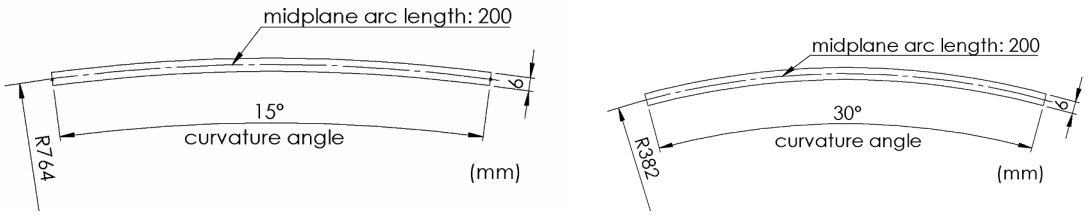
(a) $[0°]_4$ **(b)** $[90°]_4$ **(c)** $[+45°/-45°]_s$

Figure 3.2: CFRP stacking orientations for the facesheets

3.4 Sandwich Structure Manufacturing

3.4.1 Bulk Epoxy Plates

To make epoxy plates for different purposes, different moulds were used, including 6-mm-thick flat and curved moulds for manufacturing the cores of the sandwich structures, and 3-mm-thick flat moulds for manufacturing the plates for the tensile and density tests. Two types of curved moulds were used: one which had a midplane curvature radius of 764 mm for making curved core plates with a curvature angle of 15° (see Figure 3.3a), and another one which had a midplane curvature radius of 382 mm for making curved core plates with a curvature angle of 30° (see Figure 3.3b). The radii were calculated from the required midplane arc length, which was 200 mm, and the 15° and 30° curvature angles.



(a) 15° core plate **(b)** 30° core plate

Figure 3.3: Lateral sketch of curved core plates with a curvature angle of 15° or 30°

When manufacturing the epoxy plates, the moulds were cleaned with acetone, coated with a thin layer of the release agent Frekote 700-NC from Loctite, UK, and allowed to dry in a fume hood. After drying, the moulds were preheated in an oven at 60 °C.

To prepare the resins with different formulations, first the required amounts of the epoxy resin, hardener and modifiers were calculated and weighed. There are differences between the processes of dispersing SNPs and graphene into the resin. For making unmodified epoxy plates or epoxy plates containing SNPs, the required amounts of LY556, HE600 and F400 were poured into a beaker together, and then mixed by hand with a stainless steel spatula. Then the mixture was stirred using an overhead stirrer RZR 2010 from Heidolph, Germany, at 60 °C for 20 minutes. After stirring, the mixture was degassed at 60 °C and -1 atm for at least 20 minutes. The mixture was than poured into the preheated moulds and placed in a programmed oven, cured at 90 °C for 1 hour and post-cured at 160 °C for 2 hours. The ramp rate used was 1 °C per minute. After curing, the moulds were left in the oven to cool down to room temperature. The epoxy plates were then taken out from the moulds and cut to the desired sizes using a table saw.

For graphene, since it can raise the viscosity of the resin significantly, the overhead stirrer is not suitable, so a 3 roll mill was used to achieve a better degree of dispersion. The graphene and the epoxy resin (LY556) were mixed together first using a spatula, then the mixture was further

mixed by a 3 roll mill Exakt 80E from Exakt, Germany, at 40 °C (by warm water running inside the rolls) for 7 cycles. The rotation speed of the front roller was set at 220 rpm (revolutions per minute) and the ratio of the speed from the front roller to the back one was 9:3:1; the gap between each pair of rollers was 5 µm. After processing using the 3 roll mill, the mixture was then weighed again because there were some losses during the mixing step. The required amount of hardener was calculated based on the new weight and added into the mixture. The resulting mixture was then stirred using the overhead stirrer at 60 °C for 20 minutes. After stirring. the mixture was degassed, poured into the moulds and cured in the oven following the same steps used for making unmodified epoxy plates or epoxy plates containing SNPs.

Figure 3.4 shows the measured temperatures when the epoxy resin was being cured. The temperatures were measured and recorded with a thermocouple buried in the resin and another one directly placed in the oven. Although there is a difference of about 5 °C between the maximum programmed temperature (160 °C) and the measured temperatures of the oven, the rising ramps and the 90 °C curing process are very close. On the other hand, the measured ramp of cooling down is different from the program, the reason is that the oven didn't have a cooling system so it could only cool down naturally even if it had been programmed, which took more time. It can also be noted that the resin's temperature differs from the programmed temperature, this may be attributed to the thermal conduction which takes time for the heat to transfer from hot air in the oven, through the mould, to the resin. However, according to the reported value [3], which used the same epoxy polymer and curing cycle and had a similar difference of temperature in the curing profile, the glass transition temperature, T_g, was 159 °C. This indicates that the epoxy was fully cured.

3.4.2 Carbon Fibre Composite Facesheets

To make the CFRP for the facesheets of the sandwich structures and for the mechanical properties tests (tensile and density tests), first the required orientation angles and layers of UT-C300 UD carbon fibre cloth were cut to 300 by 220 mm^2 using a pair of scissors or a snap-off knife, and laid on a hot plate with other required materials in sequence. A layer of vacuum bagging plastic was placed on the top, and sealed to the hotplate using a pressure-sensitive tape, as shown in Figure 3.5. The resin was prepared following the same process as for manufacturing bulk epoxy. Resin infusion under flexible tooling (RIFT) was then used to manufacture the laminate (see Figure 3.6), causing the resin to flow into the fibre layup with the assistance of vacuum and atmospheric pressure. The hot plate was then switched on to cure the composites using the same curing cycle as curing the epoxy polymers (90 °C for 1 hour and 160 °C for 2 hours, with a ramp rate of 1 °C per minute between the set temperatures). A heat insulation barrier was placed over the stack to reduce heat loss and reduce the temperature difference between the top and base of the stack.

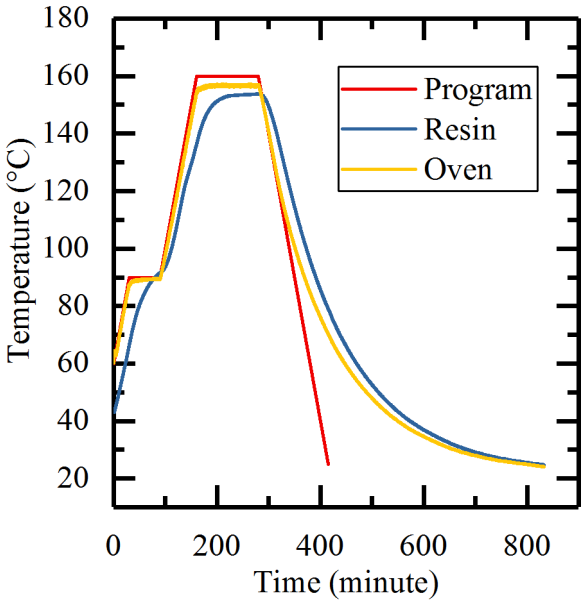


Figure 3.4: Oven curing cycle for making epoxy plates for sandwich structure cores

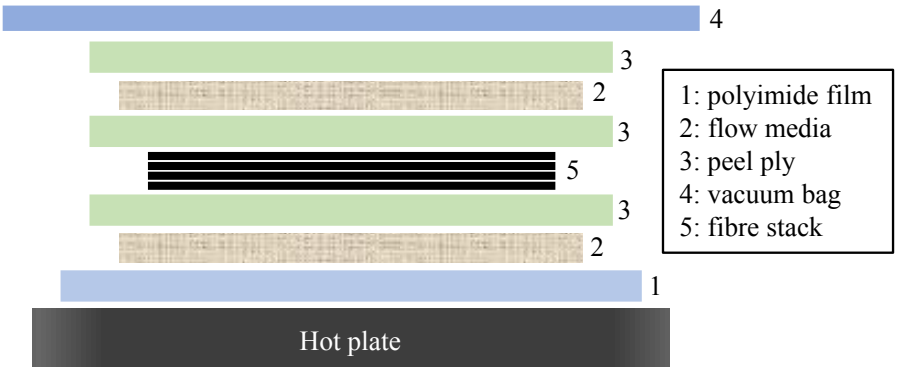


Figure 3.5: Sketch of RIFT stacking

Figure 3.7 shows the measured curing temperatures during the RIFT process. The temperatures were measured with a thermocouple placed in the middle of the carbon fibre (composite) layers and another one stuck on the hot plate. Like the oven, the hot plate has no cooling system so the cooling down process can only take place naturally; and because there was a heat insulation barrier, the cooling process took more time than in the oven. It is also noted that although the hot plate was set at 60 °C for preheating, the hotplate temperature overshot so the measured temperature rose to over 70 °C. Therefore the curves in Figure 3.7 start from 80 °C. The fast heating also affected the 90 °C curing process, as can be seen that the measured temperatures in the first rising and 90 °C curing process are higher than the programmed temperature. The measured curing temperature of composite is higher than the hot plate, this can be attributed to the exothermic reaction of epoxy curing and the effect of heat insulation resulting from the barrier.

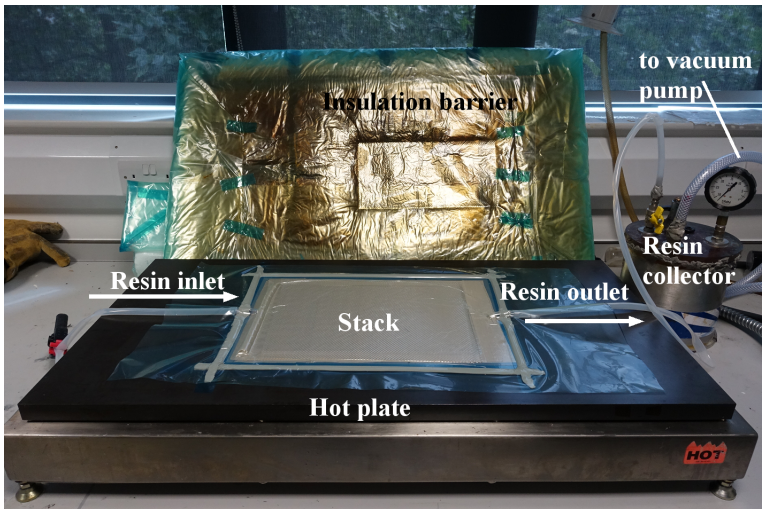


Figure 3.6: RIFT set-up

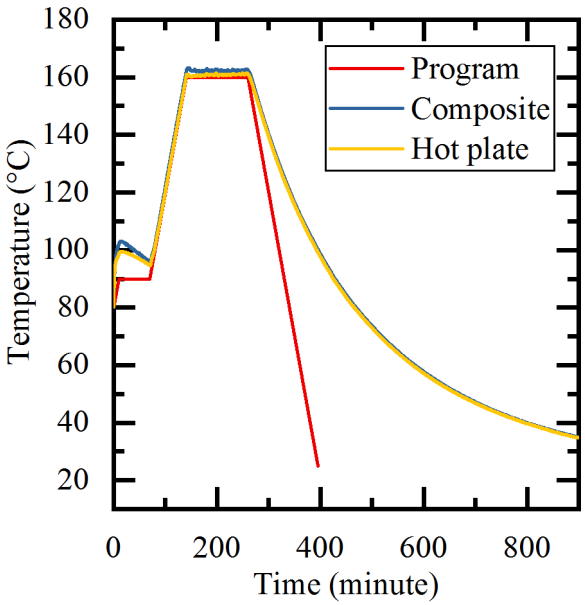


Figure 3.7: RIFT curing cycle for making CFRPs for sandwich structure facesheets

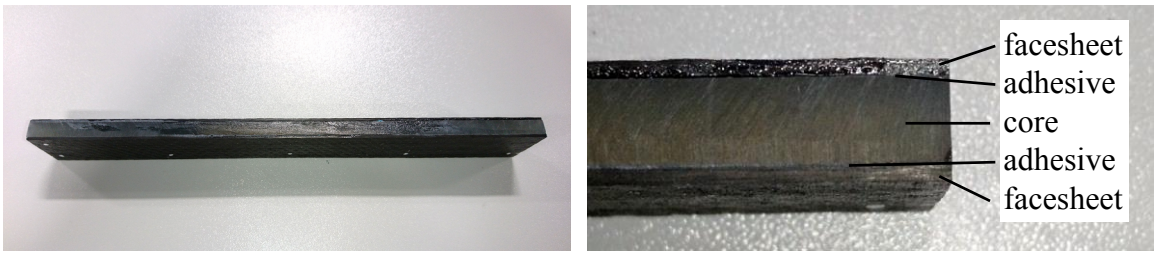
3.4.3 Sandwich Structure Construction

3.4.3.1 Flat Structures and Artificial Debonded Regions

To make flat sandwich structures, first the manufactured CFRP and the epoxy plate were cut to the desired sizes using a table saw. The surfaces of the cut CFRP and epoxy plate were grit-blasted and cleaned with acetone to remove any residual release agent before applying the adhesive. A two-component epoxy adhesive, Araldite 2014-1 [122] from Huntsman, Switzerland, was prepared with the mixing ratio of 2 : 1 (A : B) by weight. The surfaces of the epoxy core were applied with a thin layer of the prepared adhesive using a stainless steel spatula, the

facesheets were then adhered to the core. The adhered facesheets and core were placed on a flat steel plate with another steel plate placed on top of them. The stack was then placed in an oven with a weight of about 20 kg placed on the top plate to make the adhesive infuse better between the CFRP facesheets and epoxy core. The whole stack was then heated in an oven at 50 °C for 2 hours to cure the adhesive. After bonding, the sides of the sandwich structures were ground to remove the excess adhesive.

A typical flat sandwich structure was shown in Fibure 3.8. The facesheets and core can be identified in Figure 3.8b. The length and width of the manufactured flat sandwich structures were 200 mm and 25 mm, and the thickness composed of a 6 mm thick core and two 1.3 mm thick facesheets (see Table 3.3). The average thickness of the adhesive layer (and the debonded region) was about 180 µm, as shown in Figure 3.9b&c.



(a) Whole structure **(b)** Local magnification

Figure 3.8: Flat sandwich structure

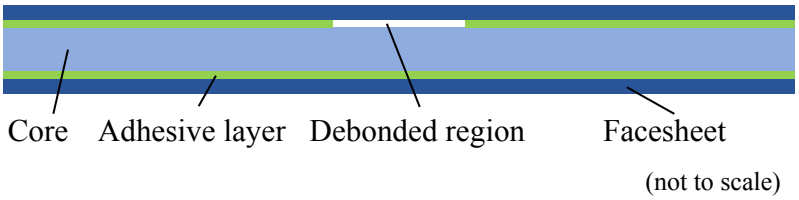
Table 3.3: Flat sandwich structure sizes

	Length (mm)	Width (mm)	Thickness (mm)
Core	200	25	6.0
Facesheet			1.3/sheet
Bonded sandwich			8.6

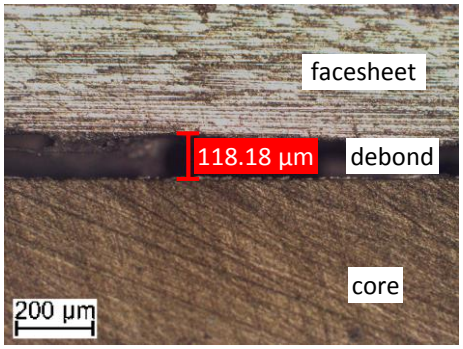
To form artificial debonded regions within the flat sandwich structures, polytetrafluoroethylene (PTFE) films with the required width were placed at the desired places between the facesheets and the core after the adhesive had been spread on the core but before the sandwich structure was assembled. The PTFE films, having a thickness of about 20 µm, were non-adhesive and prevent the adhesive agent bonding the facesheet and the core together. After curing, the PTFE film was pulled out. A lateral sketch of a sandwich structure with a debond and local magnification of the debonded region are shown in Figure 3.9.

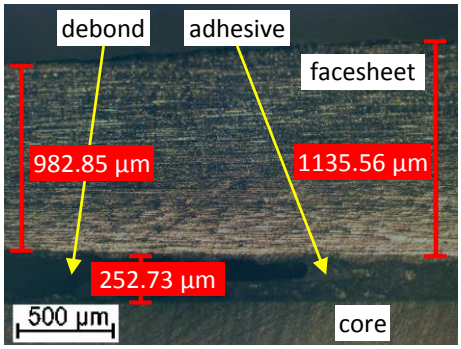
3.4.3.2 Curved Structures and Artificial Debonded regions

Two curvature angles were used for the curved sandwich structures: 15° and 30°. The curvatures are significantly different from flat, therefore there were three different shapes (flat,



(a) Lateral sketch of sandwich structure with single debonding





(b) Magnification of debonded region **(c)** Magnification of debond and adhesive

Figure 3.9: Sketch and local magnification of debonded region

15° and 30°) to be compared and show the trends. Another reason for choosing the two curvatures was the ability to manufacture the curved epoxy plates, CFRP facesheets and sandwich structures, as highly curved structures would increase the difficulty of manufacturing and could result in undesired delamination in the structures.

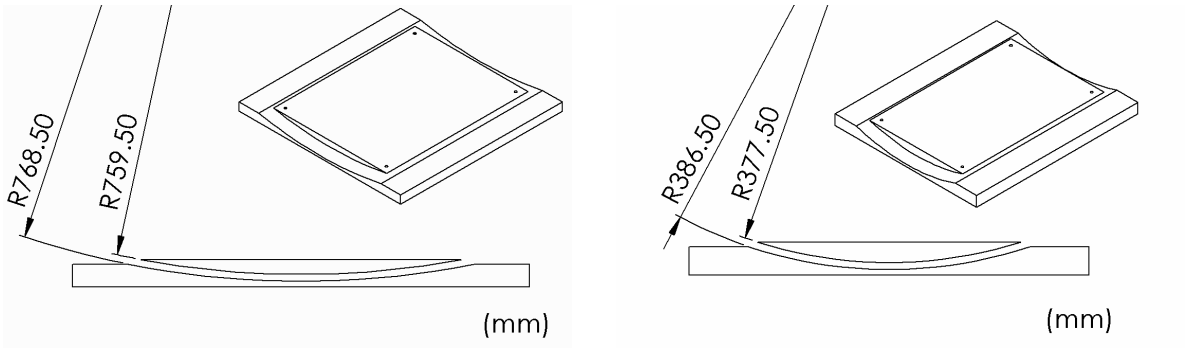
To make curved sandwich structures, two manufacturing processes were tried. The first method was the RIFT method, which cured the facesheets and bonded the facesheets to the core at the same time. However, this method led to cracking of the sandwich core, which will be discussed later. Therefore, the second method was adopted, which had been used to manufacture the flat sandwich structures.

For the first method (RIFT method), first the surfaces of the manufactured curved epoxy plates were grit-blasted and cleaned using acetone to remove any residual release agent. Unlike manufacturing the flat sandwich structures, the surfaces of the curved plates were not applied with the adhesive and then adhered with the facesheets, instead, the the infusing resin is used as the matrix of the facesheets and the adhesive. If the adhesive Araldite 2014-1 had been applied to the surfaces of the curved plates, it could infuse into the fibre cloths and affect the infusion of epoxy resin during the RIFT process.

Two sets of curved aluminium plates with different curvatures were used for making the 15° and 30°-curved sandwich structures. Sketches of the moulds are shown in Figure 3.10. The radii of the top and base plates of each set have a difference of 6 mm because the thickness of the core plate, facesheets and other RIFT materials were taken into consideration when designing the plates, the aim is to make the top and base surfaces of the curved sandwich structures

parallel. Aluminium is used as the materials for making the mould plates because of its light weight and good thermal conductivity. Before stacking the RIFT materials, the surfaces of the aluminium plates were applied with the release agent Frekote 700-NC to prevent the leaking resin from sticking on the plates during the curing process.

The required carbon fibres and RIFT materials were then laid in sequence on the base aluminium plate, as shown in Figure 3.11. The top plates shown in Figure 3.10 were not placed on the stacking when infusing the resin. It is noted that the sizes of the fibre cloths should be smaller than the epoxy plate to prevent the overhanging fibres from bonding at the sides, which can lead to the buckling of the cured facesheet and result in debonding of the facesheets from the core.



(a) Plates for 15° sandwich structures **(b)** Plates for 30° sandwich structures

Figure 3.10: Sketches of the aluminium plates used for making 15° and 30°-curved sandwich structures by RIFT

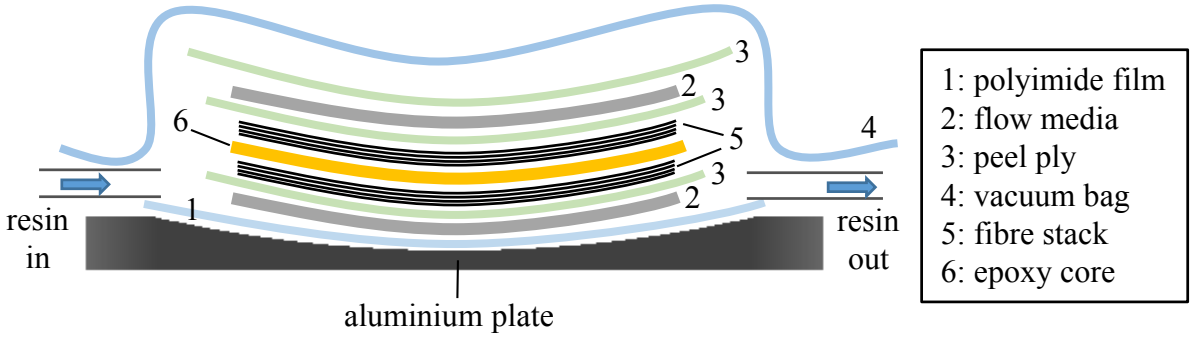
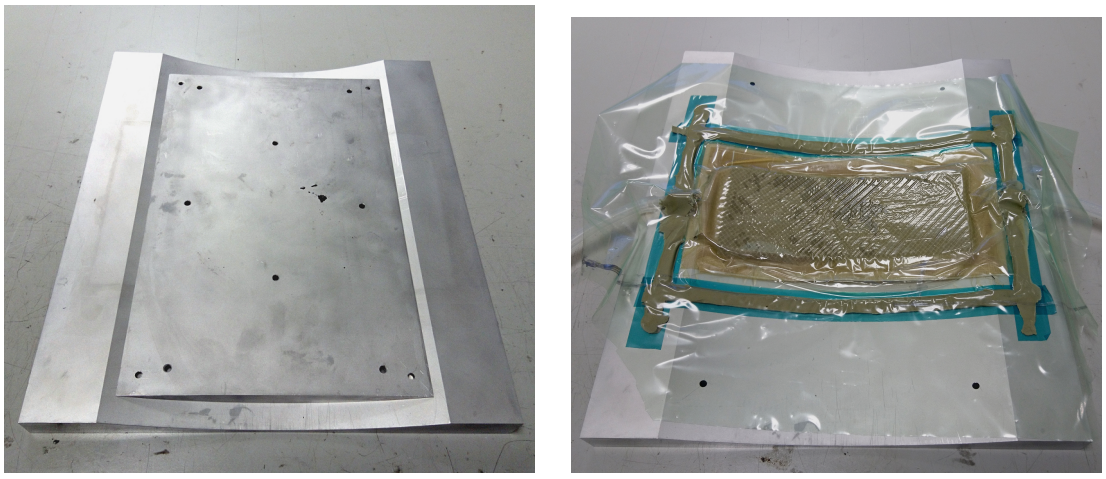


Figure 3.11: Sketch of RIFT set-up for making curved sandwich structures

Figure 3.12a shows the curved aluminium plates for making 30°-curved sandwich structures and Figure 3.12b shows the stacking. After being infused with epoxy resin, the whole set-up was placed in the oven for curing. During the curing process, the curved top plate and a weight of about 5 kg was placed on the stack to prevent air leaking into the facesheet and to achieve better adhesion between the facesheets and the core. The same curing cycle as for curing the epoxy polymers was used.



(a) Curved aluminium plates **(b)** RIFT stacking

Figure 3.12: Curved aluminium mould and the RIFT stacking for making 30° sandwich structures

To form artificial debonded regions within the curved sandwich structures, PTFE films with the required sizes were cut and placed at the desired places between the facesheet carbon fibres and the curved core before curing the sandwich structures.

After curing, a typical curved sandwich plate has a dimension of about 210 mm × 150 mm (length × width). The curved sandwich plates were then cut to the desired size using a table saw, with the midplane arc length of 200 mm and a curvature angle of 15° or 30° (see Table 3.4). Figure 3.13 shows a 30°-curved sandwich structure cut to size.

Table 3.4: Curved sandwich structure sizes

	Curvature Angle	Midplane arc length (mm)	Width (mm)	Radial thickness (mm)
Core	15° / 30°	200	25	6
Facesheet				1.3/sheet
Bonded sandwich		200		8.6

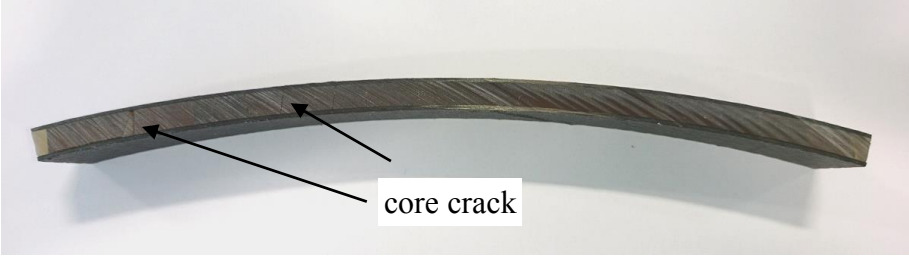


Figure 3.13: 30°-curved sandwich structure manufactured using RIFT method, crack of core indicated

Although the RIFT method could cure the facesheets and bond the facesheets to the core at the same time, it led to cracking of the core, as shown in Figure 3.13. The reason for this cracking could be the residual stress which resulted from the difference in the thermal expansion coefficients of the facesheet CFRP and the epoxy core. The facesheets CFRP were cured and bonded to the core at 160 °C, but after cooling down to room temperature, the difference in the thermal expansion coefficients resulted in different amounts of shrinkage of the facesheets and the core. The coefficient of thermal expansion of an epoxy polymer is greater than that of CFRP [123, 124], so the epoxy tries to shrink by more than the CFRP, but is not able to as it is constrained by the stiff CFRP. Thus the stress in the epoxy builds up, and the epoxy cracks when its relatively low tensile strength is reached. The difference in shrinking hence resulted in the crack of the core.

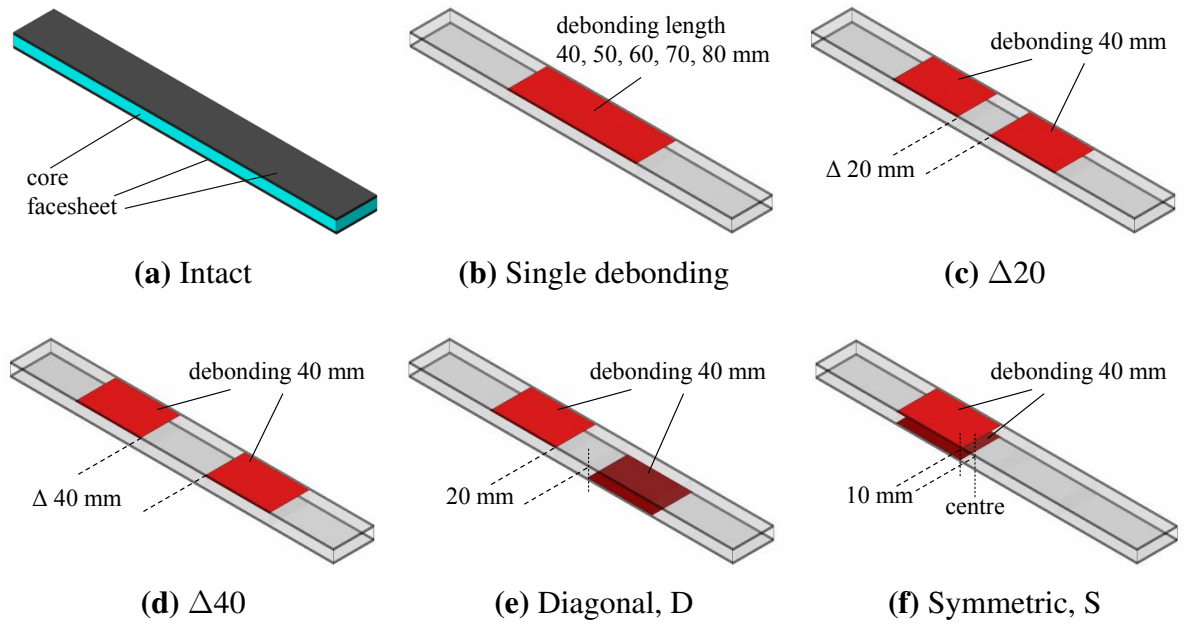
To overcome cracking of the core, the method used to manufacture the flat sandwich structures was used (see Section 3.4.3.1). First the top and base CFRP facesheets were manufactured using the RIFT method as for manufacturing the flat CFRP facesheets (see Section 3.4.2). The stacking shown in Figure 3.5 was laid on the curved aluminium plates which are shown in Figure 3.10, with the flat side of the plates down on the hot plate. The fibres were then infused with the resin and cured. Since the curved plates were made of aluminium, the heat can easily conduct from the hotplate to the fibre stacking.

After manufacturing the curved facesheets, the curved epoxy plate and facesheets were grit-blasted, cut to the desired sizes using a table saw and cleaned with acetone. The surfaces of the curved epoxy core were applied with a thin layer of the epoxy adhesive, Araldite 2014-1, and adhered with the the top/base facesheets. To form artificial debonded regions within the curved sandwich structures, PTFE films with the required width were placed at the desired places before adhering the facesheets to the core. The adhered facesheets and core were placed on the aluminium base plate with the top plate on top of them. The stack was then placed in an oven and cured at 50 °C for 2 hours with a weight of about 20 kg placed on the top plate. After bonding, the sides of the curved sandwich structures were ground to remove the excess adhesive. The sizes of the manufactured curved sandwich structures are listed in Table 3.4.

3.4.4 Location of Artificial Debonded Regions

The shortest length of the single debond (see Figure 3.14b), 40 mm, was designed to be longer than the width of the sandwich structures which was 25 mm; the length of the single debond was then increased up to 80 mm, which was twice as long as the 40-mm debond, with an increment of 10 mm. As an 80-mm debond can be regarded as two 40-mm debonds without separation ($\Delta 0$), the effects of the separation between the two 40-mm debonds ($\Delta 20$ and $\Delta 40$, see Figure 3.14c&d) and the locations (condition D and S, see Figure 3.14d&e) were considered. Figures 3.14 and 3.15 illustrate the models of the intact flat and 30°-curved sandwich structures,

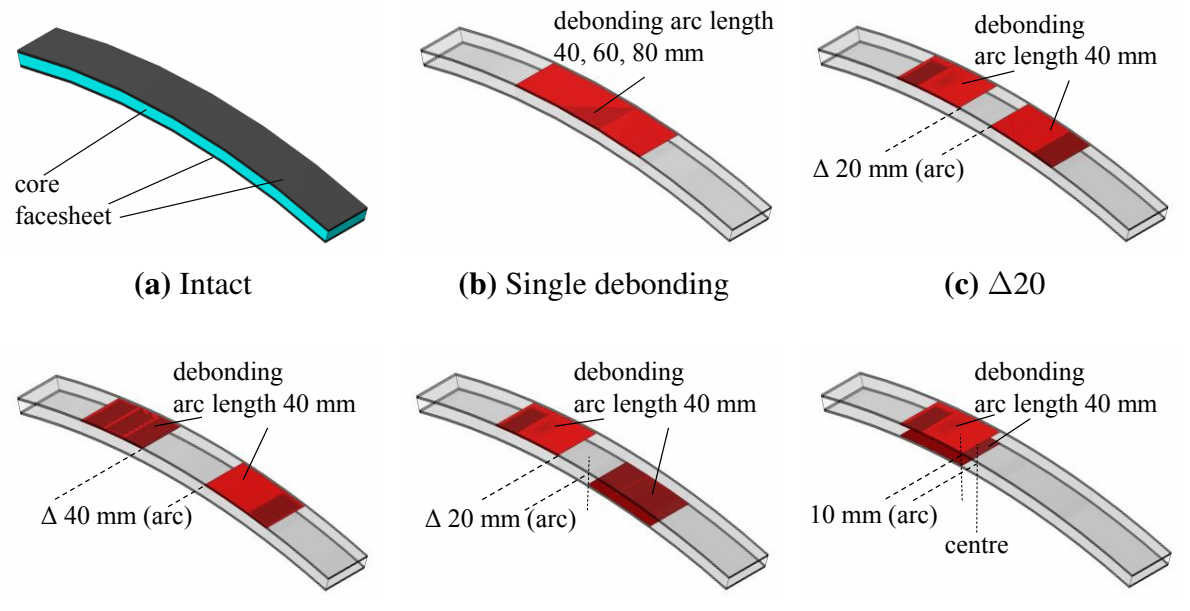
and show the lengths and locations of the debonded regions within the structures. The debond conditions of the 15°-curved sandwich structures were the same as the 30°-curved sandwich structures. The hammer impact tests were conducted on the sandwich structures with these types of debonds.



(a) Intact **(b)** Single debonding **(c)** Δ20

(d) Δ40 **(e)** Diagonal, D **(f)** Symmetric, S

Figure 3.14: Finite element models of flat sandwich structures with locations of debonded regions (shown in red)



(a) Intact **(b)** Single debonding **(c)** Δ20

(d) Δ40 **(e)** Diagonal, D **(f)** Symmetric, S

Figure 3.15: Finite element models of 30°-curved sandwich structures with locations of debonded regions (shown in red)

3.5 Conclusions

The materials and manufacturing processes of the sizing-modified carbon fibre composites using silica nanoparticles, flat and curved sandwich structures have been introduced in this chapter. The manufacturing and locations of artificial debonded regions have also been presented. The experimental methods are presented in the next chapter.

Chapter 4

Experimental Methods

4.1 Introduction

In this chapter, the experimental methods used in this research are introduced, including tensile and density tests, fibre volume fraction measurement, mode I interlaminar fracture and fatigue crack growth tests, microscopy analysis, and vibration tests. The test procedures were based on British Standard (BS) and/or American Standard (ASTM) test methods if available.

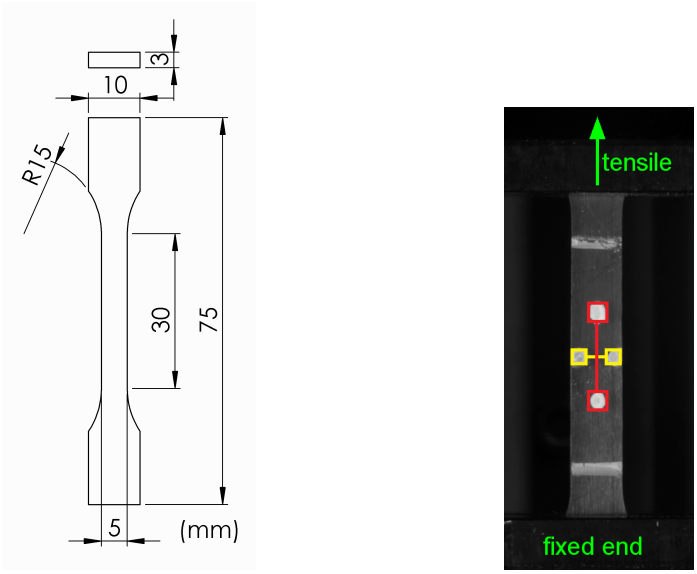
4.2 Tensile Tests

Tensile tests were conducted on the epoxy polymers used for the cores and the CFRPs used for the facesheets of the sandwich structures. The results were used in the finite element simulations of the vibration behaviours.

4.2.1 Bulk Epoxy Tensile Tests

The tensile tests of epoxy polymers for the sandwich structures were conducted at room temperature using a universal test machine Instron 5584 fitted with a 5 kN load cell, following the test standards BS EN ISO 527-1 and -2 [125, 126]. The displacement rate of the uniaxial tensile tests was 1 mm/min. Rectangular blanks were first sawn from 3-mm-thick epoxy plates, then the blanks were machined to dog-bone specimens using a table router. The specimen type was 1BA in BS EN ISO 527-2 [126], as shown in Figure 4.1a.

A video extensometer, Video Gauge MT-Pro System version 4.1.0 from iMETRUM, UK, was used to measure the axial and transverse strains. The resolution of the video camera was 1.3 mega-pixels (width 1388 $\times$ height 1038 pixels) [127]. However, for reducing the file size, the resolution of the recorded region was set to 600 $\times$ 1038 pixels (the areas beside the specimens were cut off). To help the video camera clearly identify strains from images, the specimens were marked with small dots at two points in the longitudinal direction and two points in the lateral direction. The dots were marked using permanent marker pens. The colours of the dots were contrasting to the specimens; and the four dots were symmetric to the centre. These four points were tracked by the system, which calculated the longitudinal and lateral strains. Figure 4.1b shows a dotted dogbone specimen under testing: the points in the red squares are for longitudinal strain and the points in the yellow squares are for lateral strain. During the tests, an LED panel was used to illuminate the specimens. To achieve synchronisation between the test machine and the video, the camera recording was started manually at the same time when the test was started. At least 6 samples of each epoxy formulation were prepared and tested.



(a) Type 1BA dogbone geometry **(b)** Video extensometer image

Figure 4.1: Epoxy polymer tensile dogbone dimensions and video extensometer image

The tensile modulus, E, and Poisson's ratio, ν, were calculated and averaged from the test results. The tensile modulus was calculated using the ratio of the stress to strain over the strain interval between 0.0005 and 0.0025 (see Figure 4.2) and the Poisson's ratio was calculated using the following equation:

$$\nu = -\frac{\Delta\varepsilon_{\text{lat}}}{\Delta\varepsilon_{\text{long}}} \tag{4.1}$$

where $\Delta\varepsilon_{\text{lat}}$ is the lateral strain and $\Delta\varepsilon_{\text{long}}$ is the longitudinal strain [125].

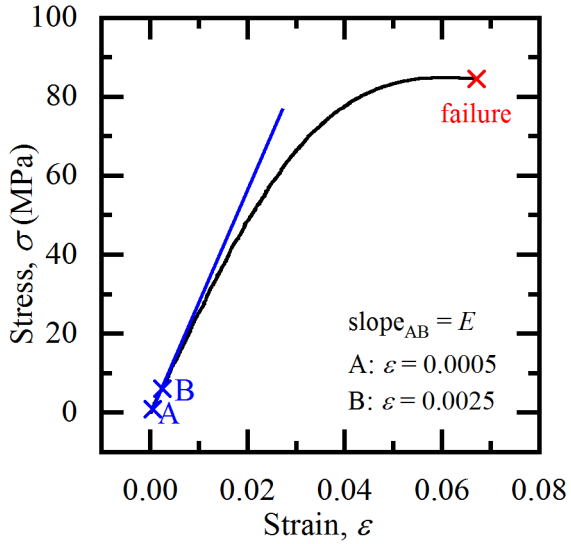


Figure 4.2: Tensile stress-strain curve of unmodified epoxy polymer showing strain range used to calculate tensile modulus, E

4.2.2 Carbon Fibre Composite Tensile Tests

The tensile tests of the CFRP used for the sandwich structures were conducted using an Instron 5584 universal testing machine fitted with a 150 kN load cell, based on the test standards ASTM D3039 [128] and ASTM D3518 [129]. The displacement rate used was 0.5 mm/min. Rectangular specimens were cut from CFRP plates of the required fibre orientation. End tabs (cut from epoxy glass fibre laminate) were bonded to the specimens or abrasive tapes were used to help the grips hold the specimens. For the UD specimens ($[0°]_4$ and $[90°]_8$), end tabs were bonded to the specimens using an adhesive Araldite 2014-1 [122], which was cured at 50 °C for 2 hours. For the symmetrically stacked specimens, $[+45°/-45°]_{2s}$, abrasive tapes were used. The difference between using end tabs or abrasive tapes is recommended in the standard ASTM D3039 [128]. The video extensometer was also used with the same preparation procedures as for testing the epoxy polymers. At least 5 samples of CFRP with each matrix epoxy formulation and stacking angles were prepared and tested.

As stated in Section 3.3.1, since a UD carbon fibre lamina is transversely isotropic, the tensile/shear modulus and Poisson's ratio in the longitudinal and lateral directions are different. In this study, the longitudinal tensile modulus, E_1, transverse tensile modulus, E_2, in-plane Poisson's ratio, ν_{12}, and shear modulus, S_{12}, were calculated and averaged from the results of tensile tests conducted on CFRP laminates with different stacking: $[0°]_4$ for E_1 and ν_{12}, $[90°]_8$ for E_2 and $[+45°/-45°]_{2s}$ for S_{12}. The dimensions of the three types of specimens and the end tabs are listed in Table 4.1

For a UD lamina, the mechanical properties in directions 2 and 3 can be assumed the same [118]. Therefore, E_2 equals E_3, ν_{12} equals ν_{13}, and S_{12} equals S_{13}. The remaining Poisson's

Table 4.1: Dimensions of CFRP and end tabs for tensile tests

	Specimen	End tab
	$L \times W \times t$ (mm)	$L \times W \times t$ (mm)
$[0°]_4$	250 × 15 × 1.2	56 × 15 × 2.4
$[90°]_8$	175 × 25 × 2.3	40 × 25 × 2.4
$[+45°/-45°]_{2s}$	250 × 25 × 2.3	abrasive tape: 56 × 15 × 0.8

ratio ν_{23} can be solved using the equation [130]:

$$\nu_{23} = \nu_{12}\left(\frac{1 - \nu_{12}\frac{E_2}{E_3}}{1 - \nu_{12}}\right) = \nu_{12}\left(\frac{1 - \nu_{21}}{1 - \nu_{12}}\right) \tag{4.2}$$

and the remaining shear modulus S_{23} can be calculated using:

$$S_{23} = \frac{E_2}{2(1 + \nu_{23})} \tag{4.3}$$

Therefore the tensile moduli, shear moduli and Poisson's ratios in the three main axes can be obtained.

4.3 Density Tests

Density measurements were conducted on the bulk epoxy and CFRP used for the sandwich structures, and the results were used in the finite element simulations. The tests took reference to the standards ASTM D792-13 [131] and ASTM D2320-98(reapproved 2017) [132]. A BP2100S analytical balance from Sartorius, UK, was used to measure the weight. The balance had a resolution of two decimal places (0.01 g) and a maximum capacity of 2100 g. A pycnometer (see Figure 4.3) with a capacity of 10 ml was used, which was cleaned and dried before the tests. First, the mass of the pycnometer filled with deionised water was measured (W_A). The temperature of the deionised water was also measured for identifying the density of water (ρ_w), since the density of water is slightly different according to the temperature. The value of the density of deionised water at the temperature was calculated using an online tool [133]. The mass of a small (smaller than the diameter of the neck of the pycnometer), clean and dry piece of epoxy or CFRP cut from the bulk epoxy or composites was measured (W_S). After measuring the dry mass, the small piece was immersed into the pycnometer. Finally, the pycnometer containing the small piece and filled with deionised water was carefully wiped and weighed (W_B).

The density of the small piece was then calculated using the following equation:

$$\rho = \frac{W_S \times \rho_w}{W_S + W_A - W_B} \tag{4.4}$$

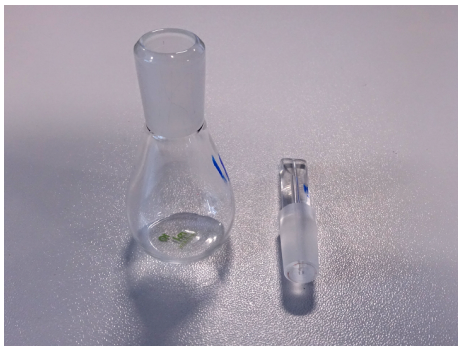


Figure 4.3: Pycnometer for measuring density

where W_S is the mass of the sample, ρ_w is the density of water at the measurement temperature, W_A is the mass of the pycnometer filled with water, and W_B is the mass of the pycnometer containing the sample and filled with water. Each formulation of epoxy and CFRP was tested 5 times, and the results were averaged.

It is noted that the capacity of the pycnometer was 10 ml so the tested specimens are relatively small (a few cubic centimetres), and the resolution of the balance used was only 0.01 g. Therefore this could result in the calculated densities having differences of about 10 % compared to the actual densities.

4.4 Sizing-modified Carbon Fibre Composite

4.4.1 Double Cantilever Beam (DCB) Specimen Preparation

Double cantilever beam (DCB) specimens were used for mode I interlaminar fracture tests and fatigue crack growth (FCG) tests. The DCB specimens were machined from the UD CFRP using unmodified and modified fibre sizings by waterjet cutting. The dimensions of each specimen were: 150 mm $\times$ 20 mm $\times$ 3 mm. A starter crack was provided by a 45 mm artificial pre-crack made by a 30-μm-thick insert film at the midplane of one end.

To connect the specimens to the test machines, the sides of the insert end were grit-blasted, cleaned with acetone and adhered with two aluminium load blocks using Araldite 2014-1, a two-component epoxy adhesive [122]. Each load block had a size of 20 mm $\times$ 20 mm $\times$ 12 mm with a 8 mm diameter pin hole at the centre. The specimens adhered with the blocks were then clamped using a jig and cured in an oven at 50 $^{\circ}$C for 2 hours for firmly adhering the blocks. After attaching the load blocks, the lateral side of the specimens for the mode I interlaminar fracture tests were painted with white correction fluid and the crack length was carefully marked with a fine marker pen, from the end of the inserted film, every millimetre for the first 25 millimetres and then every 5 millimetres; while for the DCB specimens for FCG tests, the crack length was marked every millimetre rather than using a 5 millimetre spacing.

Figure 4.4 shows a tested DCB specimen used for the mode I interlaminar fracture test.

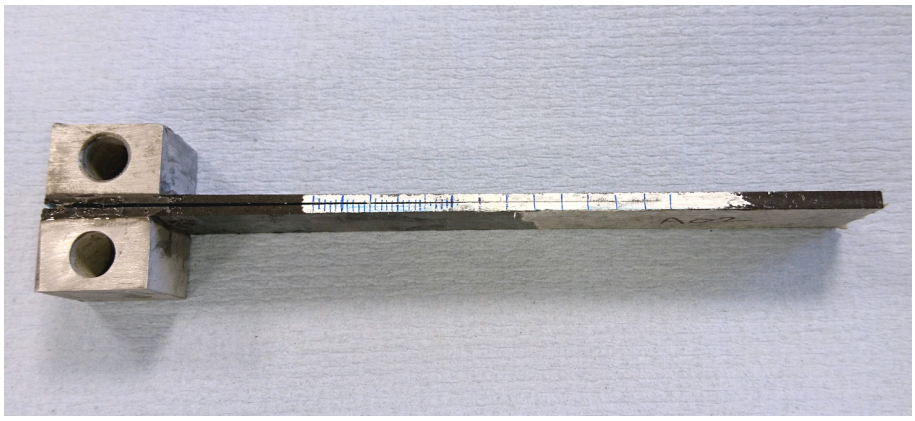


Figure 4.4: Tested specimen of mode I interlaminar fracture test

4.4.2 Mode I Interlaminar Fracture Tests

To determine the mode I fracture energy, interlaminar fracture tests were conducted according to the standards BS ISO 15024 [16] and ASTM D5528-13 [134] at room temperature. In this study, both the fracture energies at crack initiation, $G_{\text{IC,init}}$, and during crack propagation, $G_{\text{IC,prop}}$ were calculated. An Instron 5584 universal testing machine fitted with a 5 kN load cell was used to test the DCB specimens. The displacement rate was 1 mm/min. A travelling microscope was set up in front of the loaded specimen to measure the crack growth.

In the beginning, for pre-cracking and generating a natural crack, the specimens were loaded until the crack grew by up to 5 mm from the insert film, then the specimens were unloaded. After a natural crack was made, the specimens were again loaded until the crack propagated to the final mark. The displacement and load were recorded when the crack grew to each mark. Five specimens were tested for each sizing formulation.

The $G_{\text{IC,prop}}$ of each specimen was calculated using the modified compliance calibration (MCC) method [16, 134]. A graph of $(bC/N)^{1/3}$ against the thickness-normalized crack length $(a/2h)$ was plotted, where b is the specimen width, C is the compliance and N is the load block correction factor; a is the crack length and $2h$ is the thickness of the specimen. The load block correction factor, N, and large-displacement correction factor, F, were calculated using [16]:

$$N = 1 - \left(\frac{l_2}{a}\right)^3 - \frac{9}{8}\left[1 - \left(\frac{l_2}{a}\right)^2\right]\frac{\delta l_1}{a^2} - \frac{9}{35}\left(\frac{\delta}{a}\right)^2 \tag{4.5}$$

$$F = 1 - \frac{3}{10}\left(\frac{\delta}{a}\right)^2 - \frac{2}{3}\left(\frac{\delta l_1}{a^2}\right) \tag{4.6}$$

where δ is the displacement, l_1 is the distance from the centre of the pin hole to the mid-plane of the specimen and l_2 is the distance from the centre of the pin hole to the edge of the load block.

The slope, m, of a straight line fitted to the $(bC/N)^{1/3}$ against $(a/2h)$ data by linear regression was calculated.

The $G_{\text{IC,prop}}$ was then calculated using:

$$G_{\text{IC,prop}} = \frac{3m}{2(2h)} \times \left(\frac{P}{b}\right)^2 \times \left(\frac{bC}{N}\right)^{2/3} \times F \tag{4.7}$$

where P is the load.

The $G_{\text{IC,init}}$ values were calculated using the Max/5 % compliance-increase point method [16]: For the 5 % value, the initial compliance C_0 was calculated by fitting a straight line from the beginning to the limit point of linearity of the load-displacement curve, then a new line corresponding to 1.05 C_0 was drawn (see Figure 4.5). The load and displacement at the intersection of the line with the compliance of 1.05 C_0 and the load-displacement curve were used to calculate $G_{\text{IC,init}}$. If the maximum load occurred prior to the intersection point, then the $G_{\text{IC,init}}$ was calculated using the the maximum load and the corresponding displacement.

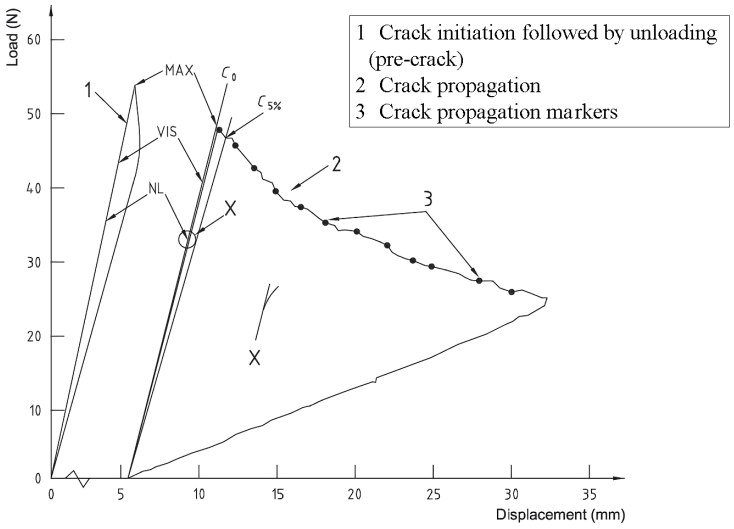


Figure 4.5: Max and 5 % increase in compliance for determining $G_{\text{IC,init}}$ for a mode I interlaminar fracture test; the reload curve has been offset by 5 mm for clarity [16]

4.4.3 Fatigue Crack Growth (FCG)

Fatigue crack growth (FCG) tests were conducted on the DCB specimens at room temperature, taking reference to the standards BS ISO 13003 [135] and ASTM E647 [136]. Displacement control was used as the method for applying cyclic loading. The maximum displacement for the cyclic loading in the fatigue test, $\delta_{\text{f,max}}$, was determined by pre-cracking the specimens using the Instron 5584 universal testing machine. The fatigue tests were then conducted on an Instron 8872 servo-hydraulic universal testing machine fitted with a 1 kN load cell. The displacement ratio ($R = \delta_{\text{f,min}}/\delta_{\text{f,max}}$) used was 0.1, at a cyclic loading frequency of 10 Hz with a sinusoidal waveform (see Figure 4.6).

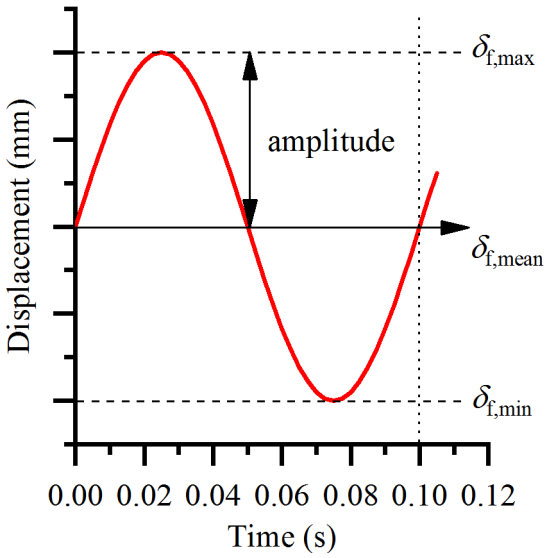


Figure 4.6: Sinusoidal waveform and displacements of FCG test

Table 4.2: FCG test recording intervals

Step	Cycles at this step	Total cycles	Step	Cycles at this step	Total cycles
1	200	200	12	5000	30000
2	300	500	13	6000	36000
3	500	1000	14	36000	72000
4	1000	2000	15	36000	108000
5	1000	3000	16	36000	144000
6	1000	4000	17	36000	180000
7	1000	5000	18	36000	216000
8	5000	10000	19	36000	252000
9	5000	15000	20	36000	288000
10	5000	20000	21	72000	360000
11	5000	25000	Frequency: 10 Hz, total time: 10 hours		

During the tests, the machine was briefly paused at certain intervals (see Table 4.2) and held at $\delta_{f,max}$, while the load and crack length (observed using a microscope) were recorded. Then the specimens were moved back to the mean displacement, $\delta_{f,mean}$ which equals $(\delta_{f,min} + \delta_{f,max})/2$, and the tests were continued. Three specimens were tested for each formulation.

The maximum strain energy release rate at each paused point, G_{Imax}, was calculated from the load at the maximum displacement ($\delta_{f,max}$) during the last cycle before pausing and the recorded crack length. The crack propagation rate per cycle, da/dN, was calculated using the incremental polynomial method described in ASTM E647 [136]. This method calculates the

crack propagation rate by fitting a second-order polynomial to sets of $(2n + 1)$ successive data points, where n was set as 3 (therefore a total of 7 points) in this study. The benefit of this method is that it can reduce scatter in the data compared to the secant method [137]. The FCG curve of $\log(\mathrm{d}a/\mathrm{dN})$ against $\log(G_{\mathrm{Imax}})$ was plotted for characterising the fatigue performance of the sizing-modified CFRP.

4.4.4 Microscopy Analysis

To identify the toughening mechanisms of the sizing-modified CFRPs, images of the fracture surfaces of the tested specimens were obtained using a scanning electron microscope (SEM), Hitachi S-3400N, or a field-emission SEM (FE-SEM), Zeiss Ultra Plus Field Emission SEM. Small samples were cut from the specimens tested by the mode I interlaminar fracture tests and the FCG tests.

For the SEM, Hitachi S-3400N, the samples were attached to aluminium stubs using a self-adhesive carbon tape. To improve the conductivity and get a better quality of the images, before placing into the chamber of SEM, fine lines of silver paint were drawn at the side of each sample; the samples were then coated with a thin gold layer by sputtering to prevent charging. The accelerating voltage used was between 10 to 15 kV and the working distance was about 12.5 mm. For the FE-SEM, Zeiss Ultra Plus Field Emission SEM, the samples were gold-palladium coated [138]. The voltage used was 3.0 kV and the working distance was about 7.6 to 8 mm.

4.5 Fibre Volume Fraction

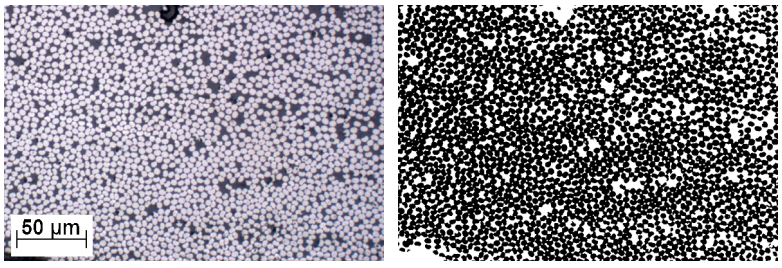
The mechanical properties of fibre composites, such as tensile modulus, strength and fracture energy, are significantly affected by the fibre content in the composites. In this study, the fibre volume fractions of the sizing modified CFRPs and the CFRPs for the facesheets of the sandwich structures were measured. Small samples were cut from the UD CFRPs and then cold-mounted using a room-temperature-cured acrylic system: VARI-SET 20 powder resin and VARI-SET hardener from Metprep, UK, at a mixing ratio 2:1 by volume. The fibre was set to be in vertical in the mounting acrylic. The samples were then ground and polished using a Saphir 520 automatic grinding and polishing machine from Metprep, UK.

At the beginning of grinding, the samples were ground with a P180 abrasive grinding paper (particle size: 82 μm), at a pressing force of 40 N and rotating speed of 150 rpm, to grind off the mounting acrylic covering the CFRP samples. After removing the covering acrylic, the samples were then ground and polished following the steps and parameters shown in Table 4.3. The samples were washed with clean water and dried after each step, to make sure there were no residues on the samples which could be larger than the particle size of the next step and scratch the samples.

Table 4.3: Grinding and polishing process for measuring fibre volume fraction

Grit size	Particle size (μm)	Time (minute)	Force (N)	Rotation speed (rpm)
Grinding (water)				
P320	46.2	3	30	100
P800	21.8	2	25	100
P1200	15.3	4	25	100
P2500	8.4	4	25	100
P4000	2.5	6	25	100
P4000	2.5	6	15	100
Polishing (without water)				
Diamond suspension	6	8	15	100
	3	15	15	100
	1	15	15	100

After polishing the samples, an optical microscope Zeiss Axio Scope.A1 from Carl Zeiss, Germany, was used to observe and capture the microstructural images of the cross-sections of the CFRPs. Image processing and analysis software, Image J [139], was used to process the pictures and calculate the fibre volume fraction (V_f). V_f was calculated using the fraction of total pixels of fibres to total pixels of the CFRP in each photo. Figure 4.7 shows an example of the original and processed images for calculating fibre volume fraction; the V_f in this image is about 63%. For each sample, images were taken from at least 3 through-thickness locations and analysed, the results were averaged.



(a) Microscope image of polished CFRP

(b) Processed image for calculating V_f ($\approx$ 63%)

Figure 4.7: Images for calculating fibre volume fraction of CFRPs

4.6 Vibration Tests

Hammer impact tests were conducted on the debonded sandwich structures to find the natural frequencies and the mode shapes. The setup of the hammer test is shown in Figure 4.8, including: a hammer to hit different points on the specimens and to measure the impact force, and an accelerometer to measure the amplitude response of the specimen. A signal acquisition card was used to record and process signals from the hammer and the accelerometer, and to transfer the results to a computer.

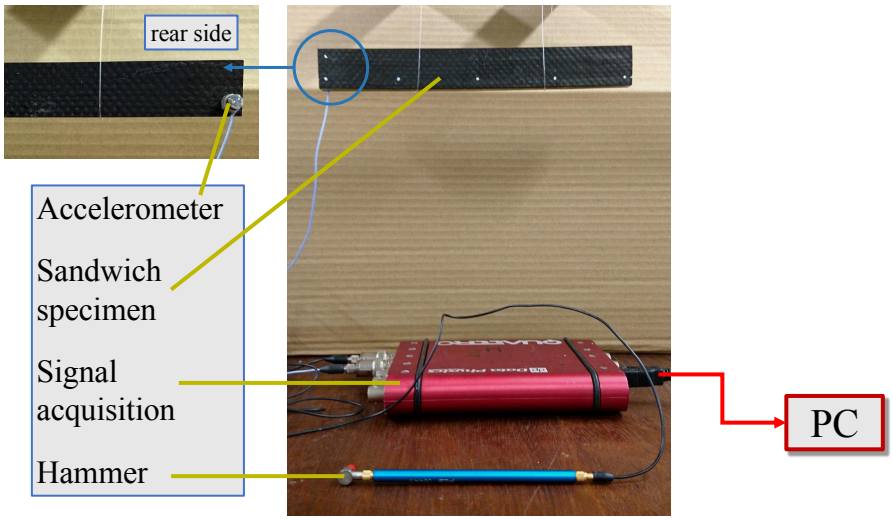


Figure 4.8: Hammer test setup

The hammer was from PCB Piezotronics, USA, and had a sensitivity of 22.5 mV/N [140]. For testing the sandwich structures, a soft cap was fitted onto the hard hammer tip, to reduce the noise signal. The accelerometer used was also from PCB Piezotronics and had a standard sensitivity 1.02 mV/m/s^2 [141], while the calibrated sensitivity of the accelerometer used for the tests was 0.981 mV/m/s^2. The accelerometer was adhered to the corner of the sandwich structures using a thin layer of wax, which could be removed and re-adhered. The portable signal acquisition card SignalCalc Ace and the analysis software SignalCalc 240 version 5.0.346 used were from Data Physics Corporation, USA. The software provides a wide range of applications such as fast Fourier transform (FFT) analysis, structural dynamics testing, modal testing, etc. In this study, FFT analysis was used to transfer the time-domain signals (from the hammer and accelerometer) to frequency-domain responses, to obtain the amplitude and phase corresponding to frequency.

The boundary conditions of the vibration tests in this study were free-free, which means that the samples were not constrained. To achieve the free-free boundary conditions, the samples were hung horizontally with two fine nylon strings having a diameter of 0.1 mm, as shown in Figure 4.8. There are three main mode types: bending mode, torsion mode and lateral bending mode. To measure the bending and torsion modes, 6 points were marked on the one side of

the sample for the hammer to strike (the white points on the sandwich structure in Figure4.8); and another point at the other face was marked for adhering the accelerometer. To measure the lateral bending modes, a point at the end of one long side was marked for tapping and the opposite side was adhered with the accelerometer. The position of these points is shown in Figure 4.9. During the tests, the struck and measured faces were turned into the lateral direction so the impact hammer can hit the points horizontally.

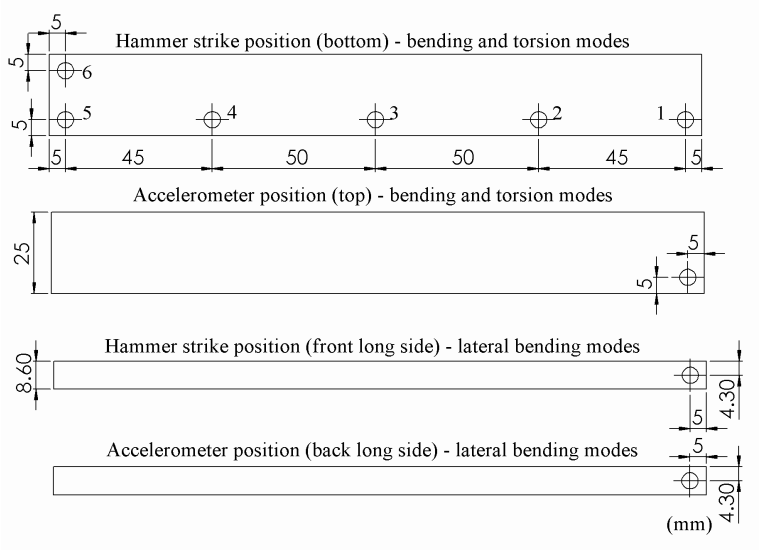
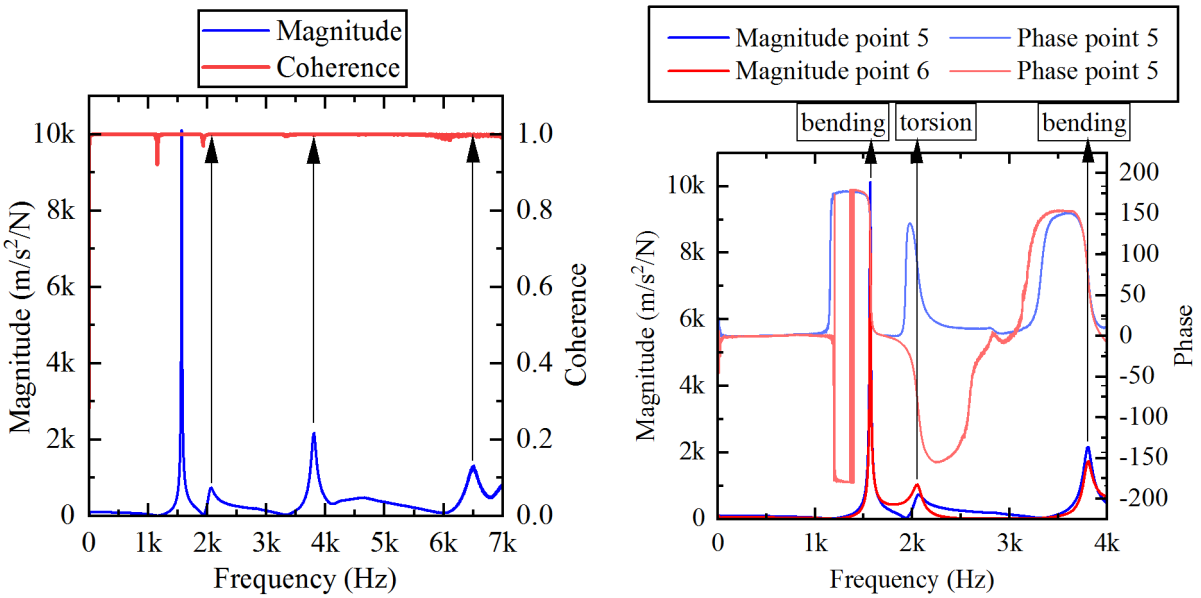


Figure 4.9: Points on the sample for hammer strike and accelerometer

To measure the frequency responses of these points, each point was tapped by the hammer at least twice. The tapping force should be light and gentle rather than strong, to prevent the signal strength from exceeding the measuring range of the hammer and accelerometer. After tapping, the coherence of the response was checked, only when the coherence of the frequency ranges at the peaks of amplitude were good would the results be taken into averaging and recorded. Figure 4.10a shows an example of the coherence and the averaged amplitude responding to the frequencies, the peaks of amplitude in the figure correspond to good coherence at the same frequencies. The averaged resultant amplitudes and phases corresponding to the frequency were then recorded. Self-developed MATLAB [142] codes (Appendix A) were used to help plot frequency response figures, find resonant frequencies and identify mode shapes.

To find resonant frequencies and modes, the resonant frequencies corresponding to the peaks of amplitude were identified through a self-developed MATLAB [142] code (Appendix A). For example, in Figure 4.10a there are four peaks so four resonant frequencies can be identified. However, since bending and torsion modes were tested and recorded at the same time, it is hard to identify the mode types from the magnitude-frequency plot alone. To distinguish bending and torsion modes, the phases associated with the magnitudes were used. If the phases of points 5 and 6 (see Figure 4.9) at the peak are both positive or negative, it means that the points are in the same direction therefore the type is a bending mode; while if the phases are



(a) Amplitude and coherence response

(b) Amplitude and phase responses of points 5 & 6

Figure 4.10: Example of amplitude, coherence and phase response of vibration tests

opposite, the points are in the opposite direction and the type should be a torsion mode. In Figure 4.10b, three peaks of magnitude can be found, according to the corresponding phases, the mode shapes of the first and third mode are bending (first, third peak), and the mode shape of the second mode is torsion (second peak). The lateral modes were tested separately from the bending and torsion modes, therefore the modes can be clearly identified.

The test procedures for the curved sandwich structures are the same as for testing the flat structures described above. The boundary conditions were also free-free, which were achieved by horizontally hanging the curved sandwich structures with two strings. The arrangement of the strike points and measuring point was the same as for the flat sandwich structures. The points were marked on the curved surfaces of the sandwich structures with the assistance of a soft roller. The bending and torsion modes were measured at the same time, and the lateral bending modes were measured independently. The MATLAB codes (see Appendix A) were also used to transform the raw data to Excel files, to plot the frequency response figures, to find the resonant frequencies and to identify mode shapes.

4.7 Replicates

The numbers of tested specimens are listed in Tables 4.4 to 4.6.

Table 4.4: Numbers of specimens used for mechanical property tests of sandwich structures

	Tensile	Density	Fibre volume fraction
Bulk epoxy	6	5	
CFRP $[0°]_4$, $[90°]_8$ and $[+45°/-45°]_{2s}$	5	5 (using $[0°]_4$)	3 (using $[0°]_4$)

Table 4.5: Numbers of specimens of sizing-modified CFRPs

	Mode I interlaminar fracture	FCG	Fibre volume fraction
Sizing-modified CFRP	5	3	3

Table 4.6: Numbers of specimens used for hammer impact tests

Flat sandwich panel	Intact	Single debond (40, 50, 60, 70, 80 mm)	Double debonds (Δ20, Δ40, D, S)
Unmodified resin, $[0°]_4$, $[90°]_4$ & $[+45°/-45°]_s$ stacking	3	1	1
Modified resin, $[0°]_4$ stacking	3	1	1
Modified resin, $[90°]_4$ & $[+45°/-45°]_s$ stacking	1	1	1
Curved sandwich panel (15° & 30°)	**Intact**	**Single debond (40, 60, 80 mm)**	**Double debonds (Δ20, Δ40, D, S)**
Unmodified resin, $[0°]_4$ & $[90°]_4$ stacking	3	1	1

4.8 Conclusions

The experimental methods of the mechanical property tests, including tensile, density, fracture and fatigue tests, and of the hammer impact tests have been briefly stated in this chapter. Microscopy analysis and fibre volume fraction measurement have also been introduced. The finite element simulations are presented in the next chapter.

Chapter 5

Finite Element Simulation

5.1 Introduction

In this chapter, the finite element (FE) simulation method used for modelling the vibration behaviour of the sandwich structures is introduced. The commercial FE software Abaqus 6.14 [143] from Dassault Systemes, France, was used in this study. The development of the three dimensional (3D) models of the flat and curved sandwich structures, modelling of the debonded regions and vibration simulations are introduced. The results of a convergence study and inspection of the overlapping of debonded regions are also discussed.

5.2 Flat Structure Model Development

5.2.1 Flat Sandwich Structure Model

The 3D models of the flat sandwich structures were developed according to the sizes listed in Table 3.3, including a core and two 4-layer facesheets. The geometries for which models were developed with or without debonded regions are shown in Figure 3.14.

The model of the core of flat sandwich structures was a rectangular cuboid with a size of 200 mm $\times$ 25 mm $\times$ 6 mm. An 8-node brick element, C3D8, was used to mesh the core structure. The C3D8 element, as shown in Figure 5.1, is a 3-dimensional, linear and fully-integrated brick element with 8 nodes at the corners, which can be used for stress/displacement analysis [144]. The material properties (Young's modulus, Poisson's ratio and density, see Table 6.1 and Figure 6.1 measured from the tensile and density tests were imported into the models.

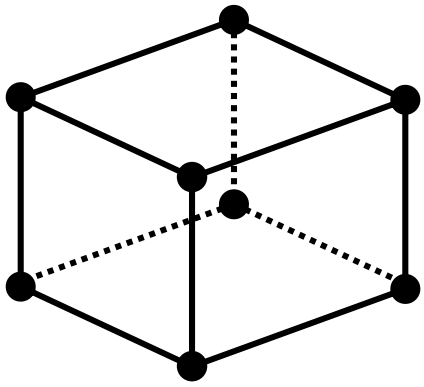


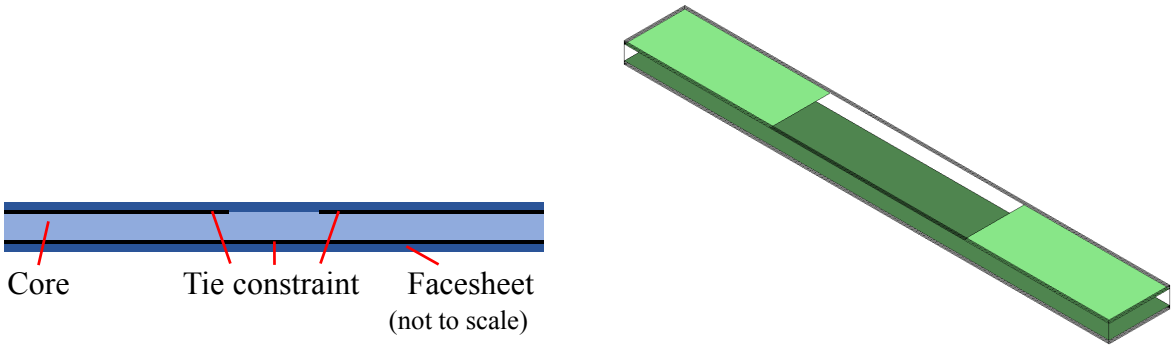
Figure 5.1: Sketch of C3D8 element

The model of the facesheets of the flat sandwich structures was a thin rectangular cuboid with a size of 200 mm $\times$ 25 mm $\times$ 1.3 mm. The facesheet model was evenly divided into 4 layers as the real facesheet was a laminate composed of 4 layers of carbon fibre lamina, so each layer model had a thickness of 0.325 mm. The C3D8 element was used to mesh the facesheet structures. The material properties (Young's moduli, shear moduli, Poisson's ratios, and density, see Table 6.4 and Figures 6.2 and 6.3) measured from the tensile and density tests were imported into the models. The effect of fibre direction of each layer in the real structures was simulated by assigning a "material orientation" to each layer model according to the real facesheet stacking orientations ($[0°]_4$, $[90°]_4$ and $[+45°/-45°]_s$).

In the FE simulation, the thickness of the adhesive layer of the real structures was neglected since it was thin (approx. 250 μm) compared to the core and the facesheets. Another reason for neglecting the adhesive layer is to make the surfaces of the facesheets and the core at the debonded regions in contact at the beginning of modelling [145]. Therefore, in the FE simulation, the core and facesheet models were assumed to be perfectly bonded together in the adhered regions. To establish the sandwich models, a core model and two facesheet models were adhered using "tie constraints" at the bonded faces (i.e. excluding the debonded regions), with the core between the facesheets. The use of "tie constraint" makes the motions equal for the nodes belonging to the paired surfaces [144]. Figure 5.2 illustrates the tie constraint applied at the bonded regions of a sandwich model with a debonded region.

5.2.2 Debonded Region Modelling

To prevent overlapping of the facesheets and the core at the debonded regions in the simulations, "symmetric surface to surface contact" was applied at the interfaces of the debonded regions. A set of "surface to surface contacts" assigned a "master surface" to one surface in the debonded region and a "slave surface" to the other one. A debonded region with a set of "surface to surface contacts" applied is shown in Figure 5.3. The "symmetric" means that two

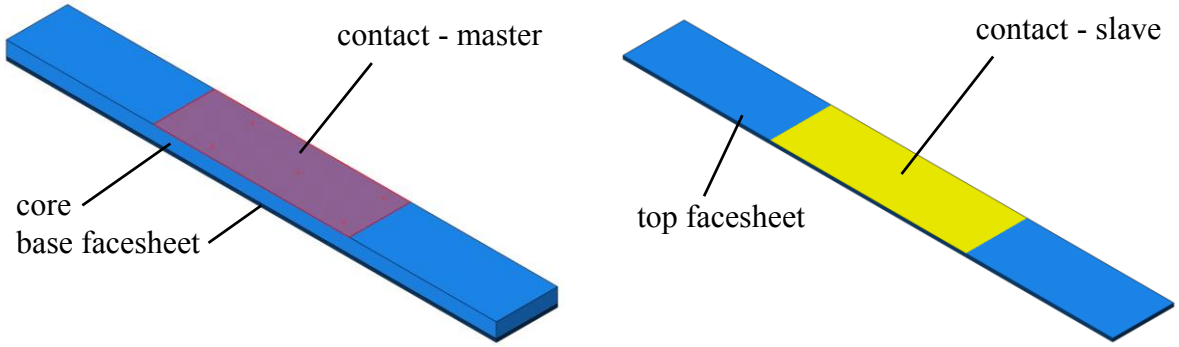


(a) Lateral sketch of tie constraint

(b) Tie constraint (shown in light green) in FE model

Figure 5.2: Tie constraint applied at the bonded regions of the sandwich structure model with an 80 mm debond

sets of "surface to surface contacts" were applied at the debonded interfaces, so that each face was assigned as both "master surface" and "slave surface". The use of "symmetric surface to surface contact" further improves the effect of preventing overlapping [144].



(a) A master surface applied at the surface of the core

(b) A slave surface applied at the surface of the top facesheet (flipped upside down)

Figure 5.3: Master (shown in red) and slave (shown in yellow) surfaces applied in the debonded region of the sandwich structure model with an 80 mm debond

5.3 Curved Structure Model Development

To develop the models of curved sandwich structures, first the 3D models were constructed in the computer aided design (CAD) software SOLIDWORKS 2015 sp4.0 [146] from Dassault Systemes, France, based on the sizes listed in Table 3.4. The central arc of the sandwich models had a length of 200 mm, the curvature angle of the structures was 15° or 30°. The core, top facesheet and base facesheet parts were built separately and then assembled to form curved sandwich structures. The built curved sandwich models were then exported from SOLIDWORKS as ".step" files which were imported into Abaqus.

After being imported into Abaqus, the top facesheet, base facesheet and the core were assembled again since only geometries had been imported. Although the structures needed to be assembled again in Abaqus, the first assembly in SOLIDWORKS ensured that the geometries were not altered during the transfer between the two softwares. The mechanical properties, element type (C3D8) and material orientations were then applied to the FE models. Like the flat models, "tie constraint" was applied at the adhered interfaces between the facesheets and the cores. "Symmetric surface to surface contact" was also applied in the debonded regions. The developed curved models are shown in Figure 3.15.

5.4 Natural Frequency and Mode Shape Simulations

The boundary conditions of the models were free-free to meet the real hammer impact test conditions. To achieve these boundary conditions, the models were assigned with no constraint.

To simulate the vibration behaviours, the Lanczos method was used. The Lanczos method is the default method for extracting eigenvalues in Abaqus because of its general capabilities [144]. By using the Lanczos method, the natural frequencies and their corresponding mode shapes of the structures were calculated in Abaqus. The frequency range was set as 100 to 10000 Hz, with the range of 0 to 100 Hz blocked out to avoid rigid body motions of the structures which result from the free-free boundary conditions.

5.5 Convergence Study

In order to save computational time and improve the accuracy of the simulation results, a convergence study was undertaken to find the optimum mesh density. The aim is to achieve little change of natural frequencies when increasing the mesh density. The convergence study was carried out on the intact, flat sandwich model using the unmodified epoxy resin as the core and the matrix of the $[0°]_4$ facesheet CFRP. Figure 5.4 shows the comparison of relative simulated natural frequencies resulted from different mesh densities. The mesh refinement process started from the coarsest mesh which contains 1536 elements. It was found that bending and lateral modes can achieve convergence with a coarser mesh, while torsion modes require a finer mesh to achieve convergence.

As shown in Figure 5.4, the mesh resulting in 60000 elements (20000 for each facesheet and 20000 for the core) was accepted for good convergence and saving of computational time (about 38 seconds for each running), and was used for the subsequent simulations of other sandwich structures. This mesh resulted in each element of the model having a size of 1 mm $\times$ 1 mm (length $\times$ width), but the thickness of the elements of the facesheets and the core were different because of the difference of the thickness between the facesheets and the core.

The elements in the core had a thickness of 1.5 mm, so there were 4 elements through the thickness of the core; while for the facesheet, as described in Section 5.2.1, the total thickness of a facesheet model,which was evenly divided into 4 layers, was 1.3 mm, therefore the thickness of the elements in the facesheets was 0.325 mm. For the curved models, the total element numbers were kept the same as the flat models, but as the arc lengths at the top and base of the structures were different, the lengths of the elements would be different. However, the radial thicknesses of the elements were the same as the flat sandwich structure models.

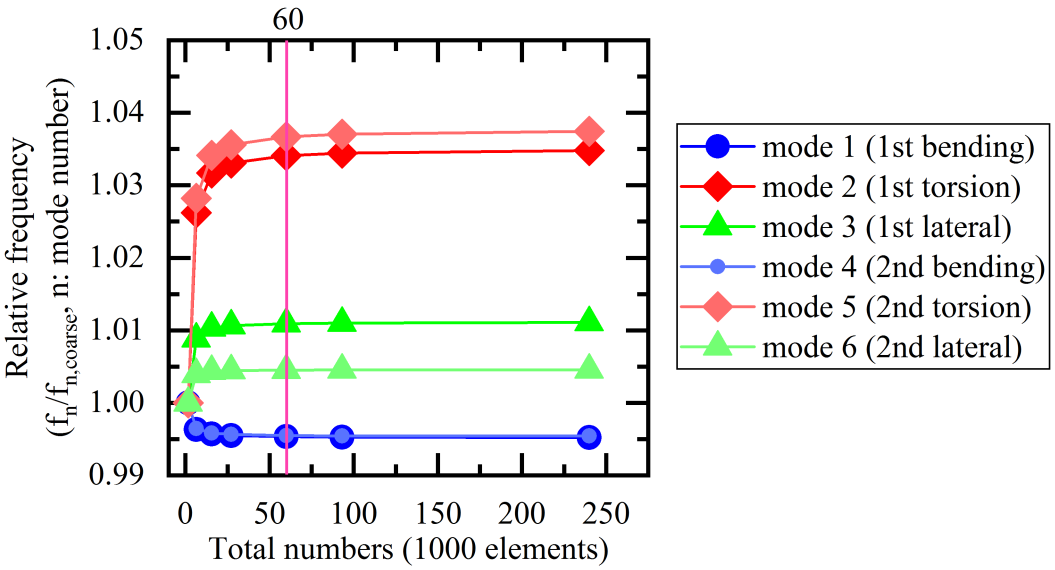
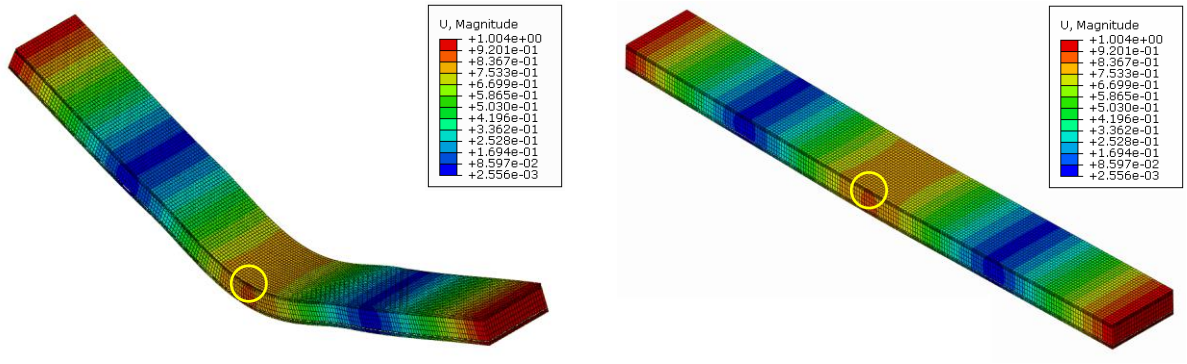


Figure 5.4: Convergence study: relative natural frequencies comparing to the coarsest mesh (1536 elements) for the modes

5.6 Overlapping Inspection

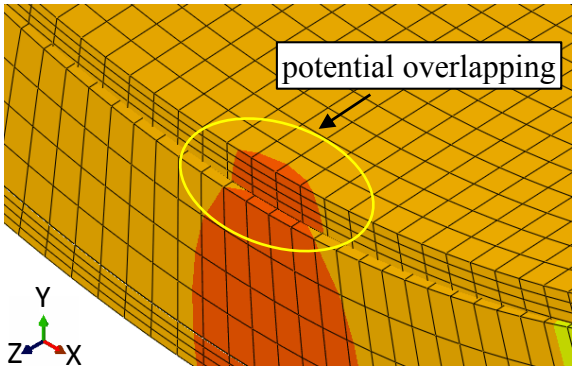
An inspection of overlapping was conducted after the convergence study. The aim of using the "surface to surface contact" is to prevent the overlapping of the facesheets and core of the sandwich structure models. The results were inspected using the flat sandwich model, which used unmodified resin and $[0°]_4$ facesheets and had a central 80 mm debonded region. To identify whether there was any overlapping, images of the mode shapes of the model and deformed coordinates of the nodes at the debonded region were investigated. It is noted that the default value of the deformation scale factor in Abaqus may not be equal to one because the software tries to make the result more obvious. The use of a scale factor of greater than one can result in overlapping being identified when it does not actually occur. When inspecting, the deformation scale factor should be changed to one to display the real deformation. The 1st vibration mode of the structure, which is a bending mode, used for the inspection is shown in

Figure 5.5a where the default deformation scale factor was twenty. In Figure 5.5b, the factor was changed to one.

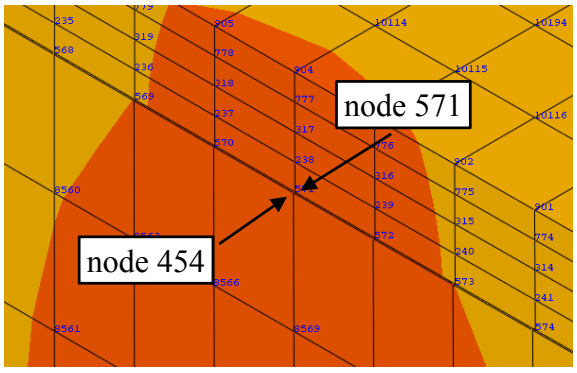


(a) Deformation scale factor: 20 **(b)** Deformation scale factor: 1

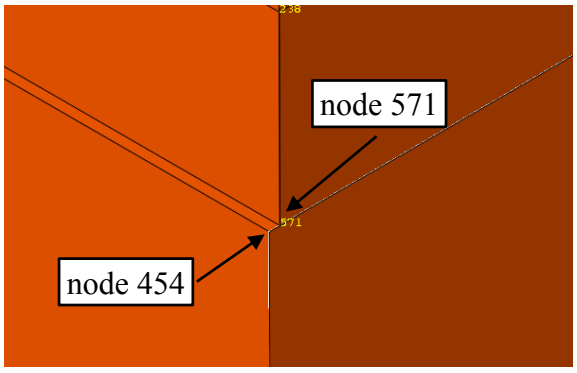
Figure 5.5: Simulation mode shape of vibration mode 1 of the flat sandwich structure: unmodified resin, $[0°]_4$ facesheets, 80 mm debonded region



(a) Local image of Figure 5.5a, deformation scale factor: 20



(b) Local image of Figure 5.5b, deformation scale factor: 1



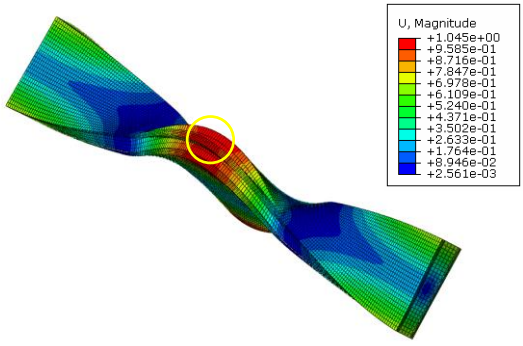
(c) Cross section of Figure 5.6b, deformation scale factor: 1

Figure 5.6: Overlapping inspection of the deformation of vibration mode 1 of the flat sandwich structure: unmodified resin, $[0°]_4$ facesheets, 80 mm debonded region

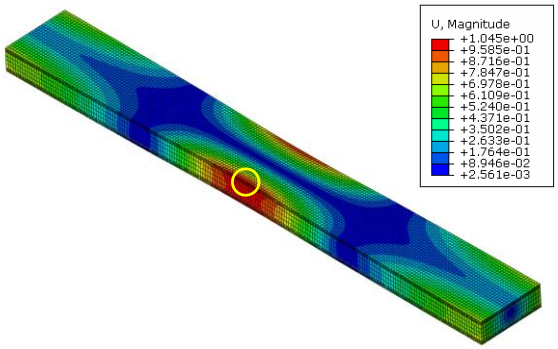
The local image of Figure 5.5 (marked by the yellow circle) is shown in Figure 5.6a&b, which shows the most significant potential for overlapping. The nodes at the middle of the

debonded region, node 571 on the top facesheet and node 454 on the core, are marked in Figure 5.6b. The cross section is shown in Figure 5.6c. It is noted that although potential overlapping can be seen in Figure 5.6a, the top facesheet and the core touch but do not overlap in Figure 5.6c, where the deformation scale factor is one. To further check that overlapping does not occur, the deformed coordinates of the nodes were investigated; the deformed coordinates of nodes 571 and 454 are (0.00, 5.16, 25.00) and (0.00, 5.16, 25.02), respectively. Therefore, the facesheet and the core are confirmed to touch in the 1 and 2 directions but do not overlap for the 1st vibration mode of the 80-mm-debonded model.

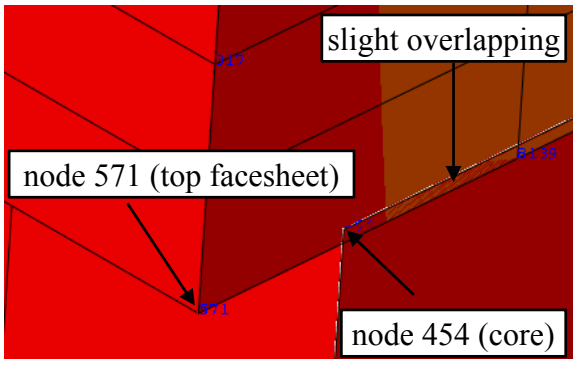
The overlapping was also checked for the higher vibration modes. An image of mode 5 of the flat sandwich structure, which is a torsion mode, is shown in Figure 5.7. It is noted that in Figure 5.7c, a slight overlapping can still be seen even if the deformation scale factor was set as 1. According to the Abaqus manual [144], when the "surface to surface contact" is used, slight overlapping may still be observed but severe overlapping should not occur. The overlapping distance in Figure 5.7c is about 0.04 mm which is 12.3 % of a single layer (0.325 mm) of the facesheet. Also, the overlapping does not penetrate to the second layer of the facesheet. Therefore, the overlapping which is found in Figure 5.7c is considered to be slight and acceptable.



(a) Whole, deformation scale factor: 20



(b) Whole, deformation scale factor: 1



(c) Cross section of Figure 5.7b, deformation scale factor: 1

Figure 5.7: Overlapping inspection of the deformation of vibration mode 5 of the sandwich structure: unmodified resin, $[0°]_4$ facesheets, 80 mm debonded region

Table 5.1: Overlapping inspection results of the 80-mm-debonded flat sandwich structure model using unmodified resin and $[0^\circ]_4$ facesheets

Mode	Mode shape	Overlapping inspection result
1	bending	touching
2	bending	slight overlapping
3	torsion	slight overlapping
4	lateral	touching
5	torsion	slight overlapping

The results of the inspection of potential overlapping of the first 5 modes of the model are listed in Table 5.1. The results show that the core and the facesheet are either touching or slightly overlapping. No severe overlapping or penetration was observed, so the effect of "surface to surface contact" is valid.

5.7 Conclusions

The finite element simulations used to model the flat and curved sandwich structures have been presented in this chapter. The development of the models and the modelling of the debonded regions have been introduced. The models have been shown to allow the vibration to be simulated. The results of a convergence study to optimise the mesh density, and of checks to ensure that overlapping does not affect the predictions have been presented. The results of the mechanical property tests are discussed in the next chapter.

Chapter 6

Mechanical Properties Results

6.1 Introduction

The results of the tensile tests and the density measurements conducted on the bulk epoxy plates and the CFRPs which were used for the sandwich structures are presented in this chapter. The measured tensile moduli and densities were used in the finite element simulation to model the vibration behaviour of the sandwich structures. The results of the fibre volume fraction measurements of the CFRPs used as the facesheets of the sandwich structures and the sizing-modified CFRPs are also shown in this chapter. The test procedures used have been stated in Chapter 4.

6.2 Bulk Epoxy

The materials used for cores of the sandwich structures were bulk epoxy plates. The resin formulations used were the unmodified epoxy resin and the resins modified with silica nanoparticles (SNPs) or graphene.

6.2.1 Tensile Tests

For the tensile tests conducted on the bulk epoxy plates, six specimens were tested for each formulation (see Table 4.4). The tensile moduli, E, of the unmodified and modified bulk epoxy polymers are shown in Figure 6.1 and Table 6.1. The Poisson's ratios, ν, are also shown in Table 6.1. The mean tensile modulus of the unmodified epoxy is 2.76 GPa, which is within the

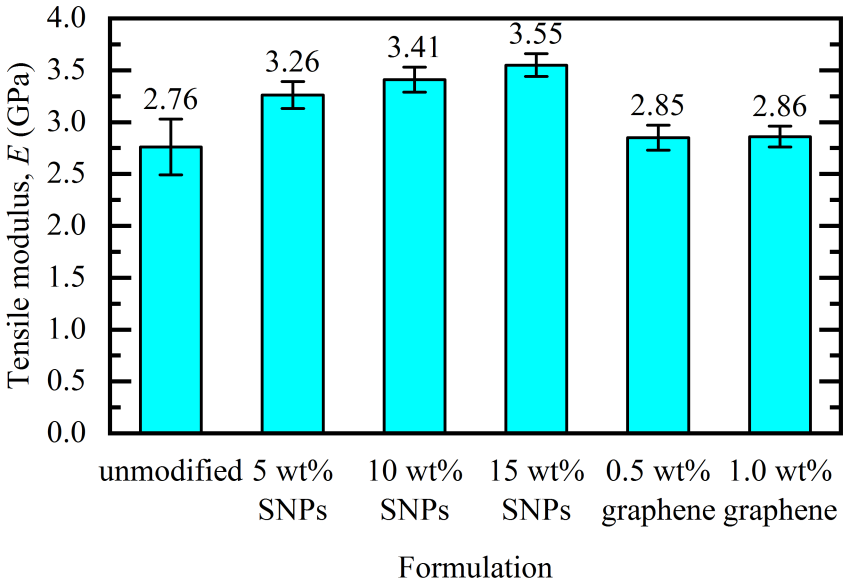


Figure 6.1: Tensile modulus of the epoxy polymers used as the core and the facesheet matrix of the sandwich structures

Table 6.1: Measured mechanical properties of the bulk epoxy used as the core of the sandwich structures

	Tensile modulus E (SD) (GPa)	Poisson's ratio ν (SD)	Density ρ (SD) (kg/m^3)
unmodified	2.76 (0.27)	0.35 (0.05)	1154 (18)
5 wt% SNPs	3.26 (0.13)	0.37 (0.08)	1163 (45)
10 wt% SNPs	3.41 (0.12)	0.36 (0.06)	1174 (34)
15wt% SNPs	3.55 (0.11)	0.36 (0.08)	1249 (50)
0.5 wt% graphene	2.85 (0.12)	0.36 (0.06)	1105 (55)
1.0 wt% graphene	2.86 (0.10)	0.39 (0.03)	1155 (34)

range of reported values of 2.7 to 2.9 GPa for this epoxy [8, 38, 147]. The measured Poisson's ratio is 0.35, which is in excellent agreement with the expected value from the literature [148]. Adding 5, 10 or 15 wt% of SNPs into the epoxy results in tensile moduli of 3.26, 3.41 and 3.55 GPa, which are increases of 18, 24 and 29 %, respectively. The reason for the increase is the higher Young's modulus of silica, which is about 70 GPa [149]. According to the rule of mixtures, adding a modifier with a higher Young's modulus increases the Young's modulus of the mixture. Since the Young's modulus of silica is significantly higher than the unmodified epoxy, the SNP-modified epoxy has a higher E than the unmodified epoxy.

According to previous work, adding the same SNPs of a concentration of 10 or 20 wt% into the same epoxy results in tensile moduli of 3.08 and 3.47 GPa [38]. Although the measured values in this work are slightly higher than the reported values, the tensile moduli of the SNP-

modified epoxy in both works increase steadily when the content of SNPs increases.

The tensile modulus of the epoxy with an addition of 0.5 or 1.0 wt% of graphene is 2.85 and 2.86 GPa, respectively. It is noted that adding the graphene into the epoxy has little effect on the tensile modulus (see Figure 6.1). Compared to the reported values of about 3.1 to 3.3 GPa which used the same epoxy and graphene [8], the measured values in this work are smaller. This difference might come from the different methods used to disperse the graphene. The method used in this research was using a 3 roll mill while the one used in the reported work was a using a ultrasonic probe and solvents [8], which may have resulted in a better dispersion and hence a greater reinforcing effect. The addition of SNPs or graphene has no significant effect on the measured Poisson's ratios, as all the values lie within one standard deviation of the value for the unmodified epoxy.

6.2.2 Density

For the density measurements conducted on the bulk epoxies, five samples were tested for each formulation (see Table 4.4). The densities, ρ, of the bulk epoxies which were measured by the pycnometer method are shown in Table 6.1. For the unmodified epoxy, the measured density is 1154 kg/m^3. When adding SNPs into the epoxy, the density increases since the density of silica, which is about 2170 to 2650 kg/m^3 [149], is higher than that of the unmodified bulk epoxy. Adding 15 wt% of SNPs into the epoxy results in an increase in density of 8.2 %.

While adding graphene into the epoxy, the density decreases slightly by 4 % with an addition of 0.5 wt% graphene but then increases to 1155 kg/m^3 with an addition of 1.0 wt% graphene, which is the same as the unmodified epoxy (1154 kg/m^3). The densities of the epoxies modified with graphene show little difference, the variations lie within the expected experimental scatter. The standard deviation (SD) range of the ρ of the unmodified epoxy covers that of the epoxies modified with graphene. The small differences in the densities of the unmodified and graphene-modified epoxies can be the effects of experimental variations. As discussed in Section 4.3, the resolution of the balance was only 0.01 g and the tested specimens are relatively small, which can have resulted in the measured densities showing small differences.

6.3 Carbon Fibre Composites

6.3.1 Fibre Volume Fraction of Sizing-modified Carbon Fibre Composite

For the fibre volume fraction measurements conducted on the sizing-modified CFRPs, images from three through-thickness locations were analysed for the laminate of each sizing formulation (see Table 4.5). The fibre volume fractions, V_f, of the unidirectional (UD) CFRPs using SNP-modified sizings are shown in Table 6.2. The fibre volume fractions of the sizing-

modified carbon fibre composites are between 35 and 50 %, the average V_f is 41.5 %. This value and the variation are expected to be typical values of V_f for the VARI manufacturing process used by Hengshen, China [111]. The fibre volume fraction of the UD carbon fibre composites using sizing N1 shows the highest V_f of 48.7 % within the CFRPs using sizing agent Neoxil 965 ; while for H1, which has the same content of SNPs (0.53 wt% on fibre mass), the V_f is 38.0 % which is the lowest within the CFRPs using sizing agent HS-1. Increasing the content of SNPs in the sizings does not affect the fibre volume fraction, since only the sizings of the fibres were changed but the matrices of the CFRPs were the same, so the viscosity of the infused resin was not changed, and the flow of the resin into the mould would not be affected. Therefore the differences in V_f will have resulted from manufacturing and experimental variations rather than from differences in the sizing used.

Table 6.2: Fibre volume fraction of the sizing-modified CFRP

Sizing formulation	N0	N1	N2	H0	H1	H2
V_f (SD) (%)	36.9 (2.0)	48.7 (3.8)	36.5 (3.5)	43.4 (2.6)	38.0 (3.4)	45.2 (3.5)
SNP content (wt%)	0	0.53	0.89	0	0.53	0.89

6.3.2 Carbon Fibre Composites of Sandwich Structures

The facesheets of the sandwich structures were UD CFRPs. The formulations of the matrix of the facesheet CFRPs were the same as the core epoxy polymers.

6.3.2.1 Fibre Volume Fraction

For the fibre volume fraction measurements conducted on the CFRP facesheets of the sandwich structures, images from three through-thickness locations were analysed for each resin formulation (see Table 4.4). The specimens were cut from the $[0°]_4$ laminates. The fibre volume fractions of the CFRPs used as the facesheets of the sandwich structures are shown in Table 6.3. The V_f of the CFRP using the unmodified matrix is 56.3 %. Adding 5 wt% of SNPs into the matrix results in a V_f of 59.1 % (an increase of 5.0 %, but not a significant increase when the SD is considered). However, increasing the content of SNPs in the matrix subsequently decreases V_f. Adding 15 wt% of SNPs into the matrix results in a V_f of 50.9 %, a decrease of 9.6 % compared to the CFRP using the unmodified matrix. This reduction in V_f is likely to be due to the increased viscosity of the resin, which results in less resin being removed from the fibres during the RIFT process, thus increasing the proportion of matrix in the composite plate.

When adding graphene into the matrix, V_f decreases. The V_f for the both addition levels of graphene (53.2 and 53.9 %) are lower than using the modified matrix, but there is little

difference between the two addition levels. This reduction in V_f is likely to be due to the increased viscosity of the resin.

Table 6.3: Fibre volume fraction of the CFRP used as the facesheets of the sandwich structures

Matrix formulation	unmodified	5 wt% SNPs	10 wt% SNPs	15 wt% SNPs	0.5 wt% graphene	1.0 wt% graphene
V_f (SD) (%)	56.3 (3.9)	59.1 (2.1)	52.8 (1.2)	50.9 (0.8)	53.2 (0.8)	53.9 (3.1)

6.3.2.2 Tensile Tests

For the tensile tests, five specimens were tested for each resin formulation and stacking orientation (see Table 4.4). The longitudinal tensile moduli, E_1, of the CFRPs used as the facesheets of the sandwich structures are shown in Figure 6.2 and Table 6.4. The lateral tensile moduli, E_2, Poisson's ratios, ν_{12} and ν_{23}, and shear moduli, G_{12} and G_{23}, are also shown in Table 6.4. The E_1 of the CFRP using unmodified resin is 122.6 GPa. It is noted that adding 5 wt% of SNPs into the matrix of the CFRP increases E_1 to 139.3 GPa (an increase of 13.6 %), however, E_1 decreases when the content of SNPs subsequently increases. Nevertheless, adding 15 wt% of SNPs into the matrix still results in a E_1 of 127.8 GPa, a decrease of 8.3 % compared to adding 5 wt% of SNPs into the matrix but an increase of 4.2 % compared to CFRP using unmodified matrix.

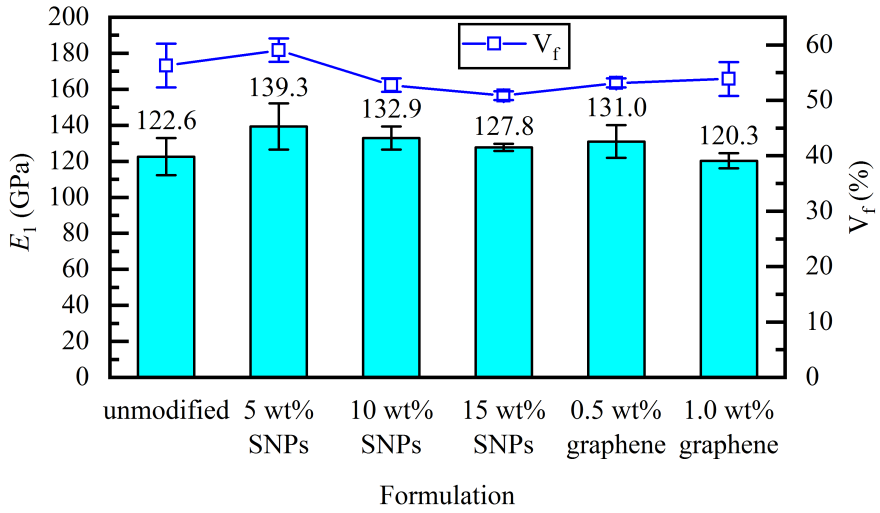


Figure 6.2: Longitudinal tensile modulus and fibre volume fraction of the CFRP used as the facesheets of the sandwich structures

Adding 0.5 wt% of graphene into the matrix increases E_1 of the CFRP to 131 GPa, an increase of 6.9 %. However, when adding 1.0 wt% of graphene into the matrix also results in a reduction in the longitudinal tensile modulus to 120.3 GPa, a decrease of 1.9 % compared to the CFRP using the unmodified matrix.

Table 6.4: Measured mechanical properties of the CFRP used as the facesheets of the sandwich structures

	E_1 (SD) (GPa)	E_2 (SD) (GPa)	ν_{12} (SD)	ν_{23}*	G_{12} (SD) (GPa)	G_{23}* (GPa)	ρ (SD) (kg/m^3)
unmodified	122.6 (10.3)	6.69 (0.51)	0.33 (0.05)	0.48	4.48 (0.29)	2.25	1557 (86)
5 wt% SNPs	139.3 (12.8)	6.52 (0.28)	0.37 (0.07)	0.58	3.96 (0.31)	2.07	1527 (55)
10 wt% SNPs	132.9 (6.4)	7.35 (0.51)	0.34 (0.06)	0.51	3.59 (0.21)	2.44	1557 (74)
15 wt% SNPs	127.8 (2.0)	6.96 (0.32)	0.36 (0.10)	0.55	3.66 (0.45)	2.24	1550 (41)
0.5 wt% graphene	131.0 (9.1)	6.09 (0.47)	0.35 (0.07)	0.53	3.42 (0.10)	1.99	1525 (40)
1.0 wt% graphene	120.3 (4.2)	6.66 (0.49)	0.36 (0.07)	0.55	4.10 (0.42)	2.15	1566 (67)

Note: $E_2 = E_3$, $\nu_{12} = \nu_{13}$, $G_{12} = G_{13}$

* By calculation

It is noted that the E_1 values of the CFRPs using different matrices have no significant differences, as the SD range of the E_1 of the CFRP using unmodified matrix covers the E_1 of the CFRPs using modified matrices. For the CFRPs using SNP-modified matrices, the E of the matrix epoxy increases when the content of SNPs increases, see Figure 6.1. However, the V_f values of these CFRPs decrease, which results in the reduction in E_1, as shown in Figure 6.2. Therefore, it can be identified that the effect of E of the matrix on the E_1 of the CFRPs is smaller than that of the fibre volume fraction. This is expected because the modulus of the fibre is much greater than that of the matrix. For the CFRPs using graphene-modified matrices, the E values of the matrices have no significant differences (see Figure 6.1) and the V_f increases slightly when the content of graphene in the matrix increases, but the E_1 of the CFRPs decreases. This may be attributed to poor adhesion between the fibre and the matrix when the matrix contains 1.0 wt% graphene.

The lateral tensile moduli of the CFRPs used as the facesheets of the sandwich structures are shown in Table 6.4 and Figure 6.3. The lateral tensile modulus of the CFRP using the unmodified matrix is 6.69 GPa. Adding SNPs into the matrix does not confirm an increase or decrease of the lateral tensile modulus. Adding 5, 10 or 15 wt% SNPs into the matrix results in changes of E_2 of -2.5, 9.9 and 4.0 %, respectively. While adding 0.5 or 1.0 wt% of graphene into the matrix results in E_2 of 6.09 GPa (a decrease of 9.0 %) and 6.66 GPa (almost the same as using the unmodified matrix). The difference between the E_2 of the CFRPs is small when considering the SD range. The SD range of the E_2 of the CFRP using unmodified matrices covers the E_2 of the CFRPs using modified matrices.

The longitudinal Poisson's ratio, ν_{12}, shows no significant difference when considering the standard deviation, see Table 6.4. The typical ν_{12} values of UD CFRPs are about 0.3 [118, 150]. Although the reported values of the ν_{12} of the UD CFRPs are lower than the values in this

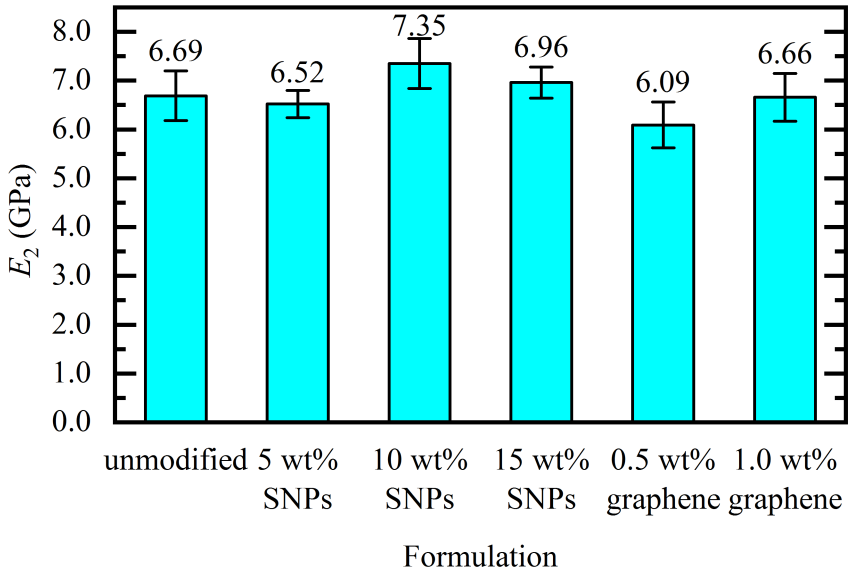


Figure 6.3: Lateral tensile modulus of the CFRP used as the facesheets of the sandwich structures

research, they are still within the SD ranges (see Table 6.4). Besides, the reported values of the V_f of the CFRPs are between 60 % and 65 %, which are higher than the values in this research (see Table 6.3). As the ν_{12} of carbon fibre is lower than that of the matrix epoxy, according to the rule of mixtures, a lower V_f results in a higher ν_{12} of the manufactured CFRP. Another reason for the difference in the ν_{12} between this research and the literature is that the fibres may not be perfectly straight or unidirectionally aligned during the manufacturing process and in the manufactured CFRPs, which also results in a higher ν_{12}.

6.3.2.3 Density

For the density measurements conducted on the CFRP facesheets of the sandwich structures, five $[0^\circ]_4$ samples were tested for each formulation (see Table 4.4). The densities of the CFRPs used as the facesheets of the sandwich structures are shown in Table 6.4. According to the table, the addition of SNPs or graphene into the matrix have little influence on the density of the CFRP. The density of the CFRP using unmodified matrix is 1557 kg/m^3, while the maximum change is 2 % when using the modifiers. The small differences in the densities of the CFRPs can be the results of experimental variations as the resolution of the balance used was only 0.01 g and the specimens are relatively small.

6.4 Conclusions

The tested mechanical properties (tensile modulus, shear modulus, Poisson's ratio and density) of the core and facesheets of the sandwich structures have been presented in this chapter.

These properties were used in the finite element simulation to model the vibration behaviours of the sandwich structures with or without debonded regions. The fibre volume fractions of the facesheet CFRPs and the sizing-modified CFRPs have also been stated. The results of the mode I interlaminar fracture tests and the fatigue crack growth tests which were conducted on the CFRP using the SNP-modified sizings are discussed in the next chapter.

Chapter 7

Fracture and Fatigue Behaviours of Carbon Fibre Composites with Silica Nanoparticle Modified Sizings

7.1 Introduction

The results of the mode I interlaminar fracture tests and the fatigue crack growth (FCG) tests of the carbon fibre composites using SNP-modified sizings are presented in this chapter. Two different sizings were used, each had three formulations: unmodified (no SNPs), 0.53 wt% SNPs and 0.89 wt% SNPs (on fibre mass), as shown in Table 3.1. The effects of the addition of SNPs to the sizings is discussed. A comparison of the fracture energies with the carbon fibre composites using SNP-modified matrices is also presented. The images of the fracture surfaces were also studied to identify the toughening mechanisms.

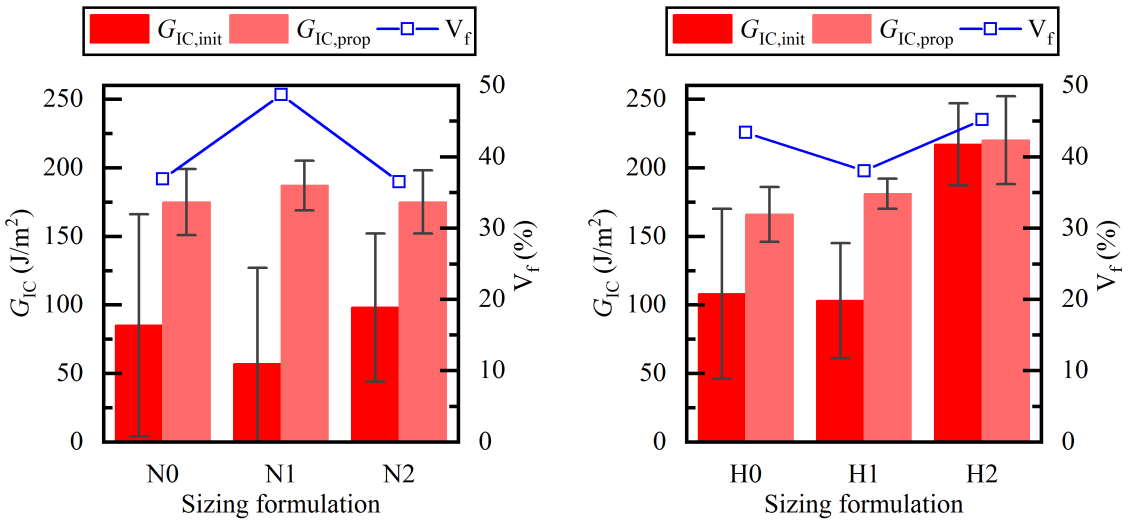
7.2 Interlaminar Fracture Energy

Five specimens of each sizing formulation were tested for calculating the mode I interlaminar fracture energies, see Table 4.5. The calculated values of the mode I interlaminar fracture energy at crack initiation, $G_{IC,init}$, and propagation, $G_{IC,prop}$, for the carbon fibre composites with the unmodified and SNP-modified sizings are shown in Table 7.1 abd Figure 7.1. For the composites using the unmodified sizings, N0 and H0, the fracture energies at crack initiation are 85 J/m^2 and 108 J/m^2 respectively, this difference results from using different sizing agents.

On the other hand, for the composites using SNP-modified sizings, the fracture energy at crack initiation only shows a small increase of 15% when the main sizing agent is Neoxil 965 with the addition of 2.22 wt% of Nanopox FW 404 (sizing N2). By comparison, the fracture energy at crack initiation increases significantly by 101% when the main sizing agent is HS-1 with the addition of 2.22 wt% of FW 404 (sizing H2), see Table 7.1 and Figure 7.1b, which indicates a significant improvement of the fracture energies at the initial stage of crack development.

Table 7.1: Fracture energies of the modified-sizing composites

Sizing formulation	$G_{IC,init}$ (SD) (J/m^2)	Change	$G_{IC,prop}$ (SD) (J/m^2)	Change	$G_{IC,prop}$ - $G_{IC,init}$ (J/m^2)
N0	85 (81)	-	175 (24)	-	90
N1	57 (70)	-33%	187 (18)	+7%	130
N2	98 (54)	+15%	175 (23)	0%	77
H0	108 (62)	-	166 (20)	-	58
H1	103 (42)	-5%	181 (11)	+9%	78
H2	217 (30)	+101%	220 (32)	+33%	3



(a) sizing N **(b)** sizing H

Figure 7.1: Fracture energies and fibre volume fraction comparison of the modified-sizing composites

The $G_{IC,init}$ values of each formulation have large standard deviations, see Table 7.1 and Figure 7.1. For example, $G_{IC,init}$ of the carbon fibre composite using sizing N2 shows a mean of 57 J/m^2 and a SD of 70 J/m^2, which results from the greatly scattered values. This indicates that crack initiation is a relatively unstable process. It is also noted that for sizing N, the value

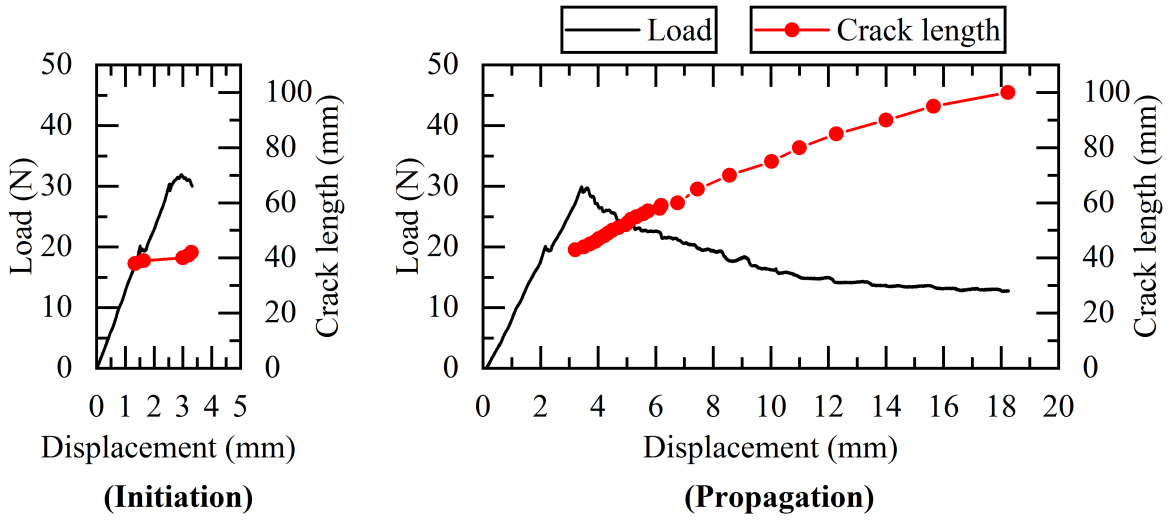
of $G_{IC,init}$ decreases when using sizing N1 while it subsequently increases when using sizing N2. However, the range of the SD values of the $G_{IC,init}$ for the three formulations (N0, N1 and N2) cover each other, see Table 7.1 and Figure 7.1a. This indicates that the improvement of the fracture energies at crack initiation is not significant when using sizing N modified with SNPs.

For crack propagation, the fracture energy shows no significant change (there is only an increase of 7% for sizing N1) when SNPs are added to the Neoxil 965 sizing agent. However, $G_{IC,prop}$ increases from 166 J/m^2 to 220 J/m^2 (an increase of 33%) with the addition of 2.22 wt% of FW 404 to the HS-1 sizing agent (sizing H2).

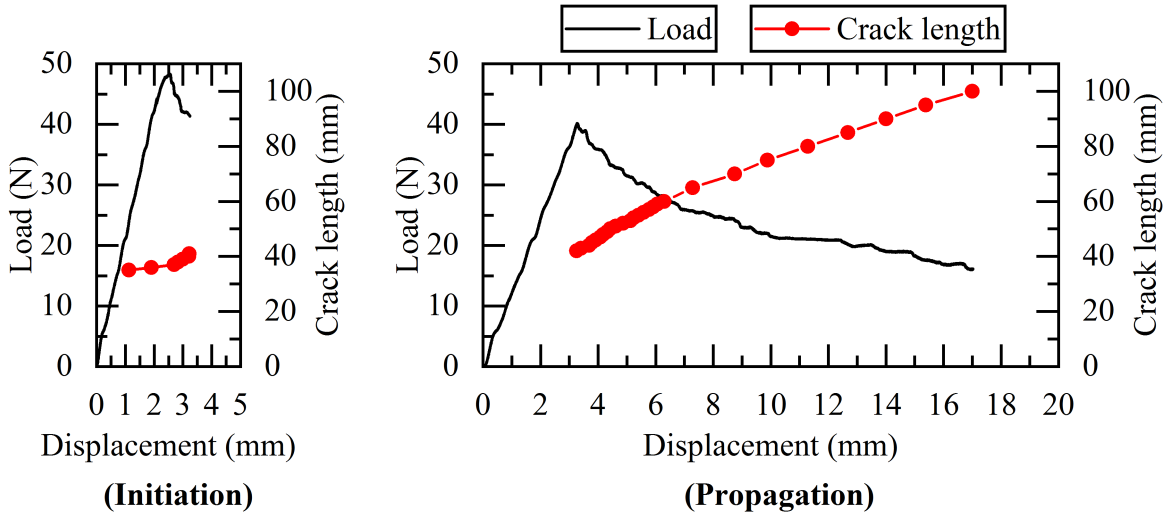
The load-displacement, from the testing machine, and crack length-displacement curves of the specimens using sizing H0 and H2 are shown in Figure 7.2. The shape of the crack length–displacement relationship shows no significant change, as the geometries of the specimens and load blocks were the same. However, it is noted that for both crack initiation and crack propagation, the loads of the specimen using sizing H2 increase. The highest load at crack initiation increases from 31.9 N (H0) to 48.3 N (H2), and the load curve of sizing H2 during crack propagation is also higher than that of sizing H0. This indicates that more load is needed for generating and propagating a crack, therefore the fracture energies, $G_{IC,init}$ and $G_{IC,prop}$, increase. It can also be seen that there are ridges on the load curves. The reason for the ridges is the fibre bridging effect during crack growth. When the crack propagated, carbon fibres were pulled out from the matrices, bridged between the crack surfaces and absorbed the energy, which resulted in the increase of the recorded load; when the load exceeded the fibres' strength, the fibres broke and caused the decrease of the recorded load.

Comparing the fracture energies at crack initiation and propagation, it is noted that for the higher addition level of SNPS (sizings N2 and H2 compared to unmodified sizings N0 and H0, see Figure 7.3), the difference between the fracture energies at crack initiation and propagation decreases. This decrease of the difference means that there is a reduction of the size of the crack resistance curve (R-curve), which is a sign of a more stable crack propagation. For sizing H2, the difference between the crack initiation and propagation fracture energies is only 3 J/m^2, see Table 7.1.

The fibre volume fraction, V_f, values of the carbon fibre composites using the SNP-modified sizings are also shown in Figure 7.1. For a carbon fibre composite, the fibres absorb most of the energy and then break, therefore a composite with a higher V_f should have higher fracture energies. However, in Figure 7.1, the correlation between the V_f and the fracture energies is not clear. The reason is that the adhesion between the fibres and the matrix also takes an important role of transferring the load from the matrix to the fibres, which can affect the fracture energies. The effect and the mechanism of the SNP-modified sizings on the fibre/matrix adhesion and the fracture energies will be discussed in Section 7.5.

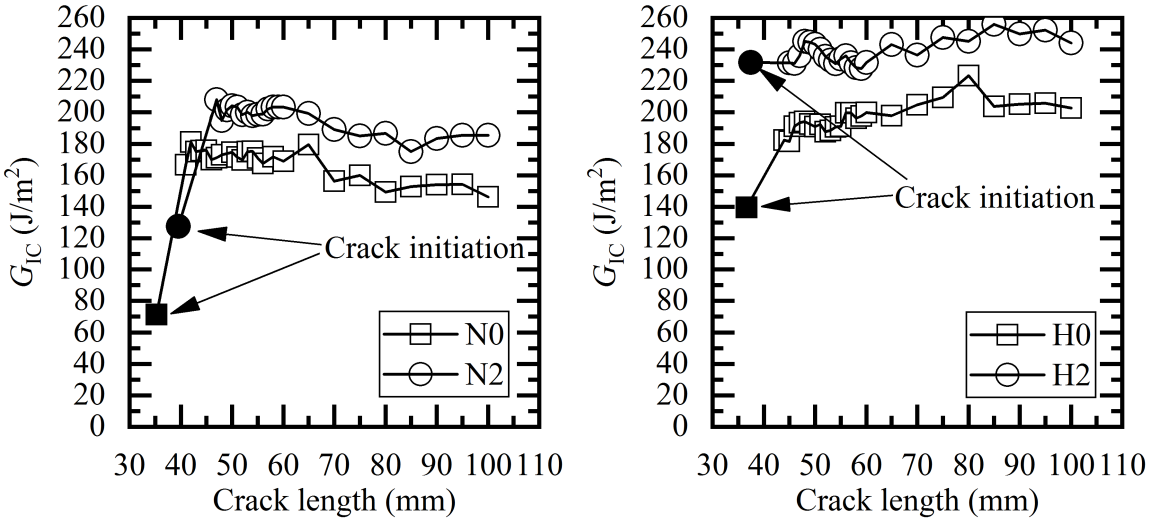


(a) sizing H0



(b) sizing H2

Figure 7.2: Load-displacement and crack length-displacement comparison of unmodified (H0) and SNP-modified (H2) UD carbon fibre composites



(a) sizing N0 & N2 **(b)** sizing H0 & H2

Figure 7.3: R-curve (resistance curve) comparison of unmodified and SNP-modified UD carbon fibre composites

7.3 Comparison with Carbon Fibre Composites Using SNP-modified Matrices

Table 7.2 shows the relative $G_{IC,prop}$ values compared with published values for which SNPs are added into the matrices of UD carbon fibre/epoxy composites [24, 25]. The epoxy system used for the modified matrices was DGEBA epoxy (Araldite-F) and piperidine hardener [24, 25]. The manufacturing processes of the carbon fibre composites using the SNP-modified matrices in the literature were vacuum assisted resin infusion moulding (VARIM) [25] or using prepreg impregnated with the modified epoxy matrices and then fabricated by vacuum bagging [24].

According to Table 7.2, it is clear that the method of adopting a modified sizing can achieve the same level of improvement using significantly fewer SNPs compared with adding the SNPs into the matrix. The increase of the fracture energy of the composite using an SNP-modified matrix, containing up to 20 wt% SNPs in the matrix, is 21%. However, sizing H2 achieves a higher increase of 33% while only adding 0.89 wt% (on fibre mass) to the sizing agent.

Table 7.2: Improvement of $G_{IC,prop}$ compared with literature

Formulation	SNP content (wt%)	Relative $G_{IC,prop}$	Reference
Sizing N0	0	1.00	
Sizing N1	0.53[a]	1.07	
Sizing N2	0.89[a]	1.00	
Sizing H0	0	1.00	
Sizing H1	0.53[a]	1.09	
Sizing H2	0.89[a]	1.33	
SNP modified matrix	0	1.00	[24, 25]
	2[b]	1.23	[24]
	4[b]	1.54	[24]
	10[b]	1.01	[25]
	20[b]	1.21	[25]

a: wt% on the fibre mass

b: wt% of the matrix

7.4 Fatigue Crack Growth

For the fatigue crack growth test, three specimens were tested for each sizing formulation, see Table 4.5. Figure 7.4 shows a typical FCG curve (on log-log axes) of a UD carbon fibre composite. The right-hand region I is where the crack grows rapidly at the beginning of the cyclic loading and G_{Imax} approaches $G_{IC,prop}$. Region II is where the crack grows steadily, and the relationship typically follows a linear Paris-Erdogan law relationship. The left-hand region III is where the crack grows very slowly or stops growing and the energy release rate reaches the threshold value, G_{th}, below which crack growth does not occur. However, in this work, although in a few FCG tests the crack propagated to region III, in most of the tests the crack remained in region II and did not develop to region III for the length of the cyclic loading used (360000 cycles, see Table 4.2).

The gradient of region II, m_G, reflects the sensitivity of the crack growth rate to the change of cyclic load, as shown in Table 7.3. In Table 7.3, the value of m_G was calculated according to the energy release rate while m_K is the related gradient when the mode I stress intensity factor (K_I) is used as the horizontal axis of the FCG curve (using $G_I = K_I^2(1-\nu^2)/E$ (plane strain) or $G_I = K_I^2/E$ (plane stress), where E is the Young's modulus and ν is the Poisson's ratio). The gradient m_G values of the composites using the unmodified sizings (N0 and H0) are 2.02

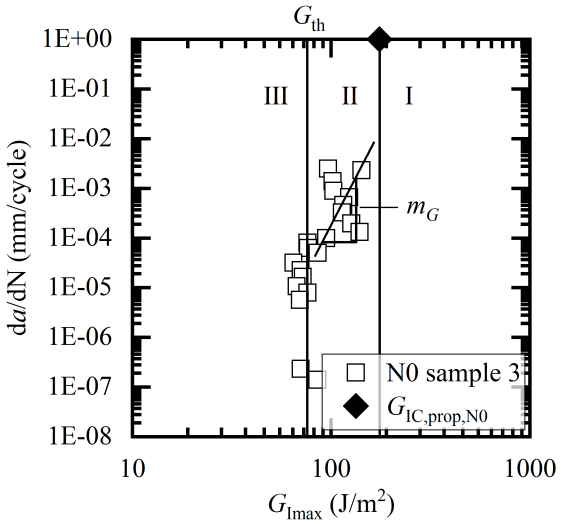


Figure 7.4: Fatigue crack growth (FCG) curve of UD carbon fibre composite using sizing N0

and 3.98. For the composites using modified sizings (N2 and H2), the m_G values are 5.90 and 3.00, and the related m_K values are 11.80 and 6.00. The m_G / m_K values of the composites using sizings N1 and H1 are relatively small, see Table 7.3, which can be attributed to experimental variations and to the unstable process of crack growth. Although in this work no significant change of the gradient was found within experimental variation for the various sizings used, the gradients are generally larger than metals whose m_K are usually taken as 3 to 4 [151, 152], see Table 7.3. This confirms that the fibre composites are more sensitive to fatigue crack growth than metals. The reason is that metals are ductile materials, while the matrices used in this work are thermoset epoxy which is highly crosslinked and very brittle, which results in the composites being more sensitive to fatigue crack and having larger values of m_G and m_K than metals.

Table 7.3: Fatigue gradient of the sizing-modified composites and comparison with metals

Formulation	Gradient m_G	Gradient m_K
Sizing N0	2.02	4.05
Sizing N1	1.17	2.34
Sizing N2	5.90	11.80
Sizing H0	3.98	7.97
Sizing H1	0.52	1.04
Sizing H2	3.00	6.00
Steel	-	3 [152]
Aluminium	-	3 [152]
Nickel	-	3.3 [152]

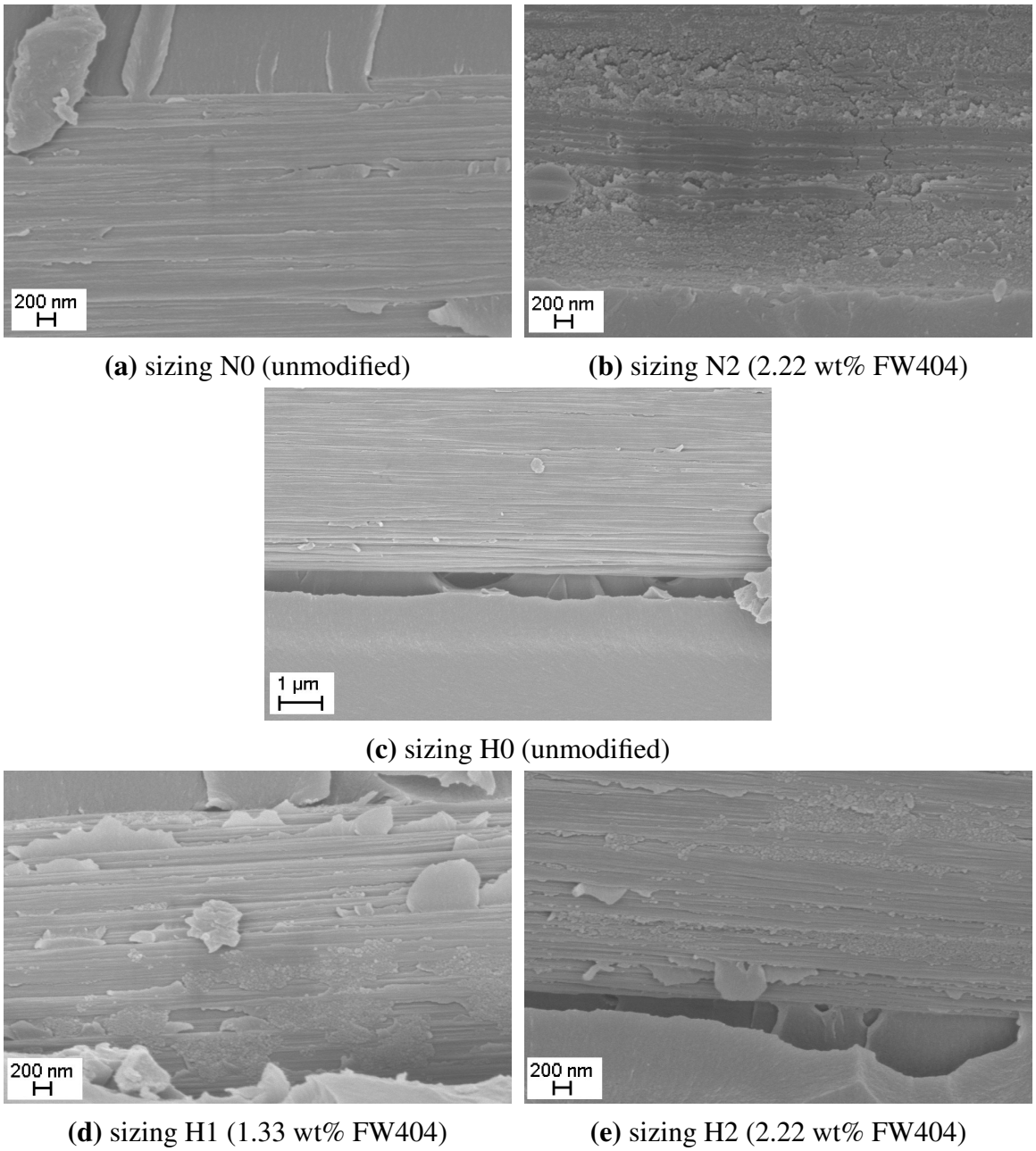
7.5 Fractographic Studies

The FE-SEM images from the tested samples of mode I interlaminar fracture tests were studied. The fibre surfaces of the composites using the unmodified sizings (N0 and H0) are clean and adhered with little epoxy (see Figure 7.5a&c). An obvious debonding of a fibre can also be seen in Figure 7.5c, which indicates a relatively poor adhesion between the fibre and the matrix. On the other hand, silica nanoparticles can be found on the fibre surfaces in the SNP-modified sizing samples (see Figure 7.5b,d&e). It is noted that a greater addition of SNPs results in a better SNP dispersion; SNPs were spread more evenly across the fibre surfaces. As can be seen in Figure 7.5d&e, both sizing H1 and H2 contain SNPs, however, the fibre surfaces in Figure 7.5e are adhered with more SNPs than in Figure 7.5d. Better SNP dispersion results in a better adhesion between the fibres and the matrix, since the surfaces of the fibres are adhered with more epoxy and SNPs after testing; the fibre surfaces shown in Figure 7.5d&e are rougher than the surfaces in Figure 7.5c.

A strong adhesion between the fibres and the matrix results in more fragmentation of the fibres when the crack grows, since the fibres cannot be pulled out so easily and are more likely to break due to the tensile force caused by the crack growing. As can be seen in Figure 7.6b&d, there are more fragmented fibres since the adhesion is better. However, if the adhesion is weak, the fibres are easier to pull out and can bridge between the crack faces (see Figure 7.6a&c). The improvement of adhesion can also be seen in the SEM images from the FCG-tested samples (see Figure 7.7), as more epoxy can be found adhered to the fibres in Figure 7.7b than in Figure 7.7a; there is debonding in Figure 7.7a, which also indicates poor adhesion.

The fibres absorb energy and then break as the crack grows. The presence of more fragmented fibres resulting from good adhesion means that more energy is absorbed by the fibres, which results in an increased difficulty of crack growth and hence an improvement of the toughness. However, if the adhesion is improved too much, there would be a negative effect such that fewer fibres break because few fibres pull out, which leads to a reduction of $G_{\mathrm{IC,prop}}$ [46]. This effect was observed in sizing N2, where in comparison with sizing N1, the adhesion is stronger but fewer fragmented fibres and so a smaller reduction of $G_{\mathrm{IC,prop}}$ was observed.

A good adhesion also contributes to the increase of $G_{\mathrm{IC,init}}$ (sizings N2 and H2 compared with the unmodified sizings N0 and H0). Since the increases of $G_{\mathrm{IC,init}}$ are more significant than $G_{\mathrm{IC,prop}}$, the magnitudes of the R-curves reduce, which results in more stable crack propagation.



(a) sizing N0 (unmodified)

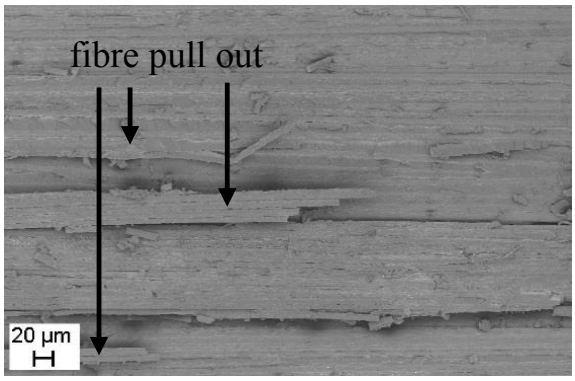
(b) sizing N2 (2.22 wt% FW404)

(c) sizing H0 (unmodified)

(d) sizing H1 (1.33 wt% FW404)

(e) sizing H2 (2.22 wt% FW404)

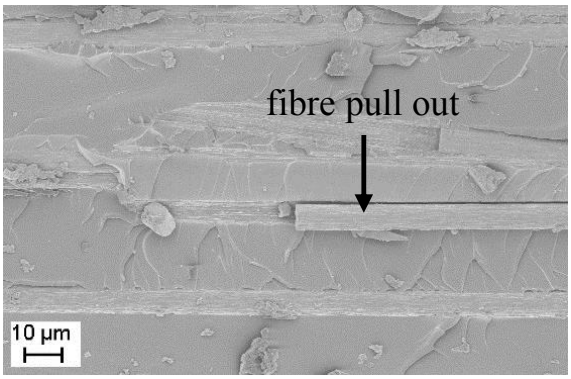
Figure 7.5: Silica nanoparticle dispersion and fibre/matrix adhesion (DCB fracture surfaces)



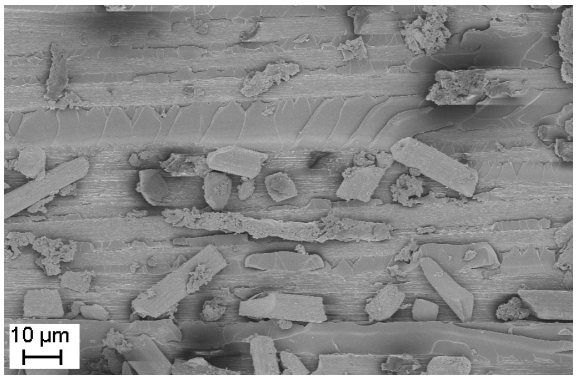
(a) sizing N0 - fibre pull out



(b) sizing N1 - fibre fragmentation

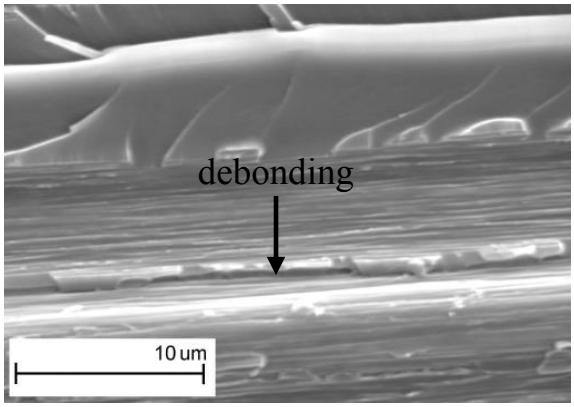


(c) sizing H0 - fibre pull out

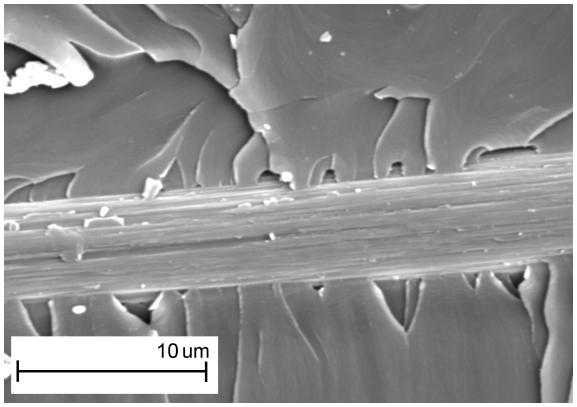


(d) sizing H1 - fibre fragmentation

Figure 7.6: Fibre pull out and fragmentation (DCB fracture surfaces)



(a) sizing N0 - poor adhesion (debonding indicated)



(b) sizing N1 - better adhesion

Figure 7.7: Fibre/matrix adhesion (fracture surfaces from FCG)

7.6 Conclusions

The results of the mode I interlaminar fracture tests and the FCG tests of the sizing-modified carbon fibre composites have been discussed in this chapter. Although the modified sizings had no significant effect on the fatigue behaviour, they improved the mode I fracture energy of the composites more efficiently compared to the matrix-modified carbon fibre composites, as significantly fewer SNPs were used. The toughening mechanisms have also been investigated. Adding SNPs into the fibre sizings improves the adhesion between the fibres and the matrix epoxy and hence improves the toughness. However, improving the adhesion too much can lead to a reverse effect where few fibres pull out and the fracture energy decreases, which implies a reduction in the toughness.

Chapter 8

Vibration Behaviours of Flat Sandwich Structures with Single or Double Face/Core Debonding

8.1 Introduction

The vibration behaviours of the flat sandwich structures affected by single or double debonded regions are discussed in this chapter. Hammer impact tests and finite element simulations using Abaqus [143] were conducted to analyse the vibration behaviours of the sandwich structures. The numbers of the tested flat sandwich structures with different configurations are listed in Table 4.6. For the control groups (flat, intact structures using the unmodified resin), three sandwich specimens were tested. For the treatment groups, three specimens were tested for the flat, intact structures using the modified resin and the $[0°]_4$ facesheets; while one specimen was tested for the other configurations for saving of time.

According to the principles of vibration mechanics, the natural frequencies of a structure are positively correlated to the structure's stiffness, which can be affected by different factors. In this work, the effects of the debonding length (for single debond), facesheet CFRP stacking orientation and material change (affected by using different modifiers in the resin and matrix) on the natural frequencies and mode shapes are presented and discussed. The experimental results are used to validate the results from the finite element simulation; the comparison and discussion are based on the simulation results. The results of simulations and hammer impact tests of the flat and curved (discussed in the next chapter) sandwich structures using the unmodified resin

are listed in full in Appendix B.

8.2 Bending Stiffness Matrix of the Flat, Intact Sandwich Structures

Since natural frequencies are positively correlated to the structure's stiffness, the bending stiffness matrices, D, of the intact sandwich structures using the unmodified resin were calculated according to the mechanics of composite materials [118]. The bending stiffness matrix, D, when using $[0°]_4$ facesheets is:

$$D_0 = \begin{bmatrix} 4373.14 & 97.56 & 0 \\ 97.56 & 292.20 & 0 \\ 0 & 0 & 175.22 \end{bmatrix} \text{(GPa-mm}^3\text{)} \tag{8.1}$$

where the subscript "0" means using $[0°]_4$ facesheets. The bending stiffness matrices when using $[90°]_4$ or $[+45°/-45°]_s$ facesheets are as follows:

$$D_{90} = \begin{bmatrix} 292.20 & 97.56 & 0 \\ 97.56 & 4373.14 & 0 \\ 0 & 0 & 175.22 \end{bmatrix} \text{(GPa-mm}^3\text{)} \tag{8.2}$$

$$D_{\pm 45} = \begin{bmatrix} 1390.33 & 1039.89 & 8.00 \\ 1039.89 & 1390.33 & 8.00 \\ 8.00 & 8.00 & 1117.56 \end{bmatrix} \text{(GPa-mm}^3\text{)} \tag{8.3}$$

According to Equations (8.1) to (8.3), it is clear that D_0 has the highest value of d_{11} of 4373.14 GPa-mm^3, which means that the structure using $[0°]_4$ facesheets has the highest bending stiffness. This will result in the highest natural frequencies of the bending modes of the sandwich structures using $[0°]_4$ facesheets. While for D_{90}, the value of d_{11} is 292.20 GPa-mm^3, which is the lowest within the three types of structures and hence results in the lowest bending stiffness of the structure using $[90°]_4$ facesheets. This will result in the lowest natural frequencies of the bending modes of the sandwich structures. For $D_{\pm 45}$, it has the highest value of d_{33} of 1117.56 GPa-mm^3, which means that the structure using $[+45°/-45°]_s$ facesheets has the highest torsional stiffness and hence will result in the highest natural frequencies of the torsion modes.

It is also noted that the value of d_{11} in D_0 is equal to that of d_{22} in D_{90}, and the value of d_{22} in D_0 is equal to that of d_{11} in D_{90}. The reasons for the equivalence are that the $[90°]_4$ facesheet

is the 90°-rotated stacking of the $[0°]_4$ facesheet, and the cores of the sandwich structures are homogeneous, which makes the related sandwich structures have the same values in the orthogonal directions (longitudinal and lateral). Besides, for $D_{\pm 45}$, the values of d_{11} and d_{22} are the same, this is because the $[+45°/-45°]_s$ facesheet is a symmetrical stacking orientation, and the sandwich structure has $[+45°/-45°]_s$ facesheet for the top and base faces, therefore the sandwich structure using $[+45°/-45°]_s$ facesheet has the same values of d in the longitudinal and lateral directions.

8.3 Effects of Debonding Length on the Flat Sandwich Structures

The natural frequencies of the first five modes of the intact sandwich structures using the unmodified epoxy resin for the core and the matrix of the CFRP facesheets are shown in Table 8.1. The simulated mode shapes of the structure using $[0°]_4$ facesheets are shown in Figure 8.1. The simulation and experiments show a maximum difference of about 12.2 % for the first five modes. By comparing to the published literature, the differences are acceptable since the common differences are also typically about 10 %. The natural frequencies of the first five modes of the 80-mm-debonded sandwich structures using the unmodified epoxy resin are shown in Table 8.2. The simulation and experimental results of the 80-mm debond configuration generally show differences of less than 10 %, while a difference of about 22.62 % is noted for the second mode of the structure using $[+45°/-45°]_s$ facesheets.

The differences may result from experimental errors, including the manufacturing process and the test set-up, and from simulation factors such as the mesh density, the element type used to mesh the models, variations in the measured material properties used as input parameters, and the analysis method selected. It is also noted that since only one sample was tested for each debonding configuration, the experimental results show more scatter rather than consistent trends (see Figure 8.2a). Therefore the differences between the simulation and experiments can further increase. However, as the experimental and simulation results show the same trends, i.e. the natural frequencies decrease more when there is a longer debonded region, and mostly differ by less than reported in the literature, the agreement can be considered to be good.

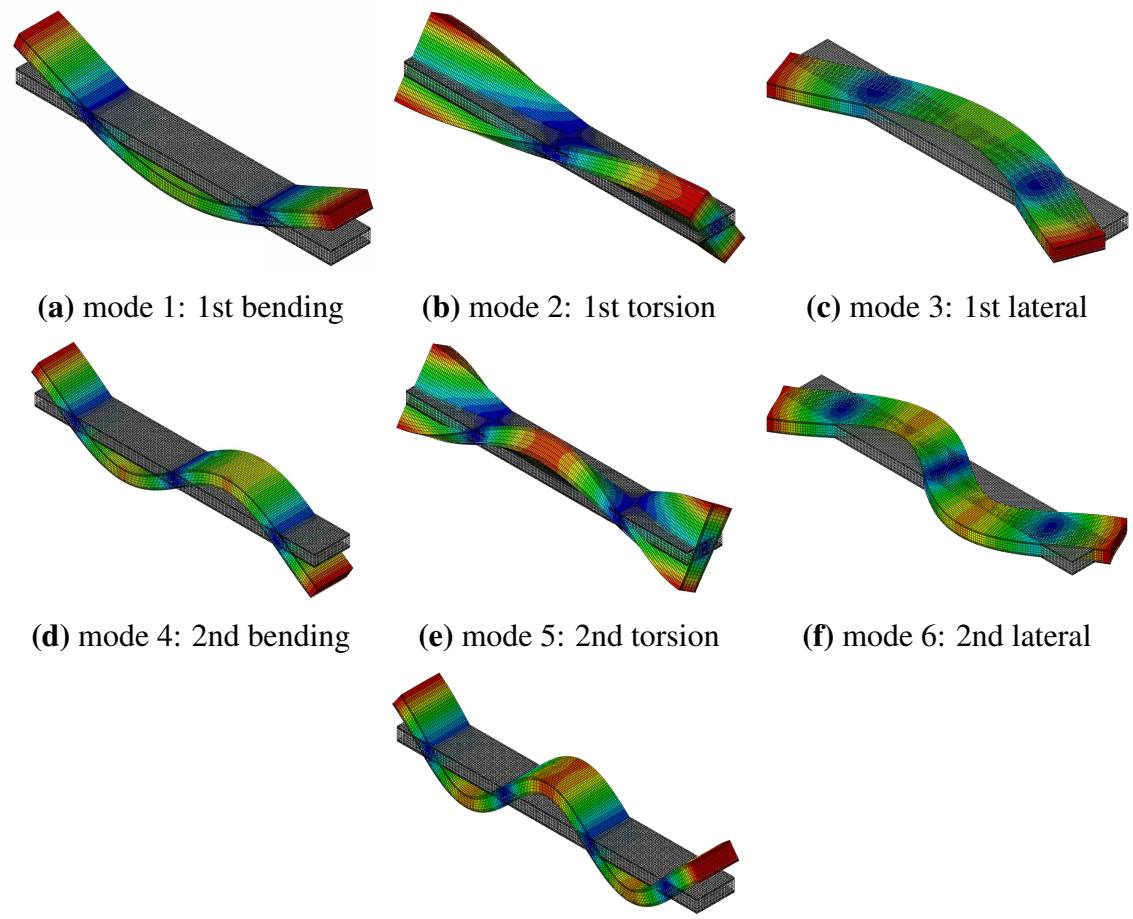
Figure 8.2 shows the relative natural frequencies ($f_n/f_{n,intact}$, where the subscript n indicates the mode) of the first five modes of the structures having a central debonded region. (Note that in Figure 8.2 and the subsequent Figures, the three mode types are indicated using the same colours: blue for bending, green for lateral and red for torsion.) It is clear that when the debonded region become longer, the natural frequencies decrease more. For the 2nd bending mode of the structures using $[0°]_4$ facesheets, the natural frequency decreases by 57 % when there is an 80 mm centre debond (see Figure 8.2b). This is because the debonded regions

Table 8.1: Natural frequencies and mode shapes of intact structure using unmodified resin

Facesheet stacking	Mode	FE (Hz)	Exp. (SD) (Hz)	Difference (%)	Shape
$[0°]_4$	1	1645.8	1512.9 (11.9)	-8.1	1st bending
	2	2095.4	1880.9 (87.2)	-10.2	1st torsion
	3	2986.4	2910.7 (22.9)	-2.5	1st lateral
	4	3890.3	3603.1 (199.8)	-7.4	2nd bending
	5	4273.6	3921.2 (145.3)	-8.2	2nd torsion
$[90°]_4$	1	452.3	447.5 (4.4)	-1.1	1st bending
	2	1092.6	1134.1 (3.5)	3.8	1st lateral
	3	1223.7	1227.7 (10.6)	0.3	2nd bending
	4	2072.0	1818.9 (84.4)	-12.2	1st torsion
	5	2336.4	2460.3 (191.7)	5.3	3rd bending
$[+45°/-45°]_s$	1	655.84	616.8 (3.1)	-6.0	1st bending
	2	1431.9	1394.5 (9.2)	-2.6	1st lateral
	3	1759.9	1616.4 (81.3)	-8.2	2nd bending
	4	3320.6	3224.4 (104.1)	-2.9	3rd bending
	5	3435.7	3212.2 (321.5)	-6.5	1st torsion

lead to the reduction of stiffness of the structures. Since the natural frequencies are positively correlated to the stiffness of the structure, a longer debonded region reduces the stiffness more significantly, which results in a greater reduction in the natural frequencies. It is also noted that for all three types of facesheet stacking used in this research, the natural frequencies of the lateral modes show little influence of debonding. This is because the debonded region is in the horizontal direction, so the effect on the stiffness in the lateral direction is less significant, therefore the natural frequency of the lateral mode decreases little.

From Figure 8.2, it can also be seen that different modes have different sensitivities to debonding, which are related to the materials, the facesheet stacking orientation and the location of the debonded regions. These factors can result in changes to the mode shape sequence. For example, for the intact structure using unmodified resin and $[0°]_4$ facesheets, the 2nd, 3rd and 4th modes (in ascending frequency order) are: 1st torsion (2095.4 Hz), 1st lateral (2986.4 Hz) and 2nd bending (3890.3 Hz) (see Table 8.1); while for the structures using the same material composition and having an 80 mm central debonded region, these three modes become 2nd bending (1671.9 Hz), 1st torsion (1673.2 Hz) and 1st lateral (2959.3 Hz) in sequence. This change of the mode shape sequence occurs because the stiffness change is greater in some



(a) mode 1: 1st bending **(b)** mode 2: 1st torsion **(c)** mode 3: 1st lateral

(d) mode 4: 2nd bending **(e)** mode 5: 2nd torsion **(f)** mode 6: 2nd lateral

(g) mode 7: 3rd bending

Figure 8.1: Simulation mode shapes of intact structure using unmodified resin and $[0°]_4$ stacking

modes (e.g. bending) than others (e.g. lateral). The same effect is observed in the structures using $[90°]_4$ and $[+45°/-45°]_s$ facesheets.

To detect face/core debonding in the sandwich structures, according to the Figure 8.2, measuring the resonant frequency of the 2nd bending mode can be helpful, since the debonded region affects the natural frequency of the 2nd bending mode the most significantly. The natural frequency of the 2nd bending mode affected by the debonded region shows a large drop when using the $[0°]_4$ facesheets, and it also shows an obvious reduction when using the $[90°]_4$ or $[+45°/-45°]_s$ facesheets.

8.4 Effects of CFRP Stacking Orientation on the Flat Sandwich Structures

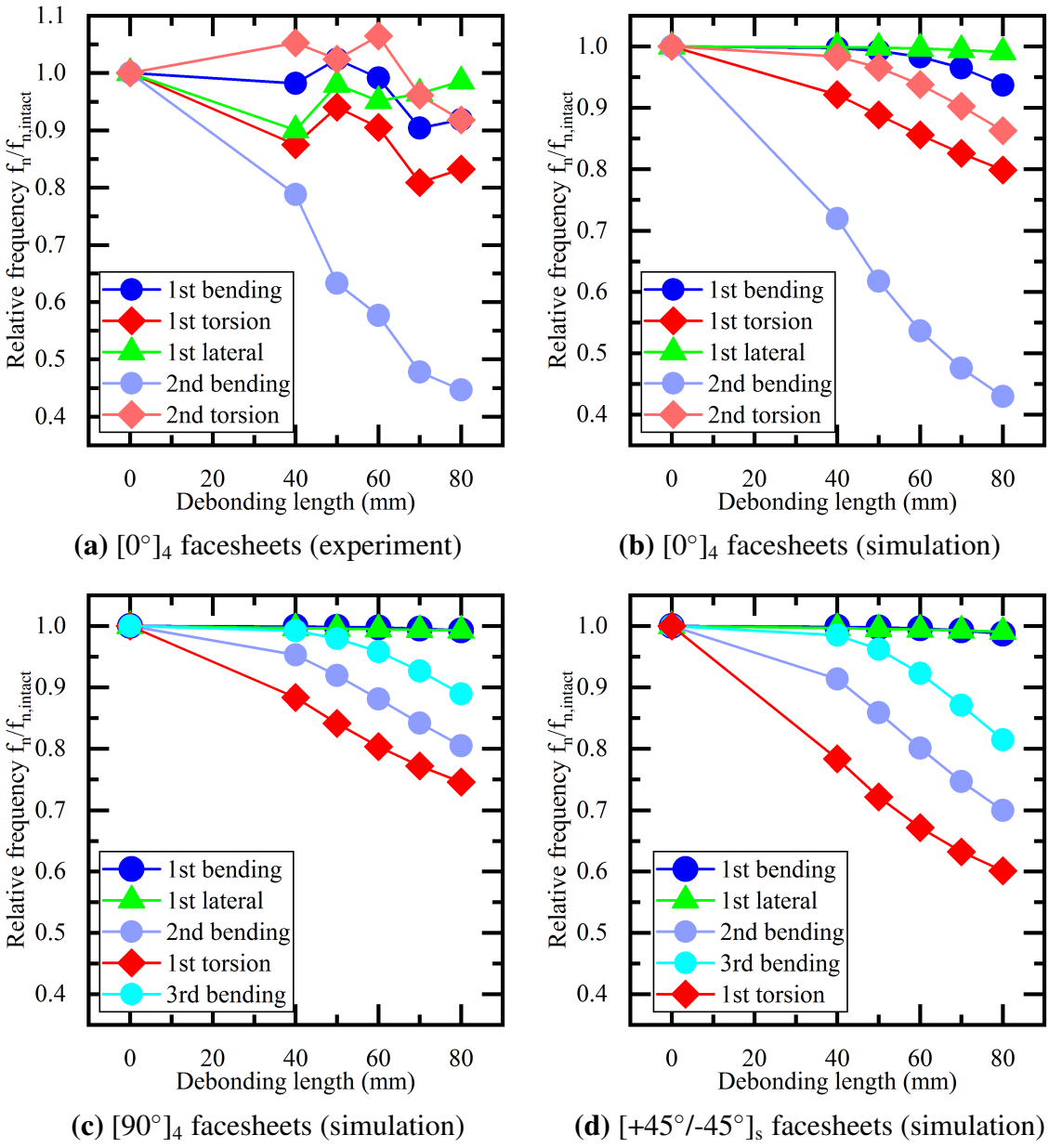
Different facesheet stacking orientations also affect the structures' reaction to debonding. Comparing the same mode in Figure 8.2, the three facesheet stacking ($[0°]_4$, $[90°]_4$ and $[+45°/-$

Table 8.2: Natural frequencies and mode shapes of 80-mm-debonded structure using unmodified resin

Facesheet stacking	Mode	FE (Hz)	Exp. (Hz)	Difference (%)	Shape
$[0°]_4$	1	1542.4	1389.5	-9.9	1st bending
	2	1671.9	1609.0	-3.8	2nd bending
	3	1673.2	1565.6	-6.4	1st torsion
	4	2959.3	2868.4	-3.1	1st lateral
	5	3686.2	3600.0	-2.3	2nd torsion
$[90°]_4$	1	449.1	475.8	5.9	1st bending
	2	985.2	907.8	-7.9	2nd bending
	3	1084.9	1119.5	3.2	1st lateral
	4	1544.9	1463.3	-5.3	1st torsion
	5	2077.8	2200.0	5.9	3rd bending
$[+45°/-45°]_s$	1	647.74	683.2	5.5	1st bending
	2	1231.2	952.7	-22.6	2nd bending
	3	1418.6	1346.9	-5.1	1st lateral
	4	2064.0	1946.5	-5.7	1st torsion
	5	2705.6	2354.7	-13.0	3rd bending

$45°]_s$) orientations result in different reductions in the natural frequencies for the same mode shape. For the bending modes, it is significant that the natural frequencies of the structure using $[0°]_4$ facesheets decrease most (decrease by 57 % for 2nd bending with 80 mm debonding), while the natural frequencies of the structure using $[90°]_4$ facesheets decrease least (decrease by 19 % for 2nd bending with 80 mm debonding). For the structure using $[+45°/-45°]_s$ facesheets, the reduction for the same condition is 30 %. The reason for this difference is that CFRP is an anisotropic material and this results in anisotropy of the sandwich structures. The $[0°]_4$ facesheets have the highest Young's modulus in the longitudinal direction and this results in the highest flexural stiffness of the sandwich structure, see d_{11} in Equation 8.1. However, when there is a debonded region, the stiffness decreases the most significantly, which leads to the greatest reduction of natural frequencies. On the other hand, the $[90°]_4$ facesheets have the lowest Young's modulus in the longitudinal direction and this results in the lowest stiffness of the structure, see d_{11} in Equation 8.2, so the debonded region reduces the stiffness of the structures less significantly, therefore the natural frequencies decrease the least.

The same effect also occurs for the torsion modes since the shear moduli are different for



(a) $[0°]_4$ facesheets (experiment)

(b) $[0°]_4$ facesheets (simulation)

(c) $[90°]_4$ facesheets (simulation)

(d) $[+45°/-45°]_s$ facesheets (simulation)

Figure 8.2: Relative natural frequencies affected by central single debonding. The order of modes in the legends follows the increasing of natural frequency

the three types of facesheet stacking. The $[+45°/-45°]_s$ facesheets have the highest shear moduli and this results in the highest torsional stiffness of the sandwich structure, see d_{33} in Equation 8.3. However, when there is a debonded region, the torsional stiffness decreases the most, which leads to the greatest reduction of natural frequencies of torsion modes. The natural frequency of the 1st torsion mode of the structure using $[+45°/-45°]_s$ facesheets decreases by 40 % when there is an 80 mm debonded region, while for the structures using $[0°]_4$ and $[90°]_4$ facesheets the reductions are only 20 % and 25 % respectively.

8.5 Effects of Material Change on the Flat Sandwich Structures

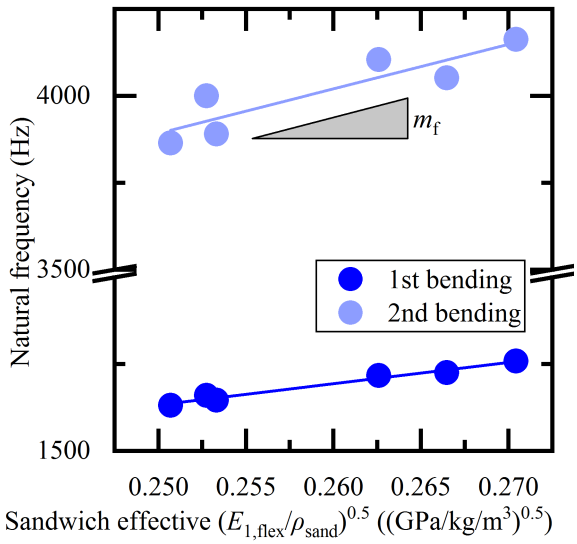
The changes of materials are achieved by using different modifiers in the core epoxy resin and the matrix of the facesheet CFRP.

By plotting the natural frequencies of the same bending mode versus $\sqrt{E_{1,\text{flex}}/\rho_{\text{sand}}}$ (where $E_{1,\text{flex}}$ is the flexural modulus and ρ_{sand} is the effective density of the sandwich structures using different modifiers, see Tables 6.1 and 6.4), it is noted that the plot shows a positive linearity (see Figure 8.3a). The parameter $\sqrt{E_{1,\text{flex}}/\rho_{\text{sand}}}$ comes from the calculation of the natural frequencies of beams in bending modes, e.g. [153]. When the density of the structure decreases or when the flexural modulus increases, then $\sqrt{E_{1,\text{flex}}/\rho_{\text{sand}}}$ increases and this results in the increase of natural frequencies. The gradient, m_{f}, describes the sensitivity of the structure's natural frequencies to the change of materials due to the addition of modifiers (silica nanoparticles and graphene). A larger m_{f} indicates that the natural frequencies of the structures are more sensitive to material change. For example, the gradient is 6.11×10^3 Hz/(GPa/kg/m^3)$^{0.5}$ for the 1st bending mode of the intact sandwich structure using $[0°]_4$ facesheets, and it is 12.81×10^3 Hz/(GPa/kg/m^3)$^{0.5}$ for the 2nd bending mode of the same structure, which means that for this structure, the natural frequency of the 2nd bending mode is more sensitive to material change.

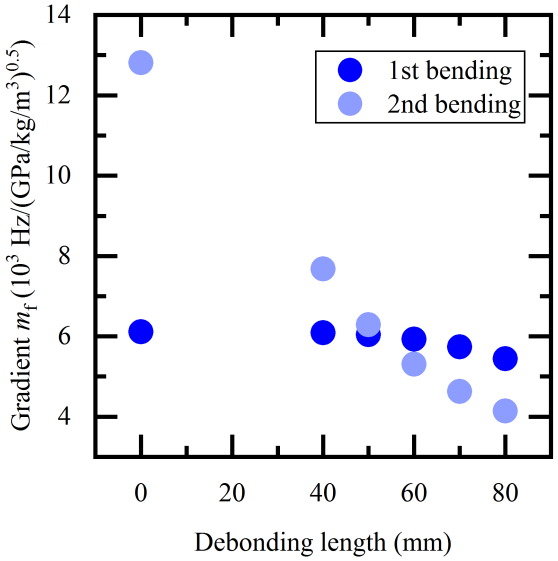
According to Figure 8.3b, increasing the length of the debonded region reduces the gradient m_{f}. Therefore, the structure with a longer debonded region is less sensitive to the change of materials. For the intact structure mentioned above, the gradients of the 1st and 2nd bending modes are 6.11×10^3 Hz/(GPa/kg/m^3)$^{0.5}$ and 12.81×10^3 Hz/(GPa/kg/m^3)$^{0.5}$ respectively, while for the same structure with an 80 mm debonded region, the gradients are 5.44×10^3 Hz/(GPa/kg/m^3)$^{0.5}$ and 4.14×10^3 Hz/(GPa/kg/m^3)$^{0.5}$ respectively. By comparing the bending modes in Figures 8.2b and 8.3b, it is noted that the trend of the natural frequencies and of m_{f}, which are affected by increasing the debond length, are the same: the natural frequency and m_{f} of the 2nd bending mode decreases more significantly than the 1st bending mode. On the other hand, it is also noted that even when the structures have different facesheet stacking orientations, the plot still shows the same linearity for the same mode when the data for all three types of facesheet stacking are combined into a single graph (see Figure 8.3c).

8.6 Effects of Double Debonding on the Flat Sandwich Structures

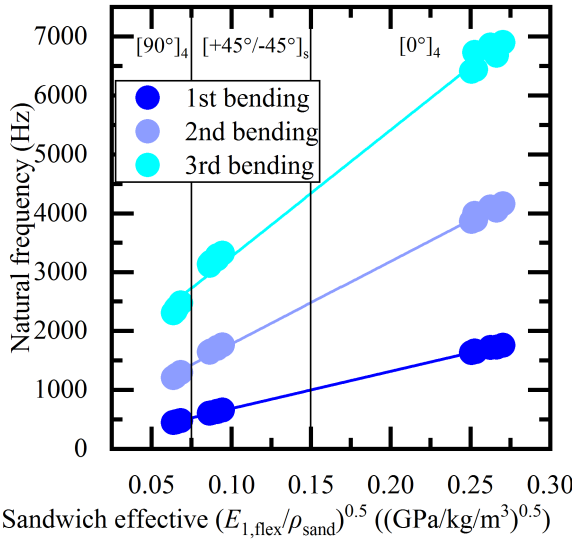
From Figure 8.4, it is clear that different facesheet stacking orientations show the same trend for the same mode under different debonding conditions for double debonding. It should



(a) Bending frequencies of intact structures, $[0°]_4$ facesheets, different modifiers



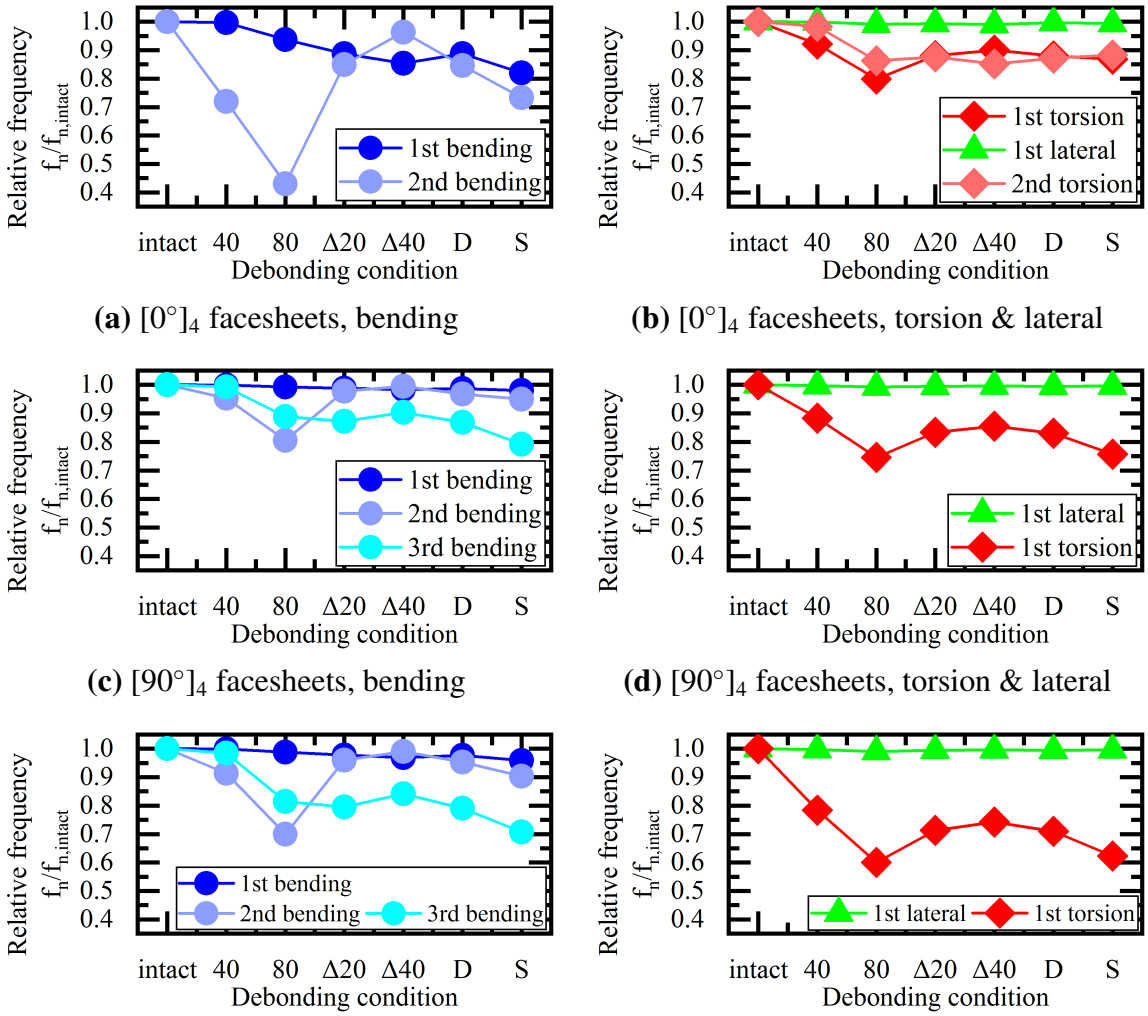
(b) Gradient m_f of debonded structures, $[0°]_4$ facesheets



(c) Bending frequencies of intact structures using different modifiers

Figure 8.3: Influence of material change on the natural frequencies of sandwich structures (simulation results)

be noted that a central 80 mm debonded region can be considered as two 40 mm debonded regions without separation (i.e. $\Delta 0$). Like the effect of CFRP stacking orientation (Section 8.4), the structure using $[0°]_4$ facesheets has the largest reduction in natural frequencies for bending modes, since the debonded regions reduce the stiffness of the sandwich structures using $[0°]_4$ facesheets more significantly than for the other two facesheet stacking orientations. While for the torsion mode, the structure using $[+45°/-45°]_s$ facesheets has the greatest reduction, since the debonded regions reduces the torsional stiffness of the sandwich structures using $[+45°/-45°]_s$ facesheets more significantly.



(a) $[0°]_4$ facesheets, bending

(b) $[0°]_4$ facesheets, torsion & lateral

(c) $[90°]_4$ facesheets, bending

(d) $[90°]_4$ facesheets, torsion & lateral

(e) $[+45°/-45°]_s$ facesheets, bending

(f) $[+45°/-45°]_s$ facesheets, torsion & lateral

Figure 8.4: Relative natural frequencies affected by double debonding (simulation results)

8.6.1 Effects of Increasing the Separation (Δ) between Two Debonds (Flat)

Increasing the distance between two debonded regions, i.e. Δ0 (80 mm in Figure 3.14b), Δ20 (see Figure 3.14c) and Δ40 (see Figure 3.14d), does not confirm the reduction or increase of natural frequencies, as the trends depend on the vibration modes. For example, according to Figure 8.4a, for the 1st bending mode of the structures using the unmodified resin and $[0°]_4$ facesheets, the natural frequency decreases when the separation increases from Δ0 to Δ40; while for the 2nd bending mode the natural frequency increases. The reason for the different trends is the locations of the vibration nodes and debonds. For the 1st bending mode, there are two vibration nodes (see Figure 8.1a). When increasing the distance between the two debonds, the debonded regions just start to overlap the nodes (for Δ20) or fully overlap the nodes (for Δ40). This overlapping results in a greater reduction in the natural frequency as the facesheet

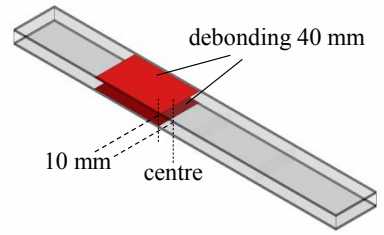
and core are not bonded together at the node, allowing relative movement, hence there is a greater reduction in the stiffness of the structure. For the 2nd bending mode, there are three vibration nodes (see Figure 8.1d). Increasing the distance between the two debonds moves the debonded regions away from the central node and no debonded regions overlap the nodes. Therefore, the natural frequency is reduced by less than for the 80-mm-debonded ($\Delta 0$) structure. However, it still decreases compared to the intact structure.

8.6.2 Effects of the Positions of Two Debonds (Flat)

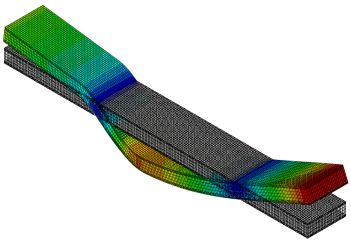
For the structures with two debonded regions on the same side ($\Delta 20$), diagonal (D) or symmetric (S) positions (each with the same distance of 10 mm from the edge of the debond to the centre axis, see Figure 3.14), it is noted that the natural frequencies of condition $\Delta 20$ and D are very close at lower modes (see Figure 8.4), therefore it is hard to distinguish between these two debonding conditions in real applications by only measuring the resonant frequencies. Although the 1st and 2nd bending modes show a decrease of natural frequencies (e.g. the relative frequency of the 2nd bending mode changes from 0.85 to 0.73 of that of the intact structure having $[0^\circ]_4$ facesheets, see Figure 8.4a), for the 1st torsion mode the natural frequency decreases, while for the 2nd torsion mode it increases slightly (e.g. the relative frequency of the 2nd torsion mode changes from 0.87 to 0.88 for the same structure, see Figure 8.4b). Therefore this still doesn't confirm a certain pattern but the change depends on the mode. On the other hand, it is noted that for the bending modes, condition S shows a greater reduction than $\Delta 20$, which results from the greater reduction in stiffness due to the debonded regions being located at the same places for both upper and lower facesheets, and this effect has been reported previously [99]. It is also noted that the reductions in the natural frequencies of the bending modes are different for conditions D and S, this is because the locations of the debonded regions are different, which affects the decrease of stiffness and therefore results in the different reductions in the natural frequencies.

Having the debonded regions at the symmetric positions also makes the structure asymmetric and affects the mode shapes and node positions, as shown in Figure 8.5. Comparing Figure 8.5b to Figure 8.1a, for the 1st bending mode, the left node moves to the right and is overlapped by the debonded regions, while the right node has little movement compared to the intact structure. For the 2nd bending mode, the left node has little movement, while the central node moves to the left and becomes overlapped by the debonded regions (see Figure 8.5d). Besides, the right node of the 2nd bending mode also moves to the right, and the mode shape is changed significantly as can be seen when Figure 8.5d is compared to Figure 8.1d. For the 1st torsion mode, the only node moves to the left and is overlapped by the debonded regions (see Figure 8.5c). As discussed in the previous section, overlapping of debonded regions and vibration nodes allows the facesheets and the core to have relative movement at the nodes and

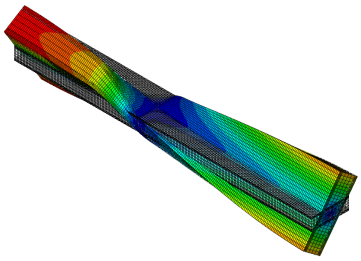
hence decreases the natural frequencies more significantly.



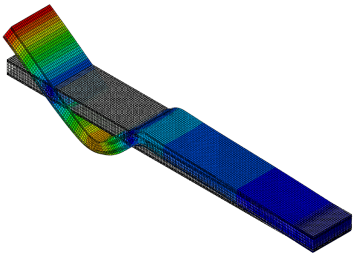
(a) symmetric debonds



(b) mode 1: 1st bending



(c) mode 2: 1st torsion



(d) mode 3: 2nd bending

Figure 8.5: Simulation mode shapes of S-debonded structure using unmodified resin and $[0°]_4$ stacking

8.6.3 Effects of Material Change on the Sandwich Structure with Two Debonds (Flat)

The gradient, m_f, of the plot of the natural frequency versus $\sqrt{E_{1,flex}/\rho_{sand}}$ of the double-debonded sandwich structures using $[0°]_4$ facesheets, is shown in Figure 8.6. Like the effect of material change on the single-debonded structures, the trends of the natural frequencies (see Figure 8.4a) and m_f of the bending modes of the double-debonded sandwich structures are the same. Although for the configurations of two debonded regions, the m_f of the 2nd bending mode of the condition Δ20, D and S decrease less than for the 1st bending mode, which is not like the situation for the bending frequencies, the trend within the same mode is the same.

According to Figure 8.6, increasing the distance between two debonded regions (Δ0, Δ20, Δ40) results in the reduction of m_f of the 1st bending mode and the increase of m_f of the 2nd bending mode. As discussed in Section 8.6.1, this results from the locations of the vibration nodes and the debonds. For the sandwich structures with the debond configuration Δ20 (debonds on the same side), D and S, the m_f values of condition Δ20 and D are close at lower modes (see Figure 8.6), which is the same as the trend of the natural frequencies. On the other hand, the m_f of condition S shows a greater reduction than condition Δ20 and D, since the debonded regions of configuration S reduce the stiffness and the natural frequencies more sig-

nificantly, which makes the natural frequencies of the structure less sensitive to material change and hence results in the greatest reduction in m_f.

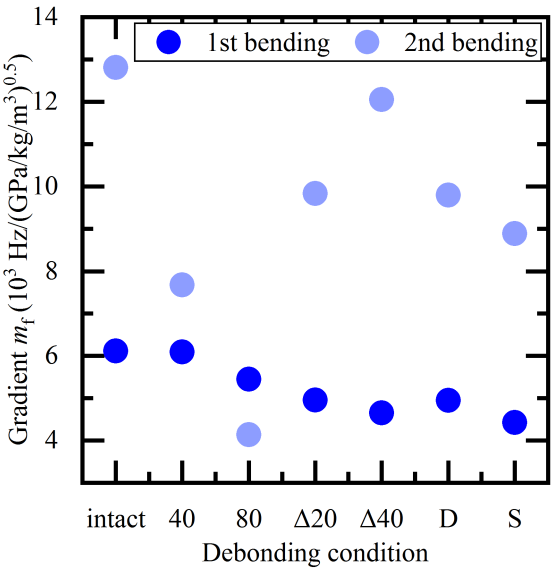


Figure 8.6: Gradient m_f of double-debonded structures, $[0°]_4$ facesheets (simulation results)

8.7 Conclusions

Comparisons of experimental and simulation results of the natural frequencies of the intact and debonded sandwich structures have been made and discussed. The effects of debonding length, locations of debonded regions, facesheet stacking orientations and material changes on the vibration behaviours of the flat sandwich structures have also been presented and discussed. According to the results, a longer debonded region results in a greater reduction in the natural frequencies. Different facesheet stacking orientations also affect the structure's reaction to debonding. The structure using the $[0°]_4$ facesheets has the highest flexural stiffness, but its stiffness decreases the most when there is a debonded region, which leads to the greatest reduction of natural frequencies. The natural frequencies of bending modes show a positive linearity, m_f, to the structure's $\sqrt{E_{1,\text{flex}}/\rho_{\text{sand}}}$. The m_f describes the sensitivity of the structure's natural frequencies to the change of materials. A longer debonded region reduces m_f, which means that the structure becomes less sensitive to the change of materials. For the structures with double debonded regions, when the two debonds are located at the symmetric positions (configuration S), the natural frequencies drop more than for the configuration $\Delta 20$ (two debonds with a separation of 20 mm). It is also noted that the trends of change of natural frequencies and m_f of the bending modes are the same for both the single and double debond configurations.

Chapter 9

Vibration Behaviours of Curved Sandwich Structures with Debonding

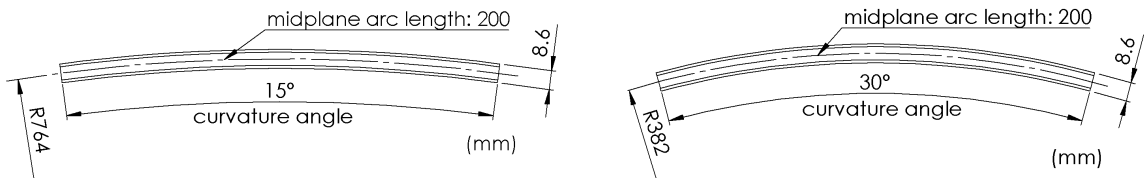
9.1 Introduction

The vibration behaviours of the curved sandwich structures affected by single or double debonded regions are discussed in this chapter. As for the flat structures, hammer impact tests and finite element simulations using Abaqus [143] were conducted to analyse the vibration behaviours of the sandwich structures. Hammer impact tests were conducted on the curved structures using the unmodified resin and the $[0°]_4$ and $[90°]_4$ facesheets. The numbers of the tested curved sandwich structures with different configurations are listed in Table 4.6. For the curved, intact structures, three sandwich specimens were tested; while for the curved, debonded structures, one specimen was tested for each debonding configuration for saving of time. FE simulations were also carried out on the structures using all types of the resins and the facesheets ($[0°]_4$, $[90°]_4$ and $[+45°/-45°]_s$).

In this chapter, the effects of the debonding length (for single debond), facesheet CFRP stacking orientation and material change (affected by using different modifiers in the resin and matrix) on the vibration behaviours of 15°-curved and 30°-curved sandwich structures are presented and discussed. The results of simulations and hammer impact tests of the curved sandwich structures using the unmodified resin are listed in full in Appendix B.

9.2 Curvature of Beam

The curved structures used in this work have a thickness of 8.6 mm, and a curvature radius of 764 mm for the 15°-curved structures or 382 mm for the 30°-curved structures, see Figure 9.1. According to the mechanics of materials [154], when the ratio of the curvature radius to the thickness is more than five, the curved beam can be considered as a flat beam. In this work, the ratios of the curved structures are about 88.8 (15°-curved) and 44.4 (30°-curved), therefore they are still relatively flat. Moreover, if the mid-plane arc length (200 mm) and the thickness (8.6 mm) are kept the same but the ratio of the curvature radius to the thickness of the structure is made equal to 5, the structure will have a curvature angle of about 266°. This is significantly more curved than the studied cases, and shows that the mechanics of all practical panels can be considered to be those of a flat beam.



(a) 15°-curved **(b)** 30°-curved

Figure 9.1: Lateral sketch of curved sandwich structures

9.3 Comparisons of Simulation and Experimental Results

The simulated and experimental natural frequencies and mode shapes of the first five modes of the intact, 30°-curved sandwich structures using the unmodified epoxy resin, $[0°]_4$ and $[90°]_4$ facesheets are shown in Table 9.1, those of the 80-mm-debonded structures are shown in Table 9.2. The differences between the simulation and experimental results are generally less than 10 %, while a difference of about 37.4 % is noted for the 80-mm-debonded structure using $[0°]_4$ facesheets. Possible reasons causing differences may include experimental errors such as the manufacturing process and test set-up, and simulation factors such as the element type and the mesh density used. Manufacturing the curved structures involves bonding the curved cores and facesheets together using the curved mould plates (see Section 3.4.3.2), which is more complicated than manufacturing the flat structures. This difficulty can affect the consistency and quality of the curved sandwich structures, and hence can further affect the results. Variations in the measured mechanical properties of the materials used as the input parameters can also cause differences. As discussed in Section 8.3, since for each debonding configuration only one sample was tested, the experimental results can show more scatter rather than consistent trends, and the differences between the simulation and experiments can further increase. Generally,

the differences are less than the published values of typically about 10 %. In addition, the simulation and experimental frequencies show the same trends, so it is considered that the agreement is good.

Table 9.1: Natural frequencies and mode shapes of intact, 30°-curved structure using unmodified resin

Facesheet stacking	Mode	FE (Hz)	Exp. (SD) (Hz)	Difference (%)	Shape
$[0°]_4$	1	1628.7	1560.2 (25.5)	-4.2	1st bending
	2	2057.9	1994.8 (43.8)	-3.1	1st torsion
	3	3132.7	2935.2 (15.9)	-6.3	1st lateral*
	4	3869.5	3776.4 (64.5)	-2.4	2nd bending
	5	4551.5	4476.3 (47.3)	-1.7	2nd torsion
$[90°]_4$	1	447.9	459.1 (4.7)	2.5	1st bending
	2	1217.6	1263.8 (13.1)	3.8	2nd bending
	3	1220.0	1265.1 (24.2)	3.7	1st lateral*
	4	2004.7	1968.1 (19.9)	-1.8	1st torsion
	5	2329.9	2424.4 (18.8)	4.1	3rd bending

*: combined with torsion

9.4 Effects of Curvature on the Intact Sandwich Structure

The simulated mode shapes of the 30°-curved sandwich structure using $[0°]_4$ facesheets are shown in Figure 9.2. The relative natural frequencies of the curved sandwich structures compared to the intact, flat structures are shown in Figure 9.3. It is noted that the natural frequencies of the bending modes decrease when the sandwich structures become more curved, i.e. from flat to 30°-curved. For the structures using the 3 types of facesheets, the reductions in the natural frequencies of bending modes are very close. When the structure is 30°-curved and using the $[0°]_4$ facesheets, the reductions for the 1st to 3rd bending modes are 1.0 %, 0.5 % and 0.3 % respectively (see Figure 9.3a), which are relatively small effects compared to the effects of a debonded region on the flat structures (see Section 8.3). According to the mechanics of materials [154], when a beam structure becomes curved, the position of the neutral axis changes. For the curved structures having rectangular cross-sections in this work, the positions of the neutral axes move down towards the curvature centres, which means that the curvature radii of the neutral axes are shorter than those of the corresponding centroids. Also, the moment needed to bend the curved structures becomes less, which indicates that the bending stiffness

Table 9.2: Natural frequencies and mode shapes of 80-mm-debonded, 30°-curved structure using unmodified resin

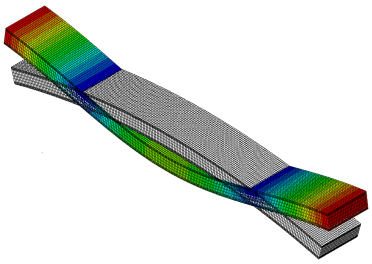
Facesheet stacking	Mode	FE (Hz)	Exp. (Hz)	Difference (%)	Shape
$[0°]_4$	1	1532.0	959.0	-37.4	1st bending
	2	1658.0	1593.4	-3.9	1st torsion
	3	1687.4	1660.9	-1.6	2nd bending
	4	2926.8	2288.7	-21.8	1st lateral*
	5	4061.2	4077.7	0.4	3rd bending
$[90°]_4$	1	444.8	365.2	-17.9	1st bending
	2	985.8	921.1	-6.6	2nd bending
	3	1204.1	1124.6	-6.6	1st lateral*
	4	1505.1	1472.7	-2.2	1st torsion
	5	2081.6	2261.7	8.7	3rd bending

*: combined with torsion

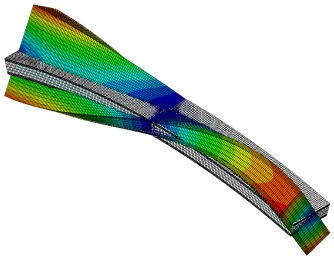
of the structures decreases. Therefore, the natural frequencies of the bending modes decrease slightly.

The effects of curvature on the natural frequencies of the torsion modes are shown in Figures 9.3d to 9.3f. Although the natural frequency of the 2nd torsion mode of the structure using the $[0°]_4$ facesheets increases, there is generally a decreasing trend in the natural frequencies of the torsion modes when increasing the curvature when the 1st torsion mode and the other facesheet stacking orientations are considered. Also, the sequences of the reduction in the same torsion mode are the same: the natural frequencies of the structure using the $[+45°/-45°]_s$ facesheets decrease the most significantly, those for the structure using the $[90°]_4$ facesheets decrease less, and for the structure using the $[0°]_4$ facesheets there is the least reduction (1st torsion) or an increase (2nd torsion). The reason for the greatest reduction being caused by the $[+45°/-45°]_s$ facesheets is that increasing the curvature results in a greater reduction in the torsional stiffness of the structure using the $[+45°/-45°]_s$ facesheets, therefore the natural frequencies of the torsion modes of the structure using the $[+45°/-45°]_s$ facesheets decrease the most.

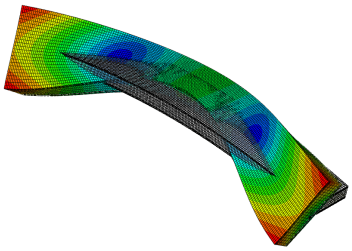
According to the modes shapes (see Figure 9.2), the bending and torsional modes of the curved sandwich structures are independent of each other. However, it is clear that the lateral modes are coupled with torsional movement. The trend in the natural frequencies of the lateral modes affected by the curvatures is opposite to that of the torsion modes: the natural frequencies for the structure using the $[+45°/-45°]_s$ facesheets increase the most significantly, those for the



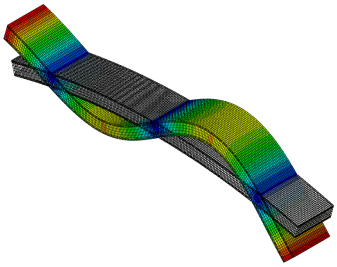
(a) mode 1: 1st bending



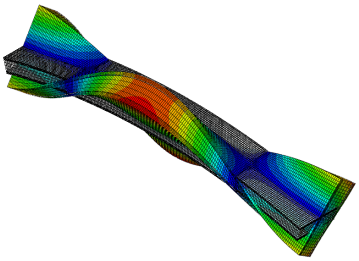
(b) mode 2: 1st torsion



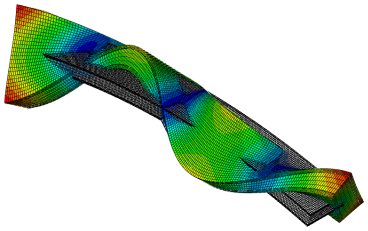
(c) mode 3: 1st lateral (combine with torsion)



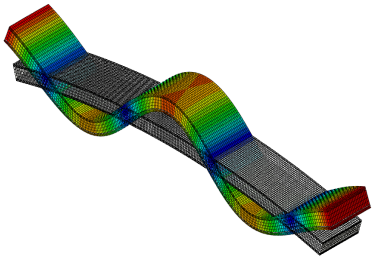
(d) mode 4: 2nd bending



(e) mode 5: 2nd torsion



(f) mode 6: 2nd lateral (combine with torsion)

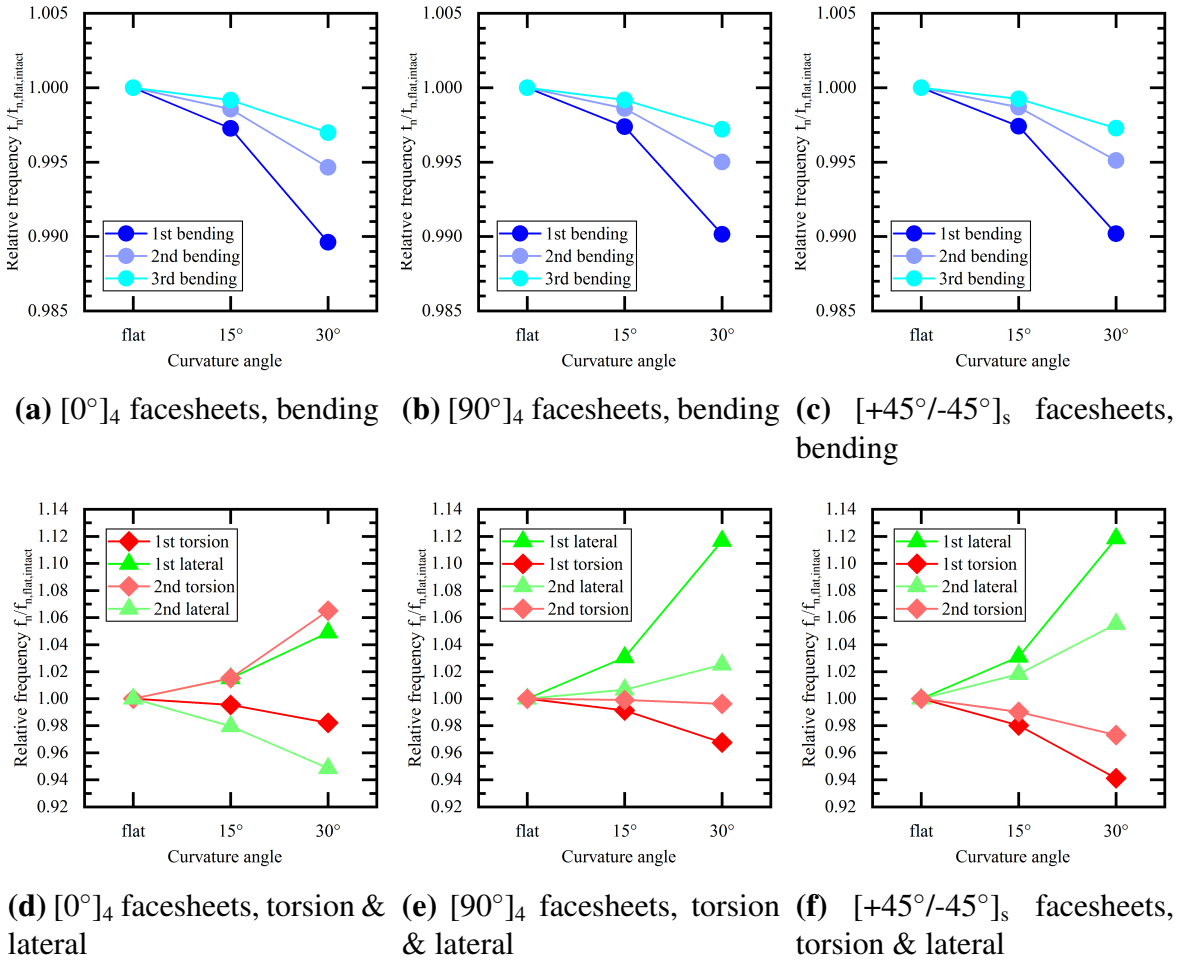


(g) mode 7: 3rd bending

Figure 9.2: Simulation mode shapes of 30°-curved, intact structure using unmodified resin and $[0°]_4$ facesheets

structure using the $[90°]_4$ facesheets increase less, and the structure using the $[0°]_4$ facesheets has the least increase (1st lateral) or a decrease (2nd lateral). Therefore, there is generally an increasing trend in the natural frequencies of the lateral modes with increasing curvature. The reason for the increase is that since the structures are curved, the mode shapes of the lateral modes become combined with torsional movement rather than having pure lateral movement (see Figures 9.2c and 9.2f), which makes the structure stiffer and hence the natural frequencies increase. The natural frequencies of the torsion-lateral modes of the structure using the $[+45°/-45°]_s$ facesheets increase the most because $[+45°/-45°]_s$ provides the most torsional stiffness to the structures.

According to Figure 9.3, it is hard to distinguish whether a flat beam structure has become slightly curved or not in practical applications by measuring the resonant frequencies of the



(a) $[0°]_4$ facesheets, bending **(b)** $[90°]_4$ facesheets, bending **(c)** $[+45°/-45°]_s$ facesheets, bending

(d) $[0°]_4$ facesheets, torsion & lateral **(e)** $[90°]_4$ facesheets, torsion & lateral **(f)** $[+45°/-45°]_s$ facesheets, torsion & lateral

Figure 9.3: Relative natural frequencies of intact, flat and curved sandwich structures (simulation results)

bending modes since the difference is not significant. However, measuring the resonant frequencies of the lateral modes has the potential to detect whether a structure has become curved since the difference is more significant.

9.5 Effects of Debonding Length on the Curved Sandwich Structures

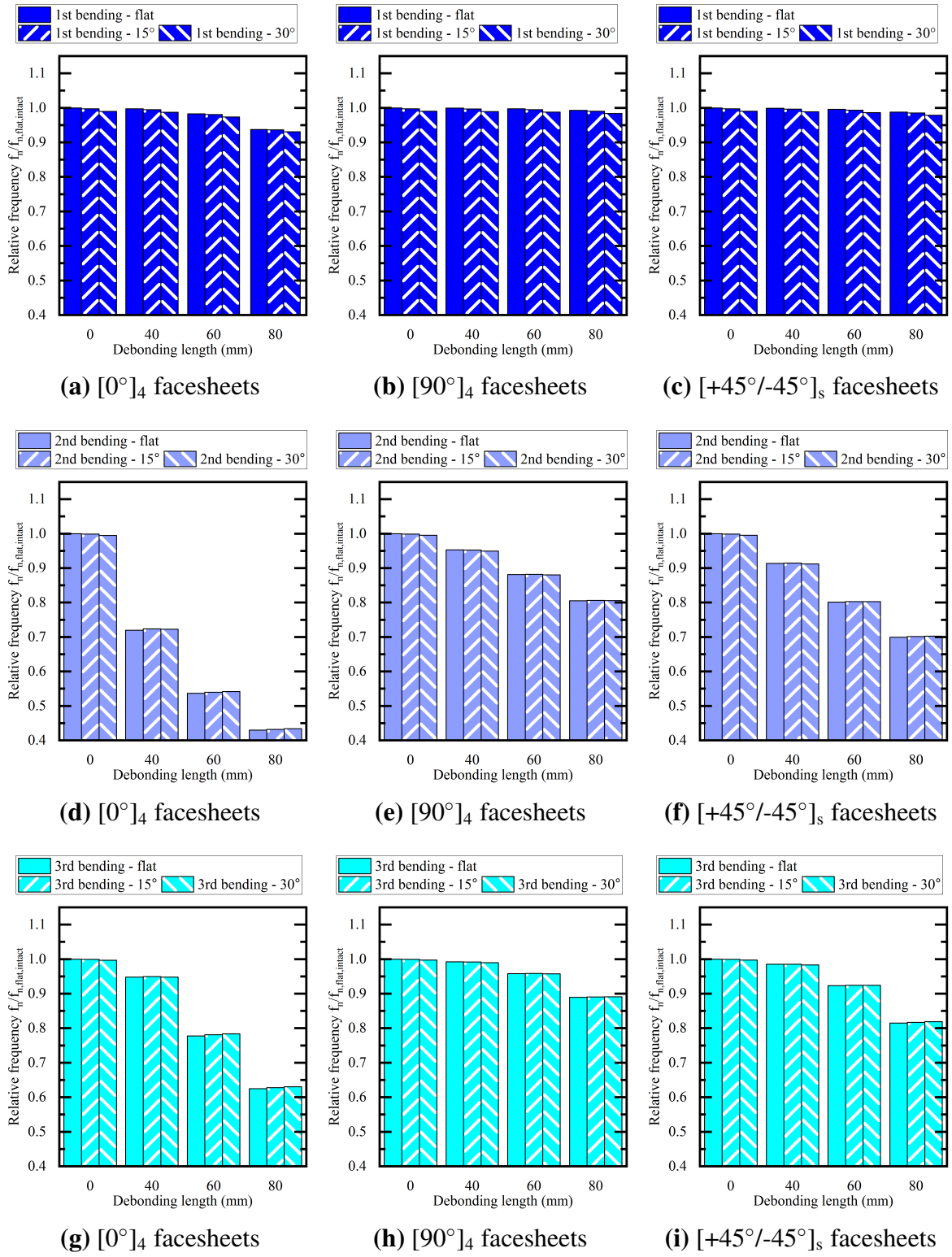
The effects of curvature and a central debonded region of different lengths on the natural frequencies of the first three bending modes are shown in Figure 9.4. As discussed in Section 8.3, increasing the length of the debonded region reduces the stiffness of the structures and hence results in a reduction in the natural frequencies. For the flat sandwich structure using the $[0°]_4$ facesheets and the unmodified resin, when there is an 80-mm debonded region, the natural frequencies of the first three bending modes decrease by 6.3 %, 57.0 % and 37.5 %, respectively; while for the 30°-curved structure with the same configurations, the frequencies

of the first three bending modes decrease by 6.9 %, 56.6 % and 37 %, respectively. Therefore, the curvature angle of 30° increases the reduction in the natural frequency of the 1st bending mode by 0.6 % but mitigates the reductions in the natural frequencies of the 2nd and 3rd bending modes by 0.4 % and 0.5 %. The reason for lesser reductions is that the curved structure is less stiff than the flat structure, as discussed in the Section 9.4. Although the natural frequencies drop due to the debonded region, the frequencies drop less for the less-stiff structures (i.e. the curved structures) than for the stiff structure (i.e. the flat structure). However, compared to the effect of debonding length, the effect of curvature on the natural frequencies of the bending modes of the debonded sandwich structures is relatively small, as can be seen in Figure 9.4.

The effects of curvature on the natural frequencies of the torsion and lateral modes of the single-debonded sandwich structures are shown in Figure 9.5. Although for the same debonding length, increasing the curvature results in an increase in the natural frequencies of the 2nd torsion mode of the structures using the $[0°]_4$ facesheets (see Figure 9.5d), for all the three types of facesheet stacking orientations, the natural frequencies of torsion modes drop when increasing the debonding length.

For the lateral mode, the natural frequencies are not significantly affected by the horizontal debonded region since the debonded region has less effect on the stiffness in the lateral direction. However, for the curved structures, it is noted that the reduction in the natural frequencies of the lateral mode is more significant than for the flat structure. For the structures using the $[0°]_4$ facesheets, when there is an 80-mm debond, the frequency drops by only 0.9 % for the flat structure, while it drops by 2.0 % for the 30°-curved structure, see Figure 9.5g. This is because the torsion-lateral mode shape caused by increasing the curvature has torsional movement rather than pure lateral movement, as discussed in Section 9.4. Since the torsional movement is involved in the mode shape, the reduction in the torsional stiffness caused by the debonded region decreases the natural frequency of the torsion-lateral mode. On the other hand, it is also noted that since the natural frequencies of the lateral modes of the curved structures can be higher than those of the flat structures, the natural frequencies of the lateral modes of a debonded, curved structure may be higher than the intact, flat structure, see Figures 9.5g to 9.5i. For example, in Figure 9.5h, the natural frequency of the 1st lateral mode of the 80-mm-debonded, 30°-curved structure using $[90°]_4$ facesheets is higher than that of the flat, intact structure using the same facesheets.

To detect damage in the flat and curved structures, considering the configurations in this work, measuring the resonant frequency of the 2nd bending mode can be useful since it is affected the most significantly when increasing the debonding length (see Figures 9.4 and 9.5). However, since the curved structures are less stiff, and their natural frequencies of the bending modes are less sensitive to the debond, it is more difficult to identify the debond. Besides, as discussed in Section 9.4, the curvature has less effect on the natural frequencies of bending



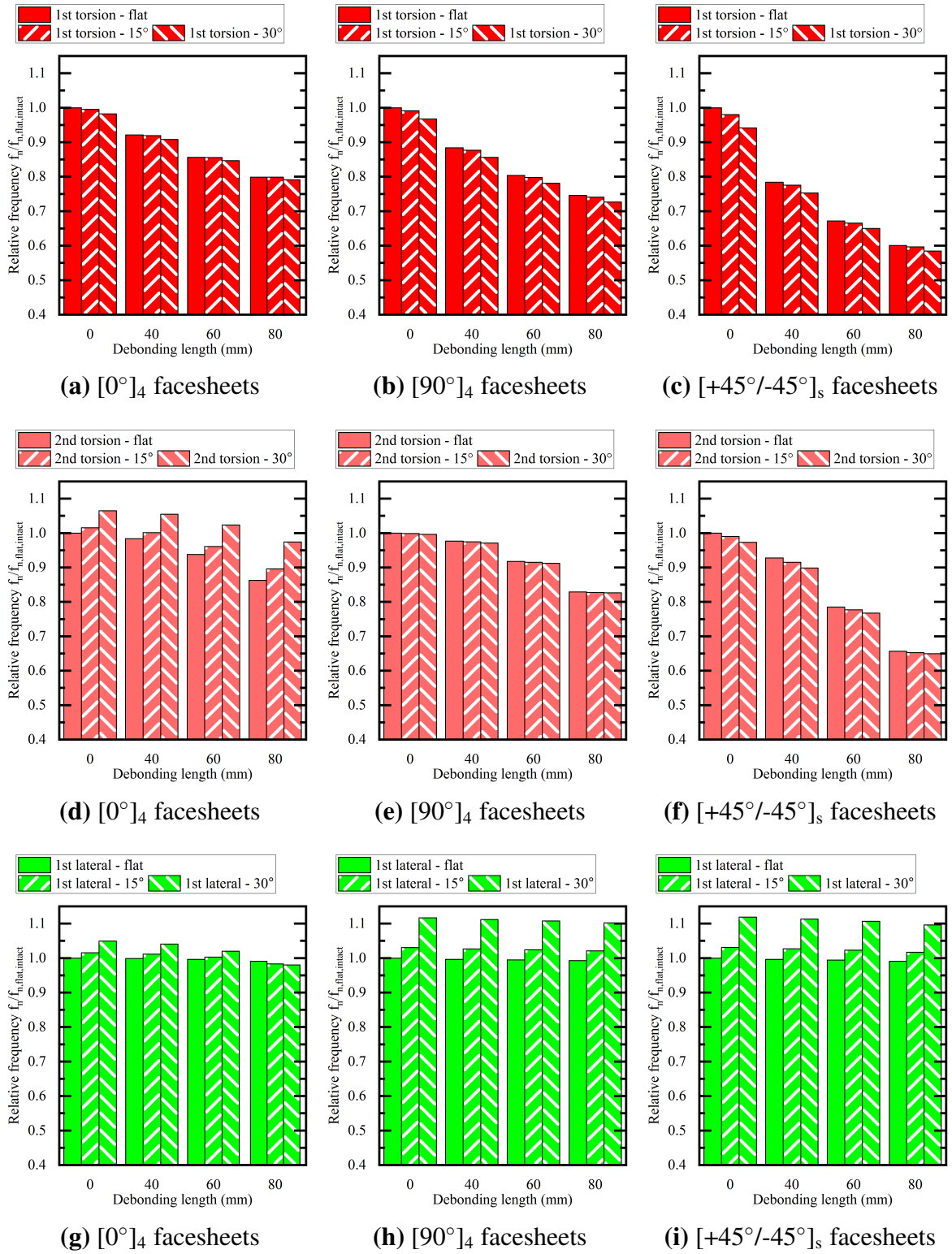
(a) $[0°]_4$ facesheets **(b)** $[90°]_4$ facesheets **(c)** $[+45°/-45°]_s$ facesheets

(d) $[0°]_4$ facesheets **(e)** $[90°]_4$ facesheets **(f)** $[+45°/-45°]_s$ facesheets

(g) $[0°]_4$ facesheets **(h)** $[90°]_4$ facesheets **(i)** $[+45°/-45°]_s$ facesheets

Figure 9.4: Relative natural frequencies of bending modes affected by a central debonding and curvature (simulation results)

modes but more on the natural frequencies of the lateral (torsion-lateral) modes. Therefore, to detect whether a structure has become damaged and curved, measuring the resonant frequencies of both the 2nd bending mode (for identifying damage) and lateral modes (for identifying



(a) $[0°]_4$ facesheets **(b)** $[90°]_4$ facesheets **(c)** $[+45°/-45°]_s$ facesheets

(d) $[0°]_4$ facesheets **(e)** $[90°]_4$ facesheets **(f)** $[+45°/-45°]_s$ facesheets

(g) $[0°]_4$ facesheets **(h)** $[90°]_4$ facesheets **(i)** $[+45°/-45°]_s$ facesheets

Figure 9.5: Relative natural frequencies of torsion and lateral modes affected by a central debonding and curvature (simulation results)

bending deformation), then comparing with those of the flat, intact structure, would be more useful than just measuring the resonant frequency of the 2nd bending mode.

9.6 Effects of CFRP Stacking Orientation on the Curved Sandwich Structures

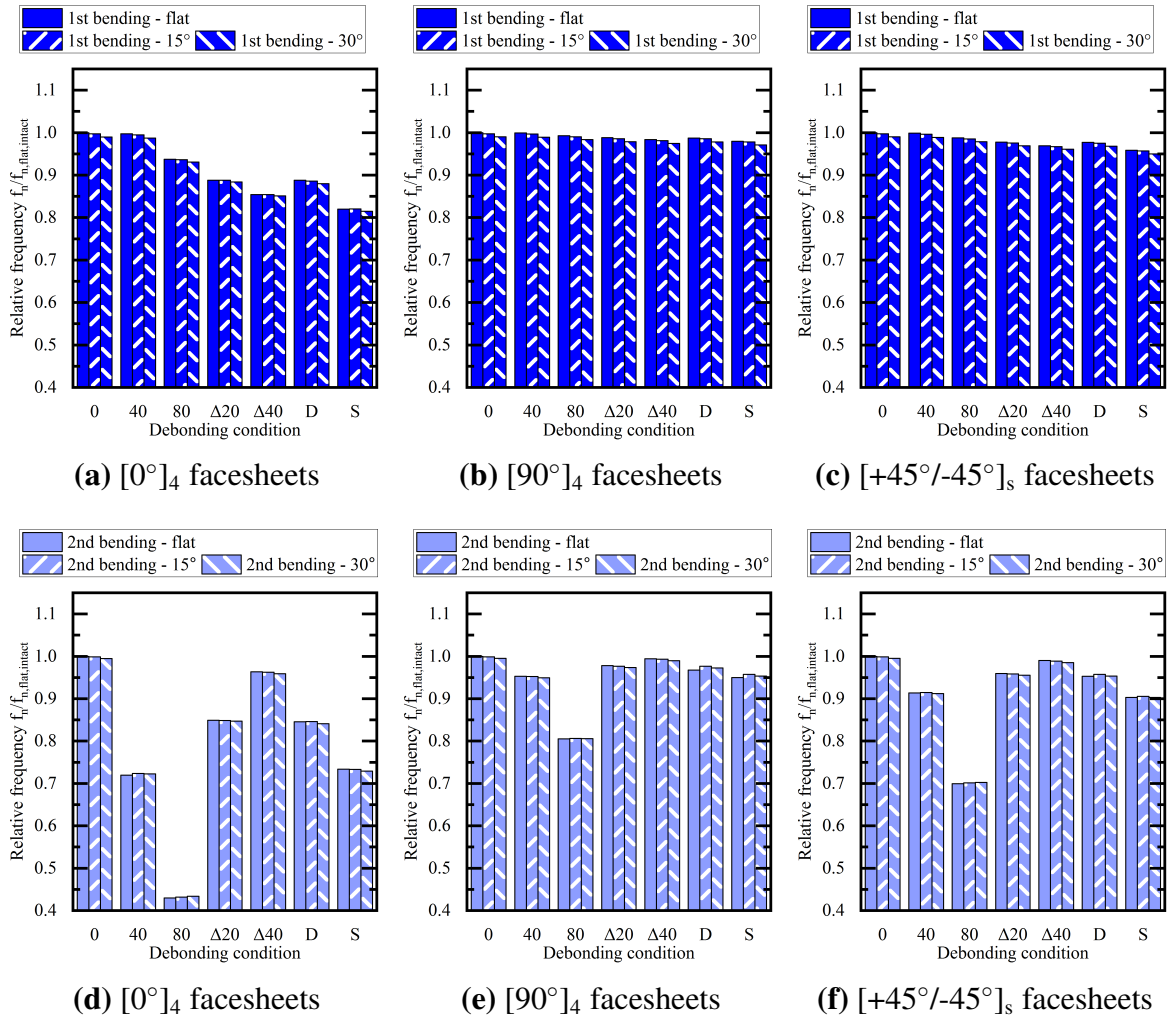
Comparing the same bending modes (same colour/row) in Figure 9.4, it is clear that structures using the $[0°]_4$ facesheets have the greatest frequency reductions of bending modes for the flat and curved structures. As discussed in Section 8.4, although the $[0°]_4$ stacking provides the highest flexural stiffness to the sandwich structure, the stiffness also decreases the most when a debonded region exists in the structure. Therefore the natural frequencies of the bending modes of the structures using the $[0°]_4$ facesheets drop the most significantly. The same effect is also found in the torsion modes, the structures using the $[+45°/-45°]_s$ facesheets have the most significant drops within the same torsion mode and curvature (see the torsion modes, red and pink bars, in Figure 9.5). This is because the $[+45°/-45°]_s$ facesheet provides the highest torsional stiffness, but the stiffness also decreases the most when the debonded region exists, which results in the greatest reductions in the natural frequencies of the torsion modes. It is also noted that the effect of facesheet stacking orientation is more significant than that of the curvature.

9.7 Effects of Double Debonding on the Curved Sandwich Structures

The effects of curvature and double debonded regions with different configurations on the natural frequencies of the sandwich structures are shown in Figures 9.6 and 9.7. It is clear that different curvatures show the same trend for the same mode under different debonding conditions. Also, as discussed before, the structures using the $[0°]_4$ facesheets have the greatest reductions in the natural frequencies of bending modes, since the bending stiffness of the flat and curved sandwich structures decrease the most when there are debonded regions, see Figure 9.6; the structures using the $[+45°/-45°]_s$ facesheets have the greatest reductions in the natural frequencies of torsion modes, since the torsional stiffness drops the most due to the debonded regions, see Figure 9.7.

9.7.1 Effects of Increasing the Separation ($\triangle$) between Two Debonds (Curved)

As discussed in Section 8.6.1, the changes of the natural frequencies don't follow a certain pattern when increasing the distance between the two 40-mm debonded regions, i.e. $\Delta 0$ (central 80-mm debond), $\Delta 20$, and $\Delta 40$ (see Figures 3.15b to 3.15d), since the positions of the debonds and of the vibration nodes also affect the natural frequencies. The positions of the vibration nodes of the intact curved structures can be seen in Figure 9.2. For the 1st bending mode,



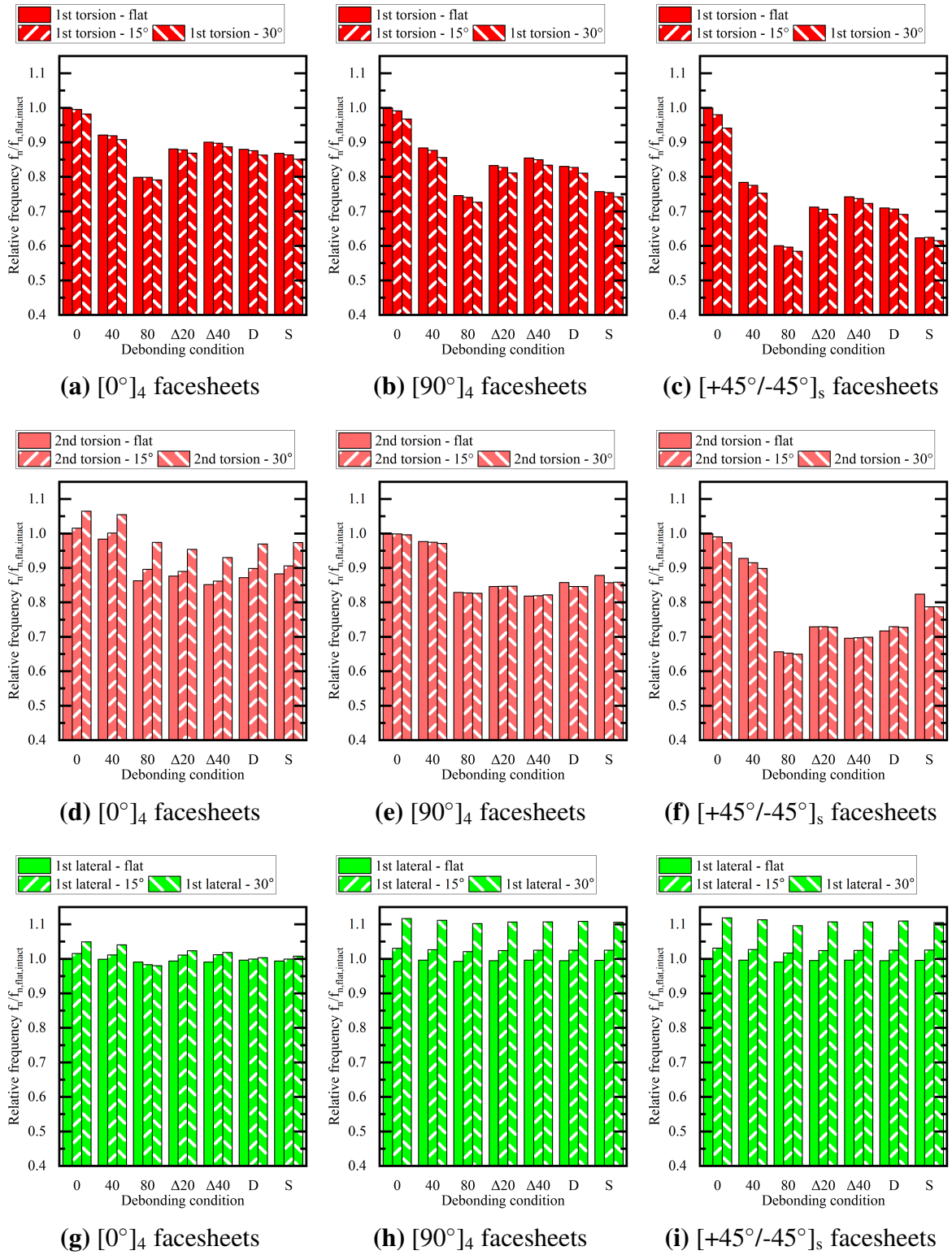
(a) $[0°]_4$ facesheets **(b)** $[90°]_4$ facesheets **(c)** $[+45°/-45°]_s$ facesheets

(d) $[0°]_4$ facesheets **(e)** $[90°]_4$ facesheets **(f)** $[+45°/-45°]_s$ facesheets

Figure 9.6: Relative natural frequencies of bending modes affected by double debonding and curvature (simulation results)

increasing the separation between the two debonds makes them just overlap the vibration nodes ($\Delta 20$) or fully overlap the nodes ($\Delta 40$) and hence allows relative movement of the facesheets and cores of the flat and curved structures as they are not bonded together at the nodes, which reduces the stiffness more, and hence the natural frequency of the 1st bending mode decreases more significantly. For the 2nd bending modes, the two debonds move away from the central vibration node and don't overlap the other two nodes when the separation increases. Since the facesheet and the core are bonded together at the nodes, relative movement is not allowed. Therefore, the reduction in the natural frequency of the 2nd bending mode is smaller than for the 80-mm-debonded structure.

According to Figure 9.6, the curvature also causes differences in the natural frequencies when increasing the distance between the two debonds. For condition $\Delta 40$, increasing the curvature slightly decreases the natural frequencies of the 1st and 2nd bending modes. However, the effect is small when compared to the effects of separation length.



(a) $[0°]_4$ facesheets **(b)** $[90°]_4$ facesheets **(c)** $[+45°/-45°]_s$ facesheets

(d) $[0°]_4$ facesheets **(e)** $[90°]_4$ facesheets **(f)** $[+45°/-45°]_s$ facesheets

(g) $[0°]_4$ facesheets **(h)** $[90°]_4$ facesheets **(i)** $[+45°/-45°]_s$ facesheets

Figure 9.7: Relative natural frequencies of torsion and lateral modes affected by double debonding and curvature (simulation results)

9.7.2 Effects of the Positions of Two Debonds (Curved)

The configurations of the structures having two debonded reigons on the same side with a separation of 20 mm (Δ20), at diagonal (D) or symmetric (S) locations can be seen in Fig-

ures 3.15c, 3.15e and 3.15f. According to Figure 9.6, like the flat structures, the natural frequencies of the lower bending modes of the curved structures with debonding condition $\Delta 20$ and D are very close. Therefore, it is hard to distinguish these two debonding conditions by only measuring the resonant frequencies in practical applications if detection of damage is required.

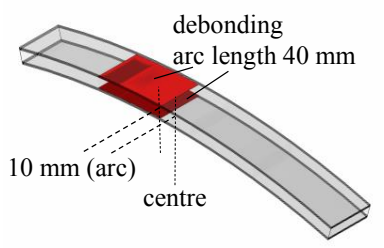
Comparing condition S to conditions $\Delta 20$ and D, for the flat and curved structures having two debonded regions of configuration S and using the $[0^\circ]_4$ facesheets, the natural frequencies of the 1st bending mode (see Figure 9.6a) and the 2nd bending mode (see Figure 9.6d) decrease, and those of the 1st torsion mode also decrease slightly, see Figure 9.7a. However, for the 2nd torsion mode, the natural frequencies of the flat and curved structures increase, see Figure 9.7d. Therefore, a certain trend cannot be confirmed but depends on the mode. On the other hand, it is clear that the debonded regions of condition S results in a greater reduction in the natural frequencies of bending modes. As discussed in Section 8.6.2, this is because of a greater reduction in the stiffness caused by two debonded regions being located at the same places for the upper and lower facesheets [99].

For the curved structures, the debonded regions of condition S make the structure asymmetric, which affects the mode shapes and the node positions (see Figure 9.8), as discussed in Section 8.6.2. Comparing Figure 9.8b to Figure 9.2a, the left node of the 1st bending mode moves to the right and is overlapped by the debonded regions, while the right node of the same mode has no significant movement. For the 2nd bending mode, the left node (in Figure 9.8d compared to Figure 9.2d) has little movement, the central node moves to the left and is overlapped by the debonded regions, and the right node also moves to the right. For the 1st torsion mode, the node moves to the left and becomes overlapped by the debonded regions (in Figure 9.8c compared to Figure 9.2b). As discussed before, relative movement of the facesheets and the core at the vibration nodes occurs when the debonded regions cover the vibration nodes, which results in a greater reduction in the natural frequencies.

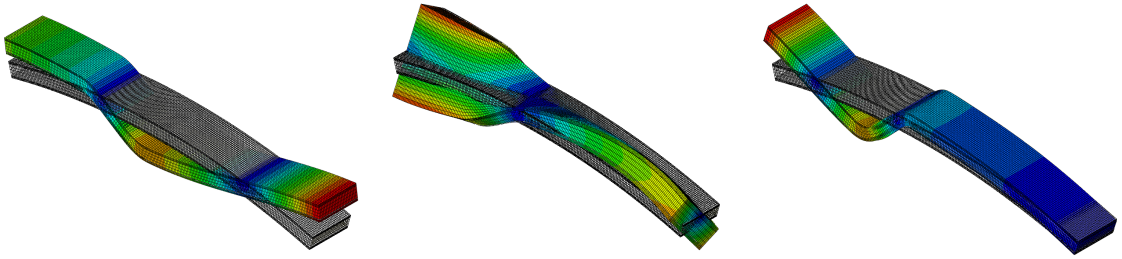
Comparing the natural frequencies of the flat and curved sandwich structures having debonded regions of condition $\Delta 20$, D and S, although increasing the curvature to 30° further decreases the natural frequencies of the bending modes of the symmetrically-debonded structures, the effect is not as significant as the reduction in the stiffness caused by two debonded regions being located at the same places (i.e. condition S).

9.8 Effects of Material Change on the Curved Sandwich Structures

To achieve changes of materials, different modifiers (silica nanoparticles and graphene) of different concentrations were added into the core epoxy resin and the matrix of the facesheet CFRPs of the sandwich structures.



(a) symmetric debonds



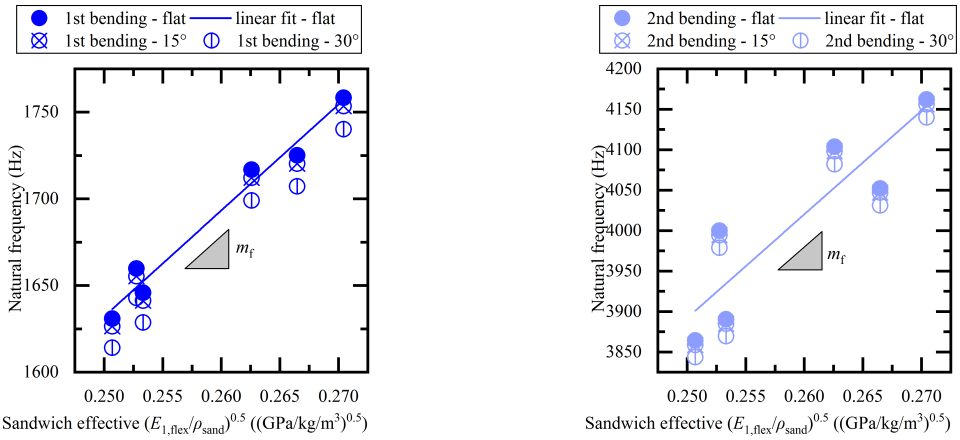
(b) mode 1: 1st bending **(c)** mode 2: 1st torsion **(d)** mode 3: 2nd bending

Figure 9.8: Simulation mode shapes of 30°-curved, S-debonded structure using unmodified resin and $[0°]_4$ stacking

As discussed in Section 9.2, since the curved sandwich structures used in this study are not highly curved (i.e. the ratio of curvature radius to thickness is larger than 5), the $\sqrt{E_{1,\text{flex}}/\rho_{\text{sand}}}$ values of the flat sandwich structures can also be applied to the 15°- and 30°-curved sandwich structures, where $E_{1,\text{flex}}$ is the flexural modulus and ρ_{sand} is the effective density of the sandwich structures using the different modifiers. Using the values in Tables 6.1 and 6.4), $E_{1,\text{flex}}$ was calculated according to the mechanics of composite materials [118]; ρ_{sand} was calculated according to the rule of mixtures [118].

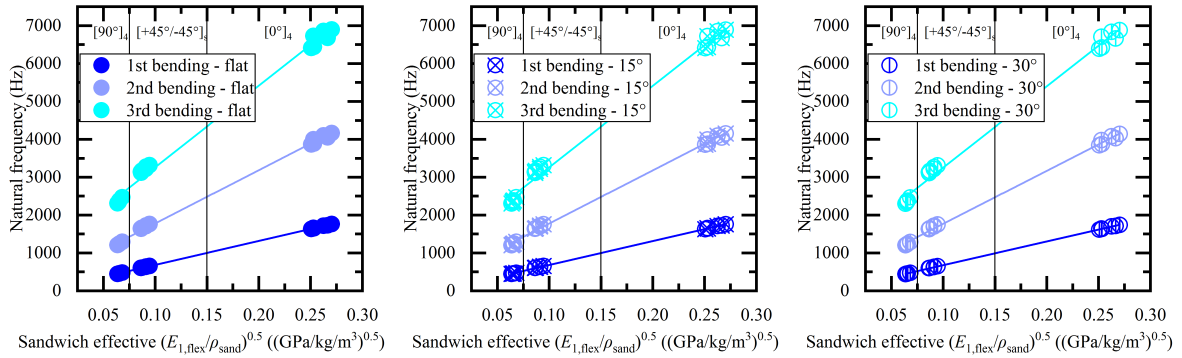
Graphs of the natural frequencies of the bending modes of the curved structures versus the $\sqrt{E_{1,\text{flex}}/\rho_{\text{sand}}}$ are shown in Figure 9.9, and show linear relationships. The values of the gradient m_{f}, which describes the sensitivity of the natural frequency to the change of materials, of the 1st bending mode of the flat, 15°- and 30°-curved sandwich structures using the unmodified resin and $[0°]_4$ facesheets are 6.11×10^3, 6.10×10^3 and 6.05×10^3 Hz/(GPa/kg/m^3)$^{0.5}$, respectively; those of the 2nd bending mode are 12.81×10^3 Hz/(GPa/kg/m^3)$^{0.5}$ for the flat and 15°-curved structures and 12.75×10^3 Hz/(GPa/kg/m^3)$^{0.5}$ for the 30°-curved structure. Therefore, the 2nd bending mode is more sensitive to material change than the 1st bending mode. Moreover, increasing the curvature decreases m_{f}, which indicates increasing the curvature makes the natural frequencies of the bending modes less sensitive to material changes. This is because increasing the curvature reduces the bending stiffness and hence reduces the natural frequencies of bending modes, see Section 9.4, which makes the natural frequencies of the bending modes of the curved structures less sensitive to material change. On the other hand, by combining the data for all the three types of facesheet stacking, it is noted that the plots still show the same

linearity for the same mode of the flat or curved structures, see Figure 9.10. This indicates that the natural frequencies of bending modes are proportional to the square root of the structure's flexural modulus ($E_{1,\text{flex}}$), which corresponds to the principles of vibration mechanics of beams [153].



(a) 1st bending **(b)** 2nd bending

Figure 9.9: Influence of material change on the natural frequencies of bending modes of intact, flat or curved structures, $[0°]_4$ facesheets (simulation results)



(a) Flat structures **(b)** 15°-curved structures **(c)** 30°-curved structures

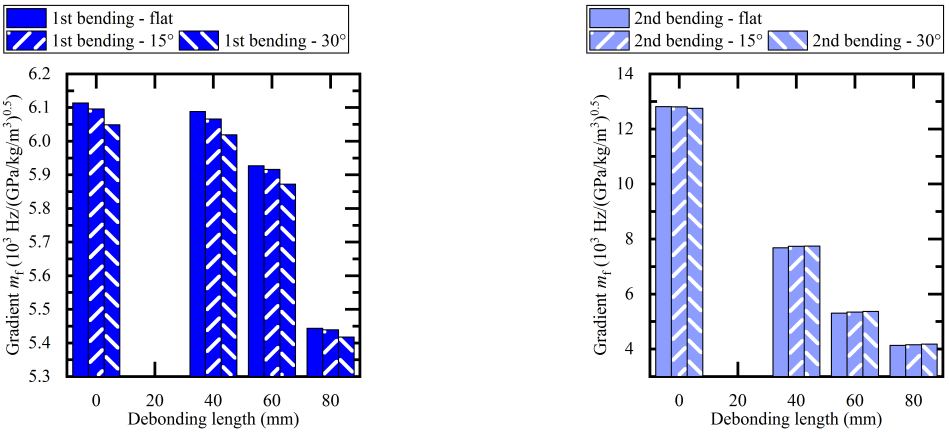
Figure 9.10: Influence of material change on the natural frequencies of bending modes of intact, flat or curved structures, all facesheets (simulation results)

9.8.1 Effects of Material Change on the Single-debonded Curved Sandwich Structures

According to Figure 9.11, increasing the debonding length reduces the gradient m_f, which indicates that the natural frequencies become less sensitive to material change. For example, the m_f values of the 1st bending mode of the flat and 30°-curved structures drop from 6.11 $\times$ 10^3 and 6.05 $\times$ 10^3 Hz/(GPa/kg/m^3)$^{0.5}$ to 5.44 $\times$ 10^3 and 5.42 $\times$ 10^3 Hz/(GPa/kg/m^3)$^{0.5}$,

respectively; the m_f values of the 2nd bending mode of the same structures decrease from 12.81 $\times$ 10^3 and 12.75 $\times$ 10^3 Hz/(GPa/kg/m^3)$^{0.5}$ to 4.14 $\times$ 10^3 and 4.18 $\times$ 10^3 Hz/(GPa/kg/m^3)$^{0.5}$, respectively.

It is noted that the trend of m_f affected by the curvature is the same as that of the natural frequencies of the same mode, for example, for the 1st bending mode (see Figures 9.4a and 9.11a) increasing the curvature reduces the natural frequencies and the m_f of the structures with a debonded region of 80 mm; while for the 2nd bending mode (see Figures 9.4d and 9.11b), increasing the curvature of the 80-mm-debonded structures increases the natural frequencies and the m_f.



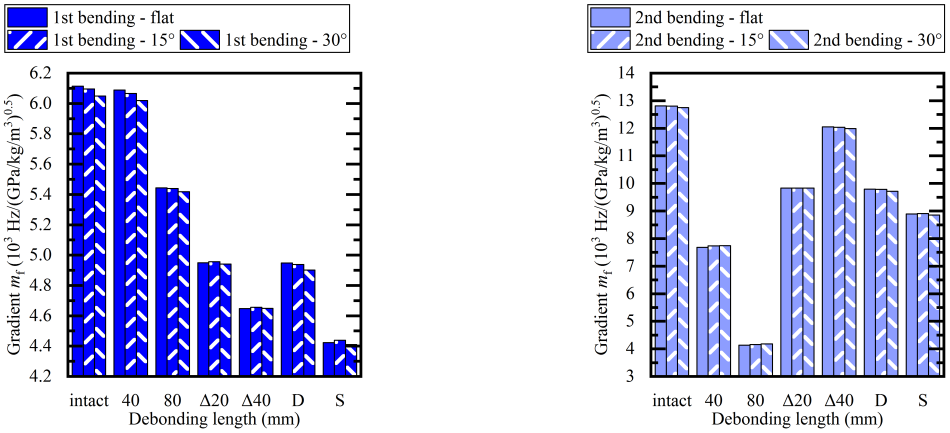
(a) 1st bending **(b)** 2nd bending

Figure 9.11: Gradient m_f of single-debonded, flat or curved structures, $[0°]_4$ facesheets (simulation results)

9.8.2 Effects of Material Change on the Double-debonded Curved Sandwich Structures

The m_f of the double-debonded, flat and curved sandwich structures are shown in Figure 9.12. Like the single debonding case, the trends of the m_f affected by the curvature are the same as the natural frequencies, see Figures 9.6a and 9.6d.

Increasing the separation between the two debonded regions (Δ0 (80 mm), Δ20, and Δ40, see Figure 9.12) reduces the m_f of the 1st bending mode while it increases that of the 2nd bending mode. The reason for the different trends is the relative locations of the vibration nodes and the debonded regions, see Section 9.7.1. For the sandwich structures with two debonded regions of configuration Δ20, D and S (see Figure 9.12), the m_f values are close for the 1st and 2nd bending modes of Δ20 and D, this results from the close natural frequencies of the two configurations. For condition S, the values of m_f drop more than for conditions Δ20 and D, this is because of the greater reduction in the stiffness and natural frequencies caused by



(a) 1st bending **(b)** 2nd bending

Figure 9.12: Gradient m_f of double-debonded, flat or curved structures, $[0°]_4$ facesheets (simulation results)

the debonding configuration, which significantly reduces the effects of material change on the natural frequencies and hence decreases the m_f values.

9.9 Conclusions

In this chapter, the differences between the experimental and simulation results of the natural frequencies of the curved structures have been discussed. The effects of curvature, debonding length, locations of debonded regions, facesheet stacking orientations and material changes on the natural frequencies of the sandwich structures have also been presented and discussed. Generally, the results of the curved structures show the same trends as the flat structures when the structures are affected by the same factors, e.g. the same debonding length or configuration of debonded regions. The curvature has more effect on the lateral modes than the bending and torsion modes because the mode shapes of the lateral vibration contain torsional movement. However, since the curved structures in this study are not highly curved, the effects of curvature are not as large as the other factors.

Chapter 10

Discussion

10.1 Introduction

In this chapter, brief discussions are presented concerning: 1. The effects of SNP-modified sizings on the fracture and fatigue behaviours of the carbon fibre composites. 2. The effects of debonded regions on the vibration behaviours of sandwich structures with different configurations, and the application of the vibration behaviours in non-destructive testing.

10.2 Fracture and Fatigue Behaviours of Carbon Fibre Composites with Silica Nanoparticle Modified Sizings

Fibre composites are widely used in aerospace and transport applications because of their light weight and high mechanical strength and stiffness, however, the brittleness of thermoset polymers used as the matrices can limit their applications. Research has shown that adding silica nanoparticles to the matrices can improve the toughness of fibre composites [13, 21–26], however, this requires significant additions of SNPs, which can be up to 20 wt% of the matrices and increase the cost of materials and manufacturing [25]. In this research, instead of modifying the matrices, the sizings of the carbon fibres were modified using SNPs, allowing much lower volumes of SNPs to be used. Two sizing agents for carbon fibres have been modified by the addition of SNPs at two concentrations. Mode I interlaminar fracture tests and fatigue crack growth (FCG) tests have been conducted on the composites made using the sizing-modified fibres.

Although the modified sizings had no significant effect on the fatigue behaviour, they improved the mode I fracture energy of the composites. Maximum improvements of 101% in the fracture energy for crack initiation and 33% for crack propagation have been found when the sizing agent composed of 1.78 wt% HS-1 and 2.22 wt% Nanopox FW 404 (sizing H2) was used. The level of improvement for the modified sizings is the same compared with the literature where SNPs were added to the matrices, while the modified sizings use significantly fewer SNPs. On the other hand, with the higher addition level of SNPs to the sizings, the magnitudes of the R-curves, which reflect the material's resistance to crack growth, are smaller, which indicates a more stable crack propagation.

The gradient of the relationship between crack propagation rate per cycle and strain energy release rate in fatigue, m_G or m_K, reflects the sensitivity of the crack growth rate to the change of cyclic load. Although in this work no significant change of the gradient was found, the gradients of the sizing-modified and -unmodified carbon fibre composites are generally larger than those of metals, which indicates that the fibre composites are more sensitive to fatigue crack growth than metals.

The toughening mechanisms of the SNPs on the composites have also been investigated using scanning electron microscopy. When the concentration of SNPs is higher, the particles were dispersed better across the fibre surfaces, which resulted in better adhesion between the fibres and the matrix epoxy. A better adhesion contributes to more fragmentation of the fibres and more energy absorption. Therefore, the toughness can be improved. It is also noted that good adhesion contributes to the reduction of the magnitudes of the R-curves. However, if the adhesion is improved too much, few fibres pull out and less fibres break, which leads to the reverse effect where the fracture energy decreases.

Directly modifying fibre sizings with silica nanoparticles has great potential for the application of fibre composites, especially for situations where high toughness is required, since it can improve the fracture energies more efficiently than directly adding modifiers into matrices. The same level of improvement can be achieved by using significantly fewer silica nanoparticles, which can reduce the manufacturing costs of fibre composite products.

10.3 Vibration Behaviours of Sandwich Structures with Debonded Regions

Sandwich structures are used in many applications in the aerospace and marine industries, however, delamination due to manufacturing defects or in-service damage can reduce the stiffness and strength of the structures, which reduces safety and affects the vibration behaviours of the structures. This research has discussed the effects of face/core debonding, curvature, facesheet stacking orientation, materials (by the addition of modifiers) and multi face/core

debonding by finite element simulation and impact hammer tests. Epoxy polymers modified with SNPs or graphene were used as the core of the sandwich structures; carbon fibre reinforced polymers (CFRPs) infused with the same resin formulation as the core were used as the facesheets.

Comparing the experimental and simulations results, although a few larger differences were noted due to experimental errors or simulation factors, the differences between the simulation and experimental results were generally less than 10 %, which showed a good agreement. The differences may result from experimental errors and simulation factors. Fewer replicates were tested for treatment groups which can further increase the differences.

For a sandwich structure with a debond, the natural frequencies decrease more significantly when the central debonded region is longer, this is because a longer debonded region decreases the stiffness of the structure more. Since natural frequencies are positively correlated to the stiffness of the structure, the larger reduction in the stiffness results in a greater reduction in the natural frequencies. A frequency reduction of 57 % was found in the 2nd bending mode of the flat sandwich structure using the unmodified resin and $[0°]_4$ facesheets.

The natural frequencies of the different modes have different sensitivities to debonded regions: for the flat structures, the lateral mode is less sensitive to a horizontal delamination. This is because the debonded regions are in the horizontal direction, which decreases the stiffness in the lateral direction less significantly and hence the natural frequencies of the lateral modes only show a small reduction. It is also noted that the sequence of different modes can be changed due to the presence of the debonded region.

The facesheet stacking orientation makes the sandwich structures have a different reaction to debonded regions. For the structure using $[0°]_4$ facesheets, the reduction of natural frequencies of bending modes is more significant than for the other two types of stacking; while for $[90°]_4$ facesheets, that of the same modes decreases the least. For $[+45°/\text{-}45°]_s$ facesheets, the reduction in the natural frequencies of torsion modes is more significant. This reason is the anisotropy of the sandwich structures which results from the anisotropic CFRP. The $[0°]_4$ facesheets contribute to the highest flexural stiffness of the sandwich structures, however, the stiffness also decreases most when there is a debonded region, which results in the greatest reduction in the natural frequencies of bending modes. The $[90°]_4$ facesheets make the sandwich structures have the lowest flexural stiffness and hence the natural frequencies of bending modes, which are affected by the debonded region, decrease the least. For $[+45°/\text{-}45°]_s$ facesheets, although they contribute to the highest torsional stiffness, the stiffness also decreases the most when there is a debonded region. Therefore the natural frequencies of torsion modes also decrease the most when $[+45°/\text{-}45°]_s$ facesheets are used.

For bending modes, the natural frequencies are positively linearly correlated to the structure's parameter $\sqrt{E_{1,\text{flex}}/\rho_{\text{sand}}}$, where $E_{1,\text{flex}}$ is the flexural modulus and ρ_{sand} is the effective

density of the sandwich structures using different modifiers. The gradient, m_f, of the linearity reflects the structure's sensitivity to the change of materials. The m_f value of the 1st bending mode of the flat, intact structure with $[0°]_4$ facesheets is 6.11×10^3 Hz/(GPa/kg/m^3)$^{0.5}$ and for the 2nd bending mode it is 12.81×10^3 Hz/(GPa/kg/m^3)$^{0.5}$, which means that when the material is changed, the natural frequency of the 2nd bending mode of this structure will differ more than that of the 1st bending mode.

It is noted that the gradient reduces more when there is a longer debonded region, which indicates that a longer-debonded structure is less sensitive to material change. Besides, using different facesheets stacking orientations results in the same linearity for the same mode of the intact structures, this is because the geometries of the structures are the same.

For multi debonding, the greatest reduction of natural frequencies of bending modes is found for the structures using the $[0°]_4$ facesheets since the flexural stiffness decreases the most due to the debonded regions. Increasing the distance between two horizontally-arranged 40-mm debonded regions does not confirm the reduction or increase of natural frequencies, it depends on the locations of the debonded regions and vibration nodes. On the other hand, comparing two debonded regions with 20 mm horizontal separation (Δ20), diagonal (D) and symmetric (S) arrangements, the natural frequencies of condition Δ20 and D are very close at lower modes, therefore it is difficult to distinguish these two debonding conditions in real applications only by measuring the resonant frequencies. However, for bending modes, condition S (debonded regions being located at the same place) shows a greater reduction than conditions Δ20 and D, this is because the debonded regions located at the same location for both upper and lower facesheets reduce the stiffness of the structure more significantly.

If the debonded regions overlap the vibration nodes, relative movement of the facesheet and the core is allowed since they are not bonded together, which results in a greater reduction in the stiffness and hence a larger frequency decrease is found. This effect is found in the 1st bending mode when increasing the separation between the two 40-mm debonded regions (Δ0 (80 mm) to Δ40), which results in overlapping of the debonded regions and the vibration nodes, and in the 1st and 2nd bending modes of the S-debonded structures for which the debonded regions also overlap the vibration nodes. While if the debonded regions do not overlap the nodes, the reduction in the natural frequency is smaller, which is found in the 2nd bending mode when increasing the separation between the two 40-mm debonded regions, which results in no node being overlapped by the debonded regions so the frequency reduction becomes less.

The curvature of the structures also affects the vibration behaviours. The curved structures (15°- and 30°-curved) used in this work are relatively flat comparing to the curved structure whose ratio of curvature radius to thickness is less than 5, which corresponds to the structure having a curvature angle of 266° if keeping the mid-plane arc length and the thickness the same. According to the mechanics of materials [154], when the ratio is less than five, the difference

between the stresses calculated from the flexure formula and from the curved-beam formula is grater than 7%, therefore the curved beam cannot be considered as a flat beam.

Increasing the curvature of the intact structures decreases the natural frequencies of the bending/torsion modes since the bending/torsional stiffness decreases. The bending and torsion modes of the curved structures are independent of each other. However, for the lateral modes, the lateral mode shapes are combined with torsional movement, therefore the stiffness increases and hence results in the increase of the natural frequencies of the torsion-lateral modes. Combining with the torsional movement makes the natural frequencies of the torsion-lateral modes more sensitive to the debonded regions, since the torsional stiffness decreases when the length of the debonded region increases.

Since the 15°- and 30°-curved structures can still be considered relatively flat, the relationship $\sqrt{E_{1,\text{flex}}/\rho_{\text{sand}}}$ used for the flat structures can also be applied to these curved structures. The m_{f} values of the structure decrease when increasing the curvature, which means that the natural frequencies of the bending modes of the curved structures are less affected by material change.

Generally, the curvature angle of 15° and 30° has more significant effect on the lateral modes of the sandwich structures but less effect on the bending and torsion modes. The effects of the curvature angles are also small compared to the other controlled factors, i.e. debonding length, facesheet stacking orientation, separation and positions of the debonds.

In conclusion, a longer debonded region causes the natural frequencies of sandwich structures to decrease more significantly, by almost 60% in some cases. Other factors such as curvature, facesheet stacking, materials, mode shapes and locations of debonded regions also have different degrees of influence on the vibration behaviours (including natural frequencies, mode shapes and node positions) of sandwich structures. Besides, the natural frequencies of less stiff structures are less sensitive to the debonded regions, i.e. they reduce less significantly compared to the stiff structures.

Since the vibration response of the sandwich structures are affected by debonds due to the reduction in the stiffness, measuring the vibration response of the damaged structures can be used for non-destructive testing (NDT). By measuring the vibration response and then compared to the results of simulation and intact structures, the debonding conditions can be identified. Compared to ultrasonic inspection, measuring the vibration response has the advantages that the tested targets do not need to be good conductors of sound, and that accessible surfaces of the targets are not necessary (if non-contact devices are used).

Based on this study, generally the 2nd bending mode of the flat sandwich structures is more sensitive to horizontal debonded regions, i.e. the natural frequency decreases more significantly; while the lateral modes are more sensitive to the change of curvature since the mode shapes are coupled with torsional movement due to the asymmetric shapes. Therefore, measuring the vibration responses of these modes and comparing with those of the flat, intact structures have

the ability to identify whether there are debonded regions in the structures and whether the structures have been curved due to the loading in service.

10.4 Conclusions

Brief discussions of the two studied topics have been made in this chapter, the conclusions and suggested future works are presented in the next chapter.

Chapter 11

Conclusions and Future Work

11.1 Introduction

Composite materials and sandwich structures have been widely adopted because of their light weight and high mechanical strength. Adhesion is a critical issue for the application of these composite materials and structures since it can significantly affect their safety. Due to manufacturing defects or in-service damage, delamination can occur in composites, and cracks may propagate due to fatigue loading. Similarly, debonding may occur between the facesheets and the core of sandwich structures. These debonded regions reduce the strength and the stiffness of the structure and also influence its response to vibration, for example enabling damaging resonance to occur in service. Vibration may cause debonded regions to grow, weakening the structure further. To address these problems, in the presented work, two main topics have been discussed:

1. The fracture and fatigue behaviours of carbon fibre composites with the fibre sizings modified using silica nanoparticles (SNPs).
2. The effects of debonded regions on the vibration behaviours of flat and curved composite sandwich structures.

Mode I interlaminar fracture tests and fatigue crack growth (FCG) tests were conducted on the carbon fibre composites using the SNP-modified sizings. On the other hand, hammer impact tests and finite element (FE) simulations were conducted on the flat and curved sandwich structures to analyse their vibration behaviours. This chapter brings together the conclusions of the results and discussions of the two topics.

11.2 Fracture and Fatigue Behaviours of Carbon Fibre Composites with Silica Nanoparticle Modified Sizings

Thermoset polymers used as the matrices of fibre composites can limit the applications since they are brittle. This research used silica nanoparticles (SNPs) to modifying the sizings of carbon fibres to improve the fracture and fatigue behaviours. Mode I interlaminar fracture tests and fatigue crack growth (FCG) tests were conducted on the carbon fibre composites using the sizing-modified fibres.

By modifying sizings using SNPs, the mode I fracture energy of the composites were improved, the fracture energies at crack initiation and propagation have been improved by 101 % and 33 %, respectively, by using the sizing agent composed of 1.78 wt% HS-1 and 2.22 wt% Nanopox FW 404 (sizing H2), which contained 0.89 wt% of SNPs (on fibre mass). This is more efficient than directly adding SNPs into matrices to improve the toughness. The magnitudes of the R-curves have also decreased, which indicates a more stable crack propagation. The toughening mechanisms are that higher concentration of SNPs resulted in a better dispersion of the particles across the fibre surfaces and hence the adhesion between the fibres and the matrix was improved, which contributed to more fibre fragmentation. More fibre fragmentation indicates that more energy was absorbed for fibre breaking during crack growth, therefore the toughness was improved. However, few fibres pull out and less fibres break if the adhesion is improved too much, which leads to the reverse effect where the fracture energy decreases.

For for fatigue behaviour, in this work no significant change of the gradient of the FCG curves has been found. However, the gradients of the studied carbon fibre composites are generally larger than those of metals, which indicates that the fibre composites are more sensitive to fatigue crack growth than metals.

11.3 Vibration Behaviours of Sandwich Structures with Debonded Regions

Delamination in sandwich structures can reduce the stiffness and strength, which affects the vibration behaviours of the structures. This research has discussed the effects of face/core debonding and other factors on the vibration behaviours of sandwich strictures by conducting finite element simulation and impact hammer tests.

For a sandwich structure with a debond, the natural frequencies decrease more significantly when the central debonded region is longer due to the greater reduction in the stiffness. A frequency reduction of 57 % was found in the 2nd bending mode of the flat sandwich structure using the unmodified resin and $[0^\circ]_4$ facesheets. Besides, the natural frequencies of different

modes have different sensitivities to debonded regions: for the flat structures, the lateral mode is less sensitive to a horizontal delamination.

The reduction in natural frequencies of bending/torsion modes is more significant for the structure using $[0°]_4/[+45°/-45°]_s$ facesheet. Highest flexural/torsional stiffness of the sandwich structures, which can be contributed to the anisotropy of facesheet CFRPs, makes they have the highest bending/torsion natural frequencies. However, the stiffness also decreases the most when there is a debonded region, which results in the greatest reduction in the natural frequencies of the corresponding modes.

For bending modes, the gradient, m_f, reduces more when there is a longer debonded region, which indicates that a longer-debonded structure is less sensitive to material change.

For multi debonding, condition S (debonded regions being located at the same place) shows a greater reduction in the natural frequencies of bending modes, this is because the debonded regions located at the same location for both upper and lower facesheets reduce the stiffness of the structure more significantly. It is also noted that relative movement of the facesheet and the core is allowed if the debonded regions overlap the vibration nodes, since they are not bonded together, which results in a greater reduction in the stiffness and natural frequencies.

Increasing the curvature of the intact structures decreases the natural frequencies of the bending/torsion modes since the bending/torsional stiffness decreases, while the two types of modes are independent of each other. For the lateral modes, the lateral mode shapes are coupled with torsional movement, therefore the stiffness and the natural frequencies increase. Combining with the torsional movement also makes the torsion-lateral modes more sensitive to the debonded regions, since the torsional stiffness decreases when the length of the debonded region increases. Generally, the curvature angle of 15° and 30° has more significant effects on the lateral (torsion-lateral) modes of the curved sandwich structures but less effects on the bending and torsion modes.

In conclusion, natural frequencies of sandwich structures decrease more significantly when there is a longer debonded region, by almost 60% in some cases. Other factors such as curvature, facesheet stacking, materials, mode shapes and locations of debonded regions also have different degrees of influence on the vibration behaviours of sandwich structures.

11.4 Future Work

The present work has discussed: 1. Improving the toughness of carbon fibre composites using SNP-modified sizings, 2. Vibration behaviours of sandwich structures affected by debonded regions. Through the projects, some potential areas that may be worth further study have been noted and are briefly presented in this section.

11.4.1 Improving the Toughness of Fibre Composites Using Modified Sizings

In the present work, sizing-modified carbon fibres were used and the tested laminates were in a UD stacking orientation of 0°. In real applications, laminates of different stacking orientations are also used since the manufactured parts may need high mechanical properties such as stiffness and strength not only in one direction but also in other directions. Besides, when toughening fibre composites using particle-modified matrices, UD and quasi-isotropic laminates showed a different degree of toughening [13]. Therefore, using the SNP-modified sizings to toughen laminates of different stacking such as [0°/90°], [+45°/-45°] or quasi-isotropic stacking would be worthy of study.

Modifying the matrix of fibre composites using SNPs together with reactive liquid rubbers has been reported to give a more significant toughening effect [13, 21]. Therefore, using such a hybrid of particles to modify fibre sizings has the potential to improve further the toughness of fibre composites. Also, combining particle-modified sizings and particle-modified matrices of the composites may also result in a further improvement of the toughness since the toughening mechanisms of bulk polymers are also found in the resin-rich regions in the fibre composites [13].

Beside carbon fibre, modifying the sizings of other fibres such as glass, Kevlar or cellulose fibre is worthy of further work as adhesion between these fibres and matrices are also important. Chemical treatment has been used to improve the adhesion between the polymer matrix and Kevlar [155] or cellulose [156] fibres. Selvarayan et al. [14] studied on the fracture and fatigue behaviours of glass fibres with SNP-modified sizings and reported the improvement of the toughness and fatigue performance.

In this work, mode I (opening) interlaminar fracture tests and FCG tests were conducted. In real applications, composite structures may experience not only opening fracture but also other modes of fracture. Therefore, mode II (shear), mode III (tearing) and mixed mode (I/II) are worthy of further tests to establish a systematic discussion.

11.4.2 Vibration Behaviours of Debonded Sandwich Structures

In this work, the sandwich structures used have different curvatures (flat, 15° and 30°), debond configurations (single debond of different lengths and double debonds at different locations), material formulations and facesheet stacking orientations ($[0°]_4$, $[90°]_4$ and $[+45°/-45°]_s$). Possible future research areas are briefly stated in this section.

It is noted that when debonded regions overlap the vibration nodes, the natural frequencies decrease more significantly. Therefore, different configurations of lengths and locations of debonded regions, which overlap the nodes or not, may be interesting for future work. For the

curved structures in this work, the single debond and debonds of condition $\Delta 20$ and $\Delta 40$ are between the top facesheet and the core, having these debonds between the base facesheet and the core can also have different results [98, 157], which can be further discussed.

Facesheet stacking orientations also have significant effects on the vibration behaviours of the sandwich structures and on the sensitivities of the natural frequencies of different modes to the debonded regions. The orientations of facesheet stacking in this work are all symmetric, asymmetric fibre stacking orientations can be an area to discuss as they can be used in aircraft fuselages [158, 159]. On the other hand, asymmetric sandwich stacking, i.e. where the top and base facesheets of the sandwich structures have different stacking orientations, can also be studied.

The shapes of sandwich structures also affect their vibration behaviours. In this work, the 15°- and 30°-curved structures can still be considered flat according to the mechanics of materials. Very curved structures, i.e. having a ratio of curvature radius to thickness of less than 5, can be worthy of future research. Besides a rectangular cross section, shapes like real structures such as wind turbine blade are also interesting for further works to study the conditions of real applications.

The boundary conditions used in this work are free-free, which means that the sandwich structures are not constrained. However, in real applications, a structure may have the boundary conditions such as a cantilever beam (clamped-free) or clamped-clamped conditions. Therefore, studying on different boundary conditions of the sandwich structures to reflect the situations of real applications is also important.

References

[1] C. Augustsson. *NM Epoxy Handbook*. Nils Malmgren AB, Ytterby, Sweden, 2004.

[2] D.J. Bray, P. Dittanet, F.J. Guild, A.J. Kinloch, K. Masania, R.A. Pearson, and A.C. Taylor. The modelling of the toughening of epoxy polymers via silica nanoparticles: The effects of volume fraction and particle size. *Polymer*, 54(26):7022–7032, 2013.

[3] T. Khaleque. *Modelling and Experimental Study of Toughening Mechanisms of Core-shell Rubber Particle- and Nanosilica Particle-modified Epoxy Polymers*. PhD thesis, Imperial College London, London, UK, 2018.

[4] Y Huang and A.J. Kinloch. Modelling of the toughening mechanisms in rubber-modified epoxy polymers, part II, a quantitative description of the microstructure-fracture property relationships. *Journal of Materials Science*, 27(10):2763–2769, 1992.

[5] A.J. Kinloch, D.L. Maxwell, and R.J. Young. The fracture of hybrid-particulate composites. *Journal of Materials Science*, 20(11):4169–4184, 1985.

[6] N. Amdouni, H. Sautereau, J.F. Gerard, F. Fernagut, G. Coulon, and J.M. Lefebvre. Coated glass beads epoxy composites: influence of the interlayer thickness on pre-yielding and fracture properties. *Journal of Materials Science*, 25(2):1435–1443, 1990.

[7] B.B. Johnsen, A.J. Kinloch, R.D. Mohammed, A.C. Taylor, and S. Sprenger. Toughening mechanisms of nanoparticle-modified epoxy polymers. *Polymer*, 48(2):530–541, 2007.

[8] H.M. Chong. *Toughening Mechanisms of Block Copolymer and Graphene Nanoplatelet Modified Epoxy Polymers*. PhD thesis, Imperial College London, London, UK, 2015.

[9] T. Kawaguchi and R.A. Pearson. The effect of particle-matrix adhesion on the mechanical behavior of glass filled epoxies. Part 2. A study on fracture toughness. *Polymer*, 44(15):4239–4247, 2003.

[10] D. Hull and T.W. Clyne. *An Introduction to Composite Materials, Second Edition*. Cambridge Solid State Science Series. Cambridge University Press, Cambridge, 1996.

[11] S. Awang Ngah. *Static and Fatigue Behaviour of Fibre Composites Infused with Rubber- and Silica Nanoparticle-modified Epoxy*. PhD thesis, Imperial College London, London, UK, 2013.

[12] D.L. Hunston, R.J. Moulton, N.J. Johnston, and W.D. Bascom. Matrix Resin Effects in Composite Delamination: Mode I Fracture Aspects. In *Toughened Composites*, pages 74–94. ASTM International, West Conshohocken, USA, 1987.

[13] T.H. Hsieh, A.J. Kinloch, K. Masania, J. Sohn Lee, A.C. Taylor, and S. Sprenger. The toughness of epoxy polymers and fibre composites modified with rubber microparticles and silica nanoparticles. *Journal of Materials Science*, 45(5):1193–1210, 2010.

[14] S.K. Selvarayan, S. Schindler, S. Küppers, and S. Sprenger. Improving fracture toughness and fatigue performance of GFRP using nanosilica in fibre sizing. In *Proceedings of SAMPE Europe Conference 2017*, Stuttgart, Germany, 2017.

[15] H.Y. Kim and W. Hwang. Effect of debonding on natural frequencies and frequency response functions of honeycomb sandwich beams. *Composite Structures*, 55(1):51–62, 2002.

[16] BS ISO 15024. Fibre-reinforced plastic composites - Determination of mode I interlaminar fracture toughness, G_{IC}, for unidirectionally reinforced materials. British Standards Institute, London, UK, 2001.

[17] S. Nikbakt, S. Kamarian, and M. Shakeri. A review on optimization of composite structures Part I: Laminated composites. *Composite Structures*, 195:158–185, 2018.

[18] A.S. Sayyad and Y.M. Ghugal. Bending, buckling and free vibration of laminated composite and sandwich beams: A critical review of literature. *Composite Structures*, 171:486–504, 2017.

[19] S.S. Yao, F.L. Jin, K.Y. Rhee, D. Hui, and S.J. Park. Recent advances in carbon-fiber-reinforced thermoplastic composites: A review. *Composites Part B: Engineering*, 142:241–250, 2018.

[20] V. Birman and G.A. Kardomateas. Review of current trends in research and applications of sandwich structures. *Composites Part B: Engineering*, 142:221–240, 2018.

[21] A.J. Kinloch, R.D. Mohammed, A.C. Taylor, S. Sprenger, and D. Egan. The interlaminar toughness of carbon-fibre reinforced plastic composites using hybrid-toughened matrices. *Journal of Materials Science*, 41(15):5043–5046, 2006.

[22] S. Awang Ngah and A.C. Taylor. Toughening performance of glass fibre composites with core-shell rubber and silica nanoparticle modified matrices. *Composites Part A: Applied Science and Manufacturing*, 80:292–303, 2016.

[23] C.M. Manjunatha, A.C. Taylor, A.J. Kinloch, and S. Sprenger. The tensile fatigue behaviour of a silica nanoparticle-modified glass fibre reinforced epoxy composite. *Composites Science and Technology*, 70(1):193–199, 2010.

[24] S.Q. Deng, P. Rosso, L. Ye, and K. Friedrich. Interlaminar fracture of CF/EP composites modified with nano-silica. *Solid State Phenomena*, 121-123:1403–1406, 2007.

[25] Y. Tang, L. Ye, D. Zhang, and S. Deng. Characterization of transverse tensile, interlaminar shear and interlaminate fracture in CF/EP laminates with 10 wt% and 20 wt% silica nanoparticles in matrix resins. *Composites Part A: Applied Science and Manufacturing*, 42(12):1943–1950, 2011.

[26] S. Sprenger. Fiber-reinforced composites based on epoxy resins modified with elastomers and surface-modified silica nanoparticles. *Journal of Materials Science*, 49(6):2391–2402, 2014.

[27] T.H. Hsieh. *Dynamic Properties of Composite Beam and Sandwich Structure with MWNTs Re-*

inforcement in Polymer Matrix. Master thesis, National Tsing Hua University, Hsinchu City, Taiwan, 2006.

[28] F. Gojny, M. Wichmann, B. Fiedler, and K. Schulte. Influence of different carbon nanotubes on the mechanical properties of epoxy matrix composites - a comparative study. *Composites Science and Technology*, 65(15-16):2300–2313, 2005.

[29] A. Allaoui, S. Bai, H.M. Cheng, and J.B. Bai. Mechanical and electrical properties of a MWNT/epoxy composite. *Composites Science and Technology*, 62(15):1993–1998, 2002.

[30] T.H. Hsieh, A.J. Kinloch, A.C. Taylor, and S. Sprenger. The effect of silica nanoparticles and carbon nanotubes on the toughness of a thermosetting epoxy polymer. *Journal of Applied Polymer Science*, 119(4):2135–2142, 2011.

[31] H. Im and J. Kim. Thermal conductivity of a graphene oxide-carbon nanotube hybrid/epoxy composite. *Carbon*, 50(15):5429–5440, 2012.

[32] M.K. Yeh and T.H. Hsieh. Bending property of sandwich beams with mwnts/polymer nanocomposites as core materials. *Key Engineering Materials*, 345-346:1265–1268, 2007.

[33] S. Chatterjee, F. Nafezarefi, N. H. Tai, L. Schlagenhauf, F. A. Nesch, and B. T. T. Chu. Size and synergy effects of nanofiller hybrids including graphene nanoplatelets and carbon nanotubes in mechanical properties of epoxy composites. *Carbon*, 50(15):5380–5386, 2012.

[34] M.A. Rafiee, J. Rafiee, Z. Wang, H. Song, Z.Z. Yu, and N. Koratkar. Enhanced mechanical properties of nanocomposites at low graphene content. *ACS Nano*, 3(12):3884–3890, 2009.

[35] J.R. Potts, D.R. Dreyer, C.W. Bielawski, and R.S. Ruoff. Graphene-based polymer nanocomposites. *Polymer*, 52(1):5–25, 2011.

[36] L.C. Tang, Y.J. Wan, D. Yan, Y.B. Pei, L. Zhao, Y.B. Li, L.B. Wu, J.X. Jiang, and G.Q. Lai. The effect of graphene dispersion on the mechanical properties of graphene/epoxy composites. *Carbon*, 60:16–27, 2013.

[37] H.M. Chong and A.C. Taylor. The effect of graphene nanoplatelets on the fracture toughness of epoxy polymers. In *Proceedings of 37th Annual Meeting of the Adhesion Society*, San Diego, USA, 2014. Curran Associates.

[38] K. Masania. *Toughening mechanisms of silica nanoparticle-modified epoxy polymers*. PhD thesis, Imperial College London, London, UK, 2010.

[39] J.G. Williams, B.R.K. Blackman, H. Steininger, and K. Zuo. Toughening by plastic cavitation around cylindrical particles and fibres. *Composites Science and Technology*, 103:119–126, 2014.

[40] T. Gentieu, A. Catapano, J. Jumel, and J. Broughton. Computational modelling of particulate-reinforced materials up to high volume fractions: Linear elastic homogenisation. *Proceedings of the Institution of Mechanical Engineers, Part L: Journal of Materials: Design and Applications*, 233(6):1101–1116, 2019.

[41] D.S. Kim, K. Cho, J.K. Kim, and C.E. Park. Effects of particle size and rubber content on fracture toughness in rubber-modified epoxies. *Polymer Engineering & Science*, 36(6):755–768, 1996.

[42] K.F. Lin and Y.D. Shieh. Core-shell particles designed for toughening the epoxy resins. II. Core-shell-particle-toughened epoxy resins. *Journal of Applied Polymer Science*, 70(12):2313–2322,

1998.

[43] D. Quan and A. Ivankovic. Effect of core-shell rubber (CSR) nano-particles on mechanical properties and fracture toughness of an epoxy polymer. *Polymer*, 66:16–28, 2015.

[44] W. Thitsartarn, X. Fan, Y. Sun, J.C.C. Yeo, D. Yuan, and C. He. Simultaneous enhancement of strength and toughness of epoxy using POSS-rubber core-shell nanoparticles. *Composites Science and Technology*, 118:63–71, 2015.

[45] D.G. Dixon, S.J. Harris, M. Dempster, and P. Nicholls. The effect of PEEK fibres and powder on joints made with a high temperature adhesive. *The Journal of Adhesion*, 65(1-4):131–162, 1998.

[46] A.J. Kinloch and A.C. Taylor. The toughening of cyanate-ester polymers. Part I: Physical modification using particles, fibres and woven-mats. *Journal of Materials Science*, 37(3):433–460, 2002.

[47] R. Griffiths and D.G. Holloway. The fracture energy of some epoxy resin materials. *Journal of Materials Science*, 5(4):302–307, 1970.

[48] L.M. McGrath, R.S. Parnas, S.H. King, J.L. Schroeder, D.A. Fischer, and J.L. Lenhart. Investigation of the thermal, mechanical, and fracture properties of alumina-epoxy composites. *Polymer*, 49(4):999–1014, 2008.

[49] L.J. Broutman and S. Sahu. The effect of interfacial bonding on the toughness of glass filled polymers. *Materials Science and Engineering*, 8(2):98–107, 1971.

[50] J. Spanoudakis and R.J. Young. Crack propagation in a glass particle-filled epoxy resin. *Journal of Materials Science*, 19(2):473–486, 1984.

[51] M.K. Yeh, N.H. Tai, and J.H. Liu. Mechanical behavior of phenolic-based composites reinforced with multi-walled carbon nanotubes. *Carbon*, 44(1):1–9, 2006.

[52] C.B. Bucknall and A.H. Gilbert. Toughening tetrafunctional epoxy resins using polyetherimide. *Polymer*, 30(2):213–217, 1989.

[53] C.B. Bucknall and I.K. Partridge. Phase separation in epoxy resins containing polyethersulphone. *Polymer*, 24(5):639–644, 1983.

[54] A.J. Kinloch, M.L. Yuen, and S.D. Jenkins. Thermoplastic-toughened epoxy polymers. *Journal of Materials Science*, 29(14):3781–3790, 1994.

[55] B.B. Johnsen, A.J. Kinloch, and A.C. Taylor. Toughness of syndiotactic polystyrene/epoxy polymer blends: microstructure and toughening mechanisms. *Polymer*, 46(18):7352–7369, 2005.

[56] A.F. Yee and R.A. Pearson. Toughening mechanisms in elastomer-modified epoxies. *Journal of Materials Science*, 21(7):2462–2474, 1986.

[57] A.J. Kinloch, S.J. Shaw, D.A. Tod, and D.L. Hunston. Deformation and fracture behaviour of a rubber-toughened epoxy: 1. Microstructure and fracture studies. *Polymer*, 24(10):1341–1354, 1983.

[58] F. Wang, L.T. Drzal, Y. Qin, and Z. Huang. Enhancement of fracture toughness, mechanical and thermal properties of rubber/epoxy composites by incorporation of graphene nanoplatelets. *Composites Part A: Applied Science and Manufacturing*, 87:10–22, 2016.

[59] J. Chen and A.C. Taylor. Epoxy modified with triblock copolymers: morphology, mechanical

properties and fracture mechanisms. *Journal of Materials Science*, 47(11):4546–4560, 2012.

[60] A.J. Kinloch, J.H. Lee, A.C. Taylor, S. Sprenger, C. Eger, and D. Egan. Toughening structural adhesives via nano-and micro-phase inclusions. *The Journal of Adhesion*, 79(8-9):867–873, 2003.

[61] J. Chen, A.J. Kinloch, S. Sprenger, and A.C. Taylor. The mechanical properties and toughening mechanisms of an epoxy polymer modified with polysiloxane-based core-shell particles. *Polymer*, 54(16):4276–4289, 2013.

[62] G. Giannakopoulos, K. Masania, and A.C. Taylor. Toughening of epoxy using core-shell particles. *Journal of Materials Science*, 46(2):327–338, 2011.

[63] R.A. Pearson and A.F. Yee. Influence of particle size and particle size distribution on toughening mechanisms in rubber-modified epoxies. *Journal of Materials Science*, 26(14):3828–3844, 1991.

[64] D. Carolan, A. Ivankovic, A.J. Kinloch, S. Sprenger, and A.C. Taylor. Toughening of epoxy-based hybrid nanocomposites. *Polymer*, 97:179–190, 2016.

[65] Y.J. Lim, D. Carolan, and A.C. Taylor. Simultaneously tough and conductive rubber-graphene-epoxy nanocomposites. *Journal of Materials Science*, 51(18):8631–8644, 2016.

[66] S.A. Xu. Miscibility and phase separation of epoxy/rubber blends. In J. Parameswaranpillai, N. Hameed, J. Pionteck, and E.M. Woo, editors, *Handbook of Epoxy Blends*, pages 1–32. Springer International Publishing, Cham, Switzerland, 2016.

[67] S. Kunz-Douglass, P.W.R. Beaumont, and M.F. Ashby. A model for the toughness of epoxy-rubber particulate composites. *Journal of Materials Science*, 15(5):1109–1123, 1980.

[68] Y. Huang and A.J. Kinloch. Modelling of the toughening mechanisms in rubber-modified epoxy polymers, part I, finite element analysis studies. *Journal of Materials Science*, 27(10):2753–2762, 1992.

[69] F.J. Guild and R.J. Young. A predictive model for particulate filled composite materials, part 2, soft particles. *Journal of Materials Science*, 24(7):2454–2460, 1989.

[70] Y. Huang. *Microstructure-property Relationships in Toughened Polymers*. PhD thesis, Imperial College London, London, UK, 1991.

[71] R.C. Batra and Z.G. Wei. Instability strain and shear band spacing in simple tensile/compressive deformations of thermoviscoplastic materials. *International Journal of Impact Engineering*, 34(3):448–463, 2007.

[72] T.H. Hsieh. *Properties and Toughening of Silica Nanoparticle- and Carbon Nanotube Modified Epoxy Polymers.* PhD thesis, Imperial College London, London, UK, 2011.

[73] J. Lee and A.F. Yee. Fracture of glass bead/epoxy composites: on micro-mechanical deformations. *Polymer*, 41(23):8363–8373, 2000.

[74] J. Spanoudakis and R.J. Young. Crack propagation in a glass particle-filled epoxy resin. Part 1, Effect of particle volume fraction and size. *Journal of Materials Science*, 19(2):473–486, 1984.

[75] T. Kawaguchi and R.A. Pearson. The effect of particle-matrix adhesion on the mechanical behavior of glass filled epoxies: Part 1. A study on yield behavior and cohesive strength. *Polymer*, 44(15):4229–4238, 2003.

[76] B. Zhang, R. Asmatulu, S.A. Soltani, L.N. Le, and S.S.A. Kumar. Mechanical and thermal proper-

ties of hierarchical composites enhanced by pristine graphene and graphene oxide nanoinclusions. *Journal of Applied Polymer Science*, 131(19):40826, 2014.

[77] R. Satheesh, G. Narayana Naik, and R. Ganguli. Conservative design optimization of laminated composite structures using genetic algorithms and multiple failure criteria. *Journal of Composite Materials*, 44(3):369–387, 2010.

[78] W.J. Cantwell and J. Morton. The significance of damage and defects and their detection in composite materials: A review. *The Journal of Strain Analysis for Engineering Design*, 27(1):29–42, 1992.

[79] W.J. Cantwell and J. Morton. The impact resistance of composite materials - a review. *Composites*, 22(5):347–362, 1991.

[80] D.L. Hunston. Composite interlaminar fracture: effect of matrix fracture energy. *Journal of Composites, Technology and Research*, 6(4):176–180, 1984.

[81] L. Ye and K. Friedrich. Fibre bridging in double cantilever beam specimens and its effect on mode I interlaminar fracture toughness. *Journal of Materials Science Letters*, 11(22):1537–1539, 1992.

[82] L. Ye and K. Friedrich. Mode I interlaminar fracture of co-mingled yarn based glass/polypropylene composites. *Composites Science and Technology*, 46(2):187–198, 1993.

[83] S. Sprenger. Improved performance of glass and carbon fibre-reinforced composites by using nanosilica in the fibre sizing. In *Proceedings of SAMPE China 2017*, Beijing, China, 2017.

[84] N. Mathew, Z. Jiang, and D. Wei. Analysis of multi-layer sandwich structures by finite element method. *Advanced Science Letters*, 4(8):3243–3248, 2011.

[85] J.A. Zapfe and G.A. Lesieutre. A discrete layer beam finite element for the dynamic analysis of composite sandwich beams with integral damping layers. *Computers & Structures*, 70(6):647–666, 1999.

[86] C.A. Steeves and N.A. Fleck. Material selection in sandwich beam construction. *Scripta Materialia*, 50(10):1335–1339, 2004.

[87] J. Kim and S.R. Swanson. Design of sandwich structures for concentrated loading. *Composite Structures*, 52(3-4):365–373, 2001.

[88] S.J. Huang. An analytical method for calculating the stress and strain in adhesive layers in sandwich beams. *Composite Structures*, 60(1):105–114, 2003.

[89] C.M. Wang, K.K. Ang, L. Yang, and E. Watanabe. Free vibration of skew sandwich plates with laminated facings. *Journal of Sound and Vibration*, 235(2):317–340, 2000.

[90] N.S. Bardell, J.M. Dunsdon, and R.S. Langley. Free vibration analysis of coplanar sandwich panels. *Composite Structures*, 38(1-4):463–475, 1997.

[91] W.X. Yuan and D.J. Dawe. Free vibration of sandwich plates with laminated faces. *International Journal for Numerical Methods in Engineering*, 54(2):195–217, 2002.

[92] M.E. Raville and C.E.S. Ueng. Determination of natural frequencies of vibration of a sandwich plate. *Experimental Mechanics*, 7(11):490–493, 1967.

[93] L.J. Lee and Y.J. Fan. Bending and vibration analysis of composite sandwich plates. *Computers & Structures*, 60(1):103–112, 1996.

[94] H.H. Kanematsu, Y. Hirano, and H. Iyama. Bending and vibration of CFRP-faced rectangular sandwich plates. *Composite Structures*, 10(2):145–163, 1988.

[95] J. Hohe and W. Becker. Assessment of the delamination hazard of the core face sheet bond in structural sandwich panels. *International Journal of Fracture*, 109(4):413–432, 2001.

[96] A.P. Mouritz and R.S. Thomson. Compression, flexure and shear properties of a sandwich composite containing defects. *Composite Structures*, 44(4):263–278, 1999.

[97] P.M. Mujumdar and S. Suryanarayan. Flexural vibrations of beams with delaminations. *Journal of Sound and Vibration*, 125(3):441–461, 1988.

[98] B.O. Baba and S. Thoppul. Experimental evaluation of the vibration behavior of flat and curved sandwich composite beams with face/core debond. *Composite Structures*, 91(1):110–119, 2009.

[99] C.N. Della and D. Shu. Free vibration analysis of composite beams with overlapping delaminations. *European Journal of Mechanics - A/Solids*, 24(3):491–503, 2005.

[100] B.T. Lee, C.T. Sun, and D. Liu. An assessment of damping measurement in the evaluation of integrity of composite beams. *Journal of Reinforced Plastics and Composites*, 6(2):114–125, 1987.

[101] Y.J. Yan, L. Cheng, Z.Y. Wu, and L.H. Yam. Development in vibration-based structural damage detection technique. *Mechanical Systems and Signal Processing*, 21(5):2198–2211, 2007.

[102] D.C. Zimmerman, T. Simmermacher, and M. Kaouk. Structural damage detection using frequency response functions. In *SPIE - The International Society for Optical Engineering*, pages 179–184. SPIE International Society For Optical Engineering, 1995.

[103] H. Baruh and S. Ratan. Damage detection in flexible structures. *Journal of Sound and Vibration*, 166(1):21–30, 1993.

[104] S. Yang, L. Gu, and R.F. Gibson. Nondestructive detection of weak joints in adhesively bonded composite structures. *Composite Structures*, 51(1):63–71, 2001.

[105] A.E. Jensen and F. Irgens. Thickness vibrations of sandwich plates and beams and delamination detection. *Journal of Intelligent Material Systems and Structures*, 10(1):46–55, 1999.

[106] L.H. Tenek, .G. Henneke, and M.D. Gunzburger. Vibration of delaminated composite plates and some applications to non-destructive testing. *Composite Structures*, 23(3):253–262, 1993.

[107] V.N. Burlayenko and T. Sadowski. Nonlinear dynamic analysis of harmonically excited debonded sandwich plates using finite element modelling. *Composite Structures*, 108:354–366, 2014.

[108] V.N. Burlayenko and T. Sadowski. Influence of skin/core debonding on free vibration behavior of foam and honeycomb cored sandwich plates. *International Journal of Non-Linear Mechanics*, 45(10):959–968, 2010.

[109] V.N. Burlayenko and T. Sadowski. Finite element nonlinear dynamic analysis of sandwich plates with partially detached facesheet and core. *Finite Elements in Analysis and Design*, 62:49–64, 2012.

[110] P. Qiao, W. Lestari, M.G. Shah, and J. Wang. Dynamics-based damage detection of composite laminated beams using contact and noncontact measurement systems. *Journal of Composite Materials*, 41(10):1217–1252, 2007.

[111] Jiangsu Hengshen. HENGSHEN Co., Ltd. Available from: https://www.hscarbonfibre.com/cn/. [Accessed: 03-July-2018].

[112] Jiangsu Hengshen. Tan-xian-wei (Carbon fibre). Available from: https://www.hscarbonfibre.com/cn/index.php/products/cfb/. [Accessed: 03-July-2018].

[113] S. Sprenger, Evonik, Geesthact, Germany. Email sent to Ambrose Taylor, Imperial College London, London, UK. June 2017.

[114] Jinling DSM Resins. Neoxil 965 safety datasheet. Jinling DSM Resins, Nanjing, China, 2015.

[115] Evonik. NANOPOX F Products material datasheet. Evonik, Geesthacht, Germany, 2008.

[116] Evonik. NANOPOX F400 material datasheet. Evonik, Geesthacht, Germany, 2014.

[117] Gurit. UT-C300 material datasheet. Gurit, Newport, UK, 2015.

[118] R.F. Gibson. *Principles of Composite Material Mechanics, Second Edition*. CRC Press, Boca Raton, USA, 2007.

[119] Huntsman. Araldite LY556 material datasheet. Huntsman, Everberg, Belgium, 2017.

[120] Evonik. Albidur HE600 material datasheet. Evonik, Geesthacht, Germany, 2008.

[121] XG Sciences. xGnP Grade M graphene material datasheet. XG Sciences, Michigan, USA, 2013.

[122] Huntsman. Araldite 2014-1 material datasheet. Huntsman, Basel, Switzerland, 2007.

[123] A. Ahmed, B. Tavakol, R. Das, R. Joven, P. Roozbehjavan, and B. Minaie. Study of thermal expansion in carbon fiber-reinforced polymer composites. In *SAMPE International Symposium Proceedings*, South Carolina, USA, 2012.

[124] O. Pirgon, G.H. Wostenholm, and B. Yates. Thermal expansion at elevated temperatures iv. carbon-fibre composites. *Journal of Physics D: Applied Physics*, 6(3):309, 1973.

[125] BS EN ISO 527-1. Plastics - Determination of tensile properties - Part 1: General principles. British Standards Institute, London, UK, 2012.

[126] BS EN ISO 527-2. Plastics - Determination of tensile properties - Part 2: Test conditions for moulding and extrusion plastics. British Standards Institute, London, UK, 2012.

[127] iMetrum, Bristol, UK. Quotation sent to Soraia Pimenta, Imperial College London. January 2014.

[128] ASTM D3039-14. Standard Test Method for Tensile Properties of Polymer Matrix Composite Materials. American Society for Testing and Materials, West Conshohocken, USA, 2014.

[129] ASTM D3518-13. Standard Test Method for In-Plane Shear Response of Polymer Matrix Composite Materials by Tensile Test of a $\pm 45^{\circ}$ Laminate. American Society for Testing and Materials, West Conshohocken, USA, 2013.

[130] R.M. Christensen. The numbers of elastic properties and failure parameters for fiber composites. *Journal of Engineering Materials and Technology*, 120(2):110–113, 1998.

[131] ASTM D792-13. Standard Test Methods for Density and Specific Gravity (Relative Density) of Plastics by Displacement. American Society for Testing and Materials, West Conshohocken, USA, 2013.

[132] ASTM D2320-98(2017). Standard Test Method for Density (Relative Density) of Solid Pitch (Pycnometer Method). American Society for Testing and Materials, West Conshohocken, USA, 2017.

[133] F.A. Senese. Online Water Density Calculator. Available from: http://antoine.frostburg.edu/chem/senese/javascript/water-density.html. [Accessed: 23-Aug-2018].

[134] ASTM D5528-13. Standard Test Method for Mode I Interlaminar Fracture Toughness of Unidirectional Fiber-Reinforced Polymer Matrix Composites. American Society for Testing and Materials, West Conshohocken, USA, 2013.

[135] BS ISO 13003. Fibre-reinforced plastics - Determination of fatigue properties under cyclic loading conditions. British Standards Institute, London, UK, 2003.

[136] ASTM E647-15. Standard Test Method for Measurement of Fatigue Crack Growth Rates. American Society for Testing and Materials, West Conshohocken, USA, 2015.

[137] S.H. Lee. *The Fatigue and Fracture Properties of Nano-modified Epoxy Polymers*. PhD thesis, Imperial College London, London, UK, 2013.

[138] D. Carolan. Personal communication, Imperial College London, London, UK. 23 June 2018.

[139] National Institutes of Health, USA. Image J version 1.50i. Available from: https://imagej.nih.gov/ij/. 2016.

[140] PCB Piezotronics. Impact Hammer Model: 086E80. PCB Piezotronics, New York, USA, 2015.

[141] PCB Piezotronics. Accelerometer Model: 352B10_010AC. PCB Piezotronics, New York, USA, 2013.

[142] The MathWorks. MATLAB R2015b version 8.5.0.197613. Available from: https://uk.mathworks.com/products/matlab.html. 2015.

[143] Dassault Systemes. Abaqus 6.14. Available from: https://www.3ds.com/products-services/simulia/products/abaqus/. 2014.

[144] Dassault Systemes. Abaqus 6.14 Analysis User's Guide. Available from: http://abaqus.software.polimi.it/v6.14/books/usb/default.htm. [Accessed: 07-Aug-2018].

[145] F.J. Guild. Personal communication, Imperial College London, London, UK. October to December, 2017.

[146] Dassault Systemes. Solidworks education edition 2015 sp4.0. Available from: https://www.solidworks.com/. 2015.

[147] X. Deng. *Toughening of natural-fibre composites using nano- and microcrystalline cellulose particles*. PhD thesis, Imperial College London, London, UK, 2018.

[148] A.J. Kinloch. *Adhesion and Adhesives: Science and Technology*. Chapman and Hall, London, UK, 1987.

[149] AZoM. Silica - Silicon Dioxide (SiO2). Available from: https://www.azom.com/properties.aspx?ArticleID=1114. [Accessed: 22-Nov-2018].

[150] Performance Composites. Mechanical Properties of Carbon Fibre Composite Materials, Fibre / Epoxy resin (120° Cure). Available from: http://www.performance-composites.com/carbonfibre/mechanicalproperties_2.asp. [Accessed: 12-December-2018].

[151] V.V. Bolotin. *Mechanics of Fatigue*, volume 11 of *Mechanical Engineering*. CRC Press, Boca Raton, USA, 1999.

[152] D. Roylance. Fatigue. MIT OpenCourseWare. Available from: https://ocw.mit.edu/courses/materials-science-and-engineering/3-11-mechanics-of-materials-fall-1999/modules/MIT3_11F99_fatigue.pdf. [Accessed: 11-July-2018].

[153] S.S. Rao. *Mechanical Vibrations, Fifth Edition*. Prentice Hall, Singapore, 2011.

[154] R.C. Hibbeler. *Mechanics of Materials, Tenth Edition in SI units*. Pearson, Harlow, UK, 2018.

[155] J.S. Lin. Effect of surface modification by bromination and metalation on Kevlar fibre-epoxy adhesion. *European Polymer Journal*, 38(1):79–86, 2002.

[156] V.K. Thakur and M.K. Thakur. Processing and characterization of natural cellulose fibers/thermoset polymer composites. *Carbohydrate Polymers*, 109:102–117, 2014.

[157] B.O. Baba. Free vibration analysis of curved sandwich beams with face/core debond using theory and experiment. *Mechanics of Advanced Materials and Structures*, 19(5):350–359, 2012.

[158] B. Castanié, J.J. Barrau, J.P. Jaouen, and S. Rivallant. Combined shear/compression structural testing of asymmetric sandwich structures. *Experimental Mechanics*, 44(5):461–472, 2004.

[159] J.R. Vinson. Sandwich structures. *Applied Mechanics Reviews*, 54(3):201–214, 2001.

Appendix A MATLAB Code

Transferring Vibration Raw Data to Excel File

```
clear
clc

Path = '  '; %Folder path where Excel at
Name = '  '; %Excel name

ExcelPath = [Path, '\', Name, '.xlsx'];

SubFolderTitle = 'ASCII0000'; % no more than 9 points
PointN = 1;

fprintf('\n');

while PointN > 0 %check Point amount
    SubFolderName = [Path, '\', Name, '.trf\', SubFolderTitle, num2str(PointN)];
    if exist(SubFolderName) == 7
        PointN = PointN + 1;
    else
        PointN = PointN - 1;
        break
    end
end

for i = 1:PointN
    MagPhaName = [Path, '\', Name, '.trf\', SubFolderTitle, num2str(i), '\', 'Hxysv0000',
        num2str(i), '.txt']; % no more than 9 points
    CoheName = [Path, '\', Name, '.trf\', SubFolderTitle, num2str(i), '\', 'Cxysv0000',
        num2str(i), '.txt'];% no more than 9 points

    fMagPha = fopen(MagPhaName, 'r');
    fCohe = fopen(CoheName, 'r');

    line_num = 0;
    LineMagPha = '1';
    LineCohe = '1';
```

```
34
35      fprintf('START LOADING Point ');
36          fprintf(num2str(i));
37          fprintf(' Data\n');
38
39      while(ischar(LineMagPha) == 1 && ischar(LineCohe) == 1);
40
41          line_num = line_num + 1;
42
43          LineMagPha = fgetl(fMagPha); % anytime use fgetl to read a line and next time it reads
                next
44          LineCohe = fgetl(fCohe);
45
46          if line_num < 10
47              MagPhaSheet(line_num, i*3-2) = {LineMagPha};
48              CoheSheet(line_num, i*2-1) = {LineCohe};
49          elseif LineMagPha == -1
50              fprintf('LOADING Point ');
51              fprintf(num2str(i));
52              fprintf(' Data End\n\n');
53              pause(0.5);
54              break
55          else
56              MagPhaValue = str2num(LineMagPha);
57              MagPhaSheet{line_num, i*3-2} = MagPhaValue(1);
58              MagPhaSheet{line_num, i*3-1} = MagPhaValue(2);
59              MagPhaSheet{line_num, i*3} = MagPhaValue(3);
60
61              CoheValue = str2num(LineCohe);
62              CoheSheet{line_num, i*2-1} = CoheValue(1);
63              CoheSheet{line_num, i*2} = CoheValue(2);
64
65          end
66
67      end
68
69      fclose('all');
70
71  end
72
73  fprintf('START Writing to Excel file\n');
74  xlswrite(ExcelPath, MagPhaSheet, 'Sheet1');
75  xlswrite(ExcelPath, CoheSheet, 'Coherence');
76  fprintf('Writing to Excel file End\n\n');
77
78  display('PROCESS END');
```

Bending and Torsion Modes: Plotting Frequency Response Figure, Finding Resonance Frequencies and Identifying Mode Shapes

```
clear
clc

Path = '  '; %Folder path where Excel at
Name = '  '; %Excel name
fPath = [Path, '\', Name, '.xlsx']; %Full Excel Path

% Path = input('folder path: ', 's'); %Enter Folder path where
% Name = input('file name: ', 's'); %Enter Excel name
% fPath = [Path, '\', Name, '.xlsx']; %Full Excel Path

DrawFig = -1;
FindPeak = -1;

StartF = '0';
EndF = '0';
StartFreq = 0;
EndFreq = 0;

PicVis = -1;
SavePic = -1;

PeakDist = -1;
ByPoint = -1;

while str2num(StartF) >= str2num(EndF) %input frequency range
    StartF = input('start freq [0/number]: ', 's');
    EndF = input('end freq [number/max]: ', 's');
end

while DrawFig < 0 | DrawFig > 1 %plot or not
    DrawFig = input('do drawing figure? [no:0/yes:1]: ');
end

if DrawFig == 1
        while PicVis < 0 | PicVis > 1
        PicVis = input('Show figure? [no:0/yes:1]: '); %show figures or not while program
            plotting
    end
        while SavePic < 0 | SavePic > 1
        SavePic = input('Save figure? [no:0/yes:1]: '); %save figures or not
    end
else
end

while FindPeak < 0 | FindPeak > 1 %find peaks or not
    FindPeak = input('do finding peak? [no:0/yes:1]: ');
end

if FindPeak == 1
```

```
50
51          while PeakDist <= 0
52          PeakDist = input('Peak Distance: '); %Peak distance
53      end
54
55          while ByPoint <= 0
56          ByPoint = input('By which point (ex 1 or [1 2 3]): '); %by which point's data to
                determine peak
57      end
58
59  else
60  end
61
62  fprintf('\n');
63
64
65  %% load magnitude and phase
66  if DrawFig == 1 | FindPeak == 1 %load data only when we want to plot or find peaks
67      fprintf('START LOADING MAGNITUDE AND PHASE DATA\n');
68
69      [status,sheets] = xlsfinfo(fPath);
70      MagPhaseSheet = sheets{1};
71      FullData = xlsread(fPath,MagPhaseSheet); %load magnitudeand phase
72      ColumnN = size(FullData,2);
73      RowN = size(FullData,1);
74      PointN = ColumnN/3;
75
76      %get start row
77      StartFreq = str2num(StartF);
78      StartRow = 8;
79          if  FullData(StartRow,1) < StartFreq
80          while FullData(StartRow,1) <= StartFreq
81
82           StartRow = StartRow + 1;
83
84          end
85          StartRow = StartRow - 1;
86          StartFreq = FullData(StartRow,1);
87      else
88      end
89
90      %get end row
91      EndRow = RowN;
92      if strcmp(EndF, 'max')
93          EndFreq = FullData(EndRow,1);
94      else
95          EndFreq = str2num(EndF);
96          while FullData(EndRow,1) >= EndFreq
97              EndRow = EndRow - 1;
98          end
99          EndRow = EndRow + 1;
100         EndFreq = FullData(EndRow,1);
101     end
102
103     fprintf('LOAD MAGNITUDE AND PHASE DATA COMPLETED\n\n');
104
```

```
105 else
106 end
107
108
109 %% load coherence data
110
111 if DrawFig == 1 & (any(strcmp(sheets,'Coherence')) | any(strcmp(sheets,'coherence'))) %load
        coherence data only when we want to plot and there are coherence data sheet
112     fprintf('START LOADING COHERENCE DATA\n');
113
114     CoheSheet = sheets{2};
115     CoheFullData = xlsread(fPath,CoheSheet);
116     CoheColumnN = size(CoheFullData,2);
117     CoheRowN = size(CoheFullData,1);
118     CohePointN = CoheColumnN/2;
119
120     CoheStartFreq = str2num(StartF);
121     CoheStartRow = 1;
122         if  CoheFullData(CoheStartRow,1) < CoheStartFreq
123         while CoheFullData(CoheStartRow,1) <= CoheStartFreq
124
125          CoheStartRow = CoheStartRow + 1;
126
127         end
128         CoheStartRow = CoheStartRow - 1;
129         CoheStartFreq = CoheFullData(CoheStartRow,1);
130     else
131     end
132
133     CoheEndRow = CoheRowN;
134     if strcmp(EndF, 'max')
135         CoheEndFreq = CoheFullData(CoheEndRow,1);
136     else
137         CoheEndFreq = str2num(EndF);
138         while CoheFullData(CoheEndRow,1) >= CoheEndFreq
139             CoheEndRow = CoheEndRow - 1;
140         end
141         CoheEndRow = CoheEndRow + 1;
142         CoheEndFreq = CoheFullData(CoheEndRow,1);
143     end
144
145     fprintf('LOAD COHERENCE DATA COMPLETED\n\n');
146
147 else
148 end
149
150
151 %% result folder
152 if SavePic == 1 | FindPeak == 1
153     if exist([Path, '\', 'Result', '\', StartF, '-', EndF, ' Hz']) == 7
154         fprintf('RESULT FOLDER ALREADY EXIST\n\n');
155         ResultPath = [Path, '\', 'Result', '\', StartF, '-', EndF, ' Hz'];
156     else
157         fprintf('RESULT FOLDER DOES NOT EXIST\nCREAT FOLDER\n');
158         mkdir(Path, ['Result', '\', StartF, '-', EndF, ' Hz']);
159         fprintf('CREAT FOLDER COMPLETED\n\n');
```

```
160     end
161 else
162 end
163
164 ResultPath = [Path, '\', 'Result', '\', StartF, '-', EndF, ' Hz'];
165
166
167 %% plot magnitude and phase
168 if DrawFig == 1
169
170     fprintf('START PLOTTING MAGNITUDE AND PHASE\n');
171
172     for i = 1:PointN
173         figMag = figure(i); %Magnitude
174         if PicVis == 0
175             set(figMag, 'Visible', 'off'); %no show while plotting
176         else
177         end
178         plot(FullData(StartRow:EndRow,i*3-2),FullData(StartRow:EndRow,i*3-1));
179 %           plot(FullData(StartRow:EndRow,i*3-2),log(FullData(StartRow:EndRow,i*3-1))); % Y axis
      by log
180         xlabel('Frequency (Hz)'); %X title
181         ylabel('Magnitude (m/s^2/N)'); %Y title
182         title(['Magnitude of Point ', num2str(i)]); %figure title
183         if SavePic == 1
184             if strcmp(StartF, '0') & strcmp(EndF, 'max')
185                 saveas(figMag,fullfile(ResultPath, ['(Full) Magnitude of Point ', num2str(i)])
                        , 'jpg'); %save
186             else
187                 saveas(figMag,fullfile(ResultPath, ['(', StartF, '-', EndF, ' Hz) ', '
                        Magnitude of Point ', num2str(i)]), 'jpg'); %save
188             end
189         else
190         end
191
192         figPhase = figure(100+i); %Phase
193         if PicVis == 0
194             set(figPhase, 'Visible', 'off');
195         else
196         end
197         plot(FullData(StartRow:EndRow,i*3-2),FullData(StartRow:EndRow,i*3));
198         xlabel('Frequency (Hz)');
199         ylabel('Phase');
200         title(['Phase of Point ', num2str(i)]);
201         if SavePic == 1
202             if strcmp(StartF, '0') & strcmp(EndF, 'max')
203                 saveas(figPhase,fullfile(ResultPath, ['(Full) Phase of Point ', num2str(i)]),
                        'jpg');
204             else
205                 saveas(figPhase,fullfile(ResultPath, ['(', StartF, '-', EndF, ' Hz) ', 'Phase
                        of Point ', num2str(i)]), 'jpg');
206             end
207         else
208         end
209     end
210
```

```
211         figAllMag = figure(999);
212         if PicVis == 0
213         set(figAllMag, 'Visible', 'off');
214     else
215     end
216         for k = 1:PointN
217         plot(FullData(StartRow:EndRow,k*3-2),FullData(StartRow:EndRow,k*3-1), 'DisplayName',['
                Point ', num2str(k)]); hold on
218     end
219     hold off;
220         legend('location','EastOutside'); %legend position
221         xlabel('Frequency (Hz)');
222         ylabel('Magnitude (m/s^2/N)');
223         title('Magnitude of all points');
224         if SavePic == 1
225         if strcmp(StartF, '0') & strcmp(EndF, 'max')
226             saveas(figAllMag,fullfile(ResultPath, '(Full) Magnitude of all points'), 'jpg');
227         else
228             saveas(figAllMag,fullfile(ResultPath, ['(', StartF, '-', EndF, ' Hz) ', 'Magnitude
                    of all points']), 'jpg');
229         end
230     else
231     end
232
233         figAllMag = figure(99);
234         if PicVis == 0
235         set(figAllMag, 'Visible', 'off');
236     else
237     end
238     plot(FullData(StartRow:EndRow,1),FullData(StartRow:EndRow,2), 'DisplayName',['Point ',
            num2str(1)]); hold on
239     plot(FullData(StartRow:EndRow,13),FullData(StartRow:EndRow,14), 'DisplayName',['Point ',
            num2str(5)]); hold on
240     plot(FullData(StartRow:EndRow,16),FullData(StartRow:EndRow,17), 'DisplayName',['Point ',
            num2str(6)]); hold on
241     hold off;
242         legend('location','EastOutside'); %legend position
243         xlabel('Frequency (Hz)');
244         ylabel('Magnitude (m/s^2/N)');
245         title('Magnitude of point 1, 5 & 6');
246         if SavePic == 1
247         if strcmp(StartF, '0') & strcmp(EndF, 'max')
248             saveas(figAllMag,fullfile(ResultPath, '(Full) Magnitude of point 1, 5 & 6'), 'jpg'
                );
249         else
250             saveas(figAllMag,fullfile(ResultPath, ['(', StartF, '-', EndF, ' Hz) ', 'Magnitude
                    of point 1, 5 & 6']), 'jpg');
251         end
252     else
253     end
254
255         fprintf('PLOT MAGNITUDE AND PHASE COMPLETED\n\n');
256
257 else
258         fprintf('PLOT MAGNITUDE AND PHASE DISABLED\n\n');
259 end
```

```
260
261
262 %% plot coherence
263 if DrawFig == 1 & (any(strcmp(sheets,'Coherence')) | any(strcmp(sheets,'coherence')))
264         fprintf('START PLOTTING COHERENCE\n');
265
266     for q = 1:CohePointN
267         CoheFig = figure(200 + q);
268         if PicVis == 0
269             set(CoheFig, 'Visible', 'off');
270         else
271         end
272         plot(CoheFullData(CoheStartRow:CoheEndRow,q*2-1),CoheFullData(CoheStartRow:CoheEndRow,
                q*2));
273         xlabel('Frequency (Hz)');
274         ylabel('Coherence');
275         title(['Coherence of Point ', num2str(q)]);
276         if SavePic == 1
277             if strcmp(StartF, '0') & strcmp(EndF, 'max')
278                 saveas(CoheFig,fullfile(ResultPath, ['(Full) Coherence of Point ', num2str(q)
                        ]), 'jpg');
279             else
280                 saveas(CoheFig,fullfile(ResultPath, ['(', StartF, '-', EndF, ' Hz) ', '
                        Coherence of Point ', num2str(q)]), 'jpg');
281             end
282         else
283         end
284     end
285
286         fprintf('PLOT COHERENCE COMPLETED\n\n');
287
288 else
289     fprintf('NO COHERENCE DATA\n\n');
290
291 end
292
293
294 %% find peak
295 if FindPeak == 1
296     fprintf('START FINDING PEAK\n');
297
298     [ByPointSizeA, ByPointSizeB] = size(ByPoint);
299
300 %     m = 1;
301 %     OldMag = 0;
302     for PeakC = 1:ByPointSizeB
303
304         if strcmp(StartF, '0') & strcmp(EndF, 'max')
305             PeakResultPath = [ResultPath, '\', '(Full) peak', ' (by Point ', num2str(ByPoint(
                    PeakC)), ')', '.xlsx'];
306         else
307             PeakResultPath = [ResultPath, '\', '(', StartF, '-', EndF, ' Hz) ', 'peak', ' (by
                    Point ', num2str(ByPoint(PeakC)), ')', '.xlsx'];
308         end
309
310         PeakResult = {[]};
```

```
311
312         PeakResult(1,1) = {['Min Peak Distance: ', num2str(PeakDist)]};
313         PeakResult(2,1) = {'Frequency (Hz)'};
314
315         for x = 1:PointN
316             PeakResult(1,1+x*3-2) = {['point ', num2str(x)]};
317             PeakResult(2,1+x*3-2) = {'Magnitude (m/s^2/N)'};
318             PeakResult(2,1+x*3-1) = {'Phase'};
319             PeakResult(2,1+x*3) = {'Side'};
320         end
321
322         [PeakMag, PeakFreq] = findpeaks(FullData(StartRow:EndRow,ByPoint(PeakC)*3-1),FullData(
                StartRow:EndRow,ByPoint(PeakC)*3-2),'MinPeakDistance',PeakDist);
323         PeakN = size(PeakFreq,1); %how many peaks found
324
325         for y = 1:PeakN
326             j = find(FullData(:,1) == PeakFreq(y,1));
327
328             PeakResult{y+2,1} = round(FullData(j,1),2); %freq, rounding to the second decimal
329
330             for z = 1:PointN
331
332                 PeakResult{y+2,1+z*3-2} = round(FullData(j,z*3-1),2); %mag
333                 PeakResult{y+2,1+z*3-1} = round(FullData(j,z*3),2); %phase
334
335                 if FullData(j,z*3) > 0
336                     PeakResult(y+2,1+z*3) = {'+'};
337                 elseif FullData(j,z*3) < 0
338                     PeakResult(y+2,1+z*3) = {'-'};
339                 else
340                     PeakResult{y+2,1+z*3} = 0;
341                 end
342
343                 if z == PointN
344                     if FullData(j,z*3-3) * FullData(j,z*3) > 0 %decide is bending or torsion
                            or unknown
345                         PeakResult(y+2,1+z*3+1) = {'bending'};
346                     elseif FullData(j,z*3-3)*FullData(j,z*3) < 0
347                         PeakResult(y+2,1+z*3+1) = {'torsion'};
348                     else
349                         PeakResult(y+2,1+z*3+1) = {'???'};
350                     end
351                 else
352                 end
353
354             end
355         end
356
357         xlswrite(PeakResultPath, PeakResult);
358
359     end
360
361         fprintf('FIND PEAK COMPLETED\n\n');
362
363 else
364 end
```

```
365
366
367 %%
368 display('PROCESS END');
```

Lateral Modes: Plotting Frequency Response Figure, Finding Resonance Frequencies and Identifying Mode Shapes

```
clear
clc

Path = '  '; %Folder path where Excel at
Name = '  '; %Excel name
fPath = [Path, '\', Name, '.xlsx']; %Full Excel Path

% Path = input('folder path: ', 's'); %Enter Folder path where
% Name = input('file name: ', 's'); %Enter Excel name
% fPath = [Path, '\', Name, '.xlsx']; %Full Excel Path

DrawFig = -1;
FindPeak = -1;

StartF = '0';
EndF = '0';
StartFreq = 0;
EndFreq = 0;

PicVis = -1;
SavePic = -1;

PeakDist = -1;
ByPoint = -1;

while str2num(StartF) >= str2num(EndF) %input frequency range
    StartF = input('start freq [0/number]: ', 's');
    EndF = input('end freq [number/max]: ', 's');
end

while DrawFig < 0 | DrawFig > 1 %plot or not
    DrawFig = input('do drawing figure? [no:0/yes:1]: ');
end

if DrawFig == 1
        while PicVis < 0 | PicVis > 1
        PicVis = input('Show figure? [no:0/yes:1]: '); %show figures or not while program
            plotting
    end
        while SavePic < 0 | SavePic > 1
        SavePic = input('Save figure? [no:0/yes:1]: '); %save figures or not
    end
else
end

while FindPeak < 0 | FindPeak > 1 %find peaks or not
    FindPeak = input('do finding peak? [no:0/yes:1]: ');
end

if FindPeak == 1

        while PeakDist <= 0
```

```
52          PeakDist = input('Peak Distance: '); %Peak distance
53      end
54
55          while ByPoint <= 0
56          ByPoint = input('By which point (ex 1 or [1 2 3]): '); %by which point's data to
                determine peak
57      end
58
59  else
60  end
61
62  fprintf('\n');
63
64
65  %% load magnitude and phase
66  if DrawFig == 1 | FindPeak == 1 %load data only when we want to plot or find peaks
67      fprintf('START LOADING MAGNITUDE AND PHASE DATA\n');
68
69      [status,sheets] = xlsfinfo(fPath);
70      MagPhaseSheet = sheets{1};
71      FullData = xlsread(fPath,MagPhaseSheet); %load magnitudeand phase
72      ColumnN = size(FullData,2);
73      RowN = size(FullData,1);
74      PointN = ColumnN/3;
75
76      %get start row
77      StartFreq = str2num(StartF);
78      StartRow = 8;
79          if  FullData(StartRow,1) < StartFreq
80          while FullData(StartRow,1) <= StartFreq
81
82           StartRow = StartRow + 1;
83
84          end
85          StartRow = StartRow - 1;
86          StartFreq = FullData(StartRow,1);
87      else
88      end
89
90      %get end row
91      EndRow = RowN;
92      if strcmp(EndF, 'max')
93          EndFreq = FullData(EndRow,1);
94      else
95          EndFreq = str2num(EndF);
96          while FullData(EndRow,1) >= EndFreq
97              EndRow = EndRow - 1;
98          end
99          EndRow = EndRow + 1;
100         EndFreq = FullData(EndRow,1);
101     end
102
103     fprintf('LOAD MAGNITUDE AND PHASE DATA COMPLETED\n\n');
104
105 else
106 end
```

```
107
108 %% load coherence data
109
110 if DrawFig == 1 & (any(strcmp(sheets,'Coherence')) | any(strcmp(sheets,'coherence'))) %load
      coherence data only when we want to plot and there are coherence data sheet
111     fprintf('START LOADING COHERENCE DATA\n');
112
113     CoheSheet = sheets{2};
114     CoheFullData = xlsread(fPath,CoheSheet);
115     CoheColumnN = size(CoheFullData,2);
116     CoheRowN = size(CoheFullData,1);
117     CohePointN = CoheColumnN/2;
118
119     CoheStartFreq = str2num(StartF);
120     CoheStartRow = 1;
121         if  CoheFullData(CoheStartRow,1) < CoheStartFreq
122         while CoheFullData(CoheStartRow,1) <= CoheStartFreq
123
124          CoheStartRow = CoheStartRow + 1;
125
126         end
127         CoheStartRow = CoheStartRow - 1;
128         CoheStartFreq = CoheFullData(CoheStartRow,1);
129     else
130     end
131
132     CoheEndRow = CoheRowN;
133     if strcmp(EndF, 'max')
134         CoheEndFreq = CoheFullData(CoheEndRow,1);
135     else
136         CoheEndFreq = str2num(EndF);
137         while CoheFullData(CoheEndRow,1) >= CoheEndFreq
138             CoheEndRow = CoheEndRow - 1;
139         end
140         CoheEndRow = CoheEndRow + 1;
141         CoheEndFreq = CoheFullData(CoheEndRow,1);
142     end
143
144     fprintf('LOAD COHERENCE DATA COMPLETED\n\n');
145
146 else
147 end
148
149
150 %% result folder
151 if SavePic == 1 | FindPeak == 1
152     if exist([Path, '\', 'Result_L', '\', StartF, '-', EndF, ' Hz']) == 7
153         fprintf('RESULT FOLDER ALREADY EXIST\n\n');
154         ResultPath = [Path, '\', 'Result_L', '\', StartF, '-', EndF, ' Hz'];
155     else
156         fprintf('RESULT FOLDER DOES NOT EXIST\nCREAT FOLDER\n');
157         mkdir(Path, ['Result_L', '\', StartF, '-', EndF, ' Hz']);
158         fprintf('CREAT FOLDER COMPLETED\n\n');
159     end
160 else
161 end
```

```
162
163 ResultPath = [Path, '\', 'Result_L', '\', StartF, '-', EndF, ' Hz'];
164
165
166 %% plot magnitude and phase
167 if DrawFig == 1
168
169     fprintf('START PLOTTING MAGNITUDE AND PHASE\n');
170
171     for i = 1:PointN
172         figMag = figure(i); %Magnitude
173         if PicVis == 0
174             set(figMag, 'Visible', 'off'); %no show while plotting
175         else
176         end
177         plot(FullData(StartRow:EndRow,i*3-2),FullData(StartRow:EndRow,i*3-1));
178 %           plot(FullData(StartRow:EndRow,i*3-2),log(FullData(StartRow:EndRow,i*3-1))); % Y axis
     by log
179         xlabel('Frequency (Hz)'); %X title
180         ylabel('Magnitude (m/s^2/N)'); %Y title
181         title(['Magnitude of Point ', num2str(i)]); %figure title
182         if SavePic == 1
183             if strcmp(StartF, '0') & strcmp(EndF, 'max')
184                 saveas(figMag,fullfile(ResultPath, ['(Full) Magnitude of Point ', num2str(i)])
                        , 'jpg'); %save
185             else
186                 saveas(figMag,fullfile(ResultPath, ['(', StartF, '-', EndF, ' Hz) ', '
                        Magnitude of Point ', num2str(i)]), 'jpg'); %save
187             end
188         else
189         end
190
191         figPhase = figure(100+i); %Phase
192         if PicVis == 0
193             set(figPhase, 'Visible', 'off');
194         else
195         end
196         plot(FullData(StartRow:EndRow,i*3-2),FullData(StartRow:EndRow,i*3));
197         xlabel('Frequency (Hz)');
198         ylabel('Phase');
199         title(['Phase of Point ', num2str(i)]);
200         if SavePic == 1
201             if strcmp(StartF, '0') & strcmp(EndF, 'max')
202                 saveas(figPhase,fullfile(ResultPath, ['(Full) Phase of Point ', num2str(i)]),
                        'jpg');
203             else
204                 saveas(figPhase,fullfile(ResultPath, ['(', StartF, '-', EndF, ' Hz) ', 'Phase
                        of Point ', num2str(i)]), 'jpg');
205             end
206         else
207         end
208     end
209
210         fprintf('PLOT MAGNITUDE AND PHASE COMPLETED\n\n');
211
212 else
```

```
213         fprintf('PLOT MAGNITUDE AND PHASE DISABLED\n\n');
214 end
215
216
217 %% plot coherence
218 if DrawFig == 1 & (any(strcmp(sheets,'Coherence')) | any(strcmp(sheets,'coherence')))
219         fprintf('START PLOTTING COHERENCE\n');
220
221     for q = 1:CohePointN
222         CoheFig = figure(200 + q);
223         if PicVis == 0
224             set(CoheFig, 'Visible', 'off');
225         else
226         end
227         plot(CoheFullData(CoheStartRow:CoheEndRow,q*2-1),CoheFullData(CoheStartRow:CoheEndRow,
                q*2));
228         xlabel('Frequency (Hz)');
229         ylabel('Coherence');
230         title(['Coherence of Point ', num2str(q)]);
231         if SavePic == 1
232             if strcmp(StartF, '0') & strcmp(EndF, 'max')
233                 saveas(CoheFig,fullfile(ResultPath, ['(Full) Coherence of Point ', num2str(q)
                        ]), 'jpg');
234             else
235                 saveas(CoheFig,fullfile(ResultPath, ['(', StartF, '-', EndF, ' Hz) ', '
                        Coherence of Point ', num2str(q)]), 'jpg');
236             end
237         else
238         end
239     end
240
241         fprintf('PLOT COHERENCE COMPLETED\n\n');
242
243 else
244     fprintf('NO COHERENCE DATA\n\n');
245
246 end
247
248
249 %% find peak
250 if FindPeak == 1
251     fprintf('START FINDING PEAK\n');
252
253     [ByPointSizeA, ByPointSizeB] = size(ByPoint);
254
255 %     m = 1;
256 %     OldMag = 0;
257     for PeakC = 1:ByPointSizeB
258
259         if strcmp(StartF, '0') & strcmp(EndF, 'max')
260             PeakResultPath = [ResultPath, '\', '(Full) peak', ' (by Point ', num2str(ByPoint(
                    PeakC)), ')', '.xlsx'];
261         else
262             PeakResultPath = [ResultPath, '\', '(', StartF, '-', EndF, ' Hz) ', 'peak', ' (by
                    Point ', num2str(ByPoint(PeakC)), ')', '.xlsx'];
263         end
```

```
264
265         PeakResult = {[]};
266
267         PeakResult(1,1) = {['Min Peak Distance: ', num2str(PeakDist)]};
268         PeakResult(2,1) = {'Frequency (Hz)'};
269
270         for x = 1:PointN
271             PeakResult(1,1+x*3-2) = {['point ', num2str(x)]};
272             PeakResult(2,1+x*3-2) = {'Magnitude (m/s^2/N)'};
273             PeakResult(2,1+x*3-1) = {'Phase'};
274             PeakResult(2,1+x*3) = {'Side'};
275         end
276
277         [PeakMag, PeakFreq] = findpeaks(FullData(StartRow:EndRow,ByPoint(PeakC)*3-1),FullData(
                StartRow:EndRow,ByPoint(PeakC)*3-2),'MinPeakDistance',PeakDist);
278         PeakN = size(PeakFreq,1); %how many peaks found
279
280         for y = 1:PeakN
281             j = find(FullData(:,1) == PeakFreq(y,1));
282
283             PeakResult{y+2,1} = round(FullData(j,1),2); %freq, rounding to the second decimal
284
285             for z = 1:PointN
286                 PeakResult{y+2,1+z*3-2} = round(FullData(j,z*3-1),2); %mag
287                 PeakResult{y+2,1+z*3-1} = round(FullData(j,z*3),2); %phase
288
289                 if FullData(j,z*3) > 0
290                     PeakResult(y+2,1+z*3) = {'+'};
291                 elseif FullData(j,z*3) < 0
292                     PeakResult(y+2,1+z*3) = {'-'};
293                 else
294                     PeakResult{y+2,1+z*3} = 0;
295                 end
296
297             end
298
299         end
300
301         xlswrite(PeakResultPath, PeakResult);
302
303     end
304
305         fprintf('FIND PEAK COMPLETED\n\n');
306
307 else
308 end
309
310
311 %%
312 display('PROCESS END');
```

Appendix B Simulation and Experimental Results of Sandwich Structures Using Unmodified Epoxy Resin

Flat Structures

Unmodified resin, flat, intact					
Facesheet Stacking	Mode	FE (Hz)	Exp. (SD) (Hz)	Difference (%)	Shape
$[0°]_4$	1	1645.8	1512.9 (11.9)	-8.1	1st bending
	2	2095.4	1880.9 (87.2)	-10.2	1st torsion
	3	2986.4	2910.7 (22.9)	-2.5	1st lateral
	4	3890.3	3603.1 (119.8)	-7.4	2nd bending
	5	4273.6	3921.2 (145.3)	-8.2	2nd torsion
$[90°]_4$	1	452.3	447.5 (4.4)	-1.1	1st bending
	2	1092.6	1134.1 (3.5)	3.8	1st lateral
	3	1223.7	1227.7 (10.6)	0.3	2nd bending
	4	2072.0	1818.9 (84.4)	-12.2	1st torsion
	5	2336.4	2460.3 (191.7)	5.3	3rd bending
$[+45°/-45°]_s$	1	655.84	616.8 (3.1)	-6.0	1st bending
	2	1431.9	1394.5 (9.2)	-2.6	1st lateral
	3	1759.9	1616.4 (81.3)	-8.2	2nd bending
	4	3320.6	3224.4 (104.1)	-2.9	3rd bending
	5	3435.7	3212.2 (321.5)	-6.5	1st torsion

Unmodified resin, flat, 40 mm single debond					
Facesheet Stacking	Mode	FE (Hz)	Exp. (Hz)	Difference (%)	Shape
$[0°]_4$	1	1641.5	1485.9	-9.5	1st bending
	2	1930.3	1645.7	-14.7	1st torsion
	3	2800.0	2840.6	1.5	2nd bending
	4	2983.5	2621.5	-12.1	1st lateral
	5	4204.0	4128.5	-1.8	2nd torsion
$[90°]_4$	1	451.9	457.0	1.1	1st bending
	2	1088.8	1070.3	-1.7	1st lateral
	3	1165.9	1171.5	0.5	2nd bending
	4	1831.0	1505.9	-17.8	1st torsion
	5	2318.0	2559.4	10.4	3rd bending
$[+45°/-45°]_s$	1	655.0	598.8	-8.6	1st bending
	2	1426.9	1315.6	-7.8	1st lateral
	3	1608.0	1497.7	-6.9	2nd bending
	4	2693.1	2153.5	-20.0	1st torsion
	5	3271.3	3530.5	7.9	3rd bending

Unmodified resin, flat, 50 mm single debond					
Facesheet Stacking	Mode	FE (Hz)	Exp. (Hz)	Difference (%)	Shape
$[0°]_4$	1	1633.7	1549.6	-5.1	1st bending
	2	1861.4	1768.8	-5.0	1st torsion
	3	2400.6	2280.5	-5.0	2nd bending
	4	2980.6	2852.7	-4.3	1st lateral
	5	4126.3	4016.0	-2.7	2nd torsion
$[90°]_4$	1	451.6	455.5	0.9	1st bending
	2	1087.8	1132.8	4.1	1st lateral
	3	1125.2	1135.2	0.9	2nd bending
	4	1742.9	1641.0	-5.8	1st torsion
	5	2289.4	2463.7	7.6	3rd bending
$[+45°/-45°]_s$	1	654.4	630.5	-3.7	1st bending
	2	1425.3	1393.0	-2.3	1st lateral
	3	1511.4	1485.2	-1.7	2nd bending
	4	2479.2	2422.7	-2.3	1st torsion
	5	3195.2	3181.3	-0.4	3rd bending

Unmodified resin, flat, 60 mm single debond					
Facesheet Stacking	Mode	FE (Hz)	Exp. (Hz)	Difference (%)	Shape
$[0°]_4$	1	1617.6	1499.6	-7.3	1st bending
	2	1793.9	1702.7	-5.1	1st torsion
	3	2087.0	2077.3	-0.5	2nd bending
	4	2976.0	2768.4	-7.0	1st lateral
	5	4008.7	4174.2	4.1	2nd torsion
$[90°]_4$	1	451.1	462.5	2.5	1st bending
	2	1078.3	1125.0	4.3	2nd bending
	3	1086.8	1144.92	5.3	1st lateral
	4	1665.4	1611.7	-3.2	1st torsion
	5	2238.7	2323.4	3.8	3rd bending
$[+45°/-45°]_s$	1	653.2	618.4	-5.3	1st bending
	2	1409.7	1396.1	-1.0	2nd bending
	3	1423.5	1384.8	-2.7	1st lateral
	4	2307.3	2225.0	-3.6	1st torsion
	5	3065.1	2991.4	-2.4	3rd bending

Unmodified resin, flat, 70 mm single debond					
Facesheet Stacking	Mode	FE (Hz)	Exp. (Hz)	Difference (%)	Shape
$[0°]_4$	1	1588.5	1367.6	-13.9	1st bending
	2	1730.7	1521.1	-12.1	1st torsion
	3	1849.8	1721.1	-7.0	2nd bending
	4	2969.2	2806.3	-5.5	1st lateral
	5	3857.0	3769.1	-2.3	2nd torsion
$[90°]_4$	1	450.3	455.5	1.1	1st bending
	2	1030.3	1035.2	0.5	2nd bending
	3	1085.9	1139.5	4.9	1st lateral
	4	1599.7	1535.2	-4.0	1st torsion
	5	2165.6	2276.6	5.1	3rd bending
$[+45°/-45°]_s$	1	651.1	599.6	-7.9	1st bending
	2	1314.4	1245.3	-5.3	2nd bending
	3	1421.2	1380.5	-2.9	1st lateral
	4	2171.4	2112.9	-2.7	1st torsion
	5	2892.0	2845.3	-1.6	3rd bending

Unmodified resin, flat, 80 mm single debond					
Facesheet Stacking	Mode	FE (Hz)	Exp. (Hz)	Difference (%)	Shape
$[0°]_4$	1	1542.4	1389.5	-9.9	1st bending
	2	1671.9	1609.0	-3.8	2nd bending
	3	1673.2	1565.6	-6.4	1st torsion
	4	2959.3	2868.4	-3.1	1st lateral
	5	3686.2	3600.0	-2.3	2nd torsion
$[90°]_4$	1	449.1	475.8	5.9	1st bending
	2	985.2	907.8	-7.9	2nd bending
	3	1084.9	1119.5	3.2	1st lateral
	4	1544.9	1463.3	-5.3	1st torsion
	5	2077.8	2200.0	5.9	3rd bending
$[+45°/-45°]_s$	1	647.74	683.2	5.5	1st bending
	2	1231.2	952.7	-22.6	2nd bending
	3	1418.6	1346.9	-5.1	1st lateral
	4	2064	1946.5	-5.7	1st torsion
	5	2705.6	2354.7	-13.0	3rd bending

Unmodified resin, flat, double debonds: Δ20					
Facesheet Stacking	Mode	FE (Hz)	Exp. (Hz)	Difference (%)	Shape
$[0°]_4$	1	1461.3	1338.7	-8.4	1st bending
	2	1845.3	2080.5	12.7	1st torsion
	3	2967.7	2809.0	-5.3	1st lateral
	4	3302.7	3175.4	-3.9	2nd bending
	5	3745	3712.9	-0.9	2nd torsion
$[90°]_4$	1	446.9	452.3	1.2	1st bending
	2	1087.1	1086.7	0.0	1st lateral
	3	1196.8	1165.2	-2.6	2nd bending
	4	1726.4	1553.9	-10.0	1st torsion
	5	2036.6	2032.0	-0.2	3rd bending
$[+45°/-45°]_s$	1	641.1	591.0	-7.8	1st bending
	2	1424.8	1322.3	-7.2	1st lateral
	3	1688.4	1548.8	-8.3	2nd bending
	4	2448.2	1907.4	-22.1	1st torsion
	5	2640.7	2697.3	2.1	3rd bending

Unmodified resin, flat, double debonds: Δ40					
Facesheet Stacking	Mode	FE (Hz)	Exp. (Hz)	Difference (%)	Shape
$[0°]_4$	1	1405.7	1342.2	-4.5	1st bending
	2	1886.8	2187.5	15.9	1st torsion
	3	2958.6	2734.4	-7.6	1st lateral
	4	3639.4	3701.2	1.7	2nd torsion
	5	3749.3	3582.8	-4.4	2nd bending
$[90°]_4$	1	444.9	456.3	2.6	1st bending
	2	1088.4	1100.8	1.1	1st lateral
	3	1216.9	1216.4	0.0	2nd bending
	4	1771.1	1575.0	-11.1	1st torsion
	5	2110.9	2026.2	-4.0	3rd bending
$[+45°/-45°]_s$	1	635.5	586.7	-7.7	1st bending
	2	1426.3	1284.0	-10.0	1st lateral
	3	1742.6	1589.5	-8.8	2nd bending
	4	2550.9	2262.5	-11.3	1st torsion
	5	2795.9	2907.4	4.0	3rd bending

Unmodified resin, flat, double debonds: diagonal (D)					
Facesheet Stacking	Mode	FE (Hz)	Exp. (Hz)	Difference (%)	Shape
$[0°]_4$	1	1461.0	1392.2	-4.7	1st bending
	2	1843.1	1559.8	-15.4	1st torsion
	3	2976.0	2718.8	-8.6	1st lateral
	4	3289.6	3160.2	-3.9	2nd bending
	5	3726.3		-4.7	2nd torsion
$[90°]_4$	1	446.6	456.6	2.2	1st bending
	2	1087.0	1067.6	-1.8	1st lateral
	3	1183.8	1197.7	1.2	2nd bending
	4	1720.4	1561.3	-9.2	1st torsion
	5	2029.8	2075.4	2.2	3rd bending
$[+45°/-45°]_s$	1	640.8	575.4	-10.2	1st bending
	2	1424.6	1310.9	-8.0	1st lateral
	3	1677.4	1523.1	-9.2	2nd bending
	4	2439.2	2122.3	-13.0	1st torsion
	5	2627.0	2410.2	-8.3	3rd bending

Unmodified resin, flat, double debonds: symmetric (S)					
Facesheet Stacking	Mode	FE (Hz)	Exp. (Hz)	Difference (%)	Shape
$[0°]_4$	1	1349.7	1232.0	-8.7	1st bending
	2	1819.5	1504.3	-17.3	1st torsion
	3	2854.3	2771.5	-2.9	2nd bending
	4	2968.1	2746.9	-7.5	1st lateral
	5	3772.9	3802.7	0.8	2nd torsion
$[90°]_4$	1	443.2	442.2	-0.2	1st bending
	2	1088.0	1080.5	-0.7	1st lateral
	3	1162.7	1148.4	-1.2	2nd bending
	4	1569.1	1439.8	-8.2	1st torsion
	5	1849.1	1835.2	-0.8	3rd bending
$[+45°/-45°]_s$	1	628.6	587.1	-6.6	1st bending
	2	1425.9	1330.5	-6.7	1st lateral
	3	1589.6	1531.3	-3.7	2nd bending
	4	2140.7	1976.6	-7.7	1st torsion
	5	2348.6	2182.0	-7.1	3rd bending

15°-curved Structures

Unmodified resin, 15°-curved, intact					
Facesheet Stacking	Mode	FE (Hz)	Exp. (SD) (Hz)	Difference (%)	Shape
$[0°]_4$	1	1641.3	1504.4 (22.0)	-8.3	1st bending
	2	2085.8	1953.8 (22.4)	-6.3	1st torsion
	3	3031.8	2895.7 (21.2)	-4.5	1st lateral*
	4	3884.7	3688.8 (40.5)	-5.0	2nd bending
	5	4338.8	4126.4 (35.1)	-4.9	2nd torsion
$[90°]_4$	1	451.1	461.6 (4.1)	2.3	1st bending
	2	1126.1	1147.4 (10.4)	1.9	1st lateral*
	3	1222.0	1266.5 (8.1)	3.6	2nd bending
	4	2053.8	1967.7 (30.5)	-4.2	1st torsion
	5	2334.5	2434.2 (14.9)	4.3	3rd bending
$[+45°/-45°]_s$	1	654.14	simulation only		1st bending
	2	1476.4			1st lateral*
	3	1757.6			2nd bending
	4	3318.1			3rd bending
	5	3367.7			1st torsion

Unmodified resin, 15°-curved, 40 mm single debond					
Facesheet Stacking	Mode	FE (Hz)	Exp. (Hz)	Difference (%)	Shape
$[0°]_4$	1	1637.2	1564.5	-4.4	1st bending
	2	1926.5	1789.8	-7.1	1st torsion
	3	2814.8	2695.7	-4.2	2nd bending
	4	3021.1	2764.8	-8.5	1st lateral*
	5	4279.1	4044.9	-5.5	2nd torsion
$[90°]_4$	1	450.7	455.9	1.1	1st bending
	2	1121.8	1133.2	1.0	1st lateral*
	3	1165.7	1187.5	1.9	2nd bending
	4	1816.4	1747.3	-3.8	1st torsion
	5	2316.9	2411.7	4.1	3rd bending
$[+45°/-45°]_s$	1	653.3	simulation only		1st bending
	2	1470.5			1st lateral*
	3	1609.5			2nd bending
	4	2663.8			1st torsion
	5	3270.6			3rd bending

Unmodified resin, 15°-curved, 60 mm single debond					
Facesheet Stacking	Mode	FE (Hz)	Exp. (Hz)	Difference (%)	Shape
$[0°]_4$	1	1614.0	1421.5	-11.9	1st bending
	2	1793.0	1700.0	-5.2	1st torsion
	3	2099.0	2031.6	-3.2	2nd bending
	4	2994.4	2483.6	-17.1	1st lateral*
	5	4106.9	4029.7	-1.9	2nd torsion
$[90°]_4$	1	450.0	437.1	-2.9	1st bending
	2	1079.0	1096.1	1.6	2nd bending
	3	1119.0	1122.3	0.3	1st lateral*
	4	1652.8	1616.4	-2.2	1st torsion
	5	2239.3	2366.8	5.7	3rd bending
$[+45°/-45°]_s$	1	651.5	simulation only		1st bending
	2	1413.0			2nd bending
	3	1464.9			1st lateral*
	4	2286.7			1st torsion
	5	3069.3			3rd bending

Unmodified resin, 15°-curved, 80 mm single debond					
Facesheet Stacking	Mode	FE (Hz)	Exp. (Hz)	Difference (%)	Shape
$[0°]_4$	1	1540.7	1091.8	-29.1	1st bending
	2	1673.9	1567.6	-6.4	1st torsion
	3	1680.5	1680.1	0.0	2nd bending
	4	2936.6	2959.4	0.8	1st lateral*
	5	3829.7	3739.8	-2.3	2nd torsion
$[90°]_4$	1	448.0	378.1	-15.6	1st bending
	2	986.4	890.6	-9.7	2nd bending
	3	1115.6	1057.8	-5.2	1st lateral*
	4	1534.3	1505.1	-1.9	1st torsion
	5	2080.4	2227.3	7.1	3rd bending
$[+45°/-45°]_s$	1	646.2	simulation only		1st bending
	2	1234.6			2nd bending
	3	1456.3			1st lateral*
	4	2048.8			1st torsion
	5	2713.2			3rd bending

Unmodified resin, 15°-curved, double debonds: Δ20					
Facesheet Stacking	Mode	FE (Hz)	Exp. (Hz)	Difference (%)	Shape
$[0°]_4$	1	1461.4	1342.2	-8.2	1st bending
	2	1840.9	1725.8	-6.3	1st torsion
	3	3018.5	2803.9	-7.1	1st lateral*
	4	3300.8	3157.8	-4.3	2nd bending
	5	3803.5	3642.2	-4.2	2nd torsion
$[90°]_4$	1	445.9	449.2	0.8	1st bending
	2	1118.9	1138.3	1.7	1st lateral*
	3	1195.3	1225.0	2.5	2nd bending
	4	1714.2	1659.0	-3.2	1st torsion
	5	2038.5	2071.9	1.6	3rd bending
$[+45°/-45°]_s$	1	639.8	simulation only		1st bending
	2	1466.0			1st lateral*
	3	1686.4			2nd bending
	4	2427.8			1st torsion
	5	2646.2			3rd bending

Unmodified resin, 15°-curved, double debonds: Δ40					
Facesheet Stacking	Mode	FE (Hz)	Exp. (Hz)	Difference (%)	Shape
$[0°]_4$	1	1406.1	1360.9	-3.2	1st bending
	2	1880.6	1782.4	-5.2	1st torsion
	3	3022.2	2787.5	-7.8	1st lateral*
	4	3681.8	3785.6	2.8	2nd torsion
	5	3744.8	3651.2	-2.5	2nd bending
$[90°]_4$	1	443.8	446.9	0.7	1st bending
	2	1119.8	1144.5	2.2	1st lateral*
	3	1215.3	1239.1	2.0	2nd bending
	4	1760.1	1717.2	-2.4	1st torsion
	5	2110.7	2161.3	2.4	3rd bending
$[+45°/-45°]_s$	1	634.2	simulation only		1st bending
	2	1467.0			1st lateral*
	3	1740.4			2nd bending
	4	2533.5			1st torsion
	5	2797.6			3rd bending

Unmodified resin, 15°-curved, double debonds: diagonal (D)					
Facesheet Stacking	Mode	FE (Hz)	Exp. (Hz)	Difference (%)	Shape
$[0°]_4$	1	1458.1	1322.7	-9.3	1st bending
	2	1834.9	1749.6	-4.6	1st torsion
	3	2984.9	2792.2	-6.5	1st lateral*
	4	3290.8	3197.7	-2.8	2nd bending
	5	3840.4	3682.0	-4.1	2nd torsion
$[90°]_4$	1	445.7	452.3	1.5	1st bending
	2	1119.8	1142.6	2.0	1st lateral*
	3	1194.9	1209.4	1.2	2nd bending
	4	1714.1	1659.8	-3.2	1st torsion
	5	2034.7	2071.1	1.8	3rd bending
$[+45°/-45°]_s$	1	639.5	simulation only		1st bending
	2	1467.9			1st lateral*
	3	1685.4			2nd bending
	4	2429.4			1st torsion
	5	2638.4			3rd bending

Unmodified resin, 15°-curved, double debonds: symmetric (S)					
Facesheet Stacking	Mode	FE (Hz)	Exp. (Hz)	Difference (%)	Shape
$[0°]_4$	1	1349.9	1185.2	-12.2	1st bending
	2	1810.2	1637.9	-9.5	1st torsion
	3	2851.8	2618.8	-8.2	2nd bending
	4	2984.5	2610.6	-12.5	1st lateral*
	5	3873.0			2nd torsion
$[90°]_4$	1	442.4	440.2	-0.5	1st bending
	2	1120.1	1147.3	2.4	1st lateral*
	3	1171.7	1158.2	-1.2	2nd bending
	4	1562.7	1510.6	-3.3	1st torsion
	5	1884.2	1859.0	-1.3	3rd bending
$[+45°/-45°]_s$	1	627.5	simulation only		1st bending
	2	1468.3			1st lateral*
	3	1593.5			2nd bending
	4	2146.7			1st torsion
	5	2360.9			3rd bending

***: combined with torsion movement**

30°-curved Structures

Unmodified resin, 30°-curved, intact					
Facesheet Stacking	Mode	FE (Hz)	Exp. (SD) (Hz)	Difference (%)	Shape
$[0°]_4$	1	1628.7	1560.2 (25.5)	-4.2	1st bending
	2	2057.9	1994.8 (43.8)	-3.1	1st torsion
	3	3132.7	2935.2 (15.9)	-6.3	1st lateral*
	4	3869.5	3776.4 (64.5)	-2.4	2nd bending
	5	4551.5	4476.3 (47.3)	-1.7	2nd torsion
$[90°]_4$	1	447.9	459.1 (4.7)	2.5	1st bending
	2	1217.6	1263.8 (13.1)	3.8	2nd bending
	3	1220.0	1265.1 (24.2)	3.7	1st lateral*
	4	2004.7	1968.1 (19.9)	-1.8	1st torsion
	5	2329.9	2424.4 (18.8)	4.1	3rd bending
$[+45°/-45°]_s$	1	649.4	simulation only		1st bending
	2	1601.7			1st lateral*
	3	1751.3			2nd bending
	4	3233.8			1st torsion
	5	3311.6			3rd bending

Unmodified resin, 30°-curved, 40 mm single debond					
Facesheet Stacking	Mode	FE (Hz)	Exp. (Hz)	Difference (%)	Shape
$[0°]_4$	1	1624.7	1472.3	-9.4	1st bending
	2	1902.4	1840.6	-3.2	1st torsion
	3	2811.3	2702.3	-3.9	2nd bending
	4	3107.5	2888.3	-7.1	1st lateral*
	5	4506.6	4493.4	-0.3	2nd torsion
$[90°]_4$	1	447.5	452.7	1.2	1st bending
	2	1161.9	1192.2	2.6	2nd bending
	3	1214.7	1255.1	3.3	1st lateral*
	4	1774.1	1757.8	-0.9	1st torsion
	5	2312.4	2401.6	3.9	3rd bending
$[+45°/-45°]_s$	1	648.6	simulation only		1st bending
	2	1593.9			1st lateral*
	3	1605.1			2nd bending
	4	2586.1			1st torsion
	5	3264.6			3rd bending

Unmodified resin, 30°-curved, 60 mm single debond					
Facesheet Stacking	Mode	FE (Hz)	Exp. (Hz)	Difference (%)	Shape
$[0°]_4$	1	1602.5	1253.9	-21.8	1st bending
	2	1773.8	1726.6	-2.7	1st torsion
	3	2106.2	2105.9	0.0	2nd bending
	4	3045.9	2637.1	-13.4	1st lateral*
	5	4374.2	4404.3	0.7	2nd torsion
$[90°]_4$	1	446.8	420.3	-5.9	1st bending
	2	1077.3	1104.7	2.5	2nd bending
	3	1210.3	1209.0	-0.1	1st lateral*
	4	1618.4	1587.1	-1.9	1st torsion
	5	2237.3	2358.6	5.4	3rd bending
$[+45°/-45°]_s$	1	646.8	simulation only		1st bending
	2	1413.0			2nd bending
	3	1584.9			1st lateral*
	4	2233.4			1st torsion
	5	3069.6			3rd bending

Unmodified resin, 30°-curved, 80 mm single debond					
Facesheet Stacking	Mode	FE (Hz)	Exp. (Hz)	Difference (%)	Shape
$[0°]_4$	1	1532.0	959.0	-37.4	1st bending
	2	1658.0	1593.4	-3.9	1st torsion
	3	1687.4	1660.9	-1.6	2nd bending
	4	2926.8	2288.7	-21.8	1st lateral*
	5	4061.2	4077.7	0.4	3rd bending
$[90°]_4$	1	444.8	365.2	-17.9	1st bending
	2	985.8	921.1	-6.6	2nd bending
	3	1204.1	1124.6	-6.6	1st lateral*
	4	1505.1	1472.7	-2.2	1st torsion
	5	2081.6	2261.7	8.7	3rd bending
$[+45°/-45°]_s$	1	641.7	simulation only		1st bending
	2	1236.2			2nd bending
	3	1569.8			1st lateral*
	4	2007.6			1st torsion
	5	2719.8			3rd bending

Unmodified resin, 30°-curved, double debonds: Δ20					
Facesheet Stacking	Mode	FE (Hz)	Exp. (Hz)	Difference (%)	Shape
$[0°]_4$	1	1454.5	1302.3	-10.5	1st bending
	2	1820.5	1733.6	-4.8	1st torsion
	3	3056.5	2739.8	-10.4	1st lateral*
	4	3295.1	3078.5	-6.6	2nd bending
	5	4056.7	3748.4	-7.6	3rd bending
$[90°]_4$	1	442.7	432.0	-2.4	1st bending
	2	1191.3	1200.8	0.8	2nd bending
	3	1209.2	1246.9	3.1	1st lateral*
	4	1681.2	1617.2	-3.8	1st torsion
	5	2038.9	2012.1	-1.3	3rd bending
$[+45°/-45°]_s$	1	635.5	simulation only		1st bending
	2	1585.0			1st lateral*
	3	1681.1			2nd bending
	4	2376.1			1st torsion
	5	2650.5			3rd bending

Unmodified resin, 30°-curved, double debonds: Δ40					
Facesheet Stacking	Mode	FE (Hz)	Exp. (Hz)	Difference (%)	Shape
$[0°]_4$	1	1400.6	1232.4	-12.0	1st bending
	2	1858.8	1763.7	-5.1	1st torsion
	3	3042.1	2727.0	-10.4	1st lateral*
	4	3730.6	3438.7	-7.8	2nd bending
	5	3974.5	3744.1	-5.8	2nd torsion
$[90°]_4$	1	440.8	440.6	0.0	1st bending
	2	1209.5	1214.1	0.4	1st lateral*
	3	1211.0	1244.1	2.7	2nd bending
	4	1728.0	1688.3	-2.3	1st torsion
	5	2108.2	2141.8	1.6	3rd bending
$[+45°/-45°]_s$	1	630.1	simulation only		1st bending
	2	1584.9			1st lateral*
	3	1734.1			2nd bending
	4	2483.6			1st torsion
	5	2796.0			3rd bending

Unmodified resin, 30°-curved, double debonds: diagonal (D)					
Facesheet Stacking	Mode	FE (Hz)	Exp. (Hz)	Difference (%)	Shape
$[0°]_4$	1	1447.7	1271.1	-12.2	1st bending
	2	1809.0	1700.8	-6.0	1st torsion
	3	2996.8	2681.3	-10.5	1st lateral*
	4	3271.1	2919.9	-10.7	2nd bending
	5	4027.9	3668.8	-8.9	2nd bending
$[90°]_4$	1	442.51	433.2	-2.1	1st bending
	2	1190.2	1182.0	-0.7	2nd bending
	3	1211.1	1247.3	3.0	1st lateral*
	4	1679.6	1627.3	-3.1	1st torsion
	5	2030.3	2074.6	2.2	3rd bending
$[+45°/-45°]_s$	1	634.9	simulation only		1st bending
	2	1589.2			1st lateral*
	3	1678.2			2nd bending
	4	2375.2			1st torsion
	5	2632.3			3rd bending

Unmodified resin, 30°-curved, double debonds: symmetric (S)					
Facesheet Stacking	Mode	FE (Hz)	Exp. (Hz)	Difference (%)	Shape
$[0°]_4$	1	1340.9	1241.8	-7.4	1st bending
	2	1783.2	1728.1	-3.1	1st torsion
	3	2835.9			2nd bending
	4	3010.3	2620.3	-13.0	1st lateral*
	5	4161.3			2nd torsion
$[90°]_4$	1	439.2	452.3	3.0	1st bending
	2	1166.8	1221.5	4.7	2nd bending
	3	1208.8	1256.3	3.9	1st lateral*
	4	1538.4	1545.3	0.4	1st torsion
	5	1881.2	2021.9	7.5	3rd bending
$[+45°/-45°]_s$	1	623.1	simulation only		1st bending
	2	1582.4			1st lateral*
	3	1589.1			2nd bending
	4	2114.1			1st torsion
	5	2358.4			3rd bending

***: combined with torsion movement**

Appendix C Publications

Journal Publications

S.N. Tsai, D. Carolan, S. Sprenger, A.C. Taylor. Fracture and fatigue behaviour of carbon fibre composites with nanoparticle-sized fibres. *Composite Structures*, 217:143-149, 2019.

S.N. Tsai and A.C. Taylor. Vibration behaviours of single/multi-debonded composite sandwich structures with nanoparticle-modified matrices. *Composite Structures*, 210:590-598, 2019.

Conference Papers

S.N. Tsai, D. Carolan, S. Sprenger, A.C. Taylor. Fracture and fatigue behaviour of carbon fibre composites with nanoparticle-sized fibres. In *Proceedings of SAMPE Europe Conference 2017*, Stuttgart, Germany, 2017.

Conference Abstracts

S.N. Tsai and A.C. Taylor. Vibration behaviours of composite sandwich beams with different face/core debonding and fibre orientations. In *Proceedings of 21st International Conference on Composite Structures*, Bologna, Italy, 2018.

Copyright Clearance Center RightsLink®

Home | Create Account | Help



Title: Fracture and fatigue behaviour of carbon fibre composites with nanoparticle-sized fibres

Author: Shang-Nan Tsai,Declan Carolan,Stephan Sprenger,Ambrose C. Taylor

Publication: Composite Structures

Publisher: Elsevier

Date: 1 June 2019

© 2019 Elsevier Ltd. All rights reserved.

LOGIN

If you're a copyright.com user, you can login to RightsLink using your copyright.com credentials.

Already **a RightsLink user** or want to learn more?

Please note that, as the author of this Elsevier article, you retain the right to include it in a thesis or dissertation, provided it is not published commercially. Permission is not required, but please ensure that you reference the journal as the original source. For more information on this and on your other retained rights, please visit: https://www.elsevier.com/about/our-business/policies/copyright#Author-rights

BACK | CLOSE WINDOW

Copyright © 2019 Copyright Clearance Center, Inc. All Rights Reserved. Privacy statement. Terms and Conditions.
Comments? We would like to hear from you. E-mail us at customercare@copyright.com

Copyright Clearance Center RightsLink®

Home Create Account Help



Title: Vibration behaviours of single/multi-debonded composite sandwich structures with nanoparticle-modified matrices

Author: Shang-Nan Tsai,Ambrose C. Taylor

Publication: Composite Structures

Publisher: Elsevier

Date: 15 February 2019

© 2018 Elsevier Ltd. All rights reserved.

LOGIN

If you're a copyright.com user, you can login to RightsLink using your copyright.com credentials.

Already **a RightsLink user** or want to learn more?

Please note that, as the author of this Elsevier article, you retain the right to include it in a thesis or dissertation, provided it is not published commercially. Permission is not required, but please ensure that you reference the journal as the original source. For more information on this and on your other retained rights, please visit: https://www.elsevier.com/about/our-business/policies/copyright#Author-rights

BACK CLOSE WINDOW

Copyright © 2018 Copyright Clearance Center, Inc. All Rights Reserved. Privacy statement. Terms and Conditions.
Comments? We would like to hear from you. E-mail us at customercare@copyright.com